BIMOLECULAR ENCOUNTERS:

ACID-BASE AND/OR ELECTRON TRANSFER IN RUTHENIUM (II) COMPLEXES.

EXPERIMENT AND THEORY.

by

Marta Kowalczyk

A dissertation submitted to the Graduate Faculty in Chemistry in partial fulfillment of the requirements for the degree of Doctor of Philosophy, The City University of New York

2013

This manuscript has been read and accepted for the
Graduate Faculty in Chemistry in satisfaction of the
dissertation requirement for the degree of Doctor of Philosophy.

03/18/1013
Date

Prof. Harry D. Gafney
Co-Chair of Examining Committee

Prof. Seogjoo Jang
Co-Chair of Examining Committee

03/18/2013
Date

Prof. Maria Tamargo
Executive Officer

Prof. Harry D. Gafney

Prof. Seogjoo Jang

Prof. Lynn Francesconi

Prof. Andrzej Jarzęcki
Supervisory Committee

THE CITY UNIVERSITY OF NEW YORK

Abstract

BIMOLECULAR ENCOUNTERS:

ACID-BASE AND/OR ELECTRON TRANSFER IN RUTHENIUM(II) COMPLEXES.

EXPERIMENT AND THEORY.

by

Marta Kowalczyk

Adviser: Harry D. Gafney and Seogjoo Jang

This work correlates experimental and theoretical studies of ruthenium diimines, $[Ru(bpy)_2L]^{2+}$ where L = bpy, or dpp. Experimental research concentrates on excited state acid-base and electron transfer properties. Although the driving force for reduction of Fe^{3+} and Ag^{+} are essentially equivalent, data presented here show that the bimolecular encounter between bis(2,2'-bipyridine)(2,3-bis(2-pyridyl)pyrazine)ruthenium(II), $[Ru(bpy)_2(dpp)]^{2+}$ in its dpp localized MLCT state, leads to coordination of Ag^{+}, but electron transfer to Fe^{3+}. Several redox reactions were performed between $[Ru(bpy)_2dpp]^{2+}$ and a strong oxidizing agents to analyze the spectroscopic signature of the oxidized form of the complex, $[Ru(bpy)_2dpp]^{3+}$. The experiments confirm electron transfer between excited state of bis(2,2'-bipyridine)(2,3-bis(2pyridyl)pyrazine)ruthenium(II), $[Ru(bpy)_2(dpp)]^{2+}$ and iron(III) in aqueous and buffered solutions. Electron transfer has been confirmed by trapping Fe(II), one of the products of excited state electron transfer. The efficiency of excited electron transfer is influenced by solvent cage, where redox pair products form by competition between back reaction and diffusion process.

Two molecules of ruthenium complexes, $[Ru(bpy)_3]^{n+}$ and $[Ru(bpy)_2dpp]^{n+}$, where n = 2+, 3+, have been investigated theoretically with a particular attention to their changes in electron density. Structural optimizations and energy calculations were performed by the Density Functional Theory (DFT) method in the Gaussian09 package including the effective core potentials (Los - Alamos ECP) for the ruthenium(II) ion. Electronic absorption spectra have been calculated and compared with experimental data. Computation of spectroscopic properties and electrochemical energies agree with experimental findings and provide a rationale for the spectroscopic properties of the oxidized form of $[Ru(bpy)_2dpp]^{3+}$. The possibility of proton-coupled electron transfer (PCET) reaction was investigated by examining the energetics and pKa's of all possible forms of $[Ru(bpy)_2dpp]^{2+}$, which suggested that the quenching by iron(III) is an electron transfer process. Theoretical electron transfer rates between iron(III) and excited state of $[Ru(bpy)_2dpp]^{2+}$ calculated with Marcus cross-relation are in good agreement with experimental findings.

In memory of my father, Tadeusz Kowalczyk

Ku pamięci mojego Taty, Tadeusza Kowalczyka

Acknowledgements

I would like to express my gratitude to my supervisor, Prof. Harry D. Gafney, for introducing me into experimental inorganic chemistry, for his guidance, encouragement, and countless hours of debates about artificial photosynthesis.

I owe my deepest gratitude to my supervisor, Prof. Segojoo Jang, who worked with me patiently from the beginning, for his understanding, supervision, constructive criticism and financial support through the course of my work.

I would like to thank my Committee members, Prof. Lynn Francesconi and Prof. Andrzej Jarzęcki for their time and helpful comments on my research project.

I would like to thank Dr. Julie Colis Leventhal for the help with experiments and equipment in the lab, her help and suggestions; to Parbatee Jagassar, Jim Dimitrakopoulos, Dr. Edward Look and Anthony Perri for taking part in my experimental research experience.

I am very grateful to Dexter Campbell for cheering me up, and for his support through the good and bad times.

To my uncle, Fr. John Michalak, and all members of Pauline fathers community, Andrzejczuk's and Gasiewskich's families for their prayers and hospitality.

Especially, I would like to give my special thanks to my family in Poland, especially my Parents, for their blessings, constant support and encouragements.

Table of Contents

List of Tables

List of Figures

Concepts and Overview

The goal of this work is to elucidate the mechanism of quenching of an excited ruthenium complex, bis(2,2'-bipyridine)(2,3-bis(2-pyridyl)pyrazine)ruthenium(II), $[Ru(bpy)_2(dpp)]^{2+}$ by $Fe^{3+}_{(aq)}$. Experiments were conducted to gain insight into photochemical reactivity of $[Ru(bpy)_2(dpp)]^{2+}$. One of the issue was to establish why the bimolecular encounter of $[Ru(bpy)_2(dpp)]^{2+}$ with different metals leads to different products despite the fact that they have similar driving forces, Chapter 3.1. The second issue was to explain the quenching mechanism of the excited state $[Ru(bpy)_2(dpp)]^{2+}$ by $Fe^{3+}_{(aq)}$, Chapter 3.2. Another important issue was to establish the spectroscopic signature of $[Ru(bpy)_2(dpp)]^{3+}$ directly through a series of redox reactions with strong oxidizing agents, Chapter 3.3. The next investigation involved examination of excited state electron transfer by trapping experiments, Chapter 3.4. By the photolysis, trapping Fe^{2+}, electron transfer has been confirmed. The discussion in Part 1 (Chapter 4) focuses on explanation of low yield of quantum yield of the formation of Fe^{2+}. Analyses of previous study of protonated $[Ru(bpy)_2(dpp)]^{2+}$ precludes the possibility of protonation. Several different methods were used to reach the same conclusion that the electron transfer is the major reaction in quenching process and its low field of product formation is due to fast back reaction.

In the second part of the thesis (Chapter 6-12) quantum chemistry calculations are use for detailed structural and energetic data of the $[Ru(bpy)_2(dpp)]^{2+/3+}$ and its prototype $[Ru(bpy)_3]^{2+/3+}$. The objectives of these studies were to understand the spectroscopic differences between $[Ru(bpy)_2(dpp)]^{2+/3+}$ and $[Ru(bpy)_3]^{2+/3+}$ and to calculate the excited state electron transfer rate. The computed geometries were in good agreement with available experimental X-rays data for those molecules, Chapter 8. The calculated absorption spectra of $[Ru(bpy)_2(dpp)]^{2+/3+}$ and $[Ru(bpy)_3]^{2+/3+}$ agreed well with experimental observation, Chapter 9. The complex of

$[Ru(bpy)_2(dpp)]^{2+}$ has two peripheral nitrogen that can be protonated in acidic solution. Also, $[Ru(bpy)_3]^{2+}$ reacts with lead dioxide and produces $[Ru(bpy)_3]^{3+}$ that is stable in acidic environment, Chapter 3.3. It is important to analyze whether proton plays any role in the electron transfer process. For this reason, the possibility of proton coupled electron transfer (PCET) is examined, which is briefly explained in Chapter 10. Detailed consideration of various mechnisms of PCET are made and the plausibility of each mechanism is assessed through analysis of energetics of $[Ru(bpy)_2(dpp)]^{2+/3+}$ complex and in its pronated and excited state equivalents. This analysis PCET leads to conclusion that standard electron transfer process is the most likely mechanism for the quenching of $[Ru(bpy)_2(dpp)]^{2+}$. The last chapter, Chapter 11, focuses on the explanation of the activation energy for self-exchange reactions of $Fe^{2+/3+}$ in the ground state, and of $[Ru(bpy)_2(dpp)]^{2+/3+}$ in the ground and excited state. The excited state electron transfer rate between $[Ru(bpy)_2(dpp)]^{2+}$ and Fe^{3+} calculated with the Marcus cross relation (Appendix B) and the Rehm-Weller approach (Appendix C) agree with experimental findings.

Part I: An experimental Study of Electron Transfer in Ruthenium Complexes

1. Introduction

Sunlight can be converted into electricity by exciting electrons in a solar cell. This leads to the production of chemical fuel via natural photosynthesis in green plants or via light-harvesting systems [1].

> *'The development of materials and methods to improve solar energy conversion is primarily a scientific challenge: Breakthroughs in fundamental understanding ought to enable marked progress. There is plenty of room for improvement, since photovoltaic conversion efficiencies for inexpensive organic and dye-sensitized solar cells are currently about 10% or less, but the best solar thermal efficiency theoretically possible is 30%. This suggests that we can do much better.' [1]*

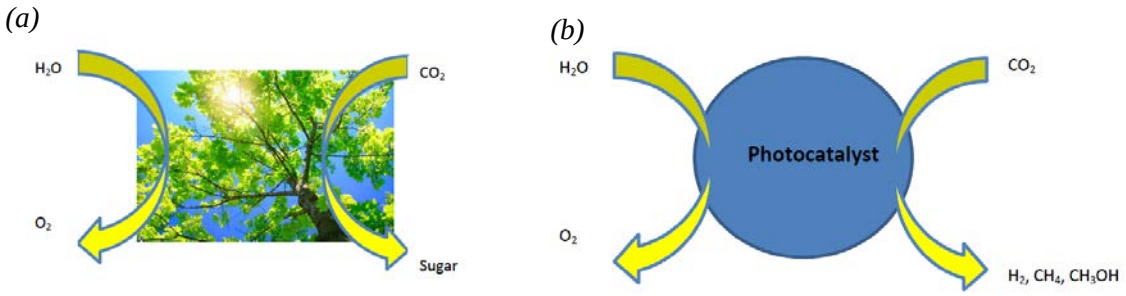

Figure 1. Sunlight conversion and solar production of fuels.

The development of systems that use solar energy has been investigated extensively in recent years. Research focusing on water splitting that leads to hydrogen production has been an important topic in the last decade (see Fig. 1). Molecules that contain transition metals have multiple redox states that lead to many possibilities for their utilization as water splitting catalysts [2-5]. Many compounds involving ruthenium metal (e.g., blue dimer, $[Ru(bpy)_3]^{2+}$) [6-13] have been characterized and analyzed for their capability of water oxidation and excited electron transfer. For water splitting process, the reduction potentials in Eqs. 1-3 indicate that a potential greater than 1.23V is required [14].

$2H_2O \rightarrow O_2 + 4H^+ + 4e^-$ E = -0.82V (1)

$4H^+ + 4e^- \rightarrow 2H_2$ E = -0.41V (2)

$2H_2O \rightarrow 2H_2 + O_2$ E = -1.23V (3)

Research in the last decade has been focused on artificial systems and their dependencies on electron transfer and proton transfer processes. Since photochemistry and excited state properties play important roles in those findings, it is important to analyze not only the nature of the donor and the acceptor but also their excited state properties.

1.1 Basic Principles of Photochemistry

1.1.1 Jabloński Diagram

When a molecule absorbs a photon, which occurs on time scale of 10^{-15} s [15], a high-energy excited state of the molecule is created. Within its excited state, several processes can occur (Fig. 2). Spin-allowed absorption may lead to emission from the first singlet excited state, S_1, which is known as a radiative process of fluorescence (F) that occurs in the 10^{-9} - 10^{-7} s time frame [15]. Internal conversion (IC) is obtained from the higher electronic excited state to the lower electronic excited state of the same spin multiplicity. This occurs within the same time frame (10^{-14}-10^{-11} s) as a vibrational relaxation between the vibrational levels of the interacting electronic excited state. Because of the fast transition, the internal conversion and vibrational relaxation occur immediately following the absorption. Fluorescence competes with other non-radiative processes that can occur from the S_1 electronic excited state.

Intersystem crossing (ISC) occurs when the electron changes spin multiplicity from any excited state singlet, S_n, to another excited state. This is often $S_n \rightarrow T_n$ transition. Since this is a forbidden process according to the selection rule, it is generally slow occurring within 10^{-8} - 10^{-3} s time scale. However, when including vibrational factors and the spin-orbit coupling of

transition metals, ISC becomes weakly allowed. From the first triplet state, T_1, a forbidden decay to the ground state might occur, which is known as phosphorescence (P). This slow (10^{-4} - 10^{-1} s) radiative emission usually competes with other non-radiative processes from T_1, such as chemical reactions and quenching.

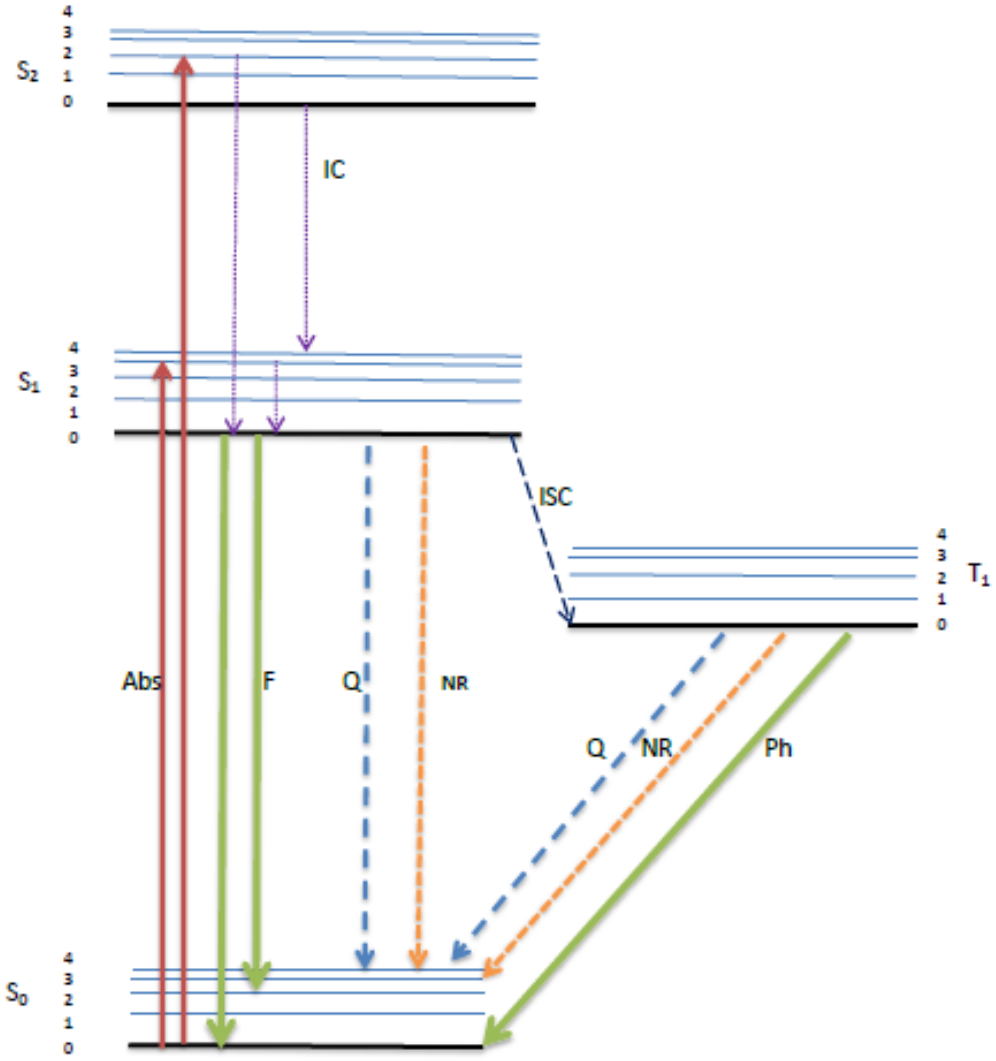

Figure 2. Jabloński Diagram. Radiative processes are in solid lines, quenching (Q), internal conversion (IC), intersystem crossing (ISC) and other non-radiative processes (NR) are in dotted/dashed lines.

1.1.2 Kinetics of the Ground State and Excited State

Possible steps following excitation can be defined by a sequence of 1st and 2nd order processes (reaction 4-10).

$$D + hv \overset{k_1}{\rightarrow} {}^*D \tag{4}$$

$${}^*D \overset{k_r}{\rightarrow} D + hv \tag{5}$$

$${}^*D \overset{k_{nr}}{\longrightarrow} D + \Delta \tag{6}$$

$${}^*D \overset{k_p}{\rightarrow} P \tag{7}$$

$${}^*D + Q \overset{k_{q1}}{\longrightarrow} D + Q + \Delta \tag{8}$$

$${}^*D + Q \overset{k_{q2}}{\longrightarrow} D^{\pm} + Q^{\mp} \tag{9}$$

$${}^*D + Q \overset{k_{q3}}{\longrightarrow} D + {}^*Q \tag{10}$$

where k_1 is the rate of excited state production. Since the excited state is created by absorption of the photon, the rate of appearance of *D can be written as d[*D] / dt =I_a, which is the intensity of absorbed light; k_r is the rate constant for radiative emission; k_{nr} is the rate constant for nonradiative excited state deactivation; k_p is the rate constant for the conversion of the excited state to products P. The bimolecular rate constant is express as k_{qi} where i = 1, 2, 3 refers to the specific processes: the rate for back reaction is defined as k_{q1}; electron transfer quenching, k_{q2} in which $D^{\pm}$ and $Q^{\pm}$ are oxidized/reduced form of reactants; energy transfer, k_{q3} from the excited state of the donor to the quencher to form *Q.

The excited state of *D can undergo competitive processes by first- and second-order kinetics. The lifetime of this excited state is defined by

$$\tau_0(\,^*D) = \frac{1}{k_r + k_p + k_{nr}} \tag{11}$$

When a quencher is included, the excited state of the donor can be quenched by second-order reaction with Q (reactions 8-10), and the lifetime of the donor is modified to

$$\tau(\,^*D) = \frac{1}{k_r + k_p + k_{nr} + k_q[Q]} \tag{12}$$

For an emitting excited state, the radiative and non-radiative rate constants k_r and k_{nr} can be calculated from excited-state lifetime and emission quantum yield measurements.

$$\tau^{-1} = k_r + k_{nr} \tag{13}$$

$$\Phi_{em} = k_r \cdot \tau^{-1} \tag{14}$$

Absorption by a molecule D produces an excited state *D, which will decay by a combination of of first and second order processes:

$$\frac{d[\,^*D]}{dt} = k_1 - k[\,^*D] \tag{15}$$

where

$$k = k_r + k_d + k_p + k_q[Q] \tag{16}$$

In the steady-state limit, the excited state concentration becomes

$$[*D] = k_1/(k_r + k_d + k_p + k_q[Q]) \tag{17}$$

Emission intensity, I, is proportional to $[*D]k_r$ and is obtained by monitoring the sample at the single emission wavelength (k_1' includes k_r).

$$I = k_1'/(k_r + k_d + k_p + k_q[Q]) \tag{18}$$

Within the class of second order reactions, all possible interactions between donor and acceptor can be defined by steps as shown in Fig. 3. In addition, an exciplex may lead to exciplex emission (e) and exciplex deactivation (f). From solvated ion pairs, geminate ion recombination may occur (g).

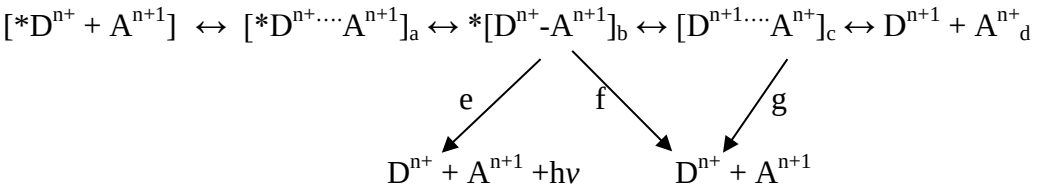

Figure 3. Possible interactions between donor and acceptor: a – Encounter (precursor) complex; b – Exciplex; c - Solvated ion pair; successor complex; d - Solvated separated ions; e – Exciplex emission; f – Exciplex deactivation; g – Geminate ion recombination.

1.1.3 Quenching Mechanisms and Stern-Volmer Kinetics

Quenching refers to non-radiative decay of an excited state induced by another species. It is a bimolecular process and includes a variety of processes, such as excited-state reactions, energy transfer, and complex formation. Regardless of the specific mechanism, the bimolecular quenching can occur by two different processes; static quenching and/or dynamic quenching. In general, static and dynamic quenching can be distinguished by their differences that depend on viscosity and combining steady-state and lifetime measurements.

In the presence of Q, the light intensity, *I* is given by Eq. 18. When quencher is not present, Q = 0

$$I_0 = k_1'/(k_r + k_d + k_p) \tag{19}$$

Taking the ratio of Eq. 19 to Eq. 18 yields to

$$(I_0/I) - 1 = K_{sv}[Q] \tag{20}$$

$$(\tau_0/\tau) - 1 = k_q\tau_0\,[Q] \tag{21}$$

$$K_{sv} = k_q/(k_r + k_d + k_p) = k_q\tau_0 \tag{22}$$

Thus, bimolecular rate quenching constants can be evaluated from a Stern-Volmer plot according to the following equations:

$$\frac{I_0}{I} = \left(\frac{\tau_0}{\tau}\right) = K_{sv}[Q] + 1 \quad (23)$$

$$K_{sv} = k_q \tau_0 \quad (24)$$

A plot of I_0/I (or τ_o/τ) *vs*. concentration of quencher [Q], as shown in Fig. 4 depicts competition between the deactivation of an excited state and bimolecular quenching. K_{sv} is a Stern-Volmer quenching constant, τ_0 is a lifetime of donor at [Q] = 0. Equation 24 provides a direct measurement of quenching constant k_q. Plots of intensity quenching I_0/I and lifetime quenching τ_o/τ provide a further clarification by distinguishing static and dynamic process. Those plots in Fig. 4 in steady-state and time-dependent measurements allow us to distinguish static and dynamic quenching.

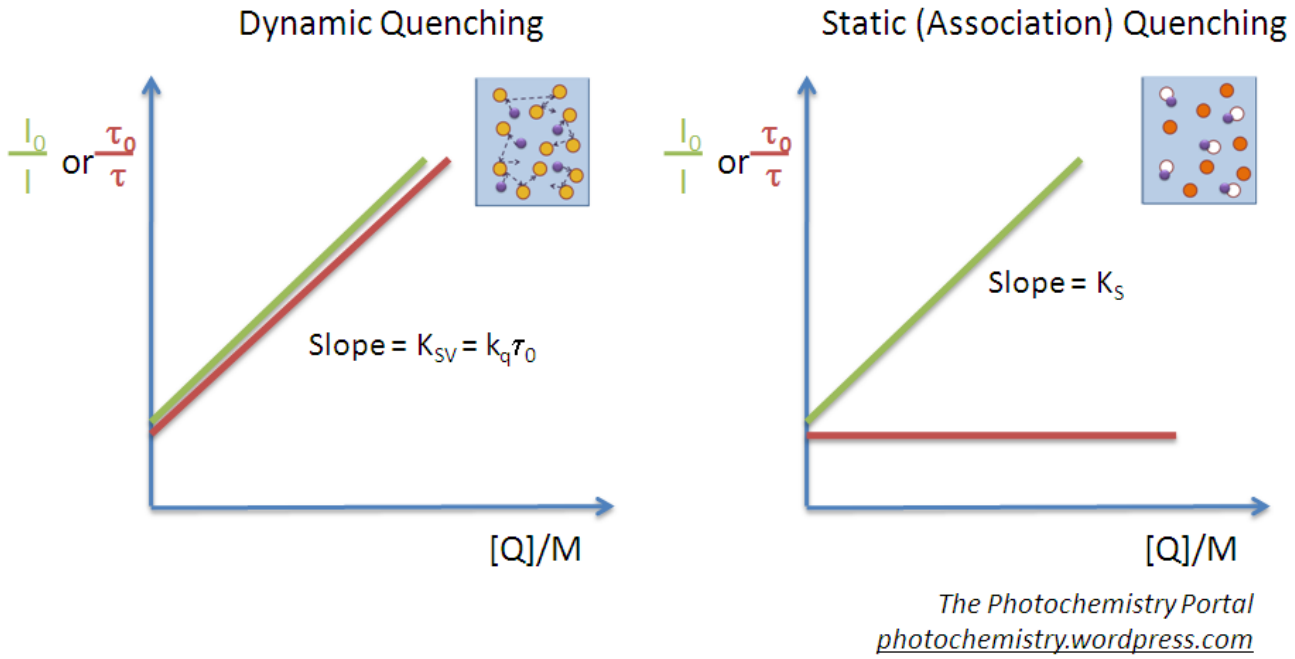

Figure 4. Difference in static and dynamic quenching mechanism.

1.1.3.1 Dynamic Quenching

Dynamic quenching only affects the excited state of the donor; therefore, no change in absorption spectra is observable. Also, the quencher must diffuse to the emissive donor, *D,

during the lifetime of the excited state. Upon contact, the donor will return to the ground state without emitting photons. A high concentration of quencher increases the probability of collision. In this case, Stern-Volmer plots of intensity and lifetime quenching coincide as presented in Fig. 4, (dynamic quenching).

1.1.3.2 Static Quenching

Static (associational) quenching refers to a thermal pre-equilibrium prior to excitation, in which the quencher form a complex with the donor; k_q then becomes an association constant. A high concentration of quencher increases the chance of association.

Intensity measurement (steady-state experiment) follows the excited state and measures both the dynamic and static aspects of quenching. A time-dependent experiment (lifetime measurement) shows only dynamic quenching. When a donor and acceptor are associated, the lifetime of the excited state becomes zero, because the donor is already being quenched. Thus, the ratio τ_0/τ remains constant and independent of quencher concentration. Consequently, a plot of I_0/I and τ_o/τ *vs*. [Q] will differ (Fig. 3, static quenching).

1.2 Photochemistry of $[Ru(bpy)_3]^{2+}$ and $[Ru(bpy)_2dpp]^{2+}$

1.2.1 Characteristic Spectroscopic Properties

Ruthenium diimines are the most experimentally studied molecules [3, 13, 16, 17]. They play an important part in the development of photochemical and electrochemical processes. Aqueous solutions of these molecules absorb ultraviolet-visible light and have strong emission bands, with long excited-state lifetimes. Also, they go through reversible redox processes in the ground state and excited state. With the continual development of molecular modeling and quantum chemistry methods in recent years, the computational study has become an essential

tool for analyzing their structure and capability of electron and energy transfer processes. There is great interest in ruthenium complexes because of the potential for developing useful supramolecular devices and photosensitizers for solar energy conversion by exploiting their remarkable chemical and photophysical properties.

For further progress it will be important to analyze the electronic structure of the sensitizer in detail, and to investigate the energy and composition of its excited states and their charge transfer processes.

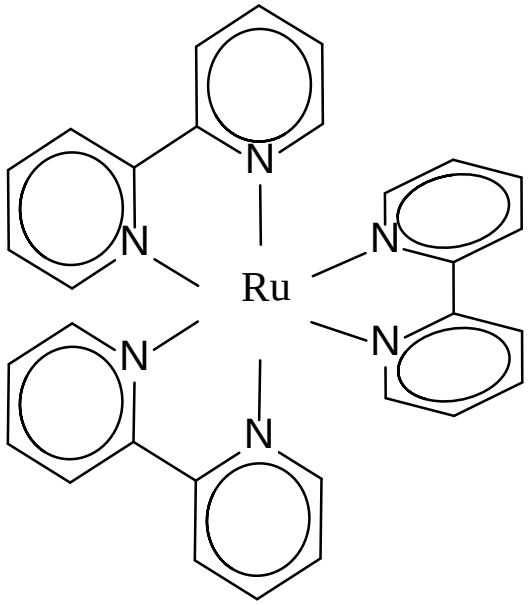

Figure 5. Tris(bipyridine)ruthenium(II), $[Ru(bpy)_3]^{2+}$.

Tris(bipyridine)ruthenium(II) $[Ru(bpy)_3]^{2+}$ is one the most experimentally studied ruthenium complex, playing a major role in the development of electrochemistry and photochemistry, Fig. 5. Counter ions are usually Cl^- or PF_6^-. This compound has remarkable chemical and photophysical properties, and is used as a photosensitizer in solar energy conversion systems. An aqueous solution of this molecule absorbs UV-vis light with a metal to ligand charge transfer (MLCT) band at 452 nm with a molar extinction coefficient of 11 500 $M^{-1}cm^{-1}$ (absorption spectra are discussed in detail in the second part of this thesis). The

molecule has a long-lived excited state of 650 ns, and a strong emission band at 600 nm in aqueous solutions. In addition, the reversible redox processes observable in the ground state and excited state, make these molecules attractive from an electrochemical point of view, Fig.9. With the ongoing development of molecular modeling and quantum chemistry methods in recent years, various computational studies analyzing their structure and capability of electron and energy transfer have been made. This molecule and hundreds of its derivatives have contributed to the development of photoinduced electron (and energy) transfer.

The main spectroscopic signature of the oxidized complex, $[Ru(bpy)_3]^{3+}$, has been assigned to a ligand to metal charge transfer (LMCT) an absorption at 685nm, [18, 19]. It is important to point out that $[Ru(bpy)_3]^{3+}$ also absorbs at 450nm [18, 20], with the absorption coefficients presented in Table I below.

Table I. Absorption coefficient, $M^{-1}cm^{-1}$, for $[Ru(bpy)_3]^{n+}$

Wavelength (nm)	Absorption coefficient, $M^{-1}cm^{-1}$	
	Ru^{2+}	Ru^{3+}
λ_{450}	14 000[a]	500[a]
λ_{685}	70[b]	420[a]

(a) Ref. [22]
(b) Ref. [18]

The absorption coefficient at 685 nm, $\varepsilon = 70\ M^{-1}cm^{-1}$ for $[Ru(bpy)_3]^{2+}$, was estimated from the difference in absorbance at 685nm between the spectra of 'outgassed' Ru^{2+} and 'outgassed' $[Ru(bpy)_3]^{3+}$ [18]. The electrogenerated chemiluminescence (ECL) of $[Ru(bpy)_3]^{3+}$ with oxalate ions was also measured [21]. The measured efficiency of this reaction, as a ratio of number of photons emitted to the amount of $[Ru(bpy)_3]^{3+}$ generated, has been shown to be 2% in deaerated solution.

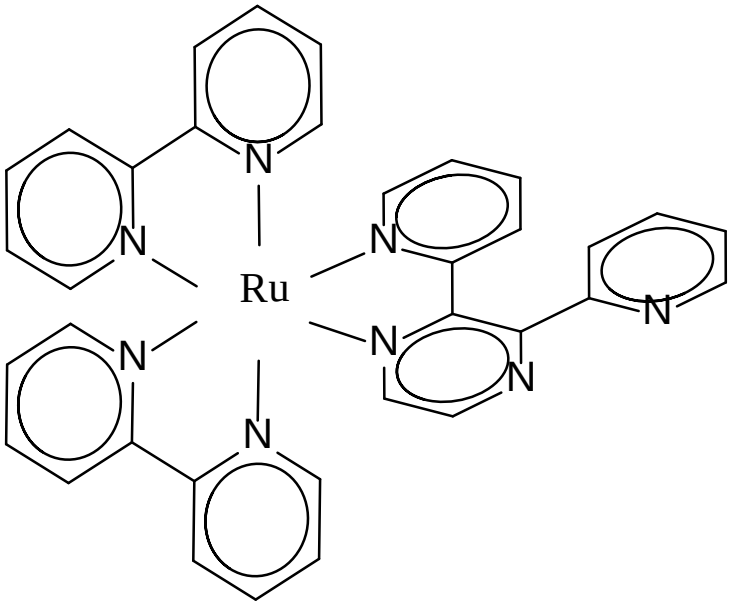

Figure 6. bis(2,2'-bipyridine)(2,3-bis(2 pyridyl)pyrazine)ruthenium(II), $[Ru(bpy)_2(dpp)]^{2+}$

Another diimine complex, bis(2,2'-bipyridine)(2,3-bis(2 pyridyl)pyrazine)ruthenium(II), $[Ru(bpy)_2(dpp)]^{2+}$ (Fig. 6), also acts as a good photocatalyst, due to its strong reducing and oxidizing abilities in the excited state.

The experimental absorbance spectra (Fig. 7) exibits three major peaks:

- Ligand-Centered (LC), $\pi \rightarrow \pi^*$ at 280nm
- Metal Centered transition (MC), $t_{2g} \rightarrow e_g$ at 325nm (This transition usually omitted in the experimental results due to poor characterization)
- Metal to Ligand Charge Transfer (MLCT), $d \rightarrow \pi^*$ at 430 nm (bpy)
- Metal to Ligand Charge Transfer (MLCT), $d \rightarrow \pi^*$ at 470 nm (dpp).

The emission spectrum of this complex (Fig. 8) has a strong band at 700 nm and is assigned to $\pi^* \rightarrow d$ (ligand charge transfer to metal), with an excited state lifetime of τ = 135 ± 14 ns (H_2O, 22°C).

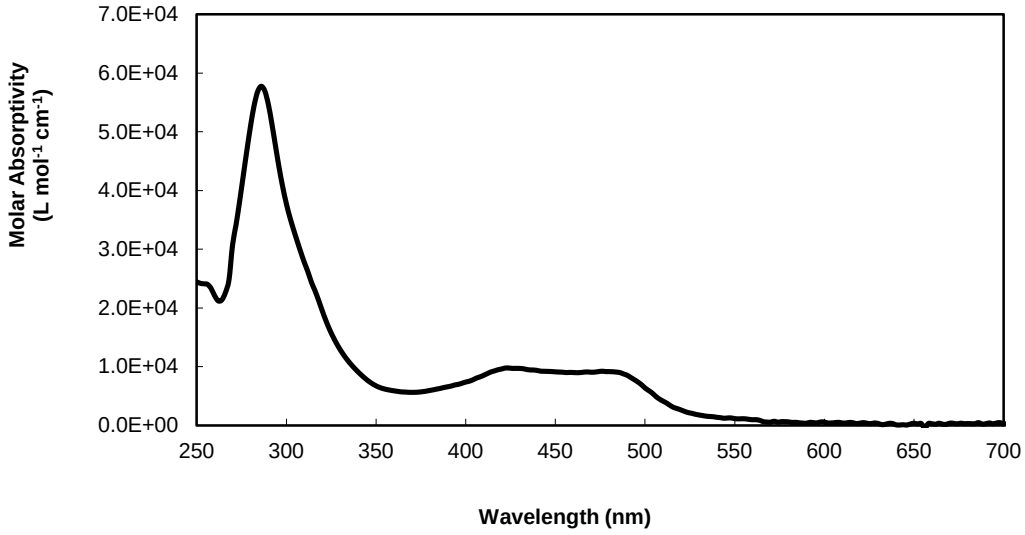

Figure 7. Absorption spectrum of $Ru(bpy)_2(dpp)]^{2+}$ in water [13].

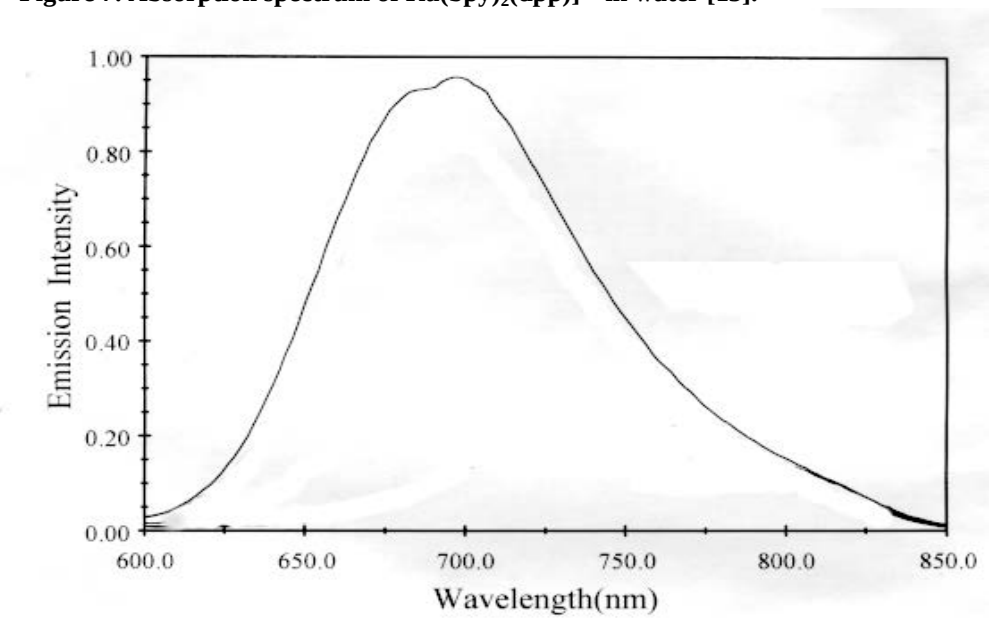

Figure 8. Emission spectrum of $[Ru(bpy)_2(dpp)]^{2+}$ in water, (λ_{exc} = 490 nm) [13].

1. 2.2 Redox Properties in The Ground State and Excited State

Ruthenium complexes have an octahedral structure, with a low spin d^6/d^5 electron configuration ($Ru^{2+/3+}$) due to the large ligand field created by nitrogen groups of the surrounding diimine ligands. The three lower energy t_{2g} orbitals are occupied, and the two higher e_g orbitals are unoccupied. The potential for reaction in the excited state is obtained as a difference from spectroscopic (a' value, Fig. 9) and cyclic-voltammetry measurements (b, c values, Table II).

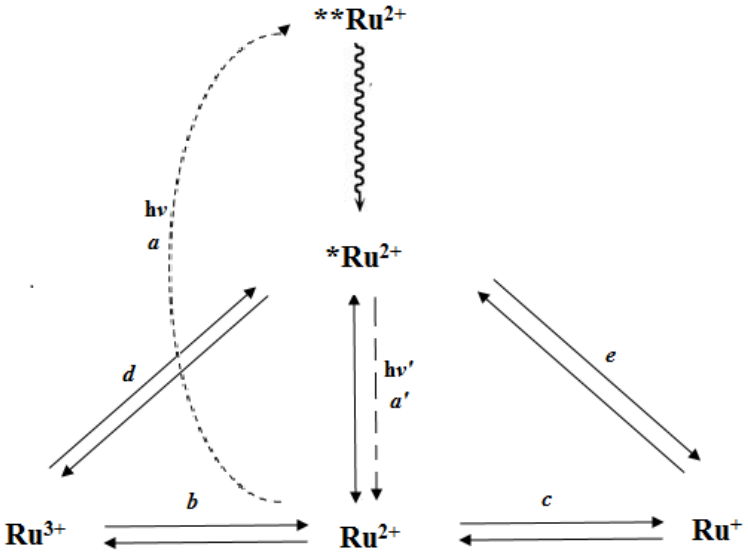

Figure 9. The relations between reduction potentials and spectroscopic properties of $[Ru(bpy)_2L]^{2+}$. Excitation with the light populates a higher singlet excited state (a), and through IC and ISC reaches the lowest triplet state, from which the observed emission (a') occurs. Adapted from [22].

Table II. Values for processes assigned in Fig. 8, in water.

process	$[Ru(bpy)_3]^{n+}$	$[Ru(bpy)_2dpp]^{n+}$
a	λ_{max} = 452 nm ε = 14 600 $M^{-1}cm^{-1}$	λ_{max} = 430 nm, 470 nm ε = 9600 $M^{-1}cm^{-1}$, 4600 $M^{-1}cm^{-1}$
a'	2.08 eV (τ = 600 ns, water)	1.76 eV (τ = 135 ns, water)
b	+1.20 eV	+1.23 eV
c	-1.31 eV	-1.00 eV
d	-0.88 eV	-0.53 eV
e	+0.77eV	+0.76 eV

1. 2.3 Aspects of Protonated Species of $[Ru(bpy)_2dpp]^{2+}$

The ground and excited state protonation of the $[Ru(bpy)_2(dpp)](PF_6)_2$ complex has been previously studied [17, 23-26]. In the ground state the addition of H^+ to a peripheral pyridine site occurs at pKa=1.12. The absorption spectra of $[Ru(bpy)_2dpp]^{2+}$ in the range of pH from 0 to 7 does not change significantly as shown in Fig. 10. There is no new visible peak formation. There is, however, a small shift from 428 nm to 422 nm MLCT band and increased intensity by 17%. Also, the other MLCT peak localized at 476 nm shifts to 490 nm, with decreased intensity by 10%. It has been found by NMR that $[Ru(bpy)_2dpp]^{2+}$ is protonated at the peripheral pyridine in the 0-2 pH range [25]. It has been proposed [26] that more than 80% of $[(bpy)_2Rudpp]^{2+}$ is in the protonated form in the pre-equilibrium environment at that low pH range. The bimolecular constant of 5.1 x 10^9 $M^{-1}s^{-1}$ has been calculated for the protonation process in solution with pH = 3-5 [25] in the ground state.

In the 0-2 pH range the emission band appears at 735 nm which corresponds to a 35 nm shift from 700 nm of the non-protonated species. The 735 nm emission is assigned to $[^*Ru(bpy)_2(dppH_y)]^{3+}$ where the proton has added to the peripheral dpp pyridine. Taking into account that those species are very short-lived, less than 16 ps, the bimolecular rate of protonation reaction is 8.6 x 10^{11} $M^{-1}s^{-1}$.

Protonation at a pyrazine site of $[Ru(bpy)_2dpp]^{2+}$ occurs in the excited state within a pH range of 0-8. However, protonation of the peripheral dpp pyrazine relaxes the excited state immediately and there is no energy present for further processes. The Hammet constant, H_o, for ground-state protonation of the peripheral dpp pyrazine nitrogen, $[Ru(bpy)_2(dppH_z)]^{3+}$, requires an $H_o < -6$.

At a very high concentration of acid (Hammet Constant region), the absorption of the diprotonated species appears at 573 nm in the absorption spectrum, Fig. 11. The ground-state and

excited-state titration presented in Fig. 12 provide insight into the high increase in basicity of the peripheral dpp pyrazine in the excited state.

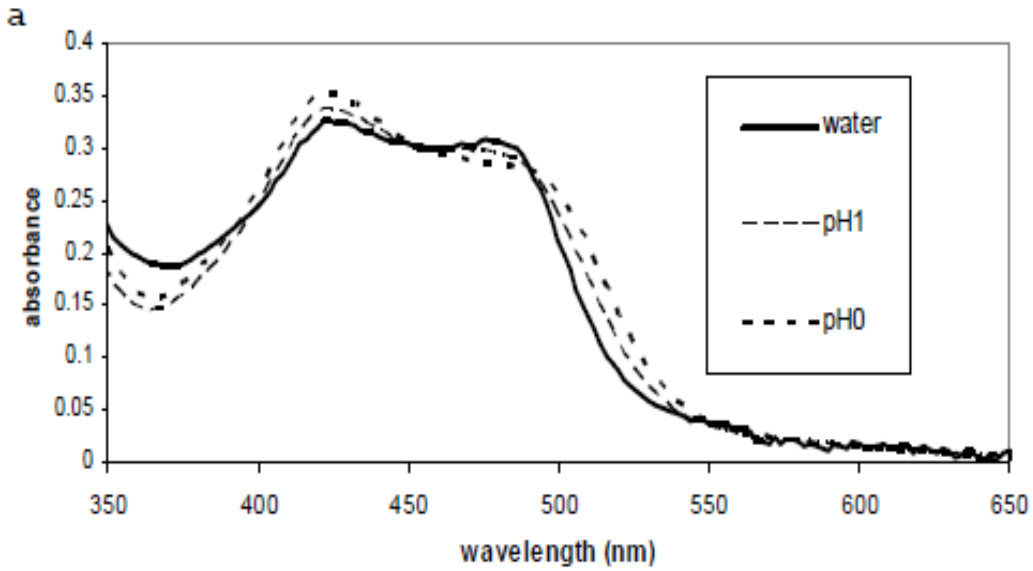

Figure 10. Absorption spectrum as a function of pH of $[Ru(bpy)_2dpp]^{2+}$ described by Zambrana [23].

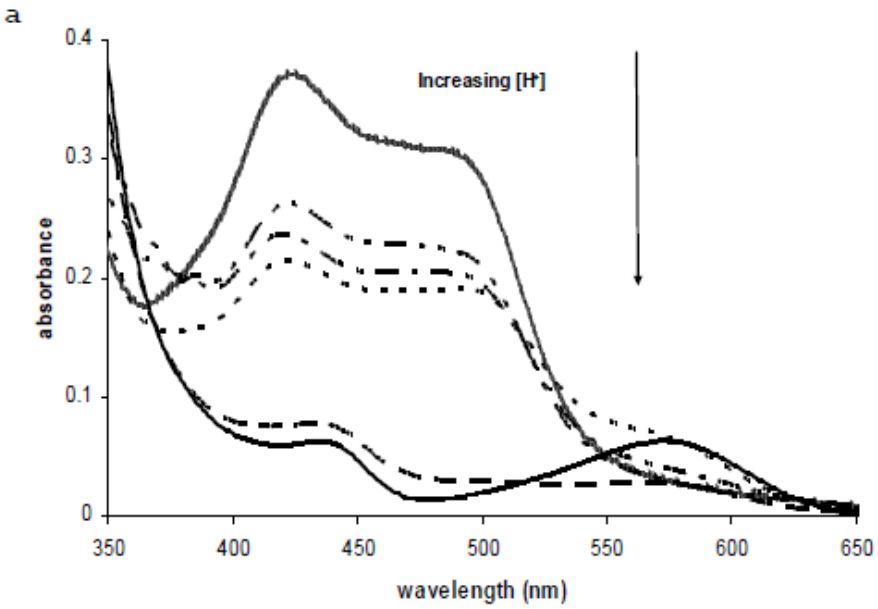

Figure 11. Absorption spectrum as a function of high acid titration of $[Ru(bpy)_2dpp]^{2+}$, when pH < 0. The absorption of diprotonated species appears at 573 nm wavelength. Measured by Zambrana [23].

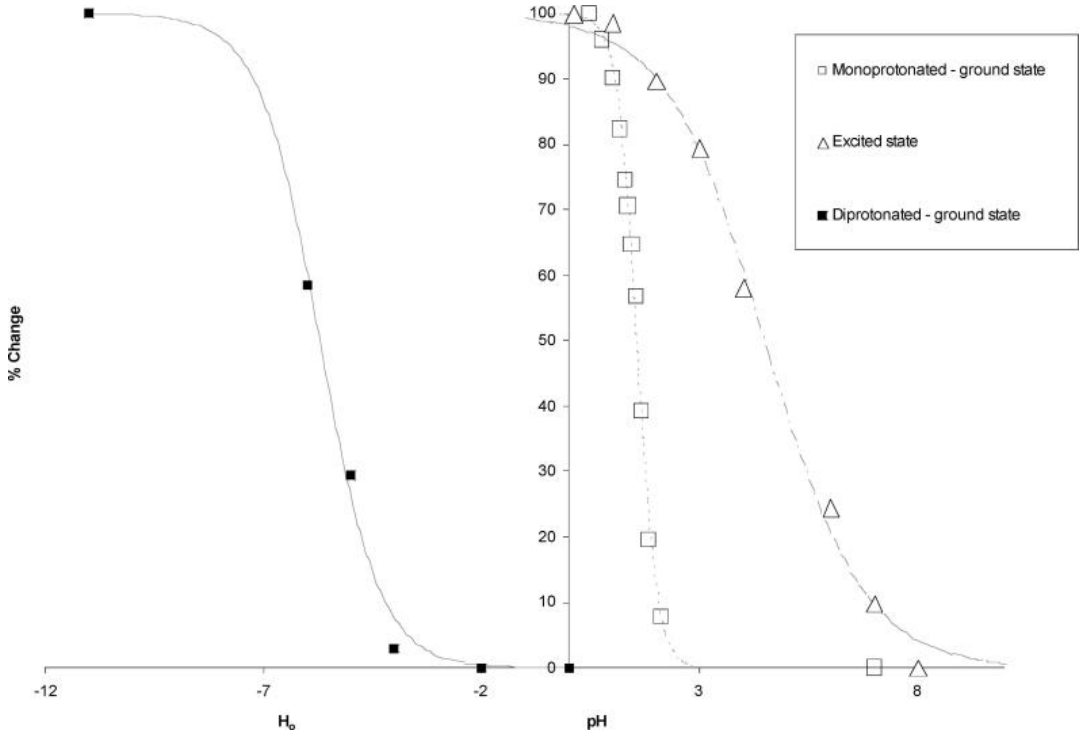

Figure 12. Titrations curves of the ground and excited state titration of $[Ru(bpy)_2(dpp)]^{2+}$. The curves correspond to diprotonation (--■--) of $[Ru(bpy)_2(dpp)]^{2+}$; (--□--) monoprotonation of $Ru(bpy)_2(dpp)^{2+}$ to $[Ru(bpy)_2(dppH_y)]^{3+}$; (--△--) protonation of the excited complex to $[*Ru(bpy)_2(dppH_z)]^{3+}$. Data are obtain from UV/vis, NMR, and emission quenching, respectively [23].

The acid-base behavior of the $[Ru(bpy)_2dpp]^{2+}$ shows that, the majority of the complex present in solution is unprotonated at pH =5 [25]. Reactions presented in this paper between $[Ru(bpy)_2dpp]^{2+}$ complex and $Fe^{3+}_{(aq)}$ occur in an acidic environment, therefore, the role of hydrogen ion was considered.

1. 2.4. Thermodynamics of $[Ru(bpy)_3]^{2+}$ and $[Ru(bpy)_2dpp]^{2+}$

Ruthenium in the excited state is a good energy donor. Also, it can be an electron donor or acceptor. The type of reaction depends on the spectroscopic and redox properties of iron(III). It has been said that spin-allowed energy transfer for aqueous solutions of iron(III) is possible with donors that have an energy of $\geq$ 1.56 eV [27]. This means that energy transfer to Fe^{3+} is possible with most Ru(II) diimine complexes.

Let's review possibilities of energy and electron transfer and their energetics.

$$*Ru^{2+} + Fe^{3+} \rightarrow Ru^{2+} + *Fe^{3+} \text{ (energy transfer, } *Fe^{3+} \text{ is nonemissive)} \quad (25)$$

$$*Ru^{2+} + Fe^{3+} \rightarrow Ru^{1+} + Fe^{4+} \text{ (reductive quenching)} \quad (26)$$

$$*Ru^{2+} + Fe^{3+} \rightarrow Ru^{3+} + Fe^{2+} \text{ (oxidative quenching)} \quad (27)$$

Energy transfer energetics

$$*[Ru(bpy)_3]^{2+} + Fe^{3+} \rightarrow [Ru(bpy)_3]^{2+} + *Fe^{3+} \quad E^0_{rxn} = 2.08eV\text{-}1.56\ eV = 0.52\ eV \quad (28a)$$

$$*[Ru(bpy)_2dpp]^{2+} + Fe^{3+} \rightarrow *[Ru(bpy)_2dpp]^{2+} + *Fe^{3+} \quad E^0_{rxn} = 1.76\ eV\ -1.56\ eV = 0.20\ eV \quad (28b)$$

Reductive quenching energetics

$$*[Ru(bpy)_3]^{2+} + Fe^{3+} \rightarrow [Ru(bpy)_3]^{1+} + Fe^{4+} \quad E^0_{rxn} = 0.77eV\text{-}1eV\ ^{[27]} = -\ 0.23eV \quad (29a)$$

$$*[Ru(bpy)_2dpp]^{2+} + Fe^{3+} \rightarrow *[Ru(bpy)_2dpp]^{1+} + Fe^{4+} \quad E^0_{rxn} = 0.76eV\ -1eV = -\ 0.24eV \quad (29b)$$

The oxidative quenching energetics

$$*[Ru(bpy)_3]^{2+} + Fe^{3+} \rightarrow [Ru(bpy)_3]^{3+} + Fe^{2+} \quad E^0_{rxn} = 0.88eV + 0.77eV = 1.65\ eV \quad (30a)$$

$$*[Ru(bpy)_2dpp]^{2+} + Fe^{3+} \rightarrow *[Ru(bpy)_2dpp]^{3+} + Fe^{2+} \quad E^0_{rxn} = 0.53eV + 0.77eV = 1.30\ eV \quad (30b)$$

Energy transfer (reaction 30a and 30b) and oxidative quenching (reaction 32a and 32b) are thermodynamically allowed, as illustrated in Fig. 13. However, it has been established [7] that quenching of $[Ru(bpy)_3]^{2+}$ by Fe(III) undergoes only electron transfer, and energy transfer is not involved. Lin and Sutin [28] showed that reactions of $*[Ru(bpy)_3]^{2+}$ with Fe(III) have bimolecular rate constant of $k_q = 2.3 \pm 0.3 \times 10^9$ (at 0.5M ionic strength), and $k_{et} = 1.5 - 1.9 \times 10^9$ which corresponds to 81 ± 16% of electron transfer (ET) quenching.

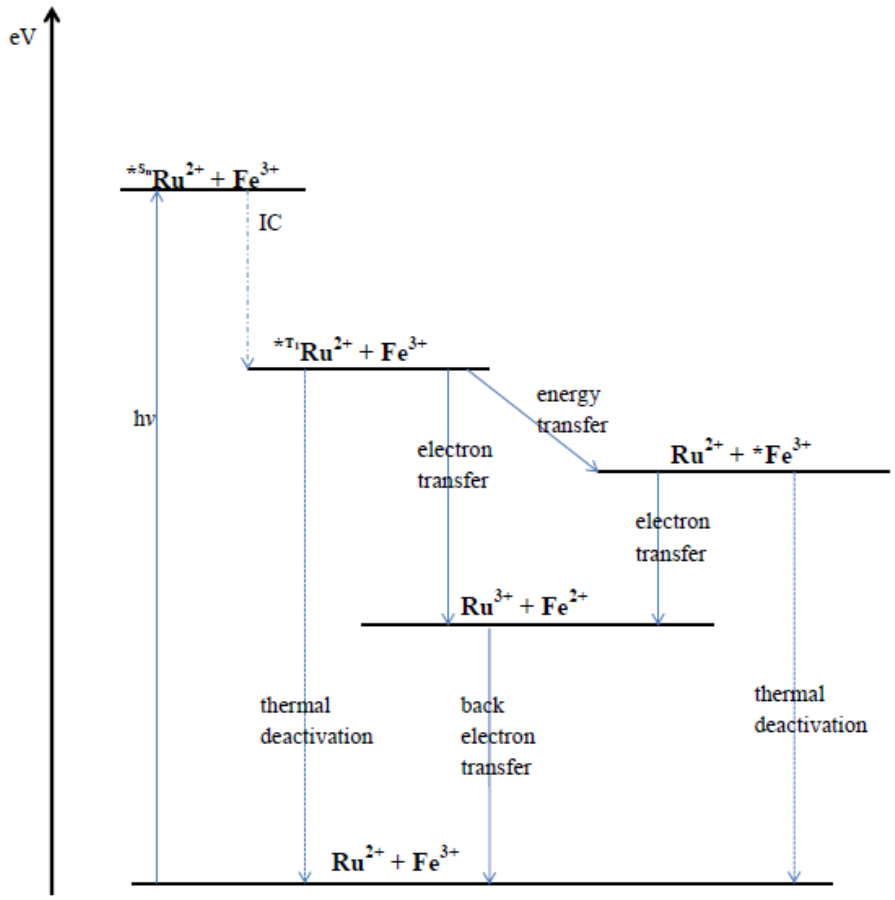

Figure 13. Energetically possible interactions of $[*Ru(bpy)_2(dpp)]^{2+}$ with iron(III).

Detailed uderstanding of the quenching mechanism of Ru(II) complexes constitutes the major issue in elucidating bimolecular reactions that may lead to excited-state electron transfer ET. Lin and Sutin [9, 29] have studied and discussed quenching by iron(III). Excited-state measurements of Ru(II) diimine and Fe(II) diimine have been analyzed in terms of excited-state electron transfer for energy conversion problems [30]. It has been found that the reducing potential of Fe^{2+} diimine complex is too low and the lifetime of excited state Fe^{2+} diimine too short to be a good photosynthesizer.

Based on spectroscopic studies, it has been found that the quenching constant k_q is equal to electron transfer constant k_{et} for $[Ru(bpy)_3]^{2+}$ and iron(III) [7, 28]. The values are presented in

Table 3, and they vary slightly depending on the medium that was used. A small quenching constant, k_q, 10^5-10^7 M^{-1} s^{-1}, represents typical "slow" electron transfer, whereas larger values are characteristic of rapid, diffusion-controlled quenching. In this study, $k_q \sim 10^9$-10^{10} (Table III) corresponds to very fast, diffusion-controlled electron transfer.

Table III. Quenching constants of ruthenium complexes and iron(III).

	10^{-9}kq, $M^{-1}sec^{-1}$	K_{sv}	Medium
$[Ru(bpy)_3]^{2+}$	3.0 (at 600ns)	1800	1M HClO4 [7]
	1.9±0.2 (at 400ns) aerated solution	760±100	0.5M HClO4 [27]
	1.5±0.1	900±100	0.11M HClO4 [9]
	2.3±0.1	1400±100	0.5M $HClO4_{(high\ con\ Fe)}$ [9, 29]
	2.7±0.2	1600±100	0.5M HCl [9]
	2.7±0.2	1600±100	0.5M H2SO4 [9]
$[Ru(bpy)_2dpp]^{2+}$	4.4	1163±50 (Ru to bpy) 472±30 (Ru to dpp)	NaAc/HAc *This work*
	18.	2352±140 (Ru to bpy) 1793±184 (Ru to dpp)	Water *This work*

3b: used [Fe(H2O)6]3+; 4,3e,6 used iron (III) perchlorate. My work, Iron (III) sulfate.

More recently, the interactions of $[Ru(bpy)_3]^{2+}$ with $[S_2O_8]^{2-}$ have been established [31, 32]. The authors proposed two possible mechanisms for this reaction. One is ground state association of Ru^{2+} and $S_2O_8^{2-}$, while the second is quenching that leads to photoinduced electron transfer. The outcome of the reaction depends on the type of solvent being used. The experiments were performed for the reaction of $[Ru(bpy)_3]^{2+}$ with $[S_2O_8]^{2-}$ in the presence of a sodium phosphate (0-200 mM) buffer at pH=7.2. The linear behavior of Stern-Volmer plot

indicates dynamic quenching at high concentration of the buffer. The Stern -Volmer plot deviates from linearity at 0-20 mM buffer concentration, which indicates the ground state association between ruthenium and peroxydisulfate ion. Based on the experimental findings, it has been concluded that the presence of the buffer reduces the I_o/I ratio, indicating that the buffer deactivates the quenching process and prevents the formation of the $Ru^{2+\cdots}S_2O_8^{2-}$ associate complex.

1.3 Electron Transfer Mechanism (ET)

The electron transfer process (ET) has been studied for decades. Libby in 1952 [33] explained how geometry change affects the electron transfer rate and applied the Frank-Condon principle to those findings. Fast electron transfer occurs when the nuclear configuration remains almost unchanged during the electron transfer. Greater bond differences between metal and ligand cause greater reorganization of the system and slow down the electron transfer. The outer-sphere mechanism occurs without the formation of a chemical bond, as opposed to the "inner-sphere," where a ligand bridges the donor and acceptor and forms an intermediate, as introduced by Taube in 1953 [34].

1.3.1 Inner-Sphere Mechanism of Electron Transfer

An inner-sphere electron transfer reaction of electron transfer occurs through a bridging ligand when a covalent bond is formed. However, the rate of electron transfer cannot go faster than substitution of the ligand. There is a step where a metal 1 complex (M1) bonds to a metal 2 complex (M2), Fig. 14.

Figure 14. Scheme for inner-sphere mechanism of electron transfer.

There must be evidence for an inner-sphere complex (contact ion pair) in the spectrum.

$$M^{n+}—L—M^{m+} \overset{hv}{\Longleftrightarrow} M^{n+1}—L—M^{m-1} \quad (31a)$$

The classic example of this mechanism was presented by Taube [35].

$$[Co^{III}Cl(NH_3)_5]^{2+} + [Cr^{II}(H_2O)_6]^{2+} \rightarrow [Co^{II}(NH_3)_5(H_2O)]^{2+} + [Cr^{III}Cl(H_2O)_5]^{2+} \quad (31b)$$

Reaction occurs by a bimetallic $Co^{III}—Cl—Cr^{II}$ bridge, with k = 6 x 10^5 $M^{-1}s^{-1}$. Often, the bridging ligand is transferred to the other reactant. Due to the lack of evidence of any coordination or ligand exchange between $[Fe(H_2O)_6]^{3+}$ and $[Ru(bpy)_2dpp]^{2+}$, only outer-sphere electron transfer is considered.

1.3.2 Outer-Sphere Mechanism of Electron Transfer

This mechanism describes two reactants whose coordination spheres remain unchanged during the electron transfer, where there is no breaking or forming of covalent bonds, Fig. 15.

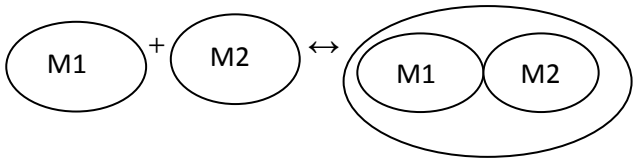

Figure 15. Scheme for outer-sphere mechanism of electron transfer.

Self-exchange electron transfer reactions for $[Ru(bpy)_3]^{2+}$, $Fe^{2+}_{(aq)}$, and $Fe^{3+}_{(aq)}$ complexes have been established by [36, 37] and are described by the outer-sphere electron transfer mechanism.

1.3.3 Photoexcited State Electron Transfer

Often, for excited-state reactions, the Rehm-Weller [38, 39] model is used, which discusses aspects of electron transfer by quenching. The model is described in details in the Appendix C. Equilibrium constant for excited electron transfer, K'_{12} is the ratio: $k'_{12}/k'_{21.}$ (Fig. C.1)

$$K'^{-1}_{12} = e^{(\Delta G^0_{12}/RT)} \tag{32}$$

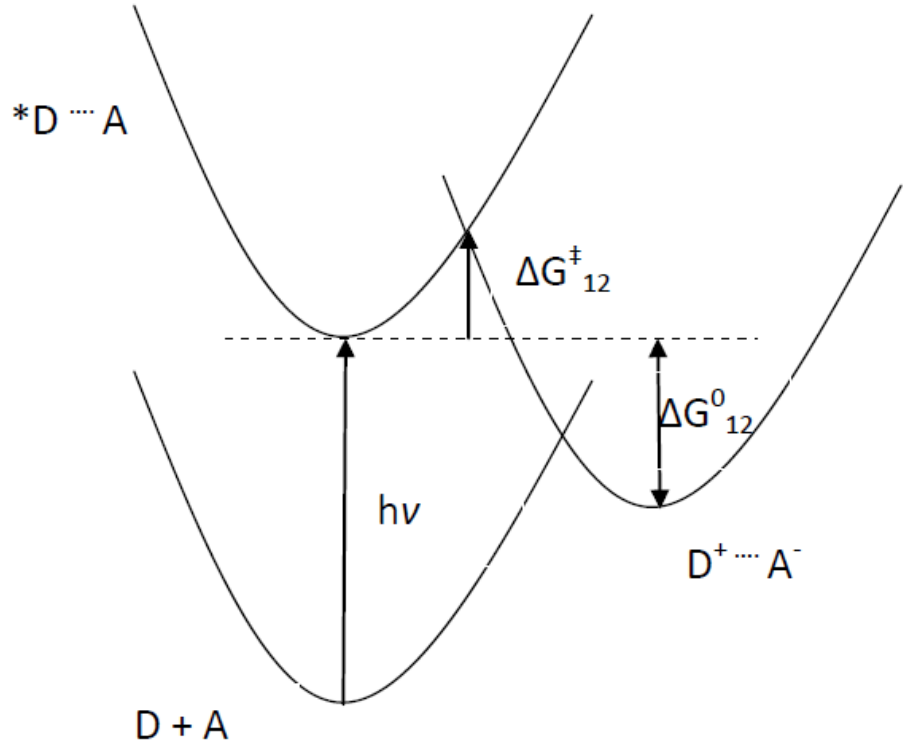

Figure 16. Energetic of excited state electron transfer process.

The rate of excited state electron transfer is given by

$$k'_{12} = \nu e^{(-\Delta G^{\ddagger}_{12}/RT)} \tag{33}$$

where *v* is the frequency factor.

The free energy of the reaction and the transition state are defined as presented in the Appendix 2 or by using the Rehm-Weller Approach (Appendix 3).

1.3.4 Diffusion Controlled Process and the Aspects of Ionic Strength

Electrostatic attractions and repulsions are important. If ions are of opposite signs, collisions between donor and acceptor will be increased by the attractive force. If ions are of the same signs, the number of collision will be reduced. The electron transfer rate constant can be estimated by Eq. 33 with the free energy of the activation, $\Delta G^{\ddagger}$, which is defined in Appendix 1 and show how repulsions and attractions can make important contributions to the free energy of activation.

The charged ions can be represented as spheres in a solvent with a fixed dielectric constant.

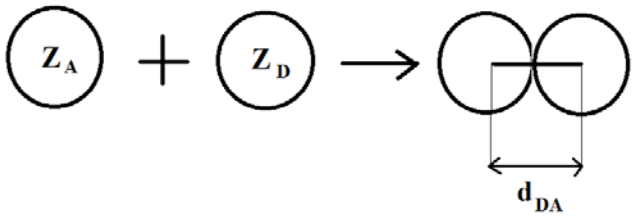

Figure 17. Model for a reaction of two ions of charges, Z_A and Z_D that form activated complex with the distance d_{AD}.
***This model is valid of outer-sphere model.**

Bimolecular reactions occur through collisional encounters between reactants. However, not every bimolecular encounter leads to a reaction. In some cases, many collisions are necessary. In these cases, the rate is less than diffusion limited process. Solvent molecules that surround reactants can form a solvent cage that reflects the number of collision between the reacting molecules as well as their separation after collision. In outer-sphere electron transfer, where both molecules remain intact in the transition-state complex, this model can be used to calculate the work that must be done in moving them together as shown in Fig. 17. This work represents the electrostatic contribution to the free energy involved in bringing the reactants together and is given by Eq. 34.

$$w = \frac{N_A Z_A Z_D e^2}{\varepsilon d_{AD}} \tag{34}$$

where e is the electronic charge, ε is the dielectric constant. When the reactants are either both positive or both negative, the work, w, has positive value. Thus,

$$\Delta G^{\ddagger} = \Delta G^{\ddagger,} + w \tag{35}$$

where $\Delta G^{\ddagger,}$ is the sum of the inner and outer sphere reorganization energy. The diffusion-controlled rate constant k_d depends only on the viscosity of the solvent and temperature as follows

$$k_{diff} = \frac{8RT}{3000\eta} \tag{36}$$

The above equation is known as Debye relation and relates the rate constant at a given temperature and viscosity of the solvent when molecules are small. Values of k_{diff} at different temperatures are presented in the Table IV.

Table IV. Rate constant for diffusion process based on Debye equation, Eq. 37a.

Viscosity; η (poise)	Temperature (°C)	k_{diff} [$M^{-1}sec^{-1}$]
0.0100	20	6.5×10^9
0.0089	25	7.4×10^9
0.0036	80	2.2×10^{10}

Since poise units of viscosity are cgs units,
with gas constant is expressed as R = 8.31×10^7 erg/mol.

However, in many cases, diffusion-controlled rates are calculated from the Smoluchowski Eq. 37, which relates the bimolecular diffusion constant k_{diff} with the encounter distance, d_{DA}, and the diffusion coefficients of donor and acceptor, D_D and D_A.

$$k_{diff} = 4\pi d_{DA} N (D_D + D_A) 10^3 \ [M^{-1}s^{-1}] \tag{37}$$

where N is the Avogadro's number and the $d_{DA} = r_A + r_D$ is the sum of radii for donor and acceptor (Fig. 17). The number 1000 converts cubic meters to cubic decimeters. Thus, k_{diff} is in the unit of $dm^3mol^{-1}s^{-1}$. Diffusion coefficients are defined by the Stokes-Einstein Eqs. 38 and 39.

$$D_A = \frac{k_B T}{6\pi r_A \eta} \tag{38}$$

$$D_D = \frac{k_B T}{6\pi r_D \eta} \tag{39}$$

Aspects of ionic strength

Under the approximation of the dilute solution, where ions are close together, the Debye-Hückel theory provides an expression for the activity coefficient of ionic species. For example in aqueous solution at 25°C, the activity coefficient turns out to be about 0.51. Thus, the rate of the reaction can be expressed as[1]

$$\log k = \log k_0 + 1.02 Z_A Z_B \sqrt{\mu} \tag{40}$$

with k_0 as the rate constant for the infinite dilute solution. The ionic strength μ is given given by

$$\mu = \tfrac{1}{2} \sum (z_i^2 c_i) \tag{41}$$

where z_i is the charge of a particular ion and c_i is its concentration of ionic species in units of mol/dm^3, while the sum is for all ions present in the solution. Ionic strength enhances the rate of reaction of ions with the same signs, and reduces the rate when ions charges of ions are of opposite signs. High ionic strength reduces electrostatic interaction between the reactants.

1.4 Aqueous Silver and Iron Complexes.

The hydration structure in aqueous solutions of iron and silver ions has been determined by extended X-ray absorption fine structure (EXAFS) [40, 41].

Water coordination by Ag^+ depends on the counter ions, and it may have different coordination numbers. Silver nitrate (3M and 9M) solutions have three to four waters around the silver ion with Ag-O bond length of 2.34 to 2.36 Å, which X-ray diffraction experiments indicate is a distorted tetrahedral configuration in crystals. [40, 41].

[1] Chemical kinetics', Keith Laidler, Secon edition, 1965, McGraw-Hill, Inc, page 220

Iron ion exits predominantly as an octahedral hexaaquairon complex in the high-spin configuration in aqueous solution [42]. For example, it has been shown that compounds such as $Fe_2(SO_4)_3 \cdot 9H_2O$ and $Fe(NO_3)_3 \cdot 9H_2O$ have $[Fe(H_2O)_6]^{3+}$ sphere with 1.98 Å and 1.99 Å Fe^{III}-O distance, respectively. Based on crystallographic studies of $Fe(H_2O)_6^{3+}$ and $Fe(H_2O)_6^{2+}$, the Fe^{III}-O bond length of coordinated water on average is 1.99 Å, whereas the the Fe^{II}-O bond length is 2.13 Å [43, 44]. $Fe(H_2O)_6^{3+/2+}$ has $t_{2g}^3e_g^2/t_{2g}^4e_g^2$ electronic configurations. It has been suggested that the longer bond length for iron(II) is due to an extra σ-nonbonding electron which enhances the Fe-O bond length by interaction with the lone-pair electrons on the oxygen atom. Theoretical investigations [45-47] show good agreement between DFT calculation results with spectroscopic experimental data, and their application to theoretical study of redox reactions of ruthenium diimines is reasonable.

Hexaaquairon complex - mononuclear or cluster formation? [44, 47]

Inorganic complexes of iron are important from geological, industrial and biological points of view. Their chemistry and properties have been studied for a considerable time ([44] and references therein). Some experimental studies have investigated hydrolysis and precipitation of iron(III) from aqueous solutions. An aqueous solution of different Fe(III) salts, as mentioned before, have $[Fe(H_2O)_6]^{3+}$ in an octahedral structure. Deprotonation of hexaaquairon leads to two forms as described in Table V below [44].

In basic solution, iron(III) precipitates, which has been observed in the present experiments. Hydrolysis of the mononuclear species $[Fe(H_2O)_6]^{3+}$, results in aggregation and precipitation. Polymeric species (a2 or b2 molecules, Table V) can be formed within 100s, Figure 18. This model indicates that $[Fe(H_2O)_6]^{3+}$ forms two hydroxylated species, $Fe(OH)^{2+}$

and $Fe(OH)_2^+$ (Table V, Fig. 18). Within 10^2 seconds, these species aggregate to form polymeric species, which lose water to form more organized dimeric forms.

Table V. Deprotonation of hexaaquairon leads to two forms [44].

Deprotonation of $[Fe(H_2O)_6]^{3+}$	$Fe(OH)^{2+}$ (a)	$[Fe(H_2O)_5(OH)]^{2+}$ (a1)	$[(H_2O)_5Fe\mathbf{O}Fe(H_2O)_5]^{4+}$(a2) oxolation process (oxygen bridge)
	$Fe(OH)_2^+$ (b)	$[Fe(H_2O)_4(OH)_2]^+$ (b1)	$[(H_2O)_4Fe\mathbf{(OH)_2}Fe(H_2O)_2]^{4+}$(b2) olation process (OH bridge) Experimental data suggest that this dimeric form may exist in equilibrium in solution

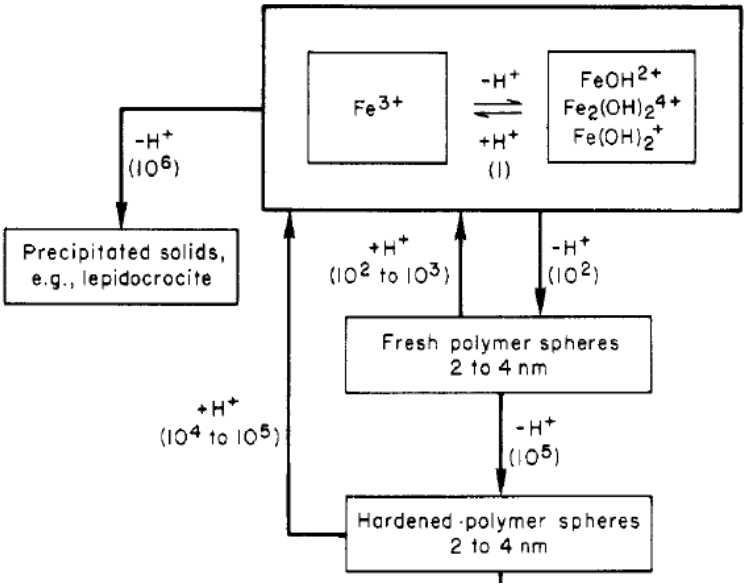

Figure 18. Hydrolysis in Fe(III) solution. Numbers in parenthesis indicate time in seconds. Figure taken from [44].

Based on speciation diagram, Fig. 18 [47], and the measurements of pH presented in this work, it was concluded that iron(III) is in the form of $[Fe(H_2O)_4(OH)_2]^+$ (b1 in Table V), which can aggregate to become $[(H_2O)_4Fe\mathbf{(OH)_2}Fe(H_2O)_2]^{4+}$ (b2 in Table V). Iron(II) remains as a mononuclear species $[Fe\ (H_2O)_6]^{2+}$ under the same experimental conditions. Ferrous complexes

form clusters only above pH 6. Although it has been suggested that as large as tetrameric polymers can be created, polynuclear forms of iron(II) are not well established [47].

Thus, on the basis of literature data and the current experimental condition it is expected that iron(III) is present as a dimeric form, with a size of 2-4nm (20-40Å) in diameter, whereas iron(II) simply exists as $[Fe(H_2O)_6]^{2+}$.

The standard reduction potential of Fe^{3+}/Fe^{2+} has been corrected due to polymeric form of iron(III), and has a value of 0.770V ± 0.002V [48], which means that polymerization of iron(III) complexes does not affect the energy required to add an electron to Fe^{3+}.

2. Experimental

2.1. Materials

Tris(bipyridine)ruthenium(II) dichloride, $[(bpy)_3Ru]Cl_2 \cdot 6H_2O$ (99.9%, Sigma Aldrich), 1,10-phenanthroline (99+%, Sigma Aldrich), sodium acetate (99+%, Sigma Aldrich), manganese(IV) oxide, MnO_2 (98%, Sigma Aldrich), triethanolamine, TEOA (98+%, Sigma Aldrich), iron (III) sulfate hydrate, $Fe_2(SO_4)_3 . H_2O$ (Alfa Aesar), potassium persulfate, $K_2S_2O_8$ (100%, Cole Palmer), silver nitrate, $AgNO_3$ (Mallinckrodt, Analytic Reagent), ferrous sulfate heptahydrate, $FeSO_4 \cdot 7H_2O$ (J.T. Baker), lead dioxide, PbO_2 (97+%, Strem Chemicals), sulfuric acid, H_2SO_4 (98+%, VWR), hydrochloric acid, HCl (38+%, VWR) and acetic acid, CH_3COOH (Pharmco-Aaper) were used as received.

2.2 Synthesis

All solutions were prepared with distilled water. Bis(2,2'-bipyridine)(2,3-bis(2pyridyl)pyrazine)ruthenium(II), $[(bpy)_2Ru(dpp)](PF_6)_2$ was synthesized and purified as previously reported [13] . Absorption and emission spectra agreed with previously published results of the complex [13].

2.3. Steady-State Measurements of $[Ru^{II}(bpy)_2dpp]^{2+}$ and Silver(I)

A series of solutions that contain 2.5 x 10^{-5} M $[bpy_2Rudpp]^{2+}$ and 1.25 x 10^{-1} to 1.25 x 10^{-4} M silver nitrate were prepared in distilled water at room temperature. All solutions were deaerated by bubbling with nitrogen gas for 5 minutes prior to any spectral measurement.

2.4. Quenching Experiment and Time Resolved Emission of $[Ru^{II}(bpy)_2dpp]^{2+}$ and Iron(III) in Water and Buffered Solution

Time-resolved lifetime measurements were conducted with 1.25 x 10^{-4} M $[Ru(bpy)_2dpp]^{2+}$ complex as a function of the concentration of the Fe^{3+} added, using either water or freshly prepared pH = 5 buffer as the solvent. Since ethanol or any basic buffer caused precipitation of the iron(II) in solution, acidic buffer was prepared with sodium acetate and acetic acid solutions at pH 4.9 ± 0.1. Absorption spectra of the aqueous solutions of Fe^{3+} in the absence of the $[Ru(bpy)_2dpp]^{2+}$ complex were also recorded. All solutions were deaerated with nitrogen gas bubbling for 5 minutes.

Table VI. Sample series used in steady state and lifetime measurement.

Sample	$[Ru(bpy)_2dpp]^{2+}$, [M]	$[Fe^{3+}]$, [M]
1	1.25 x 10^{-4}	0
2	1.25 x 10^{-4}	6.25 x 10^{-3}
3	1.25 x 10^{-4}	3.125 x 10^{-3}
4	1.25 x 10^{-4}	1.56 x 10^{-3}
5	1.25 x10^{-4}	1.05 x 10^{-3}
6	1.25 x 10^{-4}	7.75 x 10^{-4}
7	1.25 x 10^{-4}	6.25 x 10^{-4}
8	0	6.25 x 10^{-4}
9	1.25 x 10^{-4}	5.00 x 10^{-4}
10	1.25 x 10^{-4}	3.75 x 10^{-4}
11	1.25 x 10^{-4}	2.50 x 10^{-4}

2.5 Redox Reactions

2.5.1 Reaction of $[Ru(bpy)_2(dpp)]^{2+}$ and $[Ru(bpy)_3]^{2+}$ with Lead Dioxide, PbO_2

Reaction of $[(bpy)_3Ru]^{2+}$ complex with lead dioxide was performed as previously described [49]. Aqueous solutions of 2.5 x 10^{-4} M to 1.25 x 10^{-5} M $[Ru(bpy)_3]^{2+}$ were prepared in

the presence of 0.1 M, 1.0 x 10^{-3} M, and 1.0 x 10^{-5} M sulfuric acid at room temperature. Excess of PbO_2 solid was added to the solutions of $[Ru(bpy)_3]^{2+}$ and absorption spectra were recorded. The same approach was used with $[Ru(bpy)_2(dpp)]^{2+}$ except the concentration of sulfuric acid was 1.0 x 10^{-4} M. Electronic spectra of the samples were recorded.

2.5.2 Reaction of $[Ru(bpy)_2(dpp)]^{2+}$ and $[Ru(bpy)_3]^{2+}$ with Potassium Persulfate, $K_2S_2O_8$

Aqueous solutions of 2.5 x 10^{-4} M $[Ru(bpy)_3]^{2+}$ were prepared in the presence of 0.02 M hydrochloric acid or 0.02 M sulfuric acid at room temperature. To that prepared solutions, an excess (0.5g) of $K_2S_2O_8$ was added. The absorption spectra were recorded in 5 minute intervals. When no changes in absorption intensity were observed, 1M sodium hydroxide was added dropwise to reverse the reaction, and the absorption spectra of the completed reverse reaction were also recorded. Samples that contains $[Ru(bpy)_2(dpp)]^{2+}$ instead of $[Ru(bpy)_3]^{2+}$ were prepared in the same manner. To the solutions containing 2.5 x 10^{-4} M of $[Ru(bpy)_2(dpp)]^{2+}$ in the presence of 0.02 M H_2SO_4, an excess (0.5 g) of $K_2S_2O_8$ was added. Electronic spectra were recorded.

2.5.3 Reaction of $[Ru(bpy)_2(dpp)]^{2+}$ and $[Ru(bpy)_3]^{2+}$ with Chlorine Gas; , Generation of $Cl_{2(g)}$

A chlorine gas is used to investigate the presence of $[Ru(bpy)_2L]^{3+}$ (L= bpy or dpp) in solution. Generation of $Cl_{2(g)}$ was performed as previously described[2]. A sample of MnO_2, 3.62 g, was placed in a 250 mL three-neck flask, to which a cylindrical separatory funnel containing 1M hydrochloric acid is attached (Figure 19). The hydrochloric acid was carefully added to the manganese (IV) oxide using the stopcock, and chlorine gas, water and manganese (II) chloride were produced. The chlorine gas evolved, flowed through a $CaCl_2$ drying tube and was introduced into the 2.5 x 10^{-4} M $[Ru(bpy)_3]^{2+}$solution with access to air. Experiment was

[2] http://www.amazingrust.com/Experiments/how_to/Cl2.html

repeated and chlorine gas was introduce into 2.5 x 10^{-4} M $[Ru(bpy)_2(dpp)]^{2+}$ solution with no access to air. The reaction caused the $[Ru(bpy)_2(dpp)]^{2+}$ complex to turn slightly pink and within 2 seconds the steady state absorption was measured. All experiments were performed under the fume hood. A drying tube with $CaCl_2$ was used to absorb water formed in the reaction (Eq. 42) and to prevent dilution in ruthenium complex.

$$4HCl + MnO_2 \rightarrow MnCl_2 + 2H_2O + Cl_2 \qquad (42)$$

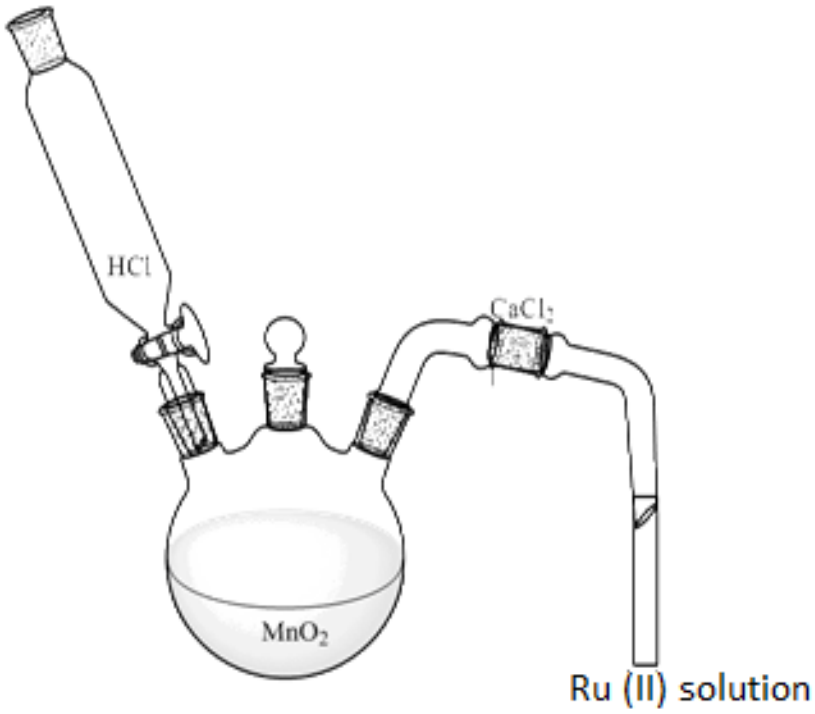

Figure 19. Schemic diagram of $Cl_{2(g)}$ generation.

2.6. Trapping Experiments

2.6.1 Trapping $[Ru(bpy)_2dpp]^{3+}$ with Triethanolamine, TEOA

Solutions were prepared as presented in [50, 51]. Samples of 5.0 x 10^{-5} M $[Ru(bpy)_2(dpp)]^{2+}$ and 2.0 x 10^{-3} M to 7.0 x 10^{-3} M [Fe(III)], and 0.2 M, 0.1 M, and 0.007 M TEOA were prepared. Absorption, emission spectra and pH values were recorded.

2.6.2 Trapping Fe(II) with 1, 10-phenanthroline

The 1,10-phenanthroline reacts with Fe(II) and forms complex $[Fe(phen)_3]^{2+}$ called "ferroin," which is used for the photometric determination of Fe(II).

$$3\ phen + Fe^{2+} \rightarrow [Fe(phen)_3]^{2+} \quad (43)$$

The three types of solutions were prepared in a darkened room. Four milliliter solutions containing 1.25 x 10^{-4} M $[Ru(bpy)_2dpp]^{2+}$ and 6.25 x 10^{-3} M Fe^{3+} were mixed with buffer. Buffer was freshly made with sodium acetate and sulfuric acid solutions [52] at pH 5 ± 0.1.

Solution #1 was irradiated for 30 minutes, while the other two solutions were kept in the dark and served as references. After irradiation of solution #1, two milliliter aliquot of the three individual (one irradiated and two dark) solutions were pipetted and mixed with 1 mL of 1,10-phenanthroline and 1 mL of buffer solution. The 1,10-phen concentration was 3 times larger than the concentration of Fe^{3+} in these solutions. The volume of the buffer solution was equal to about one-half the volume of the photolyte taken [52]. The prepared solutions were allowed to stand for 1 hour before absorbance measurements were taken. Absorption measurements were recorded at one hour interval in a 1 cm pathlength cell at 510 nm, where $[Fe(phen)_3]^{2+}$ absorbs. Solution #2 was assigned as the reference sample (no irradiated, no “spike” present). In addition, solution #3 contained small amounts of Fe^{2+} (prepared concentration of Fe^{2+} is 10 times smaller

than concentration of Fe^{3+}), named as a "spike" was kept for comparison to establish the reliability of the analyses of the photolyzed solution #1 for Fe^{2+}.

Experiments were repeated with the same concentration of $[Ru(bpy)_2dpp]^{2+}$, and varied concentrations of Fe^{3+}: 3.12 x 10^{-3} M, 1.56 x 10^{-3} M, and 7.8 x 10^{-4} M, respectively.

A standard calibration graph of $[Fe(phen)_3]^{2+}$ complex was prepared at different concentrations in the presence of 0.1% 1,10-phenathroline and buffer solutions. The molar extinction coefficient for $[Fe(phen)_3]^{2+}$ at 510 nm is (1.14 ± 0.04) x 10^4 M^{-1} cm^{-1}, which is within experimental error of the previously reported value of 1.11 x 10^4 M^{-1} cm^{-1} [52].

2.7. Instrumental

2.7.1 Absorption Spectroscopy

Absorption spectra of the sample solutions were recorded on a Cary 5000 UV-vis-NIR spectrophotometer using 1 cm pathlength cuvettes. The methacrylate cuvettes (Perfector Scientific) were transparent in the 285 – 800 nm wavelength regions. Analysis of absorption beyond 800 nm was made in quartz cells. In the 200-800 nm range, there was no difference in spectra recorded in plastic or quartz cells. The absorption spectra of water and buffer were subtracted from the spectra of the investigated solutions using the respective solvents. A portable pH meter (pH Pasco Passport Explorer PS 2000) was used for all pH measurements.

2.7.2 Emission Spectroscopy

Emission spectra were measured on a Jobin Yvon Horiba Fluoromax-3 spectrophotometer, with an excitation wavelength of 450-nm for $[Ru(bpy)_3]^{2+}$, and 423 nm and 470 nm for the $[Ru(bpy)_2(dpp)]^{2+}$ complex. The emission intensity as a function of wavelength was recorded.

2.7.3 Time Resolved Emission

Lifetime measurements of the Ru(II) complexes in the presence of the metal ions were obtained using a Quanta Ray DCR-2A Pulsed Nd:YAG (neodymium doped yttrium aluminum garnet) laser, with an excitation wavelength of 532 nm, and 5-8 ns pulse. The experimental setup is described by Zambrana and coworkers [53, 54].

2.7.4 Photolysis

All solutions were irradiated for 30 minutes by a Xenon and/or Mercury lamp. Light was filtered by a 17 cm pathlength Plexiglas container filled with water, in the presence of an additional filter that cuts off the light below 425 nm and above 2700 nm. The excitation intensity I_a = 1.2 - 2.0 x 10^{18} photons/sec, in the 425-550 nm region was measured by ferrioxalate actinometry [3].

2.8 Data Analysis

All data were imported into Microsoft's Excel (MS Office 2007, MS Office 2010) program for analysis. Curve fitting for the lifetime measurements were analyzed with IgorPro 6.0 software using a single exponential decay function.

[3] Dr. Edward Look, private communication.

3. Results

3.1 Steady State Experiment of $[(bpy)_2dppRu]^{2+}$

3.1.1 $[Ru(bpy)_2dpp]^{2+}$ and Silver(I)

Steady state UV-vis spectroscopic experiments were performed on aqueous solutions of $[Ru(bpy)_2dpp]^{2+}$ in the presence of $AgNO_3$. Selected spectra are presented in Fig. 20.

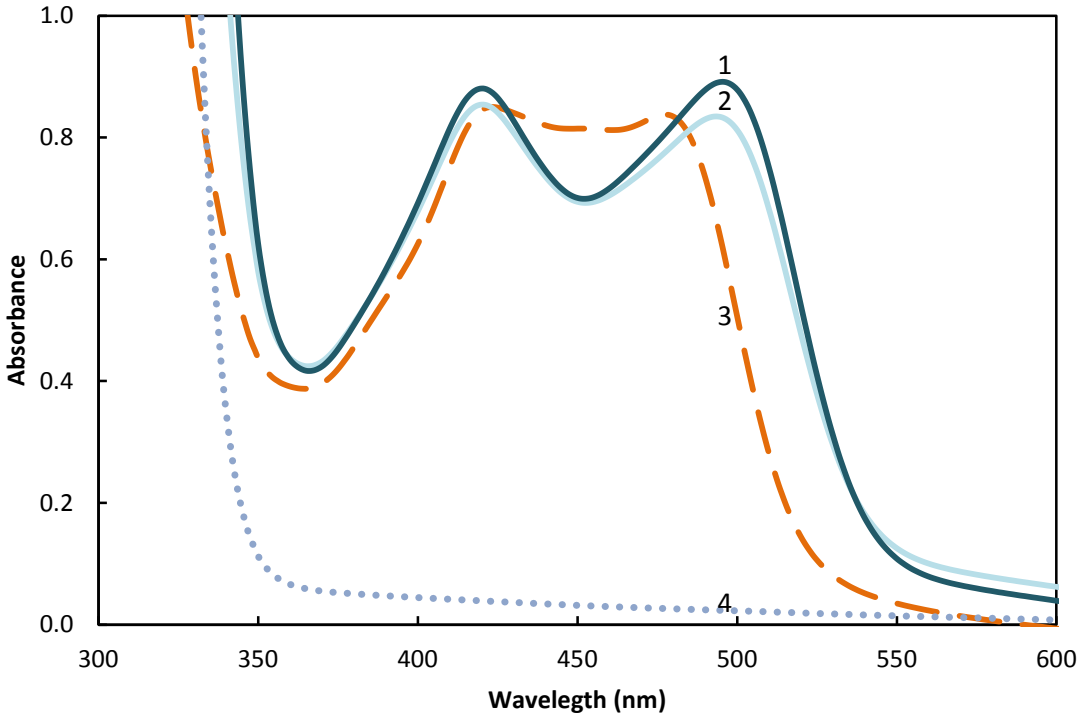

Figure 20. Absorption spectra, of 2.5 x 10^{-5}M $[Ru(bpy)_2dpp]^{2+}$ and Ag^+_{aq}. Solid lines represent solution that contains Ru(II) – Ag(I) mixed metal solutions: 2.5 x 10^{-5}M $[Ru(bpy)_2dpp]^{2+}$ and 1.25 x 10^{-4}M Ag^+ sol(1); 2.5 x 10^{-5}M $[Ru(bpy)_2dpp]^{2+}$ and 1.25 x 10^{-3} M Ag^+ sol(2). Dashed line represents 2.5 x 10^{-5}M $[Ru(bpy)_2dpp]^{2+}$ in water, sol(3). Silver(I) complex does not absorb, 1.25 x 10^{-4}M Ag^+ sol(4); dotted line.

Combination of $[Ru(bpy)_2dpp]^{2+}$ and Ag(I) metals causes shift in $[Ru(bpy)_2dpp]^{2+}$ band from 475 nm to 500 nm (Fig. 20). The shift of the ML(dpp)CT band is due to the formation of the $[Ru(bpy)_2dpp^{2+}\text{--}Ag^+]^{3+}$ dimer in which Ag^+ coordinates to the peripheral nitrogen of the dpp

ligand [23]. The equilibrium constant obtained for this dimer obtained from NMR analyses is K_{eq} = 22.5 ± 8.3 M^{-1} [23] for the following reaction:

$$*[Ru(bpy)_2dpp]^{2+} + Ag(H_2O)_{3\text{-}4}^{+} \rightarrow [Ru(bpy)_2dppAg]^{3+} \quad (44)$$

Formation of the $[Ru(bpy)_2dpp^{2+}\text{--}Ag^{+}]^{3+}$ dimer shifts the dpp localized MLCT emission from 700 nm to 740 nm (Fig. 21). The emission lifetime of the dimer is 57.5 ± 3ns and results are within experimental error of the data reported before [23]. The Stern-Volmer constant (Fig. 21) obtained from this experiment, K_{sv} = 35 M^{-1}, is comparable to K_{sv} = 30 M^{-1} as reported before [23].

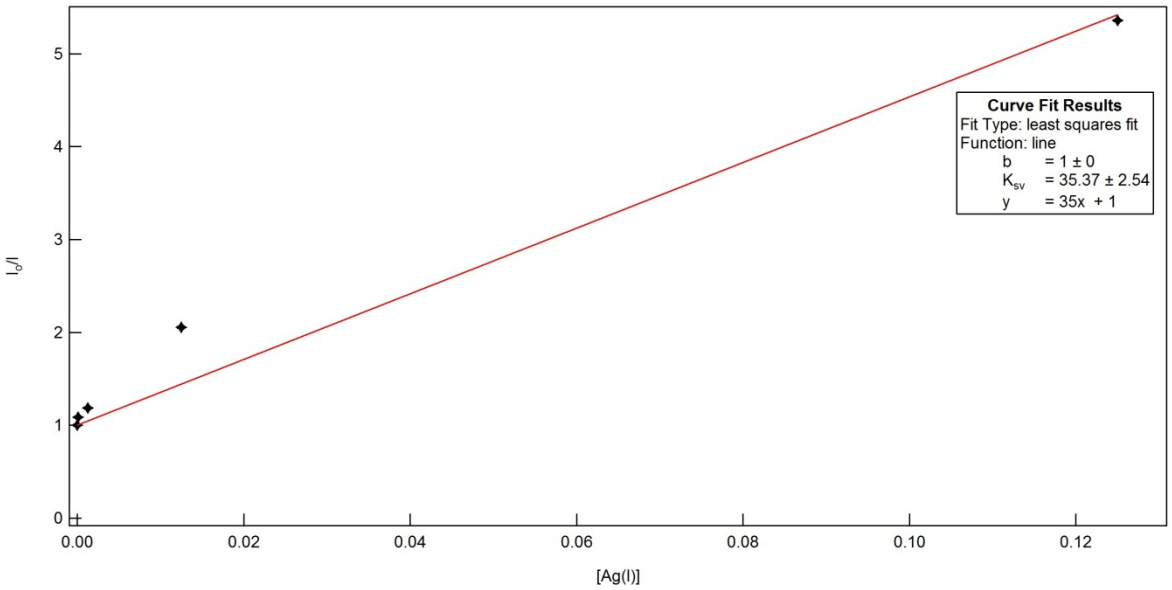

Figure 21. Stern-Volmer plot for $[(bpy)_2Rudpp]^{2+}$ in presence of Ag^{+}_{aq}, with K_{sv} = 35 ± 2.5 M^{-1}.

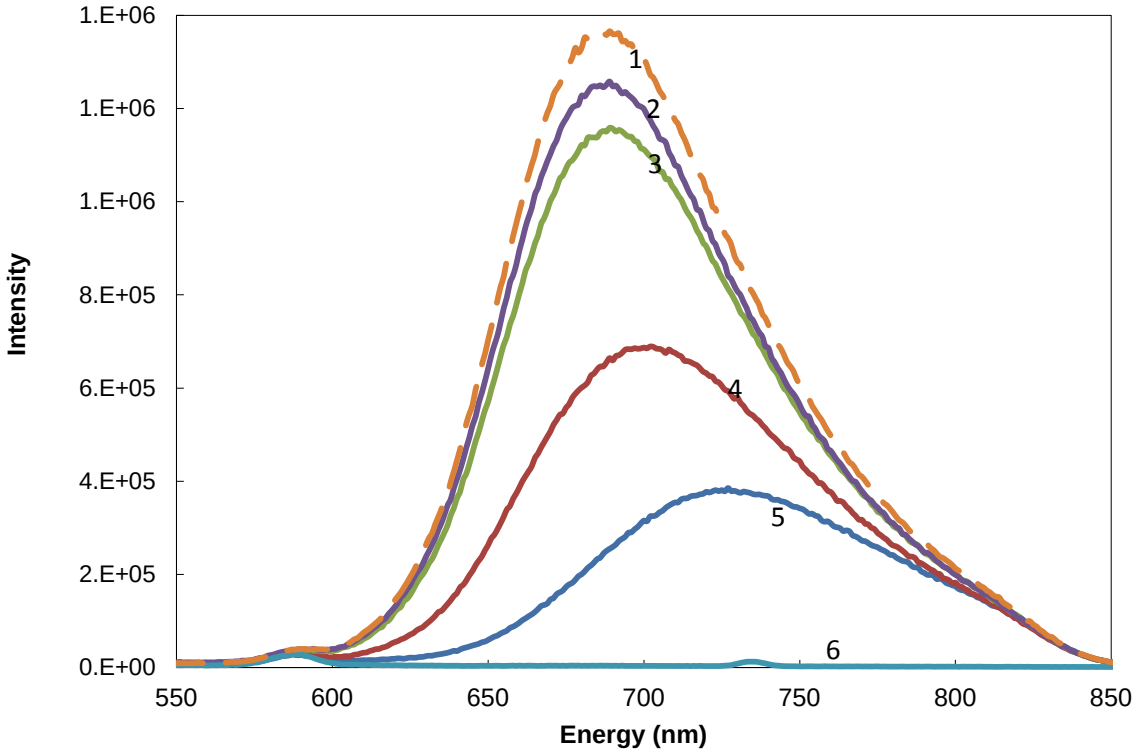

Figure 22. Emission of 2.5 x 10^{-5} M $[Ru(bpy)_2dpp]^{2+}$ and $AgNO_3$ excited at 490 nm. Dashed line represents ruthenium (II) complex in water (#1), solid lines represent solution that contains Ru (II) – Ag (I) mixed metal solutions. Concentration of ruthenium was kept constant while concentration of silver (I) varies from 1.25 x 10^{-1} to 1.25 x 10^{-4} M (#2-5). Silver (I) complex (#6) does not emit.

Quenching of the emission of a 2.5 x 10^{-5}M $[Ru(bpy)_2dpp]^{2+}$ by Ag^+ solutions were excited with 490 nm light and the concentration of Ag^+ was 1.25 x 10^{-1} M (#2); 1.25 x 10^{-2} M (#3); 1.25 x 10^{-3} M (#4); 1.25 x 10^{-4} M (#5), Fig. 22.

3.1.2 $[Ru(bpy)_2dpp]^{2+}$ With Iron(III)

The UV-vis absorption spectra of $[Ru(bpy)_2dpp]^{2+}$, $Fe^{3+}_{(aq)}$, and the mixture of the two are presented in Fig. 23**.** The UV-vis absorption spectra of the mixtures of $[Ru(bpy)_2dpp]^{2+}$and Fe^{3+} do not exhibit any new peaks, and are basically the same with the individual components. The absence of any change in the spectra implies no interaction between the complex and Fe^{3+}.

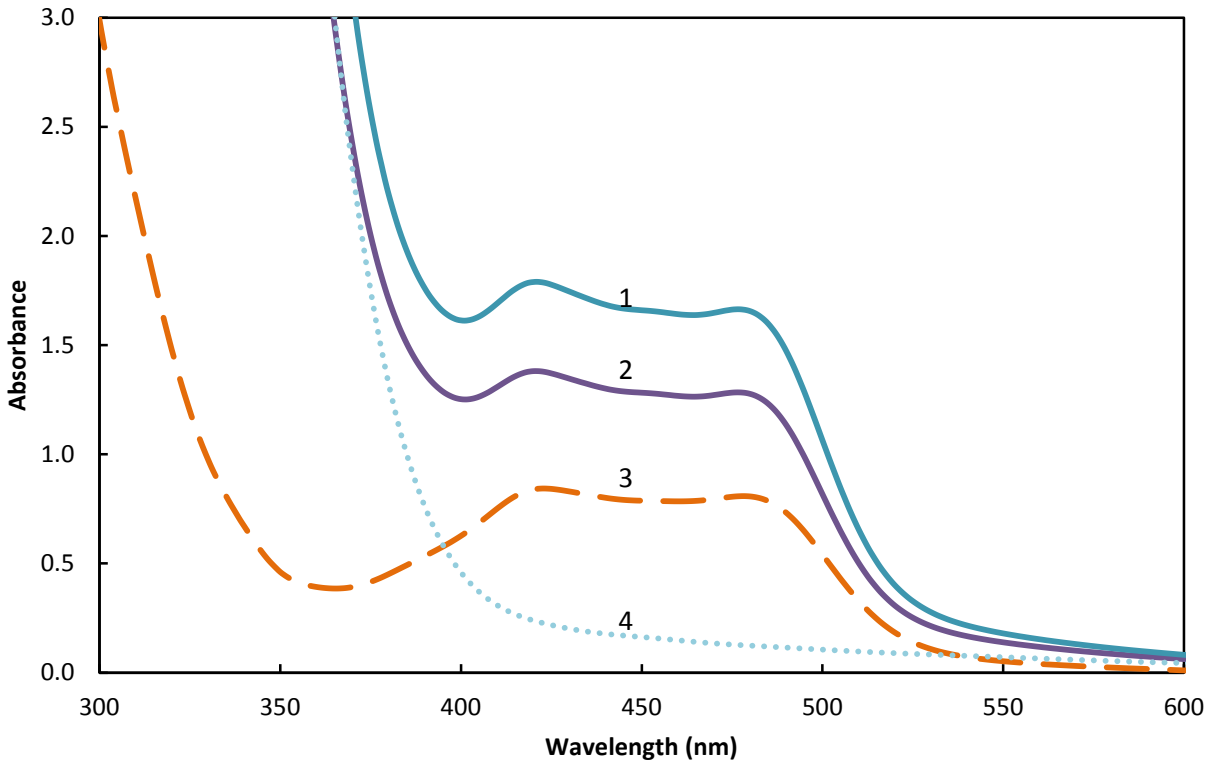

Figure 23. Absorption spectra of aqueous solutions, of $[Ru(bpy)_2dpp]^{2+}$ and iron(III). Dashed line represents 1.0 x 10^{-4} M $[(bpy)_2dppRu]^{2+}$ in water, sol(3). The solid lines represent samples that contain Ru (II) – Fe (III) mixed metal solutions; 1.0 x 10^{-4} M $[(bpy)_2dppRu]^{2+}$ and 3.75 x 10^{-3} M Fe^{3+}_{aq} sol(1), and 1.0 x 10^{-4} M $[Ru(bpy)_2dpp]^{2+}$ and 5.0 x 10^{-3} M Fe^{3+}_{aq} sol(2). Fe(III) does not absorb; dotted line, 5.0 x 10^{-3} M Fe^{3+}_{aq}, sol(4).

$$*[Ru\ (bpy)_2dpp]^{2+} + [Fe(H_2O)_6]^{3+} \rightarrow [Ru(bpy)_2dpp]^{3+} + [Fe(H_2O)_6]^{2+} \quad (45)$$

More detailed spectra of ruthenium complex in the presence of iron (III) are presented in water, Fig. 24, and in pH = 5 buffer, Fig. 25. The specific concentration of $Fe^{3+}_{(aq)}$ used are presented in the Experimental Section 2.4, Table VI.

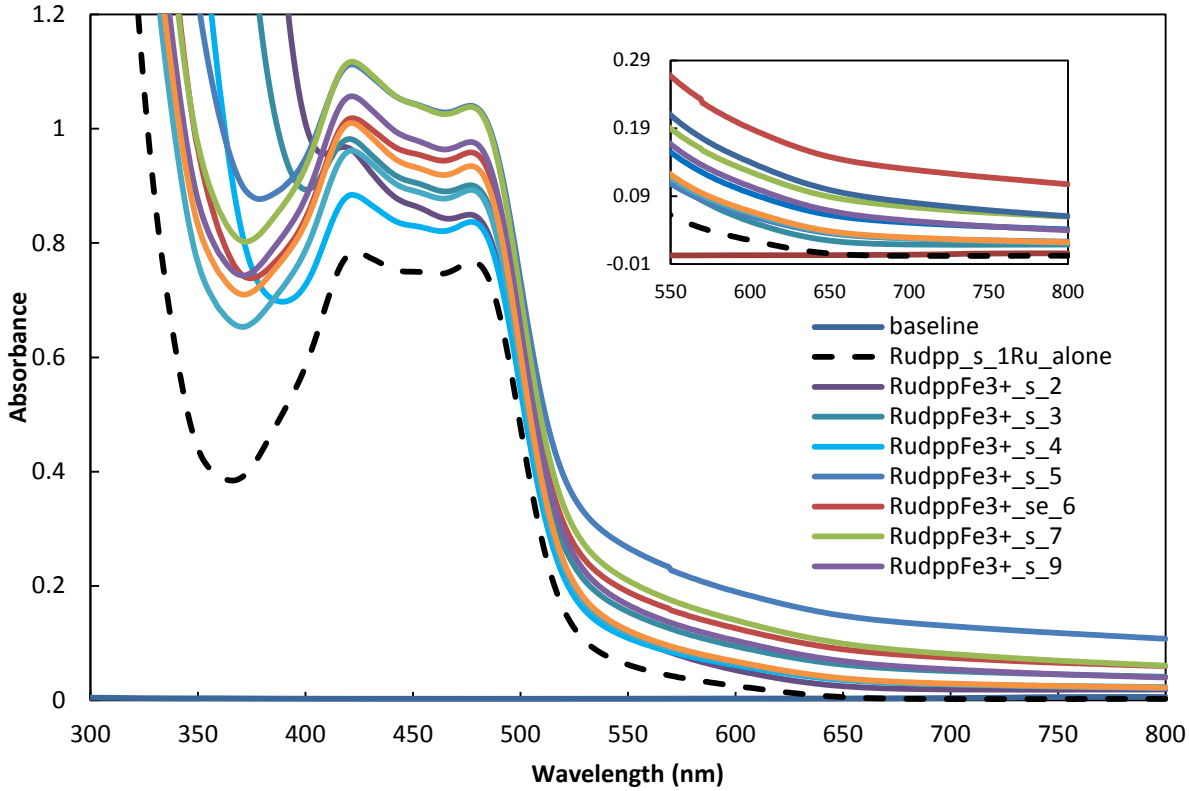

Figure 24. Absorption spectra of $[Ru(bpy)_2dpp]^{2+}$ and iron(III) in water. Spectrum of Iron(III) in water is omitted for clearer view. Inset is an expansion of the changes at longer wavelength. Dashed line – $[(bpy)_2Rudpp]^{2+}$ complex in water; solid lines – $[Ru(bpy)_2dpp]^{2+}$ in presence of iron (III). Concentrations as described in the Experimental Section, 2.4, Table VI.

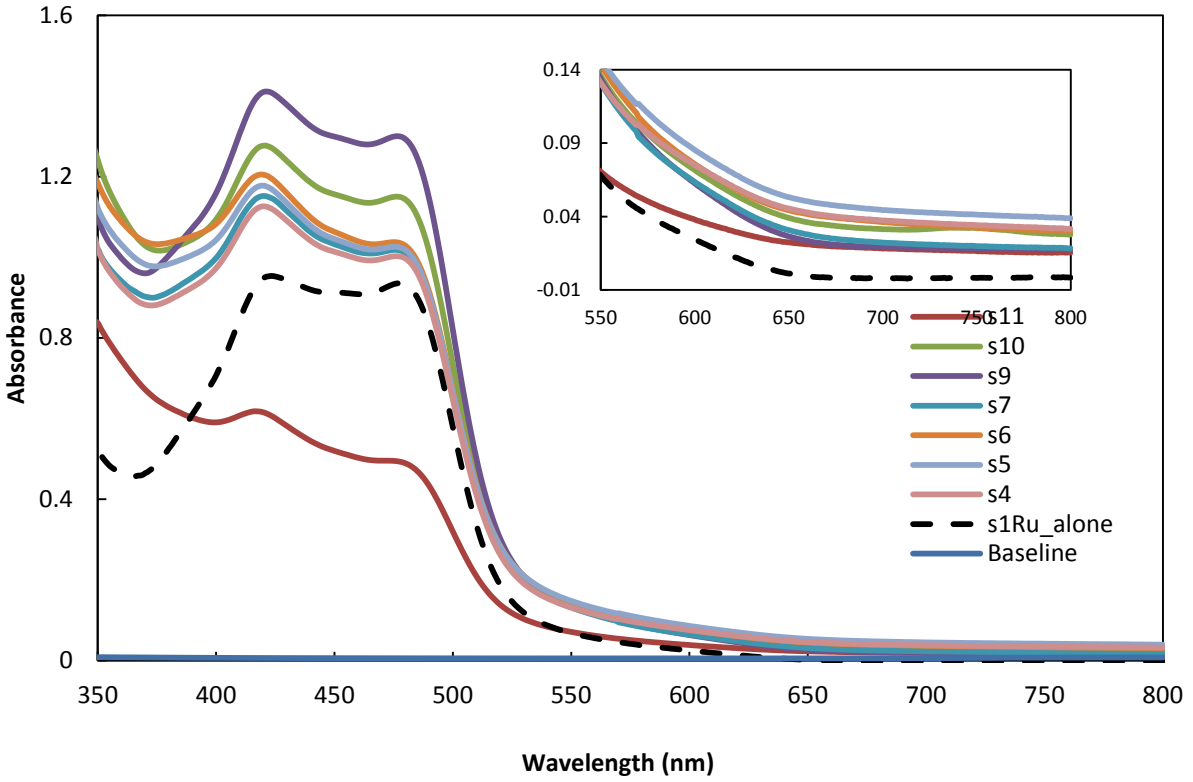

Figure 25. Absorption spectra of $[Ru(bpy)_2dpp]^{2+}$and iron(III) in buffer pH = 5. Inset provides insight for spectra in longer wavelength. Concentrations as described in the Experimental Section, 2.4, Table VI.

Spectra in 400-800 nm were normalized to compare relative intensities of the absorption bands. Normalization was carried out by taking the highest value of absorption for each spectrum and then dividing the absorbance at the other wavelength by that number. The same procedure was repeated for every spectrum. Replotted data are presented in Figs. 26 and 27.

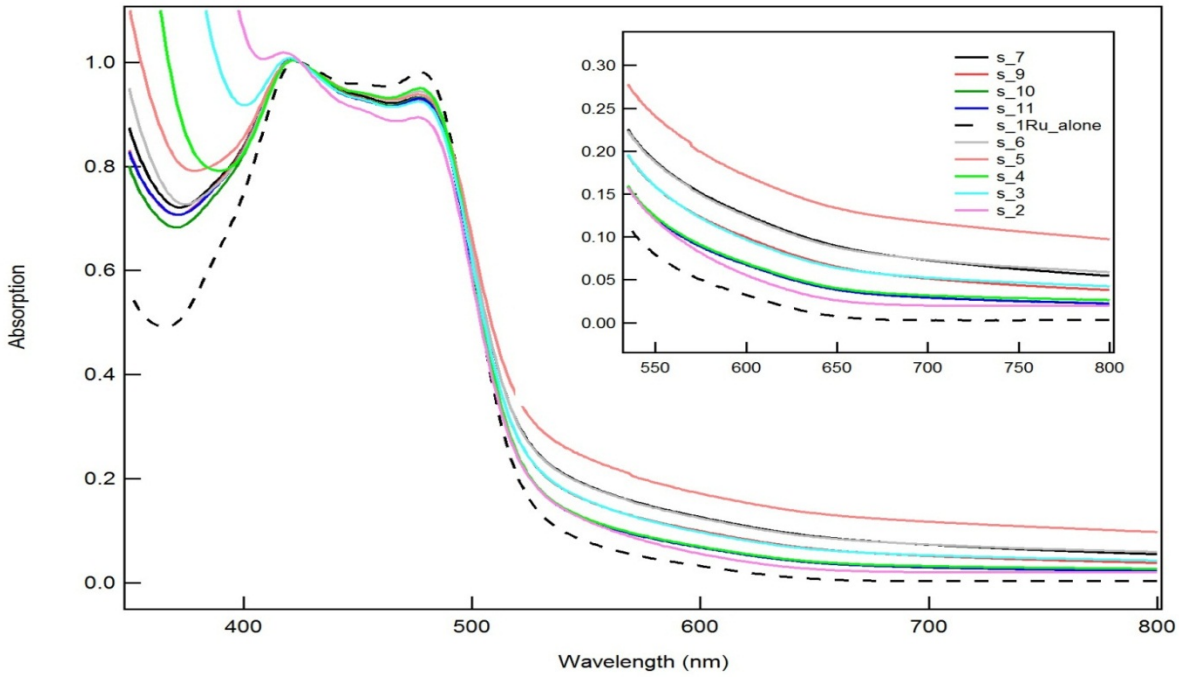

Figure 26. Normalized absorption of $[Ru(bpy)_2dpp]^{2+}$ and iron (III) in water. Dashed line represents ruthenium (II) complex. The absorption values in 400-500 nm decreased as the concentration of iron increased. The solution numbers presented in the inset represents the specific concentration of iron(III) and $[Ru(bpy)_2dpp]^{2+}$ are presented in Table VI.

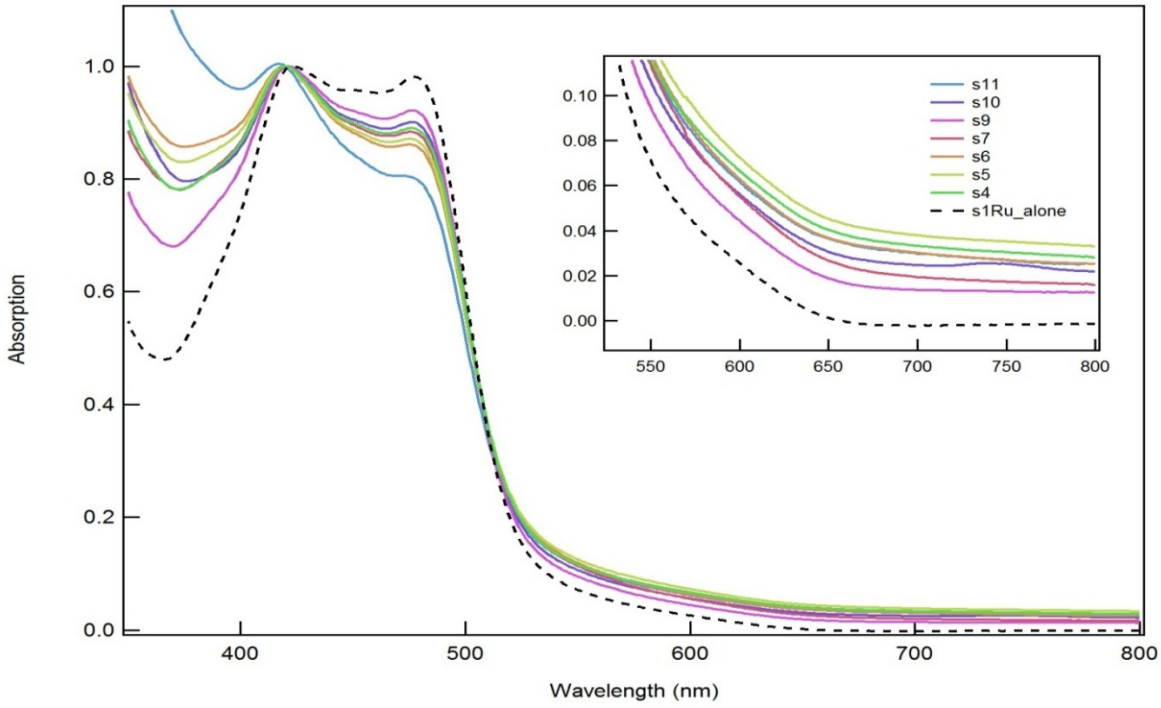

Figure 27. Normalized absorption of $[Ru(bpy)_2dpp]^{2+}$ and iron (III) in buffer pH = 5. The absorption values in 400-500 nm decreased as the concentration of iron increased. The solution numbers presented in the inset represents the specific concentration of iron(III) and $[Ru(bpy)_2dpp]^{2+}$ are presented in Table VI.

Figures 26 and 27 clearly show that the spectral changes in aqueous solution and in pH = 5 buffer differ. Specifically, a plot (Fig. 26) shows the intensity of the 480 nm absorption, which is the ML(dpp)CT transition to dpp ligand, declines relatively to the 420 nm absorption which is the MLCT to bpy as the concentration of Fe^{3+} increases in buffered solution, but not in aqueous solutions.

Measuring the pH's of the different solutions shows that $[Ru(bpy)_2dpp]^{2+}$ has relatively little effect on the values of pH, whereas Fe^{3+} has a much larger effect. Values of pH were recorded for aqueous and buffered solution. Prepared buffer (sodium acetate/acetic acid) has pH = 4.8 ± 0.1. The pH of an aqueous solution of 1.25 x 10^{-4} M $[Ru(bpy)_2dpp]^{2+}$ is 8, while the pH of 1.25 x 10^{-4} M $[Ru(bpy)_2dpp]^{2+}$ in buffer is 5. A solution in water of $[(bpy)_2Rudpp]^{2+}$ and varied concentration of Fe^{3+} has pH in the range of 2.8 - 3.34. Acidity increases with concentration of iron (III). A solution of $[Ru(bpy)_2dpp]^{2+}$ and varied concentration of Fe^{3+} in buffer has pH near 4.0 - 4.7.

3.2 Quenching Experiments of $[Ru(bpy)_2dpp]^{2+}$ by Fe(III) in Water and Buffered Solution

Steady state and lifetime emission spectroscopic measurements were made for $[Ru(bpy)_2(dpp)]^{2+}$ and Fe(III). Excitation wavelengths are 418 nm and 478 nm for aqueous solutions, and 415 nm and 477 nm in buffered solutions. Initially, solutions were N_2-purged. However, it has been shown (Table IX) that the presence of oxygen does not change the intensity of quenching significantly, due to a small value of lifetime. Latter experiments were performed without degassing. There is no significant change in emission bands of excited ML(bpy)CT and ML(dpp)CT, in both water and buffer solution.

The emission spectra were recorded for both sets of samples, in water and in pH = 5 buffered solution. There is no significant change in emission in water and buffer when excited at 418 or 478, and 415 or 477 nm, respectively, as can be seen in Fig. 28a-d. The quencher and buffer do not emit. Emission spectra of $[Ru(bpy)_2dpp]^{2+}$ and $Fe_2(SO_4)_3$ are represented by broken lines and dots, respectively, in Figs. 28a-d. Solutions that contain $[Ru(bpy)_2dpp]^{2+}$ in the presence of $Fe_2(SO_4)_3$ are shown as solids lines. Numbers (see Fig. 28c) represent concentration of the sample, as shown in Table VI, Section 2.4. Absorption spectra for aqueous solution and buffered solution are similar, with no observable spectral changes.

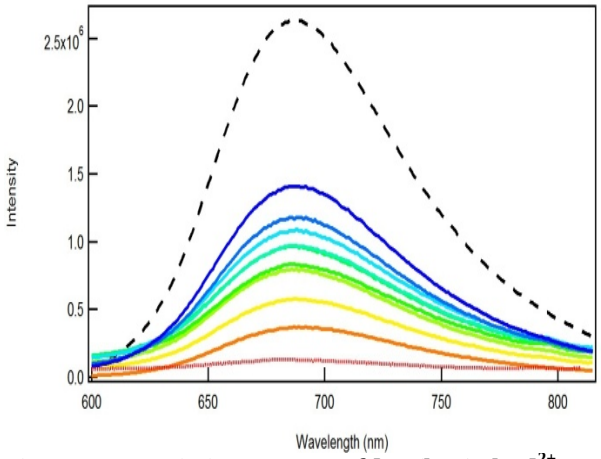

Figure 28a. Emission Spectra of $[Ru(bpy)_2dpp]^{2+}$ and $Fe_2(SO_4)_3$ in water excited at 418 nm.

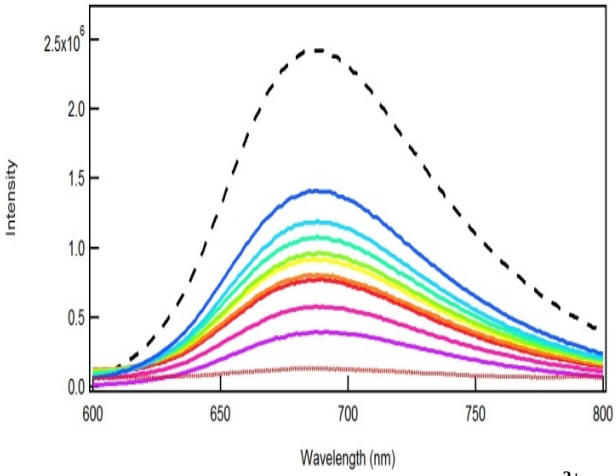

Figure 28b. Emission Spectra of $[Ru(bpy)_2dpp]^{2+}$ and $Fe_2(SO_4)_3$ in water excited at 478 nm.

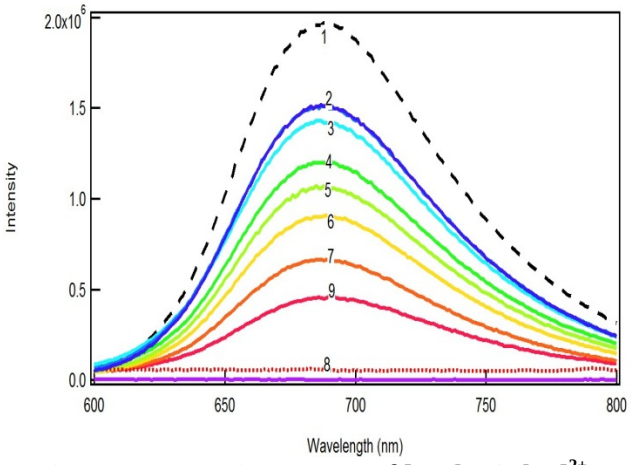

Figure 28c. Emission Spectra of $[Ru(bpy)_2dpp]^{2+}$ and $Fe_2(SO_4)_3$ in buffer excited 415 nm.

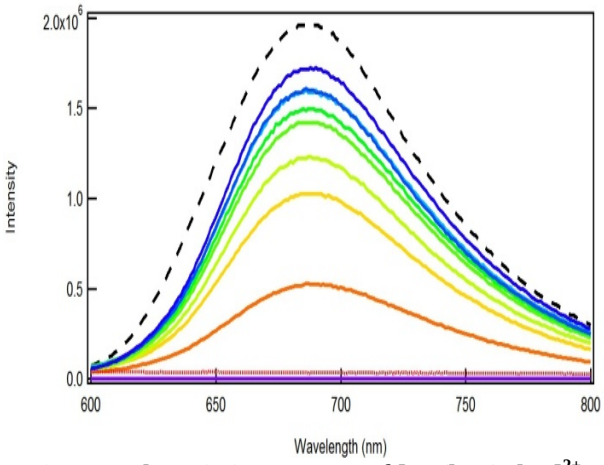

Figure 28d. Emission Spectra of $[Ru(bpy)_2dpp]^{2+}$ and $Fe_2(SO_4)_3$ in buffer excited at 477 nm.

As can be seen in Fig. 29, the Stern-Volmer plots with the buffered solutions show larger deviation from linearity, which may be due to existing pre-equilibrium (static quenching).

No quenching of $[Ru(bpy)_2dpp]^{2+}$ by Fe^{3+} was observed for the solution in the presence of TEOA.

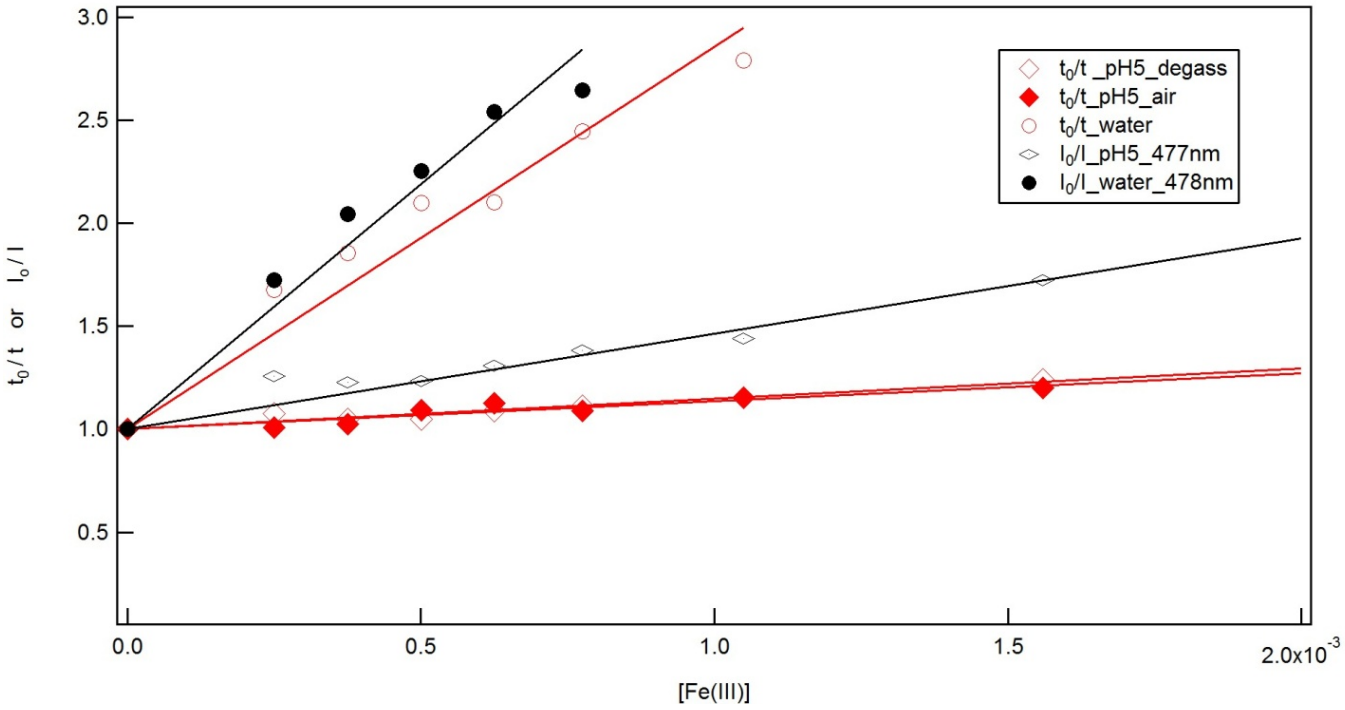

Figure 29. Stern - Volmer plot for all meassurements between $[Ru(bpy)_2dpp]^{2+}$ and $[Fe(H_2O)_6]^{3+}$. Red lines are for data from lifetime experiments, black from steady-state emissions. Cirles represent measurement in water, diamond shapes – in buffer.

Table VII. Stern - Volmer constant, K_{sv}, obtained from $[Ru(bpy)_2dpp]^{2+}$ emission at 709 nm.

K_{sv} (M^{-1})	Ru-bpy[a]	Ru-dpp[b]
In buffer	1163 ± 50	472 ± 30
In water	2352 ± 110	1793 ± 184

[a] excitation at ML(bpy)CT wavelength: 415 nm (in buffered solution), 418 nm (in aqueous solution).
[b] excitation at ML(dpp)CT wavelength: 477 nm (in buffered solution), 478 nm (in aqueous solution).

Bimolecular quenching constants were obtained from Stern – Volmer plot (Eqs. 23, 24), and the values of the bimolecular quenching rate constant, k_q, was calculated via Eq. 24 using K_{sv} = 472 M^{-1} and K_{sv} = 1793 M^{-1}.

Table VIII. Values of bimolecular quenching constant, k_q.

k_q ($M^{-1}s^{-1}$)	In water	In buffer
Steady state experiment (I_o/I)	$1.81 \pm 0.19 \times 10^{10}$	$4.37 \pm 0.27 \times 10^{9}$
Time-dependent experiment (τ_o/τ)	$1.17 \pm 0.12 \times 10^{10}$	$1.40 \pm 0.09 \times 10^{9}$; ($1.31 \times 10^{9}$,air)

Lifetimes of 1.25 x 10^{-4} M $[Ru(bpy)_2dpp]^{2+}$ (τ_0, Table IX), and lifetimes of 1.25 x 10^{-4} M $[Ru(bpy)_2dpp]^{2+}$ in the presence of iron (III) at various concentrations were determined, and are presented in Table IX. Measurements were performed on degassed aqueous and degassed buffered solution. One set of buffered solutions was not degassed, in order to analyze whether the oxygen is involved in quenching process.

Table IX. Effect of type of solvent and oxygen on the lifetime of $[(bpy)_2Rudpp]^{2+}$ and $[Ru(bpy)_2dpp]^{2+}$ in a presence of Fe(III). Lifetime (nanoseconds), τ_0 is for ruthenium (II) complex without a quencher.

[Fe(III)], M	τ (in degassed buffer) τ_0 = 106 ns	τ(in buffer, air) τ_0 = 104 ns	τ(in water) τ_0 = 131 ns
0.001560	86	87	41
0.001050	92	90	47
0.000775	96	95	54
0.000625	98	92	62
0.000500	101	95	63
0.000375	102	101	71
0.000250	99	103	78
K_{sv}	148 ± 8	136 ± 11	1543 ± 83

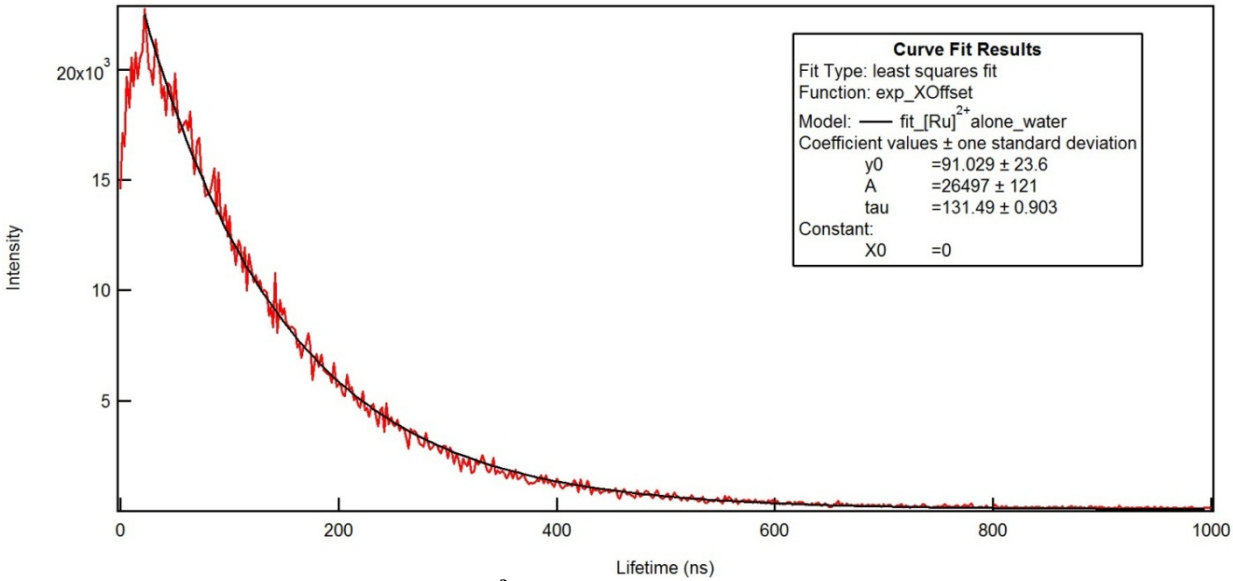

Figure 30. Lifetime decay of $[Ru(bpy)_2dpp]^{2+}$ solution water. The curve fitting with least square analysis was performed with IgorPro 6 software.

3.3 Redox Reactions

3.3.1 Reaction of $[Ru(bpy)_2(dpp)]^{2+}$ and $[Ru(bpy)_3]^{2+}$ with PbO_2

Adding lead dioxide to a $[Ru(bpy)_3]^{2+}$ solution containing a 0.1 M sulfuric acid leads to new absorption band at 700 nm, Fig. 31. The spectral change and the color change from read (orange) to green indicate a change of oxidation state as follows:

$$2[Ru(bpy)_2L]^{2+} + PbO_2 + 4H^+ \rightarrow 2[Ru(bpy)_2L]^{3+} + Pb^{2+} + 2H_2O \qquad (46)$$

where L= bpy or dpp.

The oxidation of $[(bpy)_2Ru(dpp)]^{2+}$ by lead dioxide was examined in the same manner. No visible peak has been found that indicates $[(bpy)_2Ru(dpp)]^{3+}$, as shown in Fig. 31. Even using $[(bpy)_2Ru(dpp)]^{2+}$ as the reference in order to investigate any possible spectral change, no change in absorption was found in the 550 – 650 nm region.

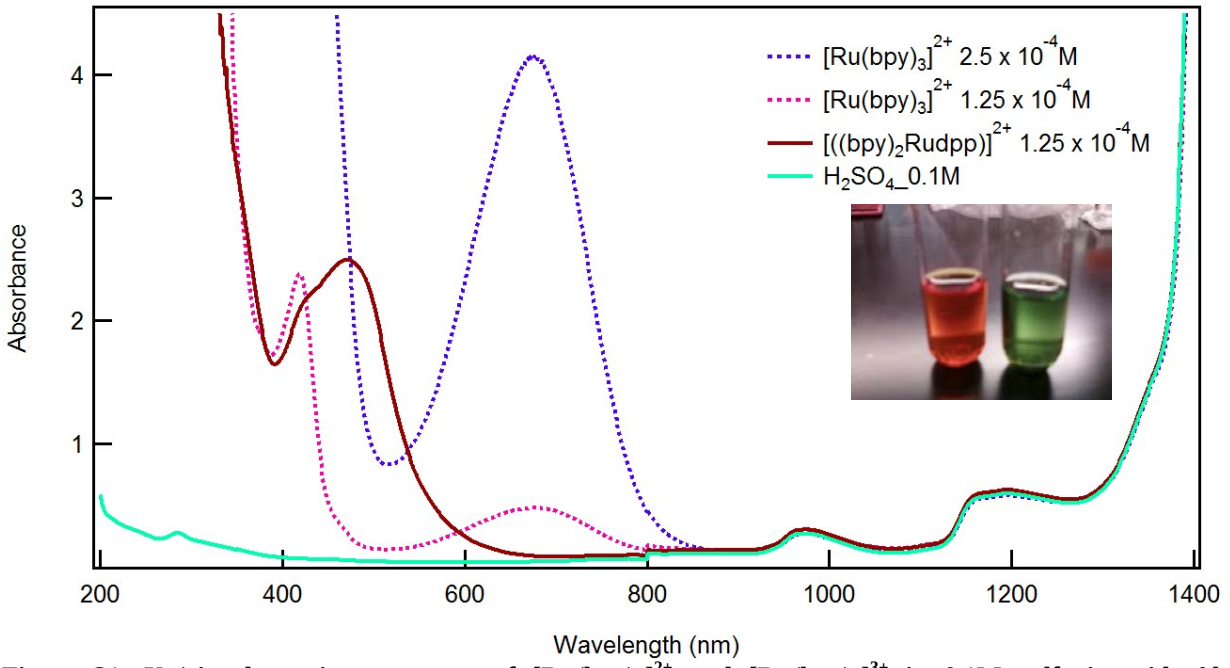

Figure 31. Uv/vis absorption spectrum of $[Ru(bpy)_3]^{2+}$ and $[Ru(bpy)_3]^{3+}$ in 0.1M sulfuric acid. Also, $[Ru(bpy)_2dpp]_{2+}$ in 0.2M sulfuric acid at pH=1.8 The sulfuric acid was added dropwise to the solution maintain acidic environment for the Ru^{3+} stability. Visible color change in reaction of $[Ru(bpy)_3]^{2+}$ with PbO_2. Left, orange solution $[Ru(bpy)_3]^{2+}$; right, green tube $[Ru(bpy)_3]^{3+}$ (inset).

3.3.2 Reaction of $[Ru(bpy)_2(dpp)]^{2+}$ and $[Ru(bpy)_3]^{2+}$ with $K_2S_2O_8$

Excess of potassium persulfate (0.5g) was added to $2.5x10^{-4}$M $[Ru(bpy)_3]^{2+}$ in 0.02M sulfuric acid. The absorption peak at 450 nm is assigned to Ru-bpy (MLCT) band while its shoulder at 425 nm is believed to be vibrionic interactions with solvents [55]. At the beginning of the reaction, the absorption peak maximum was at 450 nm with a shoulder at 425 nm, and the solution had orange color. After 30 minutes in H_2SO_4, or after 1 hour in HCl, the two 425 and 450nm peaks reached the same intensity (Fig. 32) and the solution turned yellow/green. After that point, the intensity of 425 nm-peak increased relatively to the 450 nm-peak which decreased and the solution became green. Absorption spectra were recorded in the 2-75 minutes range in H_2SO_4, and the 2-140 minutes range in HCl. After 77 minutes in H_2SO_4, and 140 min in HCl, there was no further change in the spectrum when NaOH was added to confirm reversibility of reaction, (Fig. 32, Table X).

Table X. The molar absorption coefficient (M^{-1} cm^{-1}) of $[Ru(bpy)_3]^{2+}$ in a presence of $[S_2O_8]^{2-}$ in acidic solution atcertain time of the reaction.

Absorbance measurement at given λ	2.5×10^{-4}M $[Ru(bpy)_3]^{n+}$			
	In H_2SO_4(0.02M)		In HCl(0.02M)	
	At 2 min	At 77 min	At 3 min	At 70 min
425nm[a]	1.0×10^4	3.7×10^3	8.1×10^3	1.0×10^3
455nm	1.3×10^4	2.6×10^3	9.8×10^3	3.0×10^3
675 nm[b]	0	2.8×10^2	0	1.5×10^2

[a] $\epsilon[Ru(bpy)_3]^{n+} = 1.46 \times 10^4$ at 452nm, [b] $\epsilon[Ru(bpy)_3]^{n+} = 72$ at 662nm [Coord. Chem. Rev., 46,159-244, 1982, Photochem & Photobiology 68, 141-142, 1998]

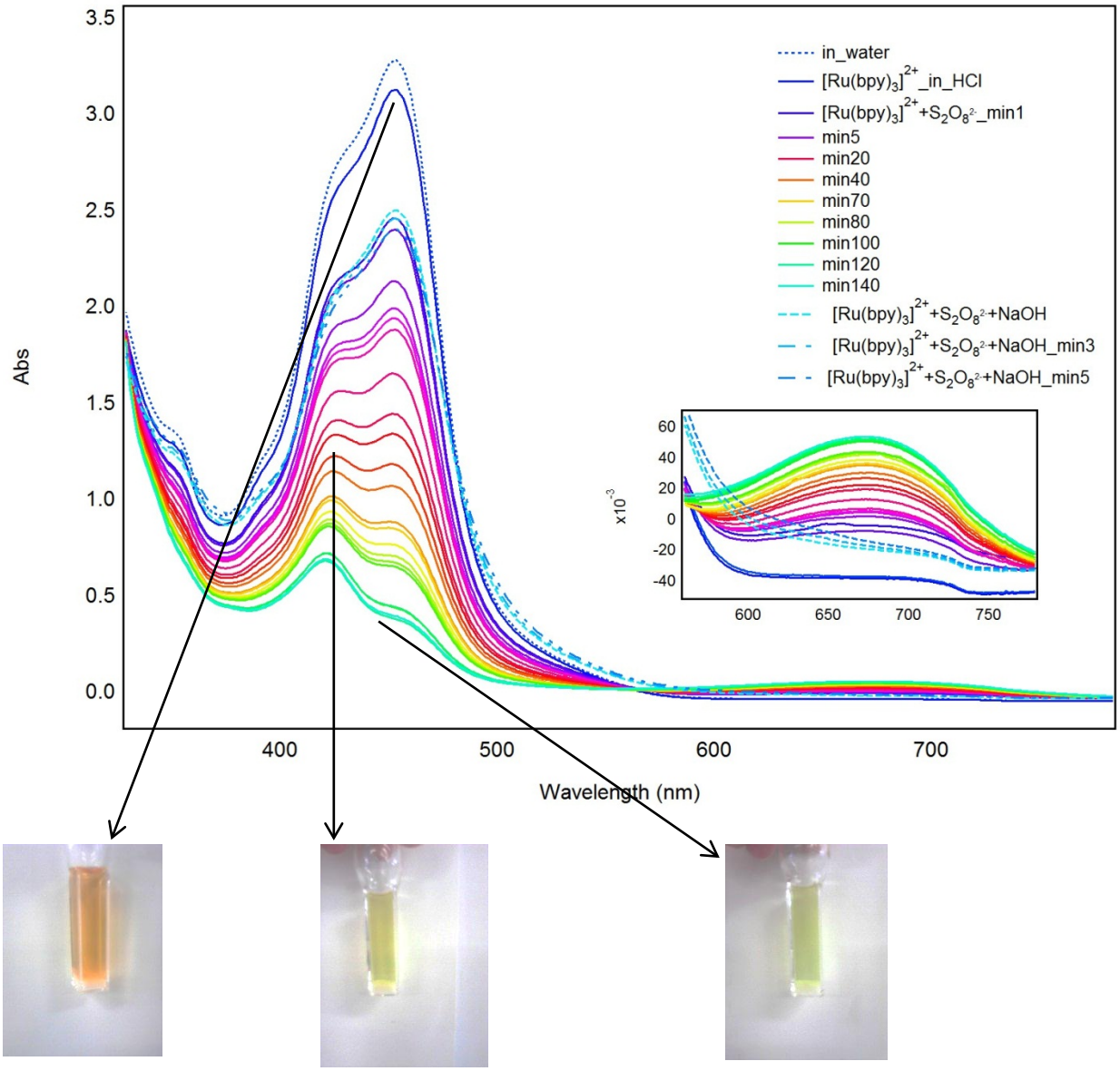

Figure 32. Absorption spectra of 2.5 x 10^{-4} M $[Ru(bpy)_3]^{2+}$ in 0.02M HCl with excess (0.5g) of $K_2S_2O_8$.

The experiment was performed in the same way with $[(bpy)_2Ru(dpp)]^{2+}$. Results are presented in Fig. 33. There was no significant change in spectra, (dashed lines vs solid blue lines) when $S_2O_8^{2-}$ was added. There was only one small broad peak (?) around 700 nm observed in first two minutes of mixing $[(bpy)_2Ru(dpp)]^{2+}$ and potassium persulfate, presented as green line on inset,

Fig. 33. For comparison with previous experiment, NaOH was added to the $[(bpy)_2Rudpp]^{2+}$-$S_2O_8^{2-}$ solution. Intensity of $[(bpy)_2Rudpp]^{2+}$ in 400-500 nm range was still dropping, after addition of NaOH. Unlike in the previous experiment with $[(bpy)_3Ru]^{2+}$ and $S_2O_8^{2-}$, where addition of OH^- reversed the spectral changes, adding the OH^- to the $[(bpy)_2Rudpp]^{2+}$-$S_2O_8^{2-}$ solution lead to a decline in the MLCT absorptions, as shown in Fig. 33 (dotted red lines).

$$4[Ru(bpy)_2L]^{2+} + 2[S_2O_8]^{2-} \xrightarrow{h\nu} 4[Ru(bpy)_2L]^{3+} + 4[SO_4]^{2-} \qquad (47)$$

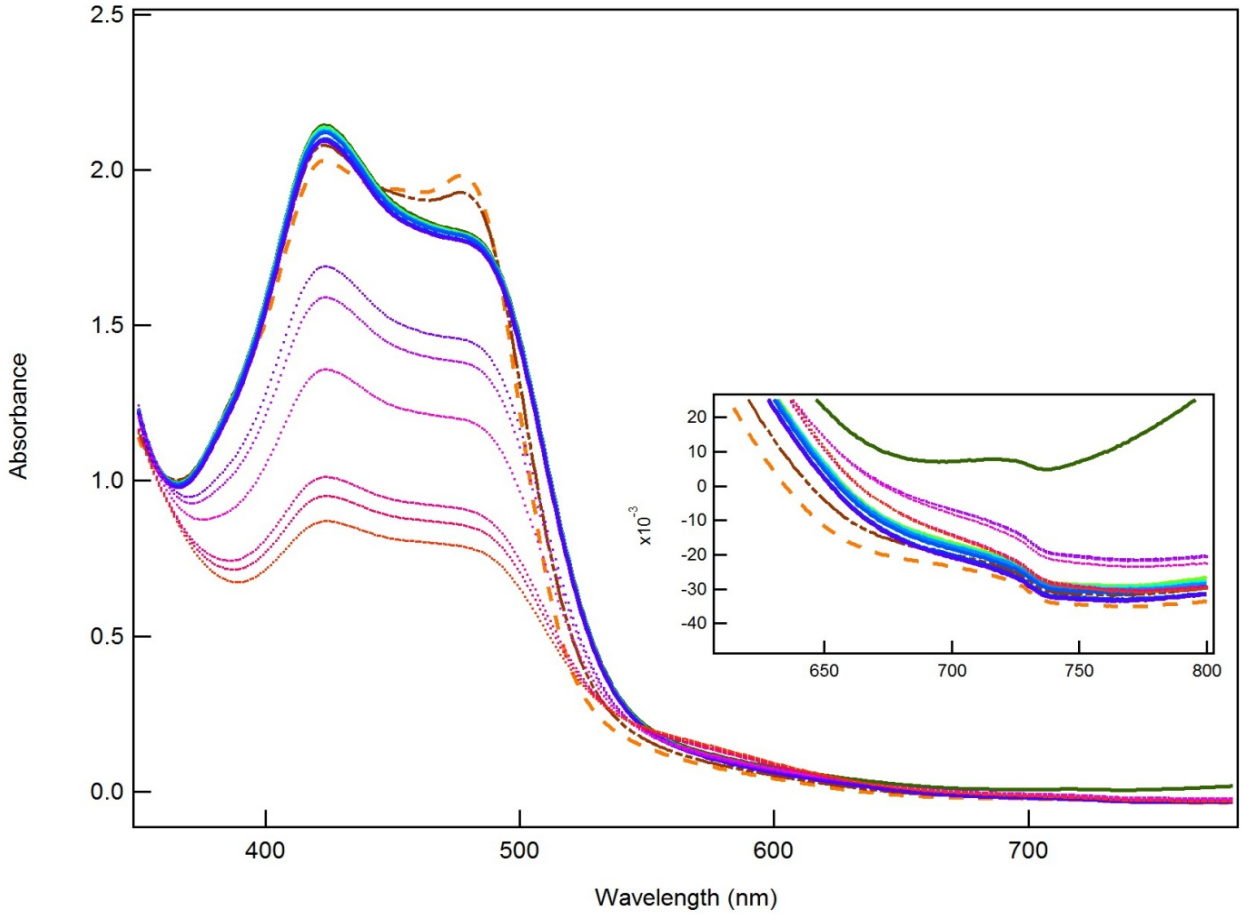

Figure 33. Electronic absorption spectra of $[(bpy)_2Ru(dpp)]^{2+}$ with $[S_2O_8]^{2-}$.
Orange dashed lines (---): $[Ru(bpy)_2(dpp)]^{2+}$in water; Green and blue solid lines represents $[(bpy)_2Ru(dpp)]^{2+}$+$[S_2O_8]^{2-}$ (in acidic solutions); Purple- red lines (⁎⁎⁎) represents $[Ru(bpy)_2(dpp)]^{2+}$+$[S_2O_8]^{2-}$ + NaOH, the latter ones shows that this reaction is not reversible after adding NaOH.

Table XI. The molar absorption coefficient (M^{-1} cm^{-1}), of $[Ru(bpy)_2dpp]^{2+}$ in a presence of $[S_2O_8]^{2-}$, in 0.02M H_2SO_4, at certain time of the reaction.

	2.5×10^{-4}M $[Ru(bpy)_2dpp]^{n+}$	
Absorbance measurement at given λ	At 1min	At 5min
425 nm	8.6×10^3	8.5×10^3
480 nm	7.2×10^3	7.1×10^3
725 nm	3.0×10^1	0

3.3.3 Reaction of $[Ru(bpy)_2(dpp)]^{2+}$ and $[Ru(bpy)_3]^{2+}$ with Cl_2 gas

Chlorine gas was generated as described in procedures. Solutions of $[Ru(bpy)_2(dpp)]^{2+}$ and $[Ru(bpy)_3]^{2+}$ were purged with chlorine gas. Results are presented in Figs. 34 and 35. Oxidized form, $[(bpy)_3Ru]^{3+}$, was produced and easily observed around 700 nm, Fig. 34. An isosbestic point was observed at 573 nm. On the other hand, an absorption due to $[Ru(bpy)_2(dpp)]^{3+}$ is not observed in the expected 600 - 800 nm wavelength range, Fig. 35. However, it is important to mention that the absorbance intensity due to $[Ru(bpy)_2(dpp)]^{2+}$ decreased and the solution changed color to light pink after adding Cl_2 gas to the sample. The expansion of the spectra (Fig. 35, Inset) reveals an isosbestic point at 530 nm, but there is only a small increase in absorbance in the 550 – 650 nm region. On addition of NaOH, the absorption intensity increased but it lost its original shape.

$$2[Ru(bpy)_2L]^{2+} + Cl_2 \rightarrow 2[Ru(bpy)_2L]^{3+} + 2Cl^- \quad (48)$$

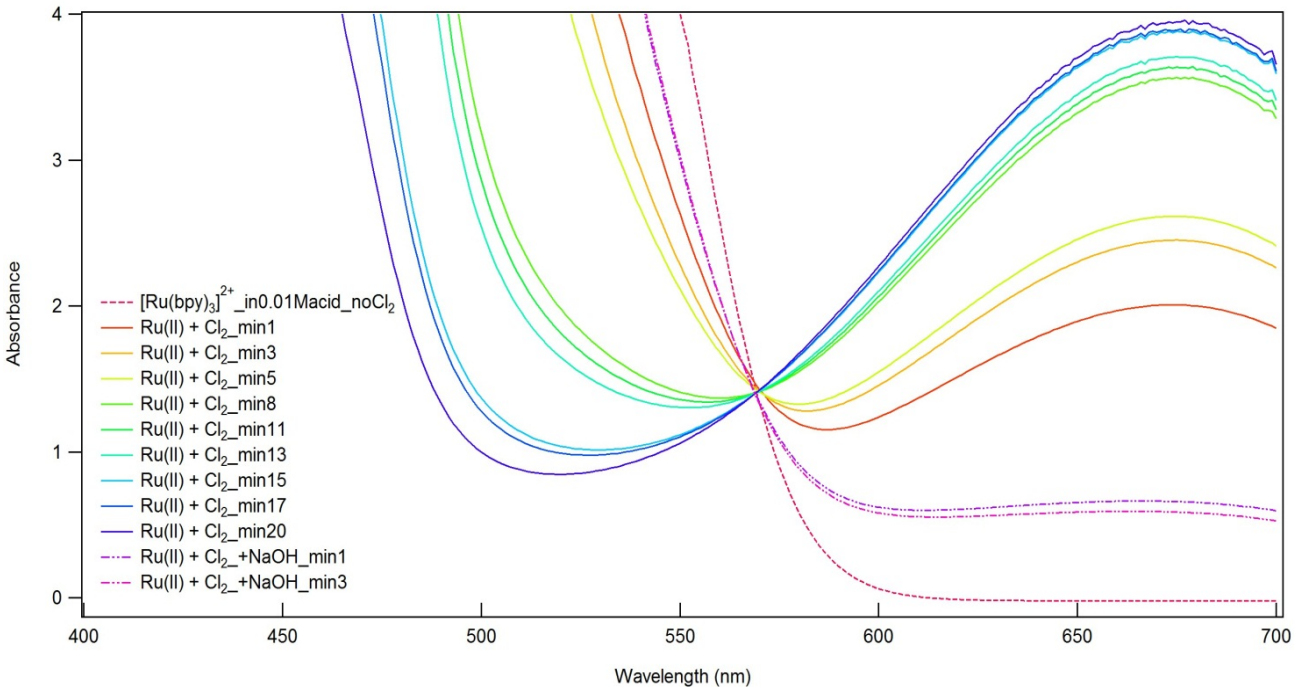

Figure 34. Characteristic peak of $[Ru(bpy)_3]^{3+}$ observed around 650-700nm. Dotted lines represent reversible reaction after adding NaOH to the solution.

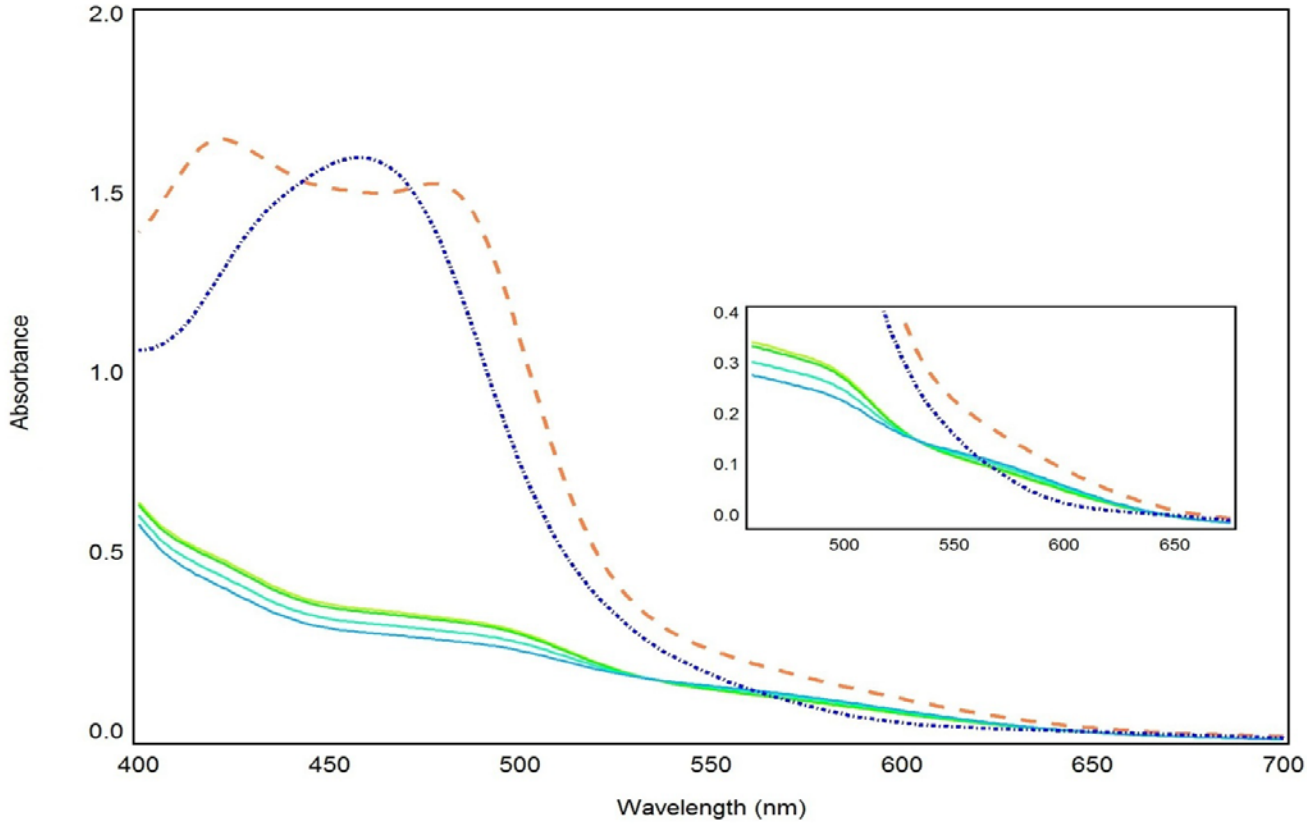

Figure 35. Electronic absorption spectra of $[Ru(bpy)_2(dpp)]^{2+}$ with Cl_2.
Orange dashed line: (---)$[Ru(bpy)_2(dpp)]^{2+}$+Cl_2; Green-blue solid lines: $[Ru(bpy)_2(dpp)]^{2+}$+ Cl_2 (in acidic solutions); Blue dotted line: (∗∗∗)$[Ru(bpy)_2(dpp)]^{2+}$+ Cl_2 (H^+) + NaOH.

3.4 Trapping Experiments.

3.4.1 Trapping Ru (III) with Triethanolamine, TEOA

Triethanolamine (TEOA) is a common sacrificial electron donor that is used with ruthenium (II) complexes, to trap Ru^{3+} and prevent the back reaction [56, 57]. However, in any acidic solutions, TEOA is not effective and gets protonated. The ruthenium complex, with concentration of $1.25x10^{-4}$ M $[Ru(bpy)_2dpp]^{2+}$ itself is in basic solution (pH = 7.9). However, when iron(III) is added, it becomes acidic. TEOA is most effective in pH = 8.5 - 11.5, since in acidic solution it gets protonated and that reduces its trapping ability.

Also, there are some interaction between TEOA and Fe(III), similar to those with EDTA. Apparently the TEOA reacts with Fe(III) because, in the presence of TEOA, Fe3+ does not quench $[Ru(bpy)_2dpp]^{2+}$ complex. Solutions cannot be made basic because at higher pH, Fe^{3+} precipitates.

3.4 2 Trapping Fe (II) with 1, 10-phenanthroline

Due to the difficulty in trapping $[Ru(bpy)_2dpp]^{3+}$, photolysis experiment was carried out to trap other product of electron transfer, iron(II), by 1,10-phenathroline. Measurements were carried out in buffered solution where 1,10-phen is not protonated yet, and iron(III) is not precipitated. Concentration of produced Fe(II) are presented in Table XII.

Quantum yield of Fe^{2+} formation, Φ_{Fe2+}, was calculated by

$$\Phi_{Fe^{2+}} = \frac{n_{Fe^{2+}}/t}{I_{abs}} \quad (49)$$

where n_{Fe2+} is the number of ions formed during the photolysis; I_{abs}-number of photons absorbed, $1.2\text{-}2.0x10^{18}$ photons/sec; t-time of irradiation, 1800sec.

Number of ions of Fe^{2+} formed during the photolysis was calculated as described previously [52] by Eq. 50 below

$$\boldsymbol{n_{Fe^{2+}} = \frac{6.023x10^{23}V_1V_3\Delta Abs}{V_2 l\varepsilon}} \quad (50)$$

where V_1 is the volume of solution irradiated (L), V_2 is the volume of aliquot taken for further analysis (L), and V_3 is the final volume to which the aliquot V_2 is diluted (L).

The path length of the cell used is l = 1 cm. The experimental value of the molar extinction coefficient of the Fe^{2+} complex as determined from the slope of calibration plot is ε =1.18 x 10^4 liters/mole-cm. The optical density of the irradiated solution at 510 nm, ΔAbs, was defined with the unirriadiated solution used as a blank in the reference beam.

Table XII. Results of experimets using 1,10-phenanthroline as an Fe^{2+} scavenger. Final concentrations of Fe(III) are in the first column.

set	$[Fe^{3+}]$ in the solution with $6.25x10^{-5}$M $[Ru^{2+}]$	Stern Volmer plots quenching Fraction of $[Ru(bpy)_2dpp]^{2+}$ quenched I_o-I/I_o	Range of $[Fe^{2+}]$ produced from Beer's Law (Efficiency of the reaction %)	Quantum yield of formation Φ_{Fe2+} [number of molecules per quanta]
I	3.13×10^{-3}	76%	$0.00 - 5.76 \times 10^{-6}$ 0-0.25%	$0.00 - 9.64 \times 10^{-6}$
II	1.56×10^{-3}	68%	$0.00 - 2.90 \times 10^{-5}$ 0-2.73%	$0.00 - 4.85 \times 10^{-5}$
III	7.80×10^{-4}	67%	$7.54 \times 10^{-6} - 9.66 \times 10^{-6}$ 1.45-1.85%	$1.26 \times 10^{-5} - 1.62 \times 10^{-5}$
IV	3.90×10^{-4}	63%	$3.73 \times 10^{-6} - 7.46 \times 10^{-6}$ 1.52-3.03%	$6.24 \times 10^{-6} - 1.25 \times 10^{-5}$

$[Fe^{3+}]$ x fraction of $[Ru(bpy)_2dpp]^{2+}$ quenched = real $[Fe^{3+}]$ used in eT; ($[Fe^{2+}]$ produced / real $[Fe^{3+}]$) x100% = efficiency

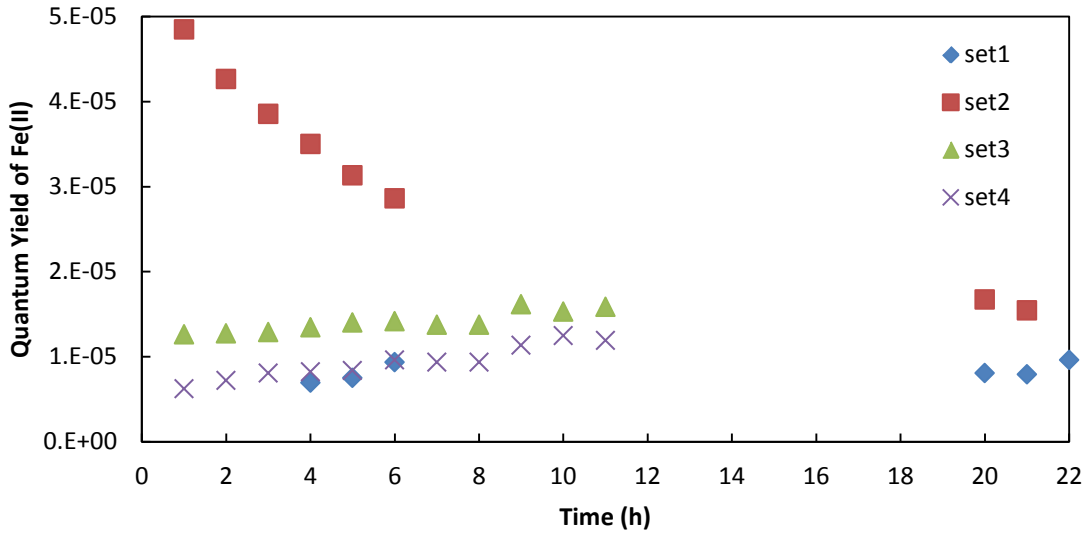

Figure 36. Quantum yield of formation of Fe(II).

4. Discussion

4.1 Steady State Measurements of $[Ru(bpy)_2dpp]^{2+}$ and Silver(I) and Iron(III)

The redox potential for Ag^+/Ag is 0.80 V and that for Fe^{3+} / Fe^{2+} is 0.77 V. Despite similar values of driving force, the outcomes of their reactions with $[Ru(bpy)_2dpp]^{2+}$ are different. When a solution of $[Ru(bpy)_2dpp]^{2+}$ is mixed with $[Ag^+]_{aq}$ solution, the dpp localized MLCT maximum of $[Ru(bpy)_2dpp]^{2+}$ shifts from 475 nm to 490-500 nm. The new absorption indicates that a new species is being formed. Also, in steady-state emission measurements, the emission intensity decreases as the concentration of $[Ag^+]$ increases, and the emission maximum shifts from 700 nm to 730 nm. The Stern-Volmer constant obtained from this experiment is K_{sv} = 35 ± 2.5 M^{-1} and agrees with the previously reported value, 30 M^{-1} [23]. NMR experiments confirmed that the spectral shifts were due to the coordination of silver, $[Ag(H_2O)_{3-4}]^+$, to the excited state $[Ru(bpy)_2dpp]^{2+}$[23].

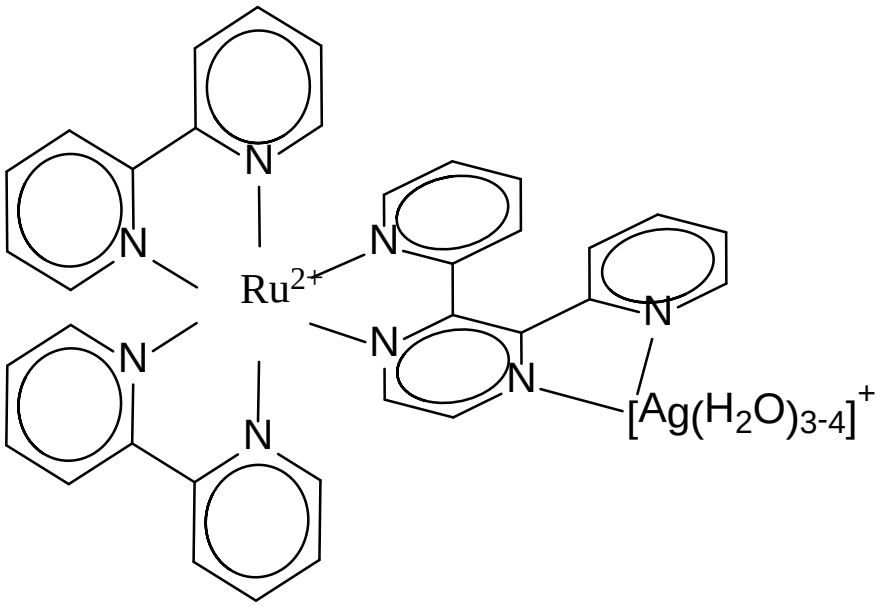

Figure 37. Proposed mechanism of $[Ru(bpy)_2dpp]^{2+}$ reaction with silver.

Despite the exergonicity of potential excited electron transfer between the $[Ru(bpy)_2dpp]^{2+}$ and silver, the coordination process occurs first precluding electron transfer. The appearance of a new emission at 730 nm precludes electron transfer quenching since oxidation or reduction of Ru(II) diimines produces a nonluminescent species. The appearance of the emission confirms that coordination of Ag^+, and not electron transfer, occurs.

In contrast, the spectra of the solution of $[Ru(bpy)_2dpp]^{2+}$ in the presence of $[Fe^{3+}]_{aq}$ did not exhibit any new visible peaks. There was no shifting in the 400-500 nm wavelength, and the Stern-Volmer constant (steady-state measurement) for this solution in water is $K_{sv} = 1793 \pm 184$ M^{-1}. The initial indication is that quenching occurs by an electron transfer mechanism. The possibility of thermochemically allowed energy transfer is discussed in Section 4.5.4.

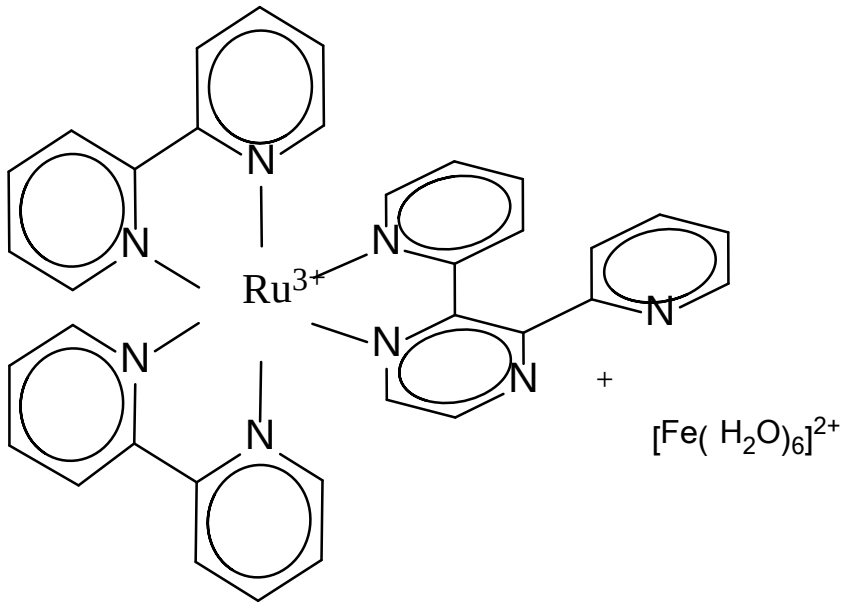

Figure 38. Proposed mechanism of $[Ru(bpy)_2dpp]^{2+}$ reaction with iron (III).

The difference in the products for the these two reactions may reflect different forms of them in aqueous solutions of $[Fe^{3+}]_{aq}$ and $[Ag^+]_{aq}$. Published results [44] indicate instant aggregation of $[Fe(H_2O)_6]^{3+}$ to form $[(H_2O)_4Fe(OH)_2Fe(H_2O)_4]^{4+}$, where two OH groups appear

as bridges. Experimental data suggest that this dimeric form may exist in equilibrium in solution [44].

$$2[Fe(H_2O)_6]^{3+} \leftrightarrow [(H_2O)_4Fe(OH)_2Fe(H_2O)_4]^{4+} + 2H^{+} \quad (51)$$

Ruthenium complex $[(bpy)_2Rudpp]^{2+}$ with a charge of plus two exhibits smaller repulsion towards the complex with a plus one charge, $[Ag(H_2O)_{3\text{-}4}]^{+}$. Thus a closer interaction between $[Ru(bpy)_2dpp]^{2+}$ and $[Ag(H_2O)_{3\text{-}4}]^{+}$ than is between $[Ru(bpy)_2dpp]^{2+}$ and $[(H_2O)_4Fe(OH)_2Fe(H_2O)_4]^{4+}$ is expected. On the other hand, assuming a dimeric form of iron(III) that has a total plus four charge, greater coulombic repulsions are expected with ruthenium(II). This does not allow any close interaction, and electron transfer is the mode of interaction. Also, silver is surrounded by 3-4 water molecules, which allows more space and flexibility for an interaction between $[Ru(bpy)_2dpp]^{2+}$ and $[Ag(H_2O)_{3\text{-}4}]^{+}$, whereas the iron(III) is an octahedral structure with less space to form any attachment to the Fe^{3+} ion.

The ratio of relative absorbance bands of $[Ru(bpy)_2dpp]^{2+}$ in the presence of Fe^{3+}, $\text{Abs}_{\text{ML(bpy)CT}} / \text{Abs}_{\text{ML(dpp)CT}}$, is presented in Fig. 39. The absorbance of those bands in aqueous solutions decrease evenly as the concentration of iron increases (Fig. 26) and the ratio of those bands are close to one, Fig. 39. On the other hand, in buffered solution of $[Ru(bpy)_2dpp]^{2+}$ in presence of Fe^{3+} (Fig. 27), the ratio of the ML(bpy)CT band to ML(dpp)CT band varies with the concentration of Fe^{3+}.

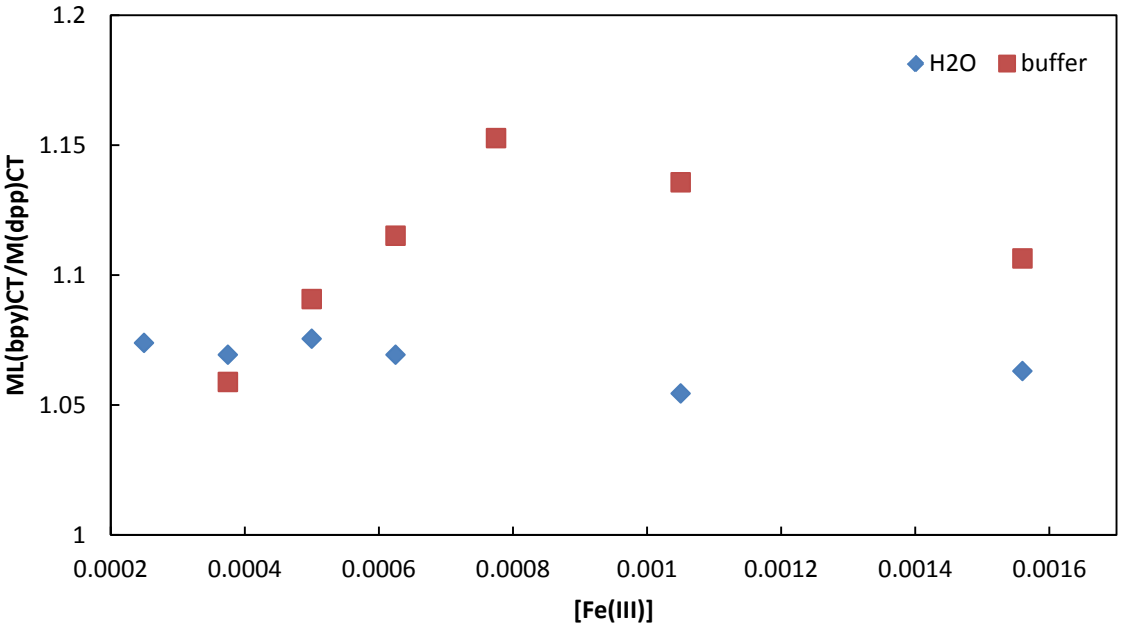

Figure 39. The ratio of relative absorbance of the ML(bpy)CT band to the absorbance of the ML(dpp)CT band of $[Ru(bpy)_2dpp]^{2+}$ in water and buffered solution. Based on the normalized spectra of those solutions. (Figs. 26, 27).

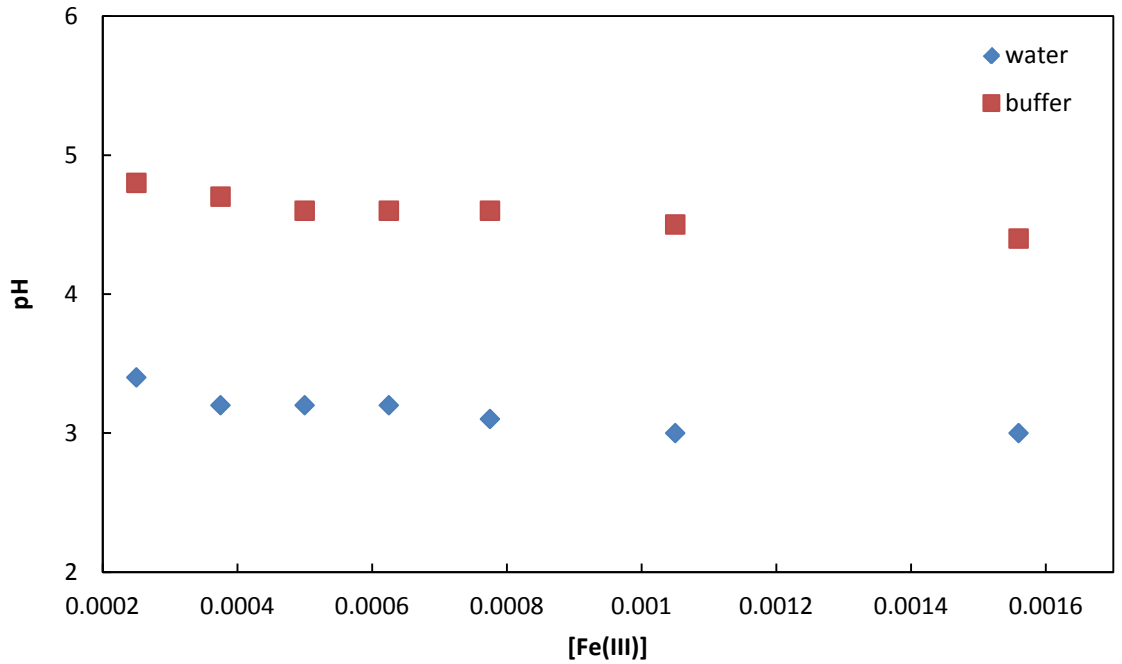

Figure 40. The pH dependence of $[Ru(bpy)_2dpp]^{2+}$ in presence of Fe^{3+}, as a function of iron concentration.

4.2 Quenching Experiments of $[Ru(bpy)_2dpp]^{2+}$ by Fe(III) in Water and Buffer Solution

The oxidative quenching of $[Ru(bpy)_2dpp]^{2+}$ by Fe(III) has been studied using steady-state and time resolved experiments. Iron(III) is not soluble in ethanol, and easily precipitates in basic solution. Thus, experiments were carried out in aqueous and pH= 5 buffered solutions. It has been found that the presence of oxygen doesn't affect the quenching constant significantly. Stern-Volmer constants, K_{sv}, of degassed and nondegassed solutions 146 ± 8 M^{-1} and 136 ± 11 M^{-1}, respectively, are within experimental error, Table 3. At higher concentrations of Fe^{3+}, the Stern-Volmer plot deviates from linearity, which could be an indication of the formation of iron(III) aggregates. At high concentration of Fe^{3+}, for example, the solution becomes cloudy which is assumed to be due to the formation of Fe^{3+} colloids. Also the Stern-Volmer plots for quenching by Fe^{3+} in aqueous solution shows more quenching than that in pH = 5 buffered solution, Fig. 28.

The bimolecular quenching constant of protonation in aqueous solution, $k_q = 5.1 \times 10^9$ $M^{-1}\cdot s^{-1}$ [23] is slower than the quenching rate constant $k_q = 1.81 \times 10^{10}$ $M^{-1}\cdot s^{-1}$ presented in this research, Table VII. The rate constant for protonation and Fe^{3+} quenching were measured under similar condition; protonations were measured in solution with pH in the 3 to 5 range, whereas the Fe^{3+} quenching was measured at pH = 2.9 to 3.4 range. The value of the quenching rate constant 1.81×10^{10} $M^{-1}\cdot s^{-1}$ indicates energy transfer or electron transfer, and is faster than protonation. Thus, based on the kinetics, the protonation can occur in aqueous solution; however this process is slower than the bimolecular rate constant for quenching by Fe^{3+}.

If we assume that the lifetime of excited state of the donor is equal to the sum of all competitive processes, unimolecular radiative and non-radiative processes and bimolecular electron transfer reaction, $k = k_r + k_{nr} + k_{et}[Q]$, and Eq. 13 can be rewritten as:

$$\tau_n = \frac{1}{k_r + k_{nr} + k_{et}[Q]} \quad (52)$$

With a simple reorganization of the Eq. 52, a linear plot can be obtained: $1/\tau = k_d + [Q]k_{et}$, with slope $k_{et,}$ and intercept $k_r + k_{knr}$, Fig. 41.

Table XIII. Reciprocal lifetime of 1.25 x 10^{-4} M $[Ru(bpy)_2dpp]^{2+}$ as a function of [Fe(III)].

Quencher conc., [M]	$1/\tau$ [s^{-1}] In buffer, degassed	$1/\tau$ [s^{-1}] In buffer, air	$1/\tau$ [s^{-1}] In water, degassed
0.001560	1.16 x 10^7	1.15 x 10^7	2.44 x 10^7
0.001050	1.09 x 10^7	1.11 x 10^7	2.13 x 10^7
0.000775	1.04 x 10^7	1.05 x 10^7	1.85 x 10^7
0.000625	1.02 x 10^7	1.09 x 10^7	1.61 x 10^7
0.000500	9.90 x 10^6	1.05 x 10^7	1.59 x 10^7
0.000375	9.80 x 10^6	9.90 x 10^6	1.41 x 10^7
0.000250	1.01 x 10^7	9.71 x 10^6	1.28 x 10^7

With the quantum yield of $[Ru(bpy)_2dpp]^{2+}$ calculated by Zambarana [23], $\Phi = 0.00175 \pm 0.0002$, we can estimate value of the non-radiative rate constant from Eq. 53,

$$\phi_{em} = \frac{k_r}{k_r + k_{nr}} \quad (53)$$

which requires to define the intercept in Eq. 52. Assuming that quantum yield is the same in water and buffered solvent, the competitive rates can be calculated as presented in Table XIV.

The absence of changes in the absorption and emission spectra lead us to preclude coordination of Fe^{3+} to $[Ru(bpy)_2dpp]^{2+}$ in either the ground or excited states of the complex. The rates for unimolecular processes, $k_r + k_{nr,}$ are much lower than the bimolecular rate constant of electron transfer, Table XIV.

Table XIV. Comparison of deactivation processes of ruthenium excited state complex and bimolecular electron transfer rate obtained from Eq. 53.

	$k_r = \Phi_{em}/\tau_0$ (Eq. 15) k_r [s^{-1}]	k_{nr} (Eq. 53) k_{nr} [s^{-1}]	$k_r + k_{nr}$ [s^{-1}]	slope=k_{et} [$M^{-1}s^{-1}$] Fig. 41 k_{et} [$M^{-1}s^{-1}$]
Buffer, degassed	1.65×10^4	9.41×10^6	9.43×10^6	1.35×10^9
Buffer, air	1.68×10^4	9.59×10^6	9.61×10^6	1.32×10^9
Water, degassed	1.34×10^4	7.62×10^6	7.63×10^6	1.25×10^{10}

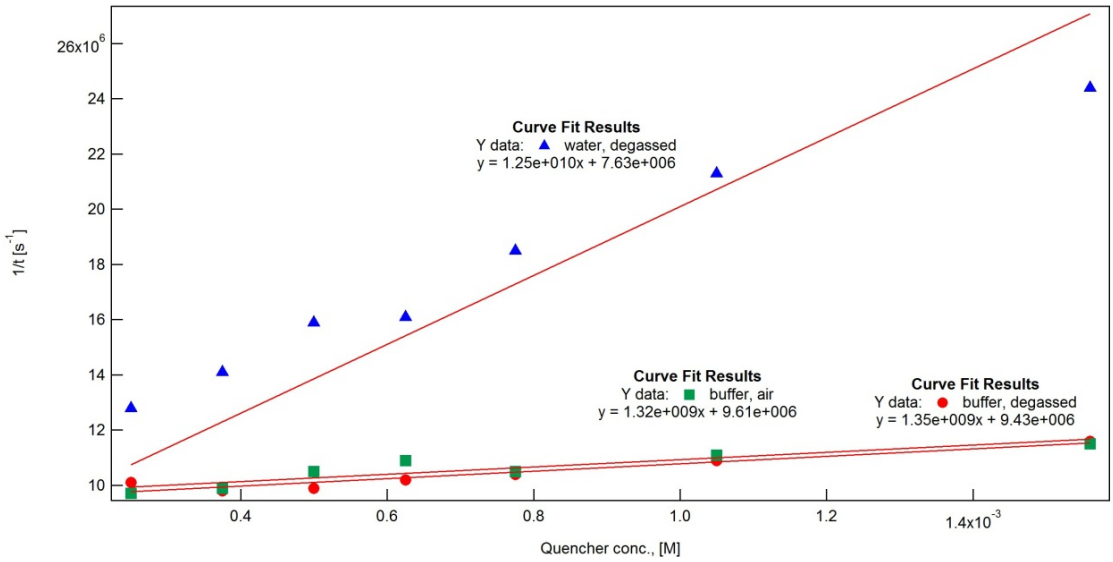

Figure 41. Data of estimated electron transfer based on Eq. 52. Electron transfer rate is quencher dependent and expressed as a slope from linear relationship of Eq. 52 and defined an intercept as a sum of $k_r + k_{nr}$.

4.2 Redox Reactions

Several different redox reactions have been performed, in order to see oxidation process of Ru^{2+} to Ru^{3+}. Redox potentials, E^0, for those reactions are positive, and make them energetically spontaneous. Selected oxidizing agents, Scheme 2, with high potential would allow the detection of products of those redox processes at the ground state with both ruthenium complexes,

$[Ru(bpy)_2dpp]^{2+}$ and $[Ru(bpy)_3]^{2+}$. Thus, the spectroscopic properties of Ru^{3+} would be determined.

$$[Ru(bpy)_3]^{2+} + A \xrightarrow{H^+} [Ru(bpy)_3]^{3+} + A^-$$

$$[Ru(bpy)_2dpp]^{2+} + A \xrightarrow{H^+} [Ru(bpy)_2dpp]^{3+} + A^-$$

$[Ru(bpy)_3]^{2+/3+}$ E^o = -1.20V $[Ru(bpy)_2dpp]^{2+/3+}$ E^o = -1.23V

$[Ru(bpy)_3]^{*2+/3+}$ E^o = +0.88V $[Ru(bpy)_2dpp]^{*2+/3+}$ E^o = +0.53V

A/A^-

$PbO_2 + 4\,H^+ + 2e \rightarrow Pb^{2+}$ $E^o_{red=}$ +1.70V

$[S_2O_8]^{2-} + 2e \rightarrow 2[SO_4]^{2-}$ E^o_{red}= +2.01V

$Cl_2 + 2e \rightarrow 2Cl^-$ E^o_{red}=+1.36V

Scheme 1. The oxidation potentials for ruthenium complexes in the ground and excite state, and the reduction potentials for the strong oxidizing agents, used in this study. The standards reduction potentials of oxidizing agents can be found in any chemical textbook.

The outcome of the reaction of $[(bpy)_3Ru]^{2+}$ with PbO_2 [49] and $[S_2O_8]^{2-}$ [31, 32] have already been published, and are repeated here for comparison.

4.2.1 Reaction with Lead Dioxide, PbO_2

The tris(2,2'-bipyridine) ruthenium (II) complex reacts with lead dioxide and forms tris(2,2'-bipyridine) ruthenium(III). The products of the reaction can be detected by the visible color change from orange to green, and a new peak at 700 nm wavelength characteristics of $[Ru(bpy)_3]^{3+}$.

$$2[Ru(bpy)_3]^{2+} + PbO_2 + 4H^+ \rightarrow 2[Ru(bpy)_3]^{3+} + Pb^{2+} + 2H_2O \quad (54a)$$

$$2[Ru(bpy)_2dpp]^{2+} + PbO_2 + 4H^+ \rightarrow 2[Ru(bpy)_2dpp]^{3+} + Pb^{2+} + 2H_2O \quad (54b)$$

The same experimental conditions were applied to $[Ru(bpy)_2dpp]^{2+}$, but no visible color change was observed, nor did a new peak form, Fig. 31. As presented in Scheme 1, the redox potentials indicate that oxidation of $[Ru(bpy)_2L]^{2+}$ is exergonic. However, in the case of $[Ru(bpy)_2dpp]^{2+}$, the expected reaction did not occur (Eq. 54b).

4.2.2 Reaction with $S_2O_8^{-}$

Oxidation of $[Ru(bpy)_3]^{2+}$ by $[S_2O_8]^{2-}$ has already been established [31, 32] and was performed for comparison. Within stoichiometric and energetics rules and using the standard potentials presented in Scheme 2, this reaction can be written as

$$4[Ru(bpy)_2L]^{2+} + 2[S_2O_8]^{2-} \rightarrow 4[Ru(bpy)_2L]^{3+} + 4[SO_4]^{2-} \quad (47!)$$

which could indicate that the reaction occur in the ground state.

However, the radical $[SO_4]^{\bullet-}$ is a strong oxidizing agent [E^0 ($SO_4^{\bullet-}$/ SO_4^{2-}) ~ 2.4V [31], so it reacts with $[(bpy)_2RuL]^{2+}$ to produce the corresponding ruthenium (III) complex; thus (Eq. 47) can be described as:

$$2[Ru(bpy)_2L]^{2+} + 2[S_2O_8]^{2-} \xrightarrow{h\nu} 2[Ru(bpy)_2L]^{3+} + 2[SO_4]^{\bullet-} + 2[SO_4]^{2-} \quad (55)$$

$$2[Ru(bpy)_2L]^{2+} + 2[SO_4]^{\bullet-} \xrightarrow{h\nu} 2[Ru(bpy)_2L]^{3+} + 2[SO_4]^{2-} \quad (56)$$

An intermediate, $[SO_4]^{\bullet-}$ removes an electron from the ruthenium, t_{2g} orbital, which leads to the oxidation of the metal complex. Thus, in detail, $[Ru(bpy)_2L]^{2+}$ is oxidized by the radical. Knowing that the potential for $S_2O_8^{2-}/2SO_4^{2-}$ is + 2.01V (scheme 1), and that E^0 ($SO_4^{\bullet-}$/ SO_4^{2-}) ~ 2.4V, we can estimate the negative potential of -0.39 V for reaction 57.

$$[S_2O_8]^{2-} \rightarrow [SO_4]^{\bullet-} + [SO_4]^{2-} \quad E^0 = -0.39 \quad (57)$$

$$[SO_4]^{\bullet-} \rightarrow [SO_4]^{2-} \quad E^0 = 2.4 \quad (58)$$

$$[S_2O_8]^{2-} \rightarrow 2[SO_4]^{2-} \quad E^0 = 2.01 \tag{59}$$

However, the stoichiometric overall reaction can be written as, Eqs. 60a and 60b

$$2[*Ru(bpy)_3]^{2+} + [S_2O_8]^{2-} \xrightarrow{H^+} 2[Ru(bpy)_3]^{3+} + 2[SO_4]^{2-} \tag{60a}$$

$$2[*Ru(bpy)_2dpp]^{2+} + [S_2O_8]^{2-} \xrightarrow{H^+} 2[Ru(bpy)_2dpp]^{3+} + 2[SO_4]^{2-} \tag{60b}$$

Thus, oxidation of $[Ru(bpy)_2L]^{2+}$ where L is bpy or dpp, occurs by quenching the excited state $*[Ru(bpy)_2L]^{2+}$ (Eqs. 60a, 60b) or by using the radical to oxidize ground state $[Ru(bpy)_2L]^{2+}$ (Eq. 56).

The absorption intensity of $[Ru(bpy)_3]^{2+}$ decreases fast, but the peak at 675 nm characteristics of $[Ru(bpy)_3]^{3+}$ increases very slowly, Fig. 42a-b, indicating the complexity of the reaction. The initial orange color of the solution changes when the absorption of shoulder at 424 nm of the 453 nm band are the same. At that point, the solution turns yellow/green. As the reaction progresses, the color changes to green and the initial shoulder at 424 nm has a higher absorptivity than the 453 nm peak.

The outcome of this redox reaction (Eq. 60a) was $[Ru(bpy)_3]^{3+}$ peak as evaluated by the 675 nm absorption.

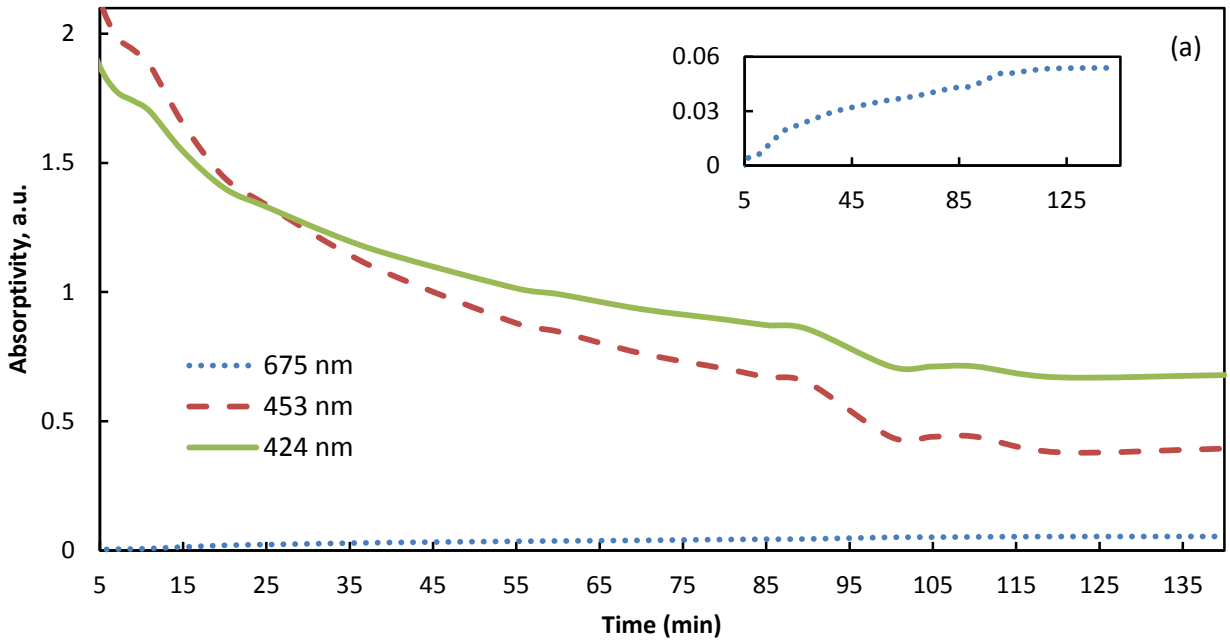

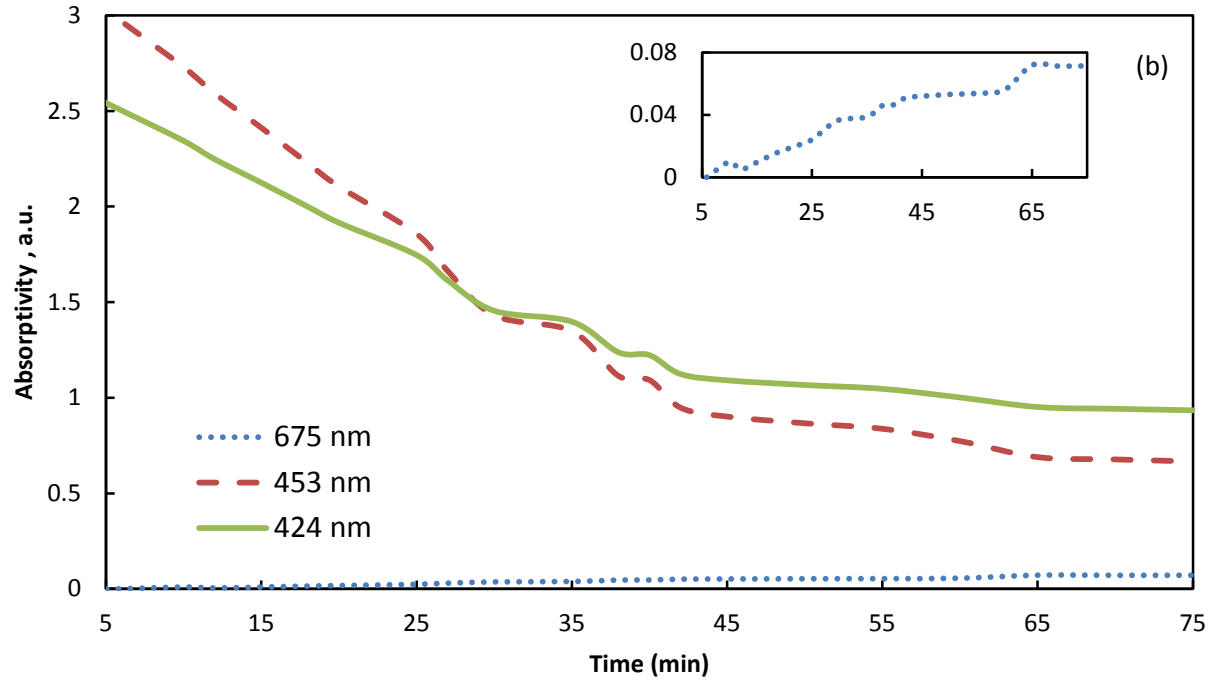

Figure 42. Change in intensity as a function of time of characteristics bands of $[Ru(bpy)_3]^{2+}$ (453nm and 424nm and $[Ru(bpy)_3]^{3+}$ at 675nm. (a) in HCl (b) in H_2SO_4.

The experiment was performed under the same conditions with $[(bpy)_2Rudpp]^{2+}$. The increased intensity by 17% in ML(bpy)CT band and decreased intensity by 10% in ML(dpp)CT band indicates that $[Ru(bpy)_2dpp]^{2+}$ got protonated and did not produce any visible peak in the 700 -800 nm range.

4.2.3 Reaction with Cl_2 gas

Due to the inability of finding $[Ru(bpy)_2dpp]^{3+}$ in experiments with peroxydisulfate, chlorine gas was chosen as an oxidizing agent. Chlorine gas was produced from MnO_2 and hydrochloric acid (Eq. 42). After purging the solution of the $[Ru(bpy)_2L]^{2+}$ with $Cl_{2(g)}$ (Eq. 48) the absorption spectra were measured. Based on reduction potentials (Scheme 1), a reaction should happen either in the ground or excited state. Again, Cl_2 gas oxidized $[Ru(bpy)_3]^{2+}$, as indicated by 675 nm absorption, with an isosbestic point at 573 nm. Whereas $[Ru(bpy)_2dpp]^{3+}$ did not show any increase in absorptivity in 600 - 800nm range. However, after loss of the MLCT absorbancies (Fig. 35), there was a small increase of absorption from 0.073 to 0.098 at 575 nm with an isosbestic point at 530 nm.

$$2[Ru(bpy)_3]^{2+} + Cl_2 \rightarrow 2[Ru(bpy)_3]^{3+} + 2Cl^- \quad (61a)$$

$$2[Ru(bpy)_2dpp]^{2+} + Cl_2 \rightarrow 2[Ru(bpy)_2dpp]^{3+} + 2Cl^- \quad (61b)$$

As a result of these experiments examining the oxidation of $[Ru(bpy)_2dpp]^{2+}$ by PbO_2, Cl_2, and $S_2O_8^{2-}$, it was clear that it would not be possible to confirm electron transfer of $[Ru(bpy)_2dpp]^{2+}$ quenching by Fe^{3+} by monitoring the increase in absorption in the 600 - 700 nm region as is the usual procedure with $[Ru(bpy)_3]^{2+}$. Although there were slight increases in the 600 -700 nm region. These were usually observed after loss of MLCT absorptions of the +2 complex and did not result in sufficient intensity to be useful as a quantitate probe. In short, the experiment confirmed that a different approach was needed. Thus, attempt was made to trap the

Fe^{2+} product. Furthermore, the addition of NaOH regenerated some of the spectral features of $[Ru(bpy)_2dpp]^{2+}$, but the shape of this spectrum had been changed, as shown in Fig. 35.

4.4 Trapping Experiments.

4.4.1 Trapping Ru (III) with Triethanolamine, TEOA

Even with a molecular structure similar to those previously studied ruthenium diimines, $[Ru(bpy)_2dpp]^{3+}$ has no visible spectral signature like $[Ru(bpy)_3]^{3+}$. A trapping experiment has been performed to trap $[Ru(bpy)_2dpp]^{3+}$ and to prevent the back reaction. The three most common sacrificial electron donors that are being used with ruthenium diimines complexes are triethanolamine (TEOA), oxalate ion, and ethylenediaminetetraacetic acid (EDTA).

Ethylenediamine-tetraacetic acid EDTA, strongly reacts with Fe(III) and would not be a trap specific to $[(bpy)_2Rudpp]^{2+}$. Therefore, EDTA was not used as a scavenger of $[(bpy)_2Rudpp]^{3+}$ [51, 56-58].

A previous study indicates that oxalate ion, $C_2O_4^{2-}$, can be used as reducing agent to trap $[Ru(bpy)_3]^{3+}$ because it can produce strongly reducing $CO_2^{\cdot-}$. Yet $C_2O_4^{2-}$ reacts too slowly with $[Ru(bpy)_3]^{3+}$, $k=10^4\text{-}10^5 M^{-1}s^{-1}$ [51, 57, 58] to be an effective trap. Another potential problem, particularly in the acidic Fe^{3+} solutions, is the formation and decomposition of oxalic acid $H_2C_2O_4$.

$$H_2C_2O_4 \rightarrow 2CO_2 + 2H^+ + 2e^- \quad (62)$$

$$Ru(bpy)_3^{3+} + e^- \rightarrow Ru(bpy)_3^{2+} \quad (63)$$

Another problem is that the Ru^{2+}/Ru^{3+} couple produces only one electron, which may leads to decomposition of $C_2O_4^{\cdot-}$ [21].

Lastly, predominant forms in acidic solutions are $H_2C_2O_4$ and $H_2C_2O_4^-$ (pKa 1.2; 4.2) [11].

$$Ru(bpy)_3^{3+} + C_2O_4^{2-} \rightarrow Ru^{2+} + C_2O_4^{-\cdot} \quad (64)$$

At pH above 3, $[(bpy)_3Ru]^{3+}$ oxidizes oxalate radical anion as follows

$$C_2O_4^{-\cdot} \rightarrow CO_2 + CO_2^{-\cdot} \quad (65)$$

$$Ru(bpy)_3^{3+} + CO_2^{-\cdot} \rightarrow CO_2 + Ru(bpy)_3^{2+} \quad (66)$$

With these considerations, it was decided not to use these sacrificial electron donors to trap $[Ru(bpy)_2dpp]^{3+}$.

Triethanolamine TEOA, (pKa = 7.8) can also acts as a scavenger, even in small concentrations. There is no ionic strength dependence for neutral TEOA. However, it has been found for anionic quenchers, the presence of TEOA reduces the rates at which these anionic species quench [51, 58]. Triethanolamine is most effective in the range of pH = 8.5 - 11.5; thus, its trapping ability will be reduced in acidic solution due to its self-protonation. The ruthenium complex $[Ru(bpy)_2dpp]^{2+}$ is in basic solution. Since Fe^{3+} makes solution acidic, pH~3, TEOA will be less effective as a scavenger. The solution could be buffered to pH 8.5 to 11 but at this pH, Fe^{3+} precipitates. The Fe^{3+} does not quench $[Ru(bpy)_2dpp]^{2+}$ in the presence of TEOA.

Experiments with $[Ru(bpy)_2dpp]^{2+}$ with Fe(III) in the presence of TEOA were performed at pH = 6 - 7. However, the results show no quenching in the presence of TEOA. Collectively, these observations precludes TEOA as a scavenger of oxidized $[Ru(bpy)_2dpp]^{2+}$.

4.4.2 Trapping Fe (II) with 1, 10-phenanthroline.

The inability to trap $[Ru(bpy)_2dpp]^{3+}$ motivated trapping another product of electron transfer, iron(II), with 1,10-phenathroline. Measurements were carried out in pH = 5 buffered solution where 1,10-phen is not protonated, and iron(III) is not precipitated. Solutions containing 6.25 x 10-5 M $[Ru(bpy)_2dpp]^{2+}$ and amounts of Fe^{3+} ranging from 3.13 x 10-3 to 3.90 x 10^{-4} M, and concentration of 1,10-phen that were three times the concentration of Fe^{3+} were evaluated

and the absorbance at 510 nm monitored. In all experiments there was a slight increase in absorbance at 510 nm indicating formation of $[Fe(phen)_3]^{2+}$ complex. A concentration of produced $[Fe(phen)_3]^{2+}$ and quantum yield of formation of $[Fe(phen)_3]^{2+}$ is shown in Table XIII. If 24-37% of $[Ru(bpy)_2dpp]^{2+}$ escaped from its excited state, it means the other 76-63% is quenched and available for electron transfer reaction. The greater amount of quenched $[Ru(bpy)_2dpp]^{2+}$ is associated with larger amount of the quencher present in the solution. A smaller concentration of iron(III) indicates a less frequent interaction with $[Ru(bpy)_2dpp]^{2+}$, which leads to greater amount of ruthenium escaping to the ground state.

Not every interaction of the excited state $[Ru(bpy)_2dpp]^{2+}$ and Fe^{3+} leads to electron transfer. Measured quantum yield of the formation of Fe^{2+} reflects the fraction of electron transfer from separated successor complex $Ru^{3+\cdots}Fe^{2+}$, Figs. 15, 39.

4.5 Efficiency of Electron Transfer in $[Ru(bpy)_2dpp]^{2+}$

Due to the inability to trap $[Ru(bpy)_2dpp]^{3+}$, a photolysis experiment was carried out to trap the other product of electron transfer, iron(II), by 1,10-phen. Measurements were performed with a buffered solution where 1,10-phen is not protonated, and iron(III) is not precipitated. The concentration of produced Fe(II) and quantum yield of formation of iron(II) are presented in Table XIII. The low efficiency of net Fe(II) formation is attributed to the rapid rate of the thermal back reaction and /or the low efficiency of redox product separation on escape form the solvent cage.

As mentioned in the introduction, the reaction of $[Ru(bpy)_3]^{2+}$ with Fe^{3+} can produce electron transfer products up to 25% of initial concentration of $[Ru(bpy)_3]^{2+}$ [29]. Energy transfer and electron transfer within this reaction have been discussed [7, 9, 27, 28] and it has been shown, by

flash photolysis experiment, that $k_q = k_{et}$, which is a near diffusion controlled process and energy that transfer is not involved here [7, 9, 27, 28].

Despite the large quenching rate constant, k_q, the low efficiency of excited state electron transfer between $*[Ru(bpy)_2dpp]^{2+}$ and iron(III) can be explained as a result of the competition of possible reactions: deactivation, diffusion, protonation, energy transfer, electron transfer, and back electron transfer.

4.5.1 Deactivation

Based on the comparison of the unimolecular deactivation rate of the $*[Ru(bpy)_2dpp]^{2+}$ in excited state, $k = k_r + k_{nr}$, (Table XIV) with the quenching rate, we find that $k << k_q$. The amount of $*[Ru(bpy)_2dpp]^{2+}$ being quenched rather than being deactivated depends on quencher concentration, Table XIII. Thus, the deactivation of $*[Ru(bpy)_2dpp]^{2+}$ is not a major component in the reaction between $*[Ru(bpy)_2dpp]^{2+}$ and $[Fe(H_2O)_6]^{3+}$.

4.5.2 Diffusion

The diffusion rate in an aqueous solution between two positively charged species can be determined by using the Smoluchowski equation (Eq. 37b). The viscosity of water at 25°C is $\eta = 8.90 \times 10^{-4}$ [kg · m^{-1} · s^{-1}, Pa · s]. Calculated diffusion coefficients have units of m^2/s, derived below as a function of radii of particular species, with the Boltzmann constant, $k_B = 1.38 \times 10^{-23}$ [m^2·kg/s^2·K].

$$D = \frac{k_B T}{6\pi\eta}\frac{1}{r} = 2.44 \times 10^{-19}\frac{1}{r}\ \left[units: \frac{m^3}{s}\frac{1}{m} = \frac{m^2}{s}\right] \quad (67)$$

Assuming spherical shapes for the donor and acceptor using the estimated radii presented in Table XV and the calculated values of diffusion coefficients at at 25°C, the Smoluchowski equation (Eq. 37b) yields 8.39×10^9 for rate of diffusion, Table XV.

Table XV. Calculated diffusion rate with Smoluchowski equation.

	Ionic molecules
$r_{*Ru(II)}$ [m]	6.5×10^{-10}
$r_{Fe(III)}$ [m]	$3.2\ 10 \times 10^{-10}$
$D_{*Ru(II)}$ [m^2s^{-1}]	3.77×10^{-10}
$D_{Fe(III)}$ [m^2s^{-1}]	7.66×10^{-10}
k_{diff} [$M^{-1}s^{-1}$]	8.39×10^{9}

This calculated value, $k_{diff} = 8.39 \times 10^9$ $M^{-1}s^{-1}$ (Table XV) is slightly larger than the value calculated via Eq. 37a, $k_{diff} = 7.4 \times 10^9$ $M^{-1}s^{-1}$ (Table IV). We can see that the experimental quenching constant, k_q, are near the diffusion rate. Now, having the eq $1/k_q = 1/k_{et} + 1/k_{diff}$ in mind (Appendix C, Eq. C.4b), we can estimate the rate constant of electron transfer based on the following relation:

$$k_q = \frac{k_{diff}k_{et}}{k_{diff}+k_{et}} \tag{68}$$

The results are shown in Table XVI.

Table XVI. Calculated electron trasfer rate with distance defined as: $r_{Fe} + r_{Ru} + r'$; $k_{diff} = 8.39 \times 10^9$

Experimental conditions (* steady- state experiment) (** time-dependent experiment)	Values of observed k_q	k_{et} (at r' = 0 Å)	k_{et} (at r' = 10Å)
Water,(*)	1.81×10^{10}	(a)	5.13×10^{11}
Water (**)	1.17×10^{10}	(a)	3.11×10^{10}
Buffer(*)	4.37×10^{9}	9.10×10^{9}(b)	5.07×10^{9}
Buffer(**)	1.40×10^{9}, 1.31×10^{9},air	1.68×10^{9}, 1.55×10^{9} air	1.51×10^{9}, 1.41×10^{9} air

(a) physically impossible values of electron transfer rate
(b) this value is little larger than kdiff, it is however within experimental error, $9.10 \pm 0.72 \times 10^9$

When donor and acceptor form an activated complex the bimolecular encounter in water provides negative, physically impossible values of k_{et}. Thus, we can conclude that $k_{et} << k_{diff}$, and $k_q \sim k_{et}$. Even with 10Å distance between the spheres, and the consideration of electron

transfer through the solvent, the theoretical estimate of k_{et} becomes positive but exceeds the k_{diff} value.

In a buffered solution, k_{et} is obtained as presented in Table XVI (above), and the electron transfer rate is within diffusion process. Excited $[Ru(bpy)_2dpp]^{2+}$ may undergo two competing processes: unimolecular deactivation, (Eq. 6), and the diffusion that proceeds to collision and successful electron transfer (Eq. 9). The deactivation rate of excited ruthenium complex, $k_0 = 1/\tau_0$, is 7.63×10^6 s^{-1} and 9.61×10^6 s^{-1} for solution in water and buffer, respectively. We find that diffusion is faster than deactivation, $1/\tau_0 << k_{diff}$, which means more species of $[Ru(bpy)_2dpp]^{2+}$ should go under the encounter process with iron. The electron transfer must occur within the lifetime of that precursor complex, $[*Ru^{2+}, Fe^{3+}]$. From the lifetime measurements (Table X), it is clear that buffered solvent stabilizes the excited complex. In water, there are only two charges species, Ru^{2+} and Fe^{3+}. Due to coulombic repulsion, like charged molecules diffuse away from each other very fast and the lifetimes of those encounters are relatively short. Buffered solutions have additional sodium ions, acetate ions and acetic acid. There is a possibility that CH_3COO^- stabilizes $[Ru(bpy)_2dpp]^{2+}$ and iron ions, holding them together longer, which can be observed as longer lifetime in those solutions, Table X. As the lifetime of activated complex $[*Ru^{2+}, Fe^{3+}]$ increases, more collisions occur between donor and acceptor and the higher the concentration of $[*Ru^{2+}, Fe^{3+}]$ encounter pairs. However, in buffer, the lifetime of $*[Ru(bpy)_2dpp]^{2+}$ is longer, the concentration of the encounter pairs is higher, and therefore the probability of electron transfer is greater. Not every collision between $*[(bpy)_2Rudpp]^{2+}$ and $Fe^{3+}{}_{aq}$ leads to successful electron transfer, which results in very small efficiency of the reaction.

4.5.3 Protonation

There are several questions to be addressed about $[Ru(bpy)_2dpp]^{2+}$ in describing reaction between $[Ru(bpy)_2dpp]^{2+}$ and $[Fe(H_2O)_6]^{3+}$, Eq. 45

- Is $[Ru^{II}(bpy)_2dpp]^{2+}$ in the ground state?

The reduction potentials (Scheme 3, page 64) for reacting species of $[Ru(bpy)_2dpp]^{2+}$ and $[Fe(H_2O)_6]^{3+}$ indicate endergonic reaction (E^0 = - 0.46 V), and the electron transfer in ground state is discounted.

On the other hand, the potential of the reaction for $*[Ru(bpy)_2dpp]^{2+}$ with $[Fe(H_2O)_6]^{3+}$ is positive, E^0 = +1.30V (ΔG is negative). Therefore excited state electron transfer is thermodynamically allowed.

$$
\begin{array}{lll}
*[Ru(bpy)2dpp]^{2+} \rightarrow [Ru(bpy)2dpp]^{3+} & E^0 = +0.53V & \\
\underline{[Fe(H_2O)_6]^{3+} \rightarrow [Fe(H_2O)_6]^{2+}} & \underline{E^0 = +0.77V} & \\
[Fe(H_2O)_6]^{3+} + *[Ru(bpy)2dpp]^{2+} \leftrightarrow [Fe(H_2O)_6]^{2+} + *[Ru(bpy)2dpp]^{3+} & E^0 = +1.30V & (45)
\end{array}
$$

- Is the product of the reaction (Eq. 45), $[Ru^{III}(bpy)_2dpp]^{3+}$ in the ground state?

$[Ru^{III}(bpy)_2dpp]^{3+}$ is not a stable complex, and there are no previous experimental studies and no experimental evidence of this molecule. In this research, $[Ru^{III}(bpy)_2dpp]^{3+}$ has a very small absorption band at 663 nm and is difficult to confirm.

- Is protonated form of $[Ru^{II}(bpy)_2dpp]^{2+}$, $[Ru^{II}(bpy)_2dppH]^{3+}$ present in the ground state?

Protonation of $[Ru^{II}(bpy)_2dpp]^{2+}$ on the peripheral pyridine ring to form $[Ru^{II}(bpy)_2dppH_y]^{3+}$ occurs in the solutions where pH range is 0 - 2 and protonation on the peripheral pyrazine ring to form $[Ru^{II}(bpy)_2dppH_z]^{3+}$ occurs in the solution with at higher acidity (much lower pH) [25].

The pH of the present system, $[Ru^{II}(bpy)_2dpp]^{2+}$ with $[Fe(H_2O)_6]^{3+}$ is from 3 to 5. Thus, the protonation will not occur in the ground state of $[Ru^{II}(bpy)_2dpp]^{2+}$.

- Where does protonation occur in the excited state in $*[Ru^{II}(bpy)_2dpp]^{2+}$?

Binding the proton to the peripheral dpp pyridine nitrogen, $*[Ru^{II}(bpy)_2dppH_y]^{3+}$ results in a new emission band at 735 nm, which has not been observed in the present study. The lifetime of these species is less than 16ps. Electron transfer (ET) may happen within those 16ps only with certain condition, which are limited by the quencher's concentration. Based on the Stern-Volmer equation (Eqs. 23 and 24), the smallest possible amount of iron is two to three orders of magnitude larger than that present in my solution. Given that values of $k_q = 9.7 \pm 2.3 \times 10^9$ $M^{-1}sec^{-1}$ for solutions in water, $k_q = 6.7 \pm 5.4 \times 10^9$ $M^{-1}sec^{-1}$ for solutions in buffer and the lifetime of excited state $\tau_0 \leq 16 \times 10^{-12}$ s, the concentration of iron(III), the quencher, must be within the 0.145-33.0 M range in order for Fe^{3+} to quench those protonated species. Concentrations in the present study are less than 10^{-3}M in $[Fe^{3+}]$. Thus, the reaction

$$*[Ru^{II}(bpy)_2dppH_y]^{3+} + [Fe(H_2O)_6]^{3+} \rightarrow [Ru^{III}(bpy)_2dppH_y]^{4+} + [Fe(H_2O)_6]^{2+} \quad (69)$$

is discounted.

Binding the proton to the peripheral dpp pyrazine nitrogen, $*[Ru^{II}(bpy)_2dppH_z]^{3+}$ does not result in any new emission peak. The absence of any emission assignable to $*[Ru^{II}(bpy)_2dppH_z]^{3+}$ indicates the complex is non-emissive and is thought to relax instantly by protonation of peripheral dpp pyrazine nitrogens. Because, of this apparent short lifetime, $*[Ru^{II}(bpy)_2dppH_z]^{3+}$ accepting an electron from Fe^{3+} is also discounted.

$$*[Ru^{II}(bpy)_2dppH_z]^{3+} + [Fe(H_2O)_6]^{3+} \rightarrow [Ru^{III}(bpy)_2dppH_z]^{4+} + [Fe(H_2O)_6]^{2+} \quad (70)$$

Based on the reasoning aand observation provided above it is reasonable to conclude that the stepwise proton transfer-electron transfer does not happen in both the ground and excited

states. The only options that remain, are electron transfer-then-proton transfer (ETPT), electron transfer (ET), or simply back reaction to the ground state $[Ru(bpy)_2dpp]^{2+}$.

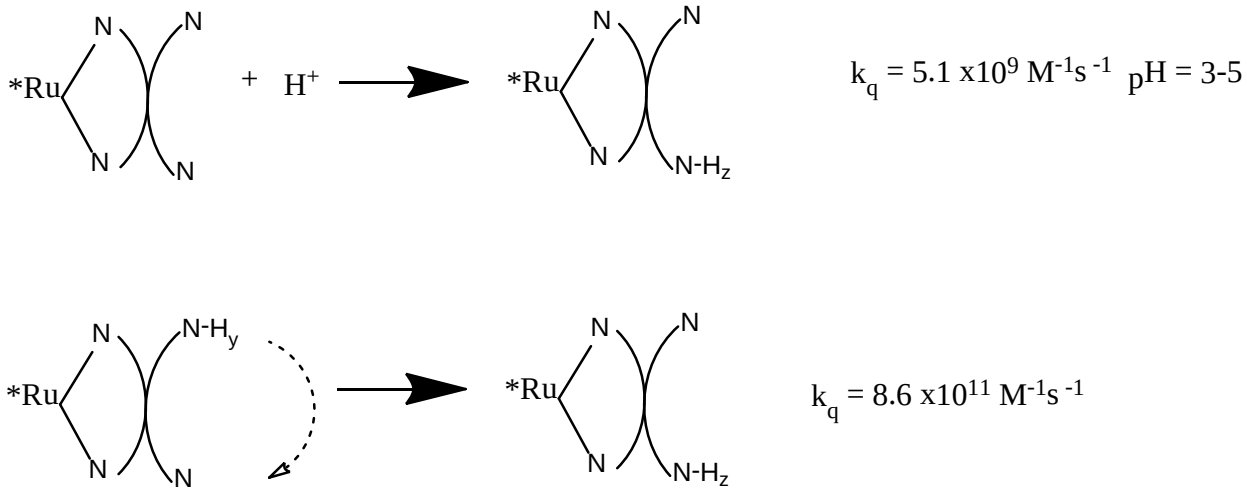

Figure 43. Quenching constant of protonation $[Ru(bpy)_2dpp]^{2+}$.

Based on the value of the bimolecular quenching constant k_q, it is clear that the rate of protonation (Fig. 41) is slower than the quenching constant presented in this research (Table IX). In addition, there is no spectroscopic evidence for the presence protonation species in the solutions that have investigated. Thus, protonation can be excluded from further analysis, Fig. 38.

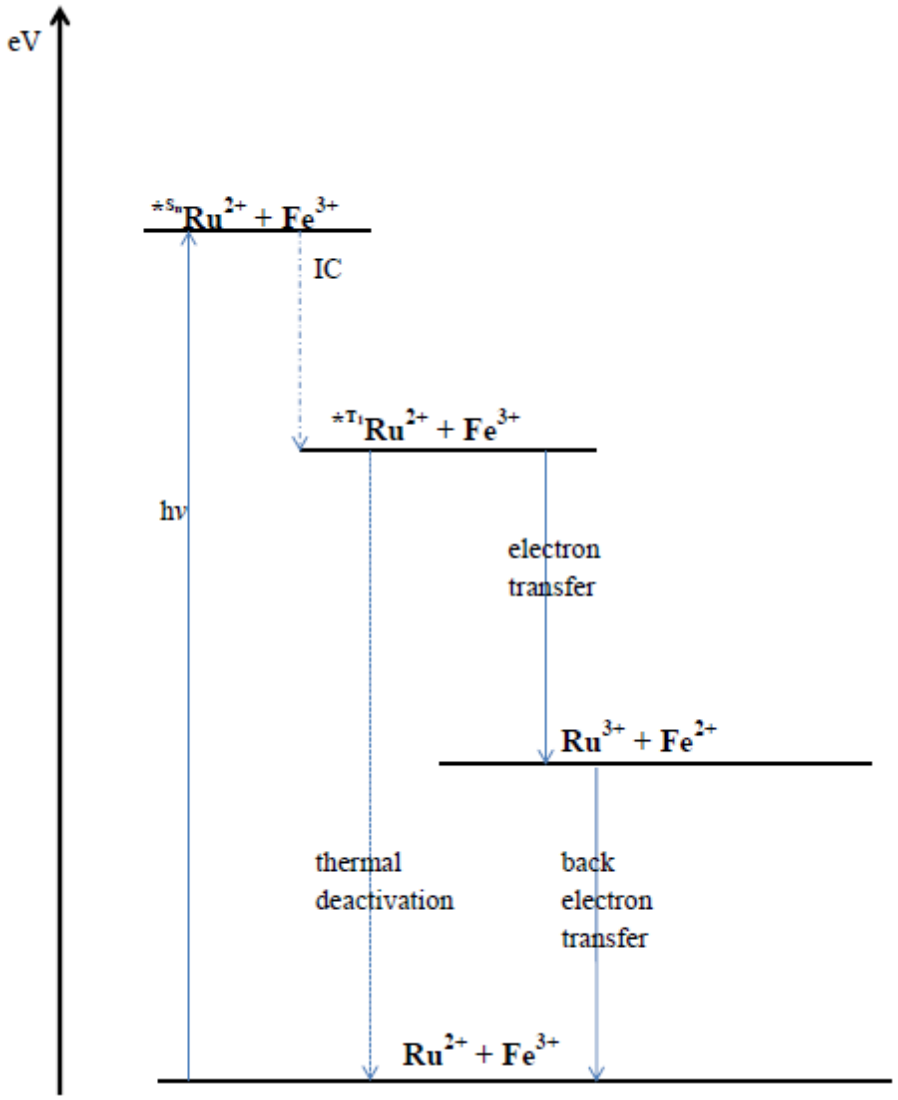

Figure 44. Model of possible reactions between iron(III) and excited state $[Ru(bpy)_2dpp]^{2+}$.

4.5.4 Energy Transfer

Excitation leads to higher electronic and vibrational levels. Some of this excitation energy is lost quickly when the molecule relaxes to the lowest vibrational level of the first spin allowed excited state. Emission is defined by transitions from the excited state (S_1, T_1) to the higher vibrational level of the ground state. Further loss of excitation energy is due to thermal equilibration (vibrational relaxation). Excitation energy can also be transferred to another

molecule by coupling electronic orbitals between donor and acceptor. An excited donor may transfer resonance energy to the acceptor by long-range dipole-dipole or higher order nultiple interactions. This process requires overlap between the donor emission (here: $[Ru(bpy)_2dpp]^{2+}$) and acceptor (here: Fe^{3+}) absorption spectra. The efficiency of this process varies with the degree of spectral overlap. Also, diffusion between donor and acceptor within the lifetime of the excited state of the donor enhances the chances of transfer efficiency.

The atomic spectrum of iron has been analyzed [59]. 'Energy levels of Iron, Fe(I) through Fe(XXVI)' has been presented by J. Reader and J. Sugar [59]. Transitions between donor and acceptor can occur even between metals that have different spin states. Those spin-forbidden transitions, may not be visible, but still may occur, and are thought to be important in the reaction between $[Ru(bpy)_2dpp]^{2+}$ and Fe^{3+}. Ruthenium complex $[Ru(bpy)_2dpp]^{2+}$ exhibits an emission in the 600 - 850 nm (16,667 cm^{-1} – 11,765 cm^{-1}) with a maximum at 700 nm.

The ground state of Fe^{3+} is $1s^2 2s^2 2p^6 3s^2 3p^6 3d^6$ with term $^5D_4$. Absorption bands near the emission of ruthenium are located at 1,027 cm^{-1} for $^5D_0$ (J=0) and 19,405 cm^{-1} for $^3P_1$ (38%) + $^3P_2$ (61%). Thus emission of the donor $[Ru(bpy)_2dpp]^{2+}$ does not overlap with the absorption of the acceptor, $[Fe(H_2O)_6]^{3+}$.

All possible interactions between $[Ru(bpy)_2dpp]^{2+}$ and iron(III) can be defined by an encounter complex (a); solvated ion pair (c) in which two competitive processes can occur: solvated separated ions (d) after electron transfer, or back ion recombination (g) to the initial forms of reactants, Figure 45. Also, there are no evidence for an exciplex formation, or its emission, or an exciplex deactivation, as presented in Fig. 3. Therefore, the interaction between $[Ru(bpy)_2dpp]^{2+}$ and iron(III) does not involve the formation of a distinct $[[Ru(bpy)_2dpp]^{2+\cdots} Fe^{3+}]$ complex.

$$[{}^{*}Ru^{2+} + Fe^{3+}] \leftrightarrow [{}^{*}Ru^{2+\cdots}Fe^{3+}]_a \leftrightarrow [Ru^{3+\cdots}Fe^{2+}]_c \leftrightarrow Ru^{3+} + Fe^{2+}{}_d$$

$$\downarrow g$$

$$Ru^{2+} + Fe^{3+}$$

Figure 45. Possible interactions between $[Ru(bpy)_2dpp]^{2+}$ and iron(III).

4.5.5 Electron Transfer (ET)

Direct evidence for electron transfer from the reaction of $[Ru(bpy)_3]^{2+}$ and Fe(III) has been established by detection of $[Ru(bpy)_3]^{3+}$ and reduced quencher, in time resolved experiment of reversible system; and in the trapping experiment of the irreversible system. The value of electron transfer of this reaction has been compared to quenching constant of $[Ru(bpy)_2dpp]^{2+}$ and Fe(III) system.

Indirect evidence of electron transfer rather than energy transfer can be establish by (a) quenching rate constant, (b) spectroscopic considerations [8], and (c) the degree of redox reaction by measuring back electron transfer for relatively slow back reaction.

4.5.5.1 Calculation of Electron Transfer Rate Constant From the Stern-Volmer Equation

The absorption rate is proportional to I_a, in the following excitation reaction

$$[Ru(bpy)_2dpp]^{2+} + h\nu \rightarrow {}^{*}[Ru(bpy)_2dpp]^{2+} \quad (71)$$

The rate of the emission is the sum of radiative and non-radiative decay rates, $k = k_r + k_{nr}$

$${}^{*}[Ru(bpy)_2dpp]^{2+} \rightarrow [Ru(bpy)_2dpp]^{2+} + h\nu + \Delta \quad (72)$$

where Δ is an additional relaxation energy. In the presence of quencher, Fe(III), an additional deactivation process of the following electron transfer occurs with the rate $k = k_{et}$

$${}^{*}[Ru(bpy)_2dpp]^{2+\ 2+} + Fe^{3+} \rightarrow [Ru(bpy)_2dpp]^{3+} + Fe^{2+} \quad (45!)$$

The change of $[Ru(bpy)_2dpp]^{2+}$ in time can be written:

$$\frac{d\,{}^*[Ru]^{2+}}{dt} = I_a - k\,{}^*[Ru^{2+}] - k_{et}\,{}^*[Ru^{2+}][Fe^{3+}] \quad (73)$$

With steady state approximation of d*[Ru^{2+}]/dt = 0,

$$I_a = {}^*[Ru^{2+}]((k + k_{et})[Fe^{3+}]) \quad (74)$$

When considering intensity with and without the quencher, I, and I_0, respectively, the Stern-Volmer plot is expressed as:

$$\frac{I_0}{I} = \frac{(k+k_{et})[Fe^{3+}]}{k} = 1 + \left(\frac{k_{et}}{k}\right)[Fe^{3+}] \quad (75)$$

Assuming that all quenching occurs by electron transfer, with the assumption that $[Fe]^{3+}$ >> *$[Ru]^{2+}$, the $[Fe]^{3+}$ is assumed to be approximately constant in the experiment. The Stern-Volmer constant K_{sv} leads to the expression for the ratio k_{et}/k.

$$K_{SV} = \frac{k_{et}}{k_r + k_{nr}} \quad (76)$$

Given the quantum yield of emission Φ for *$[Ru(bpy)_2dpp]^{2+}$, the values of k_r and k_{nr}, thus the electron rate constant can be obtained. The quantum yield for radiative and non-radiative processes is equal to unity. From the experimental lifetime τ, of *$[Ru(bpy)_2dpp]^{2+}$ (Table XX) and the quantum yield Φ = 0.00175 ± 0.0002 calculated before [23], the rates of radiative and non-radiative decays are obtained, Table XIV. The values of k_r, k_{nr} presented in Table XIV are within experimental error of previously measured values, k_r= 2.0 ± 0.3 x 10^4 s^{-1} and k_{nr} = 9.8 ± 1.0 x 10^6 s^{-1} , as reported in Ref. [23].

Thus, with $k = k_r + k_{nr}$ and with the values of K_{sv} in Table VIII, K_{sv} = 472 M^{-1} (buffer) K_{sv} = 1793 M^{-1} (H_2O), the estimated values of electron transfer rates are k_{et} = 4.45 ± 0.28 x 10^9 $M^{-1}s^{-1}$ (buffer, degassed), k_{et} = 4.54 ± 0.29 x 10^9 M^{-1} s^{-1} (buffer, air) and k_{et} = 1.37 ± 1.0 x 10^{10} $M^{-1}s^{-1}$ (H_2O). Since the present estimate of diffusion constant is k_{diff} = 8.39 x 10^9 M^{-1} s^{-1}, the calculated value of electron transfer in water exceeds the diffusion rate. Thus, the diffusion

limited electron transfer is specific for the outcome of the reaction in water. On the other hand, in buffered solution, the electron transfer competes with diffusion process. Given that estimates of k_{et} and k_{diff} are correct, it is reasonable to conclude that diffusion process is the only rate limiting step in water. In buffered solution, the k_{diff} rate is slightly larger than $k_{et.}$ Thus, both processes contribute to the observed quenching rate.

4.5.5.2 Photoinduced Electron Transfer - Rehm - Weller Formula

Photoinduced electron transfer is defined by Rehm-Weller behavior, Fig. 40, and has been described briefly in Part 1.1.3. The excited state electron transfer processes are usually very exergonic, $\Delta G^0 << 0$, which normally corresponds to the inverted regime in the Marcus theory. In many cases, electron transfer rate goes up to certain values and then becomes limited by the diffusion rate. Eberson [60] analyzed the Marcus inverted region and Rehm –Weller plot. With larger reorganizational energy λ, Marcus's parabolic shape becomes more squared and fits the Rehm- Weller plot better [60].

The kinetics of electron transfer quenching of the excited state are shown in Fig. 46, where k_d and k'_d are the rates for species diffusing together to form encounter (precursor) complex between ruthenium and the iron (quencher). Formation of the successor complex occurs by electron transfer (k_{12}, k'_{12}) within these complexes, in the ground state (k_{12}) or excited state (k'_{12}). The rate for separation of ions to form products Ru^{3+} and Fe^{2+} is k_p, and the back electron transfer rate to the ground state of Ru^{2+} and Fe^{3+} is represented by k_{21}.

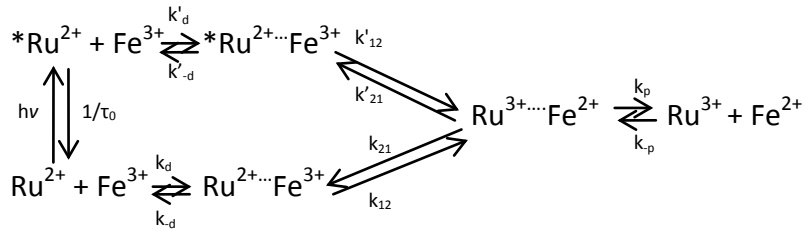

Figure 46. **Posible reactrons between iron(III) and photoexcited $[Ru(bpy)_2dpp]^{2+}$.**

As indicated in the diagram of Fig. 46, the ground state forward electron transfer cannot occur, due to substantially positive value of the free energy of the reaction. The excited state electron transfer reaction and its transition state can be defined by Rehm-Weller approach and Marcus Theory (see Appendix A.2, A.3).

At the simplest level, the electron transfer rate can be interpreted in terms of Eyring's Eq. A.1, $k_{eT} = \nu \cdot \exp(-\Delta G^{\ddagger}/RT)$. Using the Rehm-Weller equation, the free energies for forward and back reactions and the electron transfer rates can be estimated. The free energy of the reaction ΔG^0 (Eq. C.5) was calculated with the excitation energy $E_{0\text{-}0}$ = 475nm = 60.88 kcal/mol for $[Ru(bpy)_2dpp]^{2+}$, and $E_{0\text{-}0}$ = 700 nm = 40.85 kcal/mol for $[Ru(bpy)_2dpp]^{3+}$; Columbic repulsions were estimated to be about 2.53 kcal/mol, with r_{AB} = 10 Å, (Table XXXVIII, Eq. A.5). In order to calculate the activation energy, the reorganization energy is needed. A more detailed discussion is included in Part II, but rough estimate canbe made here based on published data. Eberson [60] indicates that λ_i = 48.4kcal/mol for the reorganizational energy for $[Fe(H_2O)_6]^{2+/3+}$, and Meyer [36] assumes that inner sphere reorganizational energy for $[Ru(bpy)3]^{2+/3+}$ is close to zero due to almost no change in bond length between ruthenium and bypyridine ligands. The solvent reorganization for the reaction between $[Ru(bpy)_2dpp]^{2+}$ and $[Fe(H_2O)_6]^{3+}$ can be calculated from the radii of spheres (Eq. A.12) and is equal to λ_0 = 18.32 kcal/mol (with 10Å)

(see Section 11.1.2). Thus, the total reorganizational energy used in calculations presented in Table XVII is 66.72 kcal/mol.

Table XVII. Comparison of energetics and rate constant for electron transfer quenching and corresponding thermal back reaction between $[Ru(bpy)_2dpp]^{2+}$ and Fe^{3+}. Electron transfer rate was calculated with Eyring's equation (Appendix A).

Reaction	$*Ru^{2+} + Fe^{3+} \rightarrow Ru^{3+} + Fe^{2+}$	$Ru^{3+} + Fe^{2+} \rightarrow Ru^{2+} + Fe^{3+}$
E(D/D+)	-1.23eV = -28.36 kcal/mol*	-0.77eV = -17.8 kcal/mol
E(A/A-)	0.77eV = 17.8 kcal/mol	1.23eV = 28.36 kcal/mol
E_{0-0}	475 nm = 60.88 kcal/mol	700 nm = 40.85 kcal/mol
ΔG^0 (Eq. C.5) Rehm-Weller $\Delta G_{12}^0 = E_{(D/D+)} - E_{(A/A-)} - E_{0-0} - \frac{e^2}{D(r_D + r_A)}$	-109.6 kcal/mol	-89.5 kcal/mol
$\Delta G^{\ddagger}$ (Eq. C.8) Rehm-Weller $\Delta G_{12}^{\ddagger} = \frac{\Delta G_{12}^0}{2} + \left[\left(\frac{\Delta G_{12}^0}{2}\right)^2 + \left(\frac{\lambda}{4}\right)^2\right]^{1/2}$	2.48 kcal/mol	3.01 kcal/mol
k_{et}	**$k'_{12} = 9.39 \times 10^{10}$**	**$k_{21} = 3.84 \times 10^{10}$**
$\Delta G^0 = -nFE^0$	-33.88 kcal/mol	-11.99 kcal/mol
$\Delta G^{\ddagger}$ (Eq. A.18)Marcus $\Delta G^{\ddagger} = \frac{(\Delta G^0 + \lambda)^2}{4\lambda}$	4.04 kcal/mol	11.22 kcal/mol
k_{et}	**$k'_{12} = 6.74 \times 10^{9}$**	**$k_{21} = 3.64 \times 10^{4}$**

* if use +0.53eV, ΔG^0 = - 68.99 kcal/mol, $\Delta G^{\ddagger}$ = 3.82 kcal/mol, k = 9.77×10^9 $M^{-1}s^{-1}$

The efficient quenching, large k_q, but slow back reaction is required to create intermediates in the excited state reaction. A fast back reaction does not provide high efficiency for a net excited state electron transfer. It is suggested that the reaction in the excited state with the rate k'_{12}, is followed by comparably fast back reaction with rate of k_{21}, to the ground state within classical Rehm-Weller approach. However, according to the Marcus theory, the back reaction is much slower than the excited electron transfer, k'_{12}. Data are comparable with values

for the reaction of $*[Ru(bpy)_3]^{2+}$ with Fe^{3+}, where $k'_{12} = 1.9 \times 10^9$ and thermal back reaction rate of $k_{21} = 6.41 \times 10^5$ [36].

There is reasonably good agreement between calculated (Table XVII) and experimental values of the electron transfer (Table XIV, XVI). The excited electron transfer rate calculated with Rehm-Weller equations, $k'_{12} = 9.39 \times 10^{10}$ (Table XVII) is much higher than the excited electron transfer rate calculated by the Marcus theory, $k'_{12} = 6.74 \times 10^9$ (Table XVII). This could be related to the inverted regime ($\Delta G^0 << 0$) behavior of the photoexcited electron transfer process; see Fig. C.2, and Fig. B.1. It is important to examine reorganization energy λ, in detail and analyze its influence on electron transfer rate.

Experimental electron transfer rates were found to be different in buffer solution and in pure water, even though they are both aqueous solvents. For theoretical rates the dielectric constant of water is used for both samples. In Part II, details of the application of the Marcus theory and effect of ionic strength on the activation energy will be analyzed in detail.

5. Conclusions from Experiments

1. Electron transfer quenching has been established for the photoinduced reaction between $[Ru(bpy)_2dpp]^{2+}$ and Fe^{3+} by trapping Fe(II), one of the products of this reaction. It has been suggested that the low efficiency of this reaction is due to a fast diffusion process, a competition with bimolecular quenching, and fast back electron transfer. The possibility of energy transfer has been ruled out based on the consideration of atomic spectra (no overlap in the emission of donor and absorption of acceptor).

   Note: A band characteristics of $[Ru(bpy)_2dpp]^{3+}$ has been identified in experimental absorption spectra with the help of DFT calculations. Due to the very low intensity of the experimental peak, it could not have been possible to assign the peak to $[Ru(bpy)_2dpp]^{3+}$ without theoretical results.

2. The existence of inverted region in the photoinduced electron transfer process needs to be analyzed in detail, for which more accurate value of the reorganization energy λ is needed. The possibility of a different reaction path (deactivation, protonation, diffusion-controlled process) between $*[Ru(bpy)_2dpp]^{2+}$ and Fe^{3+} minimizes the possibility of the inverted-region mechanism.
3. Measurements can be performed without degassing samples. Solutions with and without oxygen have results within experimental error.
4. It has been concluded that protonated species are not formed as a final product of the reaction. Even though absorption spectra of solutions that consist of $[Ru(bpy)_2dpp]^{2+}$ and Fe^{3+} look similar to those of $[Ru(bpy)_2dppH]^{3+}$, emission spectra show no presence of protonated species.

5. Silver and iron have similar reduction potentials. However, the outcomes of their reactions with $[Ru(bpy)_2dpp]^{2+}$ are different. It has been shown that iron(III) forms instantly aggregated species in the solution. Therefore, the iron molecules are large enough not to fit in within dpp ligand dimensions. Also, the cluster formations of iron(III) increase the total charge of the quencher and enhance repulsion from the positively charged ruthenium(II). A review of the literature provides no evidence that Ag^+ in room temperature aqueous solution forms any polynuclear species. Thus, a silver molecule is small enough to form a coordinated complex with $[Ru(bpy)_2dpp]^{2+}$.
6. The experimental excited-state electron-transfer rates from Stern-Volmer analysis and diffusion equation exhibit reasonably good agreement. The rates are different in buffered and pure water solution. The calculated value within the Rehm-Weller approach cannot distinguish such difference because they are both aqueous solutions. The calculated free energy of photoexcited electron transfer (Marcus Theory) and its transition energy are in good agreement with the experimental value of electron transfer. The electron transfer rates obtained with Rehm-Weller equation and with Marcus theory (Table XVII) provide good agreement with the experimental value of electron transfer (Table XIV, XVI).

Part II: Quantum Chemistry Application

6. Introduction

Octahedral ruthenium complexes have been the subject of extensive experimental and theoretical studies due to their applications to photochemistry, ability to bind DNA and their possible use in water splitting reaction [3, 6, 22, 25, 31, 61-69]. The redox properties in the ground and excited state and their long lived excited states can be of great utility for solar energy conversion. Due to extensive experimental research involving ruthenium complexes, it is important to investigate their properties. Insight into molecular properties such as frontier molecular orbitals, energy-structure correlation, charge population, will help us to explain spectral features in more detail and to elucidate different photochemical properties.

Thus, detailed electronic structure calculation can provide important information on the electronic structure of molecules in their ground and excited state and help explain experimental findings [68, 70-73].

Two ruthenium diimines were investigated, and their electron distributions have been examined. $[Ru(bpy)_3]^{2+/3+}$ and $[Ru(bpy)_2dpp]^{2+/3+}$ were fully optimized in both ground and excited states. Electronic spectra have been calculated and compared with experimental data. $[Ru(bpy)_3]^{2+}$ is one of the most studied transition metal complexes. It has been the subject of numerous studies over decades [5, 32, 55, 70, 72] and will be used here as a reference to compare results of $[Ru(bpy)_2dpp]^{2+/3+}$. Its oxidized form, $[Ru(bpy)_3]^{3+}$, will also be analyzed in detail, and the information will be used for the analysis of electronic properties of $[Ru(bpy)_2dpp]^{2+/3+}$.

As a parent molecule of ruthenium-polypyridine type complexes, $[Ru(bpy)_3]^{2+}$ has been one of the most studied molecule from both experimental and theoretical points of view [5, 32, 55, 70]. However, due to the large size of the molecule ($C_{30}H_{24}N_6Ru$, 31atoms) and limitations in computer power in the past, most computational studies were focused mainly on the ground state geometry and molecular orbital (MO) analysis. With recent advances in Density Functional Theory (DFT) and computational power there is new opportunity to investigate different oxidation states, properties in solvents, and excited states. However, there still remain big challenges in understanding the chemistry of transition metal complexes because of unsettled issues in the choices of appropriate basis sets and functionals.

6.1 Geometry and Activation Energy of Iron Complexes

The second part of this dissertation focuses maily on the molecular properties of $[Ru(bpy)_3]^{2+/3+}$ and $[Ru(bpy)_2dpp]^{2+/3+}$. The investigated reaction (Eq. 45) involves excited electron transfer between $*[Ru(bpy)_2dpp]^{2+}$ and $[Fe(H_2O)_6]^{3+}$. Thus, molecular properties of $[Fe(H_2O)_6]^{3+/2+}$ are important. Experimental and theoretical studies of iron complexes and their thermochemical properties will also be addressed.

Kuharski et al. [74] conducted calculation of electron transfer rate between Fe^{2+} and Fe^{3+} in liquid water. The activation free energy of the electron transfer for those species was successfully obtained by using Monte Carlo simulation. The interionic distance of 5-7 Å was found to be the most optimum separation for electron transfer between ferric and ferrous ions. Activation free energy is equal to 20.8 kcal/mol when intermolecular distance Fe^{2+}- Fe^{3+} is 5.5 Å, and $\Delta G^{\ddagger}$ = 25 kcal/mol for r_{12} equal to 6.5 Å. Experimental value is provided as 15-20 kcal/mol [74] and references therein. The short distance of 5.5Å in iron ionic separation suggests complexity of the dynamics including classical adiabatic and quantum nonadiabatic electron

transfer. The constructed interaction has Fe^{3+} - oxygen distance of 2.0 Å, and Fe^{2+} - oxygen: 2.13 Å. The simulations involved one Fe^{3+} ion and 249 water particles at constant water density and room temperature. According to the simulation, oxygen - Fe^{3+} bond length is 2.02 Å, and oxygen – Fe^{2+} bond length is 2.15 Å, see Table XVIII.

A different set of calculations were performed by A. Jarzęcki et al.[75], which provide optimized structure of $[Fe(H_2O)_6]^{2+/3+}$ and vibrational modes. Density Functional Theory (DFT) and B3LYP functional were used, with 6-31G* basis set (for oxygen and hydrogen atoms) and Aldrichs' triple-ξ (VTZ) basis set (for iron atom). Polarization Continuum Model (PCM) was also included. Because of high spin electronic configurations of iron, only quintet and sextet multiplicity were used for Fe^{2+} and Fe^{3+}, respectively.

The latest research [76] investigated iron geometry in four complexes by using DFT/B3LYP method and the empirical Spectroscopic Potential Algorithm for Simulating Biomolecular Conformational Adaptability (SPASIBA). The basis set implemented in Jaguar program, LAVCP**, was used for iron and 6-31g(tm)** for the rest of the atoms. The primary use of DFT in this study was to obtain conformational and vibrational data of the complexes, and their further use to obtain SPASIBA force parameters to perform molecular dynamics studies in the future. Experimental data used in this paper are almost the same as those in the work by Jarzęcki et al. [75], and are omitted from Table XVIII.

The hexaaquairon(III) complex can be constrained to T_h (or S_6) point group. On the other hand, the iron(II) complex, with d^6 configuration, belongs to O_h point group, without Jahn-Teller distortion constrain, which force the molecule to change to more stable symmetry of C_i. In this case, the metal-ligand bond lengths are not the same and the Table XVIII shows average distance.

Table XVIII. Results of iron-oxygen bond length presented by different authors. Experimental data are in parenthesis.

	Kuharski et al. [74]	Jarzęcki et al. [75]		Yapo-Kicho et al. [76]	
Bond length [Å]	Monte-Carlo simulation	DFT/B3LYP gas phase, T_h symmetry	DFT/B3LYP PCM (T_h - S_6 symmetry for Fe^{3+})	DFT/B3LYP	SPASIBA
O-Fe^{3+}	2.15 (2.10[a])	2.039	1.996-2.005 (1.994[b])	2.052	1.957-2.003
O-H	-	0.982	0.995-0.998 (0.995[b])	0.978	0.996
O-Fe^{2+}	2.02 (1.98[a])	2.129	2.106 (1.126[b'])	2.114	2.049
O-H	-	0.973	0.982 (0.867[b'])	-	-

a. EXAFS data; b. Diffraction spectra of $CsFe(SO_4)_2 \cdot 12H_2O$; b' X-ray data of $(NH_4)_2[Fe(H_2O)_6]SO_4)_2$.

6. 2 Short Introduction to Proton - Coupled Electron Transfer (PCET)

Proton-coupled electron transfer (PCET) is an important mechanism in biological processes and electrochemistry. The examples where PCET occur include enzyme reactions, photosynthesis, and solar cells [77-81]. It has been used to understand and explore mechanisms of many reactions in solutions and also in electrochemistry [78, 81, 82]. PCET can be sequential or concerted. In sequential PCET, proton transfer (PT) can follow electron transfer (ET), or vice versa. In concerted PCET, proton and electron are transferred at the same time in a single step. Also, electron and proton can be transferred in the same direction or opposite direction. Hydrogen atom transfer (HAT) can be viewed as an example of PCET, and it will be explained later. While research on PCET in early days were limited to ground state reactions, recent years have seen studies of PCET in photoexcited states. Theoretical study of PCET is under ongoing development and remains challenging due to hydrogen tunneling, excited electronic/vibrational

states and their adiabatic and nonadiabatic behavior, complex coupling between solute and solvent [80, 83-86].

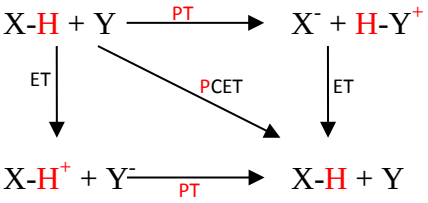

Figure 47.Basic PCET model [81].

Based on literature data, stepwise ET-then-PT or vice versa appears to be favorable than concerted PCET. However, this is not what happens in many cases. The two step processes ET/PT or PT/ET involve intermediates, which are normally uphill from the reactant. Thus, ΔG for concerted PCET is different and can be more negative than that for the first step of stepwise ET (or PT). This example has been presented in reaction of DHA with Fe^{III}Hbim [81]. Concerted PCET is favored over stepwise mechanism by 53 kcal/mol for initial ET, and by 30 kcal/mol for initial PT. Similar discussion is made for vitamin C that concerted PCET is favorable over stepwise process [81]. The goal of applying PCET theory is to provide detailed information for proposed electron transfer process between $[(bpy)_2Rudpp]^{2+}$ and iron(III).

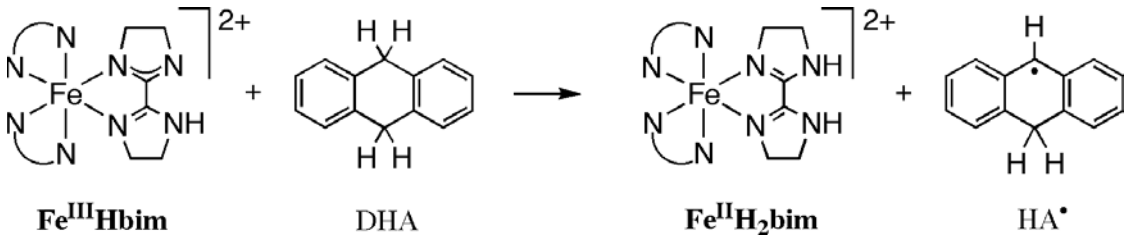

Figure 48. Example given by Mayer, where PCET is favored over the stepwise mechanism, [81] and references therein.

6.2.1 Pourbaix Diagram.

From practical and industrial point of view, the values of pH and reduction potentials allow forming Pourbaix diagram that helps to identify ET, PT and PCET. The diagram has been

used in analysis of natural waters allowing more accurate predictions of the forms in which different elements can exist. In addition, it helped establishing corrosion products such as $Fe(OH)_2$ or Fe_3O_4.

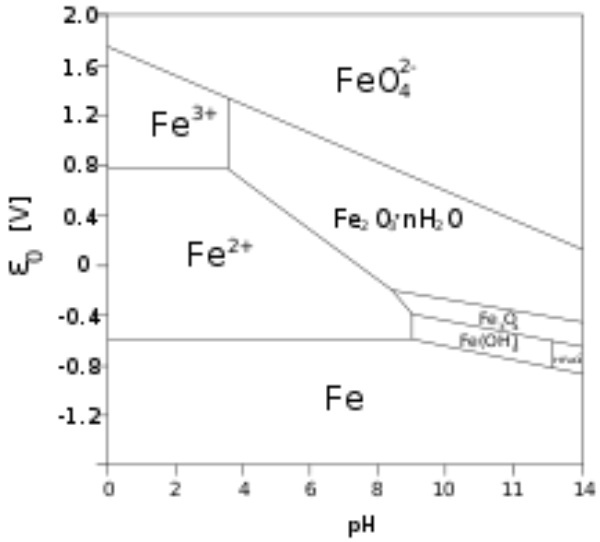

Figure 49. Pourbaix diagram of Iron[4].

Figure 49 shows an example of Porbaix diagram. The lines are drawn for ions at 1M concentrations and represent equilibrium for that concentration (additional lines may be drawn for other concentrations). Vertical lines, separate species related by acid-base equilibria, and its position depends on the total concentration of iron. Horizontal lines separating species are related to redox equilibrium (electron transfer process). Redox species involving H^+ or OH^- appear as diagonal boundaries because they are in part acid-base equilibria of PCET. Experimentally, values of pH are measured and combined with the reduction potentials from square-wave voltammetry.

[4] http://en.wikipedia.org/wiki/File:Pourbaix_Diagram_of_Iron.svg#globalusage

6.2.2 pKa Calculation

Diagram 1 represents relationship between free energies of protonated and unprotonated species in the gaseous and aqueous environment.

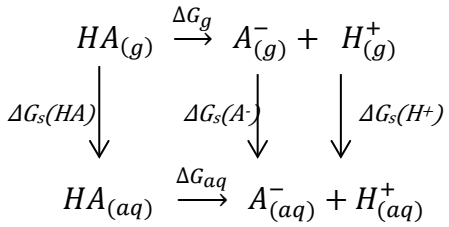

Diagram1. Thermodynamic cycle of the ΔG for proton transfer reaction. Subscript (g), stands for gas phase, (s) solvation energy, and (aq) represents values of an aqueous solution.

For the cycles presented in the above diagram, the following thermodynamic relations hold [68, 69, 87].

$$pK_a = \frac{\Delta G_{aq}}{2.303RT} \tag{77}$$

$$\Delta G_{aq} = \Delta G_g + \Delta\Delta G_s + \Delta G^{o\rightarrow *} \tag{78}$$

$$\Delta\Delta G_s = \Delta G_s(A^-) + \Delta G_s(H^+) - \Delta G_s(HA) \tag{79}$$

where $\Delta G^{o\rightarrow *}$ = RTln (24.46) = + 1.89 kcal/mol, the free energy difference between the standard states of the gas phase and aqueous phase [68, 69, 88]. The value of the free energy of the proton in the gas phase is $\Delta G^o_{(g)}(H^+)$ = - 6.28 kcal/mol as described previously [68, 69]. In Eq. 79, the aqueous solvation free energy of the proton is $\Delta G_{(s)}(H^+)$ = -265.9 kcal/mol. This is the value used in two recent papers [69, 88] among various values available in the literature.

6.2.3 Redox Potentials

Diagram 2 represents relationship between free energies of reduced and oxidized species in the gaseous (g) and aqueous environment (aq).

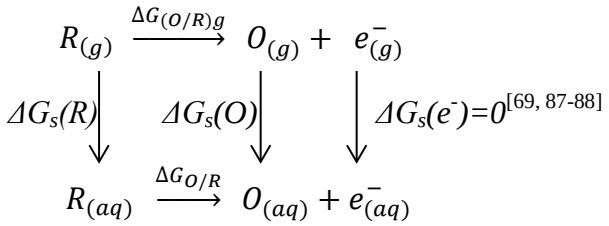

Diagram 2. Thermodynamic cycle of the ΔG for redox reaction of reduced (R) and oxidized (O) species. $\Delta G_{O/R}$ is a free energy in aqueous solution. Subscript, *aq*, is omitted for cleared view.

In the above diagram, $\Delta G_g(e^-)$= - 0.006kcal/mol, which is the free energy of the electron in the gas phase as stated in [69]

$$\Delta G_{O/R} = \Delta G_{O/R(g)} + \Delta G_s(O) - \Delta G_s(R) \quad (80)$$

$$\Delta G_{O/R(g)} = G_g(O) + G_g(e^-) - G_g(R) \quad (81)$$

From the free energy we can calculate potential, E, of the reaction according to ΔG = - nFE.

The final free energy in aqueous solution, $\Delta G_{O/R}$, represents the value of the absolute free energy change for the reduction process. In order to compare potentials with experimental data, the values have to include the absolute free energy change of the standard hydrogen electrode, ΔG^0_{SHE} associated with the half reaction, $H^+_{(aq)} + e^-_{(g)} \rightarrow 1/2H_{2(g)}$

Thus, potential can be calculated from

$$E^0_{O/R} = -\frac{\Delta G_{O/R} - \Delta G^0_{SHE}}{nF} \quad (82)$$

Details on how to obtain absolute free energy of SHE in various solvents and further references were presented in [87].

Equation 82 uses ΔG^0_{SHE} = 4.28 eV = 98.70 kcal/mol, which is free energy of standard hydrogen electrode in water [69, 88]. As in the case with $\Delta G_{(s)}(H^+)$, ΔG^0_{SHE} has many similar values. Batista et al. [71] uses 4.43V as an absolute potential of the SHE, whereas studies published at [88] and [69] suggested to use 4.28 V [71].

6.3.4 Aspects of Solvation Energy

Solvation free energy, ΔG_S, refers to the interaction free energy of a molecule A and its solvent. It also represents the change in free energy for a solute leaving the gas phase and entering a solvent phase. The free energy can be determined from equilibrium constant, namely, the partition coefficients of a solute A between the gas and solvent phase at equilibrium as follows:

$$\Delta G_s^0 (A) = - RT\ln(A^{eq}_{sol}/A^{eq}_{gas}) \quad (83)$$

Experimental solutions are prepared in standard condition of 1mol/L concentration. While most of the experimental works were interested in ΔG_s^0 of water, there have been many experimental and theoretical studies on ΔG_s^0 of other solvents as well [87-91]. There are two distinct theoretical approaches to calculate ΔG_s^0. Explicit solvation models that included directly even a several dozen or hundred solvent molecules around the solute and implicit solvation models that place the solute in the cavity of the solvent, where solvent is described as a dielectric constant.

Diagrams 1 and 2 present gas phase and aqueous phase reactions including solvation free energies of all the species. This is an approach when optimization calculations in the solvent are difficult to converge [68, 69]. These studies present optimization and frequency analysis of the species in the gas phase and then simple single-point calculation with C-PCM model with particular solvent. Thus, equation below is used to calculate aqueous free energy.

$$\Delta G_{aq} = \Delta G_g + \Delta\Delta G_s + \Delta G^{o\rightarrow *} \quad (84)$$

6.4 Electron Transfer Theory

6.4.1 Marcus Theory

Electron transfer (ET) reactions have been subject to numerous theoretical and experimental investigations over many decades [38, 92-100]. Some of them have been realized only recently thanks to the development new laser spectroscopy techniques. At simple thermodynamic level, the rate of electron transfer reaction can be related to the net free energy change of reaction. According to the Marcus theory, the rate of electron transfer can be expressed as

$$k = \kappa Z e^{-\Delta G^{\ddagger}/RT} \tag{85a}$$

where κ is the transition probability, Z - collision frequency, $\Delta G^{\ddagger}$ is the activation energy for the reaction. Within the transition state theory, the rate of electron transfer can be expressed as

$$k_{ET} = \nu_n e^{(-\Delta G^{\ddagger}/RT)}, \tag{85b}$$

where ν_n is the nuclear frequency of the charge-transfer complex. In the simplest theory, it can be expressed as $\nu_n = k_B T/h = 6.2 \times 10^{12}\ s^{-1}$, with values of $k_B T = 0.592$ kcal/mol and Planck's constant, $h = 9.54 \times 10^{-14}$(kcal/mol)·s.

The activation energy $\Delta G^{\ddagger}$ within Marcus theory is given by

$$\Delta G^{\ddagger} = \frac{\lambda}{4}\left(1 + \frac{\Delta G^{o\prime}}{\lambda}\right)^2 \tag{86}$$

which is the simplest form mostly used in solvents with large dielectric constant such as water with $\varepsilon(H_2O) = 78.3$ at 25^0C where electrostatic and work contributions can be neglected. Equation 87 shows the reorganizational energy λ, which is expressed as the sum of inner and outer sphere reorganizational energies as follows:

$$\lambda = \lambda_i + \lambda_0 \quad (87)$$

where λ_i is the inner-sphere reorganization energy of D and A, and λ_0 is the outer-sphere (solvent) reorganization.

6.4.2. Reorganization Energy

6.4.2.1 Inner Sphere

The inner-sphere reorganization energy $\boldsymbol{\lambda_i}$ originates from changes in bond length between metal and ligand and in the type of ligand attached to the metal.

The bond length change of transition metal complexes is related to the change that occurs in the occupancy of dπ orbitals, see Table II. If the change in the number of electrons occurs in t_{2g} nonbonding orbitals, the bond lengthens by very small amount. On the other hand, the change of the number of electrons in e_g orbitals induces a large change in bond lengths. The complexes of $[Ru(NH_3)_6]^{3+/2+}$ [92] and $[Co(NH_3)_6]^{3+/2+}$ [101] serve as good examples for such bond length changes, see Eqs. 88 and 89.

$$\begin{array}{ccccc} t_{2g}^6/e_g & & \xrightarrow{\text{slow } k_{et}=10^{-6}\,M^{-1}s^{-1}} & & t_{2g}^5/e_g^2 \\ d(Co^{3+}\text{-}\,NH_3) = 1.97\text{Å} & & \Delta\, d(Co\text{-}\,NH_3) = 0.19\text{Å} & & d(Co^{2+}\text{-}\,NH_3) = 2.16\ \text{Å} \end{array} \quad (88)$$

$$\begin{array}{ccccc} t_{2g}^5/e_g & & \xrightarrow{\text{fast } k_{et}=10^{3}\,M^{-1}s^{-1}} & & t_{2g}^6/e_g \\ d(Ru^{3+}\text{-}\,NH_3) = 2.104\text{Å} & & \Delta\, d(Ru\text{-}NH_3) = 0.04\ \text{Å} & & d(Ru^{2+}\text{-}\,NH_3) = 2.144\ \text{Å} \end{array} \quad (89)$$

Large changes of geometry that occur during the self-exchange reaction can be correlated with significant contribution to the inner-sphere reorganization energy, λ_i.

Another factor to consider for λ_i and the rate of electron transfer is the type of ligand attached to metal. Those ligands with low-lying π* (π acceptor ligands) such as CO, phenanthroline, bypyridine, after accepting the electron, usually causes the electron to be

delocalized over the ligand. This delocalization weakens changes in geometry and metal – ligand distances (see Table below).

Table XIX. Electron rate constants that depend on electronic configuration and type of ligands.
[Cotton, F.A.; Wilkinson, G. Advanced Inorganic Chemistry, 5th Edition Wiley, New York, 1987, p.1308]

Redox Pair	Metal configuration	k_{et}, $M^{-1}s^{-1}$ 25^0C	Δ(M-L) Å
$[Fe(bpy)_3]^{3+/2+}$	t_{2g}^5/t_{2g}^6	10^6	~0.01
$[Fe(H_2O)_6]^{3+/2+}$	$t_{2g}^3 e_g^2/t_{2g}^4 e_g^2$	4	0.14
$[Ru(H_2O)_6]^{3+/2+}$	t_{2g}^5/t_{2g}^6	20	0.09
$[Ru(NH_3)_6]^{3+/2+}$	t_{2g}^5/t_{2g}^6	10^3	0.04
$[Ru(phen)_3]^{3+/2+}$	t_{2g}^5/t_{2g}^6	$\geq 10^7$	~0.01
$[Co(NH_3)_6]^{3+/2+}$	$t_{2g}^6/t_{2g}^5 e_g^2$	10^{-6}	0.18

The inner-sphere reorganization energy λ_i, can be estimated from change of metal-ligand bond length as follows:

$$\lambda_i = \sum_j \frac{k_j^R k_j^P}{k_j^R + k_j^P} \left(q_j^R - q_j^P\right)^2 \tag{90}$$

where k_j^R, k_j^P are force constant of the j^{th} vibrational mode of the reactant and product, and ($q_j^R - q_j^P$) are the changes in bond lengths and angles in going from reactant to product. The dependence of λ_i on overall geometry of the molecule is less obvious.

The inner sphere reorganization energy λ_i of $[Fe(H_2O)_6]^{2+/3+}$ and its free energy of inner sphere reorganization, $\Delta G_i^{\ddagger}$ (Eq. A.10) have been calculated by Sutin [102] using Eq. 90 and presented by Eberson [60] as $\Delta G_i^{\ddagger}$ =12 kcal/mol. A recent study [103] uses computational methods to estimates $\Delta G_i^{\ddagger}$, see Table XX.

Table XX. Inner sphere reorganization energy for $Fe^{2+/3+(high\ spin\ states)}$.
Adapted from (J. Phys. Chem. B, Vol. 105, 2001, 5546-5552)
All distances are the same for equatorial and axial positions.

$[Fe(H_2O)_6]^{n+}$	ΔG_i (kcal/mol)	Fe-O bond (Å)
n=2+	7.3	2.15
n=3+	8.3	2.05

* 12 kcal/mol (Eberson, L.; Adv. Phys. Chem. 1982, 18, 79-185)

Optimizations for iron molecules were performed by unrestricted DFT calculation with basis B3LYP/6-31G* (Turbomole software). It has been shown and discussed that the greater basis set and other functionals do not further improve the geometry significantly. The inner-sphere reorganization energy for Fe^{3+} was obtained by difference in free energy between optimized Fe^{3+} and single-point calculated structure Fe^{3+}, taken from optimized Fe^{2+} structure, as shown in Eq. 91. The reorganization energy for Fe^{2+} was estimated as the difference between Fe^{2+} in its optimized geometry, and Fe^{2+} geometry calculated at the structure of optimized Fe^{3+} as shown in Eq. 92.

$$\Delta G_i^{\ddagger} = \Delta G[Fe^{3+}]_i = \Delta G[Fe^{3+}]_{opt} - \Delta G[Fe^{3+}]_{\text{at the geom. for } Fe^{2+}} \quad (91)$$

$$\Delta G_i^{\ddagger} = \Delta G\,[Fe^{2+}]_i = \Delta G\,[Fe^{2+}]_{opt} - \Delta G\,[Fe^{2+}]_{\text{at the geom. for } Fe^{3+}} \quad (92)$$

Their findings of $\Delta G_i^{\ddagger} =$ 15.6 kcal/mol (Table III) are in reasonably good agreement with the value of 12.1 kcal/mol reported by Sutin [102].

6.4.2.2 Outer-Sphere Reorganizational Energy

Outer – sphere reorganizational energy, $\lambda_{0,}$ represents the effects of the solvent molecules that surround the reactants during transition-state complex formation in electron transfer reaction. There are two major components that describe this value: polarization of the solvent and its induced dipole moments of solvent molecules.

Reorganization of permanent dipoles occurs within 10^{-11} - 10^{-13} s, and the change of polarization due to nuclear and electronic motion are even faster. Charge distribution remains in equilibrium during the reaction. However, if the reorientation of solvent dipoles is slow and becomes a rate-limiting step, λ_0 may make the major contribution to the reorganizational energy.

The inner-sphere contribution λ_i can dominates $\lambda_{0,}$ and $\lambda_{i} >> \lambda_0$ in the inorganic complexes. However, for electron transfer reaction that does not involve e_g metal orbital and includes ligands with delocalized electron density (see 6.4.2.1), the contribution of λ_i can be very small.

Meyer et al. [36] discussed measurement of electron transfer rates for various transition metal complexes. The inner sphere reorganization energy in $[Ru(bpy)_3]^{2+}$, $[Ru(phen)_3]^{2+}$, $[Fe(phen)_3]^{2+}$ complexes was neglected due to almost the same distance between metal and ligands. Also, the repulsion energy term (here expressed as $\Delta G_c^{\ddagger}$) was neglected due to the high ionic strength of the solution. By using Eyring Eq. (A.1), experimental rate $k = 2 \times 10^9\ M^{-1}s^{-1}$ (for self-exchange reaction of $[Ru(bpy)_3]^{2+/3+}$), and $Z \sim 10^{11}$, they calculated the activation energy barrier, and expressed as $\Delta G^{\ddagger} = \Delta G_o^{\ddagger} = \lambda / 4 \approx 2.3$ kcal/mol. On the other hand, the outer sphere reorganizational energy, which can be expressed by the values of the radii spheres of donor and acceptor and the polarizability of the solvent (Eq. A.12), was calculated to be 3.5 kcal/mol (and 4.0 kcal/mol for thermal back electron transfer). They provided estimates for the ground state electron transfer process but were uncertain about the excited state mechanisms stating, *"The conclusions reached here are germane to the reactivity of the excited state and in particular to the excited state self-exchange reaction"[36]*. In general λ_o and collision frequency are expected to be the same (or very similar) for both the ground and excited state reactions. Thus, given that the inner sphere activation energy $\Delta G_i^{\ddagger}$ for the ground and excited state is the same, the rates of electron transfer are expected to be similar.

6.4.3 Self-Exchange Reaction

Self-exchange electron transfer reaction has been established also for $Fe(H_2O)_6^{3+/2+}$ [104], Table 3. Although they have the same octahedral structure, bond lengths in Fe-O are different by 0.13Å between $Fe^{3+/2+}$. During the electron transfer, the bond length of Fe^{2+}-O decreases as that of Fe^{3+}-O increases. These changes are reflected within the inner-sphere reorganization energy λ_i.

Table XXI. Self-exchange rate constants for iron and ruthenium complexes.

Molecule	Solvent	k ($M^{-1}s^{-1}$) at (^oC)	$\Delta H^{\ddagger}$ (kJ/mol)	$\Delta S^{\ddagger}$(J/molK)
(1) $Fe(H_2O)_6^{3+/2+}$	$NaClO_4$, 1M, μ=0.55	3.3 at 21.6^{o}C	38.9	-105
(2) $[Ru(bpy)_3]^{3+/2+}$	MeCN, PF_6^-, 0.048M	8.3 ± 1.6 x 10^8 at 25 ^{o}C	15.4 ± 12.5	-6.3± 4.2

(1) Silverman, J.; Dodson R.W. J. Phys. Chem. 1952, 56, 846
(2) Young, R. C.; Keen, F. R.; Meyer, T. J. J. Am. Chem. Soc. 1977, 99, 2468

6.4.4 The Marcus Cross –Reaction

In many cases, the Marcus theory is used in cross-redox reactions (reactions that result in a net chemical change). Two self-exchange reactions can be combined together as a non-bonded electron transfer reaction between two different reactants. Its methodology is described in the Appendix B.

7. Computational Details

The ab initio calculations were performed with gaussian09 program [105]. It was shown that the Density Functional Theory (DFT) performs reasonably well for ruthenium complexes, and thus no other ab initio methods were considered for this study [70, 73, 106]. Ruthenium metal was described with LanL2DZ basis set and the corresponding effective core potentials (ECP)[5]. For other atoms, the basis of 6-31G and B3LYP functional was used for optimization and energy calculation. Calculations were performed in gas phase and in aqueous solution modeled at the level of Polarizable Continuum Model (PCM), which places the molecule "in a cavity within the solvent reaction field". Frequency analyses were performed in order to confirm the minimum of energy. The complex of $[Ru(bpy)_3]^{2+}$ was calculated in D_3 symmetry (gas phase, T_1 and S_0 electronic state) and used as a reference.

The hybrid functional B3LYP consists of exchange functional of Becke's gradient correction and correlation functional derived by Lee, Yang, and Parr for non-local density [107]. The basis set of LanL2DZ represents the Dunning and Huzinaga's valence double-zeta basis D95V [108].

The results section will provide detailed description and discussion of the geometry for optimized structures of ruthenium complexes and their comparison with the experimental data. The analysis of the absorption spectra of $[Ru(bpy)_3]^{2+}$ and $[Ru(bpy)_2dpp]^{2+}$ in the gas phase and aqueous solution will also be included. The Marcus and PCET theories will be used to evaluate the excited electron transfer rate between $*[Ru(bpy)_2dpp]^{2+}$ and $[Fe(H_2O)_6]^{3+}$.

[5] https://bse.pnl.gov/bse/portal

8. Geometry of $[Ru(bpy)_2dpp]^{n+}$ and $[Ru(bpy)_3]^{n+}$

8.1 $[Ru(bpy)_3]^{n+}$, where n=2,3

Crystallographic data of Ru(II) and Ru(III) from ($[Ru(bpy)_3](PF6)_2$) and ($[Ru(bpy)_3](PF6)_3$) were presented in Ref. [109]. Dark green-black crystals of Ru^{3+} ($[Ru(bpy)_3](PF6)_3$) were obtained by oxidation of Ru^{2+} with MnO_2 (in 7M H_2SO_4) . Ruthenium(III) crystals are not stable and decompose rapidly, and no reliable crystallographic data are available in the literature. X-ray measurement data presented in [109] were obtained at low temperature in order to obtain high resolution crystal structure. The experimental bond lengths and angles were averaged within D_3 symmetry, and presented in the Table XXII. Calculated data presented in this thesis are for $[Ru(bpy)_3]^{2+/3+}$ without consideration of counter ions. The electronic ground state is represented as S_0, and stands for a singlet of Ru^{2+} (t_{2g}^6) and doublet of Ru^{3+} (t_{2g}^5). The star notification $*Ru^{n+}$, symbolizes excited state, triplet and quartet for Ru^{2+} and Ru^{3+}, respectively.

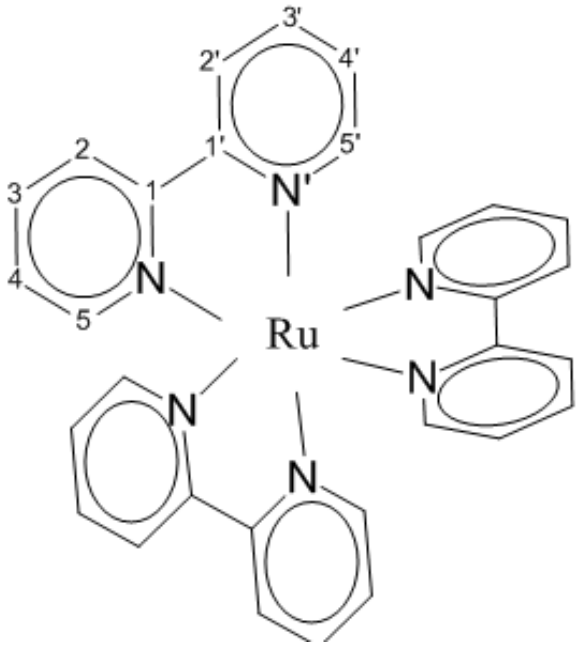

Figure 50. The structure of $[Ru(bpy)_3]^{n+}$.

Table XXII.Comparison of experimental and calculated geometry of $[Ru(bpy)_3]^{n+}$.

	Ru^{3+} Biner et al.	Ru^{2+} Biner et al.		$[^{S0}Ru]^{2+}$		$[^{S0}Ru]^{3+}$	$[^{*}Ru]^{2+}$		$[^{*}Ru]^{3+}$
				gas	*soln*	gas	gas	*soln*	gas
	105K	105K	298K	298K	298K	298K	298K	298K	298K
Ru-N	2.057	2.053	2.056	2.110*	2.104	2.120	2.102	2.104	2.102
C1-N	1.360	1.352	1.355	1.375	1.374	1.376	1.386	1.372	1.386
C1-C2	1.389	1.381	1.363	1.401	1.400	1.402	1.408	1.399	1.408
C2-C3	1.381	1.389	1.376	1.396	1.395	1.396	1.390	1.396	1.390
C3-C4	1.389	1.379	1.347	1.399	1.399	1.399	1.409	1.400	1.409
C4-C5	1.379	1.372	1.365	1.393	1.392	1.394	1.387	1.393	1.387
C5-N	1.353	1.352	1.351	1.358	1.357	1.359	1.362	1.355	1.362
C1-C1’	1.450	1.482	1.476	1.471	1.470	1.471	1.452	1.470	1.452
Angles									
N-C1-C1’-N’	11.0	6.6	5.9	2.1	1.92	2.0	-1.5	0.3	-1.5
C1-N-Ru	115.0	116.2	115.9	115.7	115.7	115.8	115.3	116.0	115.3
C5-N-Ru	125.3	125.5	126.1	125.2	125.0	125.1	125.0	124.0	125.0
C5-N-C1	119.4	118.4	117.9	119.1	119.3	119.1	119.7	120.1	119.7
N-C1-C2	120.9	121.9	120.8	120.6	120.7	120.6	119.7	120.3	119.7
C1-C2-C3	119.4	119.0	120.2	119.9	119.8	120.0	120.2	119.6	120.2
C2-C3-C4	119.5	119.0	119.2	119.0	119.1	119.0	119.3	119.4	119.3
C3-C4-C5	118.9	119.4	119.4	118.9	119.0	118.8	118.9	118.9	118.9
C4-C5-N	121.7	122.2	122.6	122.4	122.2	122.6	122.2	121.7	122.2
N-Ru-N	78.9	78.6	78.6	78.8	77.9	77.5	78.2	77.2	78.2
	90.4	89.4	89.1	88.4	88.6	88.6	86.8	85.8	86.8
	172.3	172.6	173.0	173.0	173.0	97.6	97.6	98.7	97.6
	95.6	95.7	96.3	97.1	96.3	172.6	174.3	174.5	174.3

* 2.10 Å (b3lyp/LANL2DZ), and 2.06 from X-ray as noted in S. I. Gorelsky, lever, J. Organometallic Chem 635 (2001) 187-196

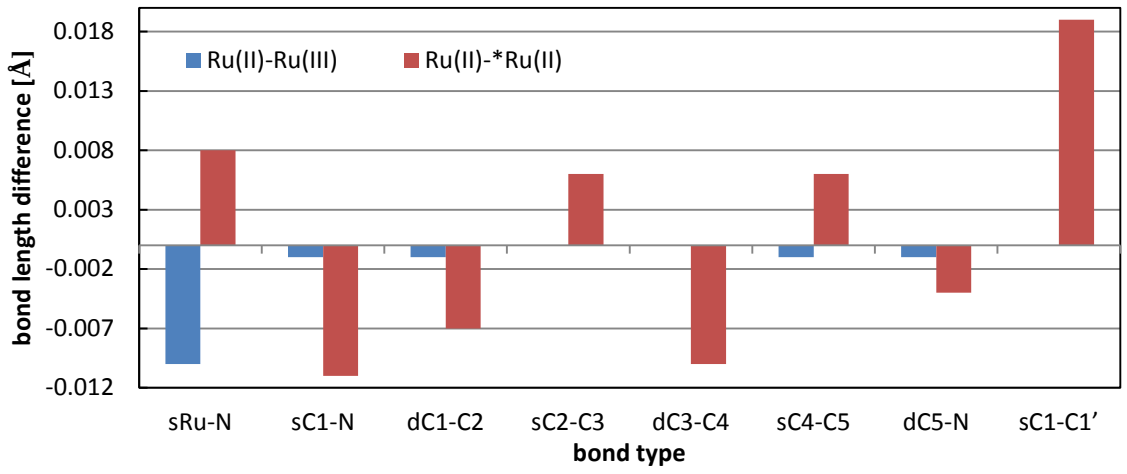

Figure 51. Bond length difference, at 298K, between Ru(II)-Ru(III), and Ru(II)-*Ru(II). s-is assigned for single bonds, and d-double bonds.

Biner et al. [109] concluded that Ru-N distance of Ru^{2+}-N and Ru^{3+}-N are 'virtually indistinguishable', (2.053Å vs. 2.057Å). In their work, orbital population shows that single bonds shorten and double bonds tend to lengthen in the excited state of Ru^{2+}.

Optimization of geometries was performed employing DFT method with unrestricted formalism in order to accommodate cationic moieties without consideration of counter ions. B3LYP functional was used with LANL2TZ basis set including effective core potential for ruthenium and 6-31G basis set for carbon, nitrogen, and hydrogen atoms. Full optimizations were performed for the ground state and lowest triplet state. Frequency analysis with the same method confirmed minimum energy at a given geometry. Optimizations were also performed with water as a solvent, within the polarizable continuum model (PCM), as implemented in G09 software.

Data obtained in the present calculation are similar to those presented in the work of Biner et al. Bond length differences in Ru^{3+} molecule and Ru^{2+} molecule are very small (close to zero), and Ru^{3+} tend to have longer bonds. In addition, it was found that C1-C1' has the greater effect on charge distribution. The excited state ruthenium $*Ru^{2+}$ has longer double bonds than Ru^{2+} and shorter single bond, (except for C1-N bond), which are similar to those reported by Biner et al. [109].

8.2 $[Ru(bpy)_2dpp]^{n+}$, where n=2,3

The X-ray data from brown crystals of $[Ru(bpy)_2dpp]Cl_2 \cdot 3H_2O \cdot CH_3CN$ were previously recorded [110]. Data for X-ray structure of $[Ru(bpy)_2dpp][PF_6]_2$ could not be obtained and only NMR in solution were only available [110]. Selected bond lengths and angles from experiment are compared with calculation results in Table XXIII below.

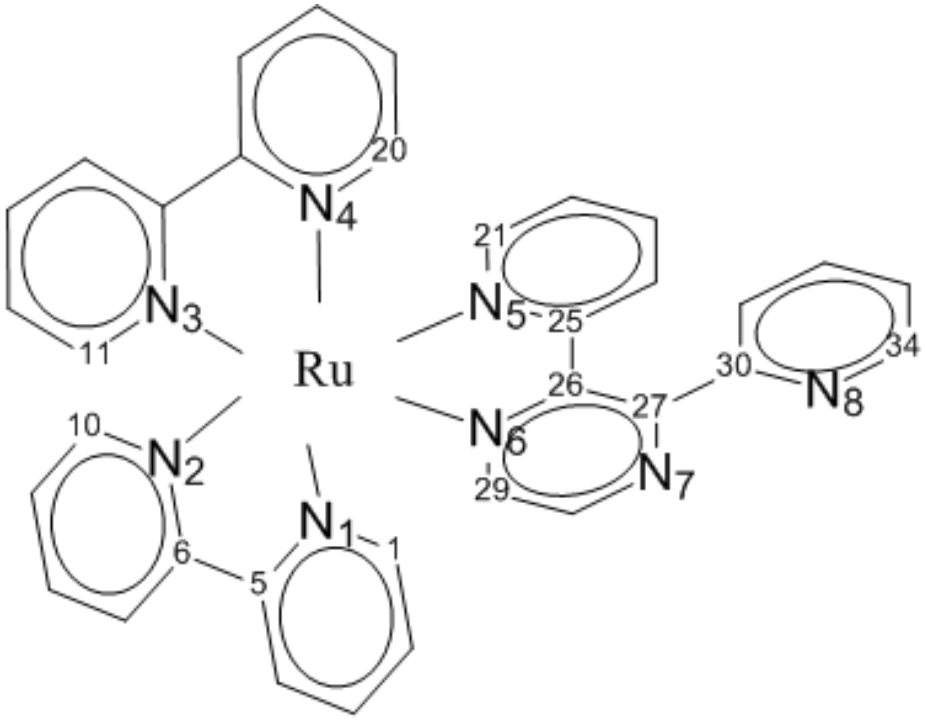

Figure 52. The stucture of $[Ru(bpy)_2dpp]^{2+}$.

Table XXIII. Comparison of experimental and calculated geometry of $[Ru(bpy)_2dpp]^{2+}$.

$[Ru(bpy)_2dpp]^{2+}$	$[^{S0}Ru]^{2+}$	$[^{S0}Ru]^{2+}$		$[^{S0}Ru]^{3+}$		$[^{*}Ru]^{2+}$		$[^{*}Ru]^{3+}$	
	Ferrari et al.								
	exp	gas	*soln*	gas	*soln*	gas	*soln*	gas	*soln*
Ru-N1(bpy)	2.049	2.112	2.110	2.113	2.108	2.112	2.107	2.118	2.111
Ru-N2 (bpy)	2.058	2.112	2.106	2.113	2.102	2.131	2.120	2.121	2.107
Ru-N3 (bpy)	2.056	2.111	2.106	2.121	2.107	2.136	2.127	2.120	2.105
Ru-N4 (bpy)	2.059	2.116	2.109	2.119	2.113	2.112	2.107	2.110	2.107
Ru-N5 (dpp)	2.046	2.103	2.099	2.099	2.101	2.076	2.085	2.104	2.112
Ru-N6 (dpp)	2.040	2.095	2.086	2.113	2.112	2.064	2.066	2.100	2.102
N5-C21	1.345	1.358	1.357	1.361	1.356	1.366	1.364	1.352	1.344
N5-C25	1.379	1.376	1.376	1.380	1.377	1.407	1.402	1.417	1.413
N6-C26	1.350	1.379	1.379	1.352	1350	1.427	1.423	1.437	1.438
N6-C29	1.342	1.394	1.354	1.380	1.375	1.368	1.363	1.342	1.325
N7-C27	1.334	1.355	1.355	1.396	1.354	1.328	1.333	1.335	1.340
N7-C28	1.303	1.342	1.346	1.400	1.342	1.379	1.381	1.350	1.344
N8-C30	1.345	1.358	1.358	1.362	1.358	1.360	1.359	1.362	1.369
N8-C34	1.360	1.348	1.350	1.345	1.348	1.349	1.351	1.336	1.340
N5-Ru-N6	78.2	77.4	77.6	77.4	77.2	78.9	78.4	78.1	77.6
N4- Ru-N6	97.9	96.2	97.3	97.9	98.5	96.9	97.5	98.3	98.4
N4- Ru-N5	89.1	88.2	89.0	86.1	85.6	85.4	85.9	86.6	85.8
N3- Ru-N6	173.2	172.3	172.4	174.5	174.1	173.7	174.3	174.6	174.1
N3- Ru-N5	95.7	97.5	96.4	98.6	99.1	97.3	98.3	97.7	97.4
N3- Ru-N4	78.8	77.7	77.8	78.0	77.9	77.5	77.6	77.9	78.0
N2- Ru-N6	97.1	97.5	97.5	98.1	98.7	97.7	98.2	98.3	99.4
N2- Ru-N5	173.6	172.8	172.8	174.5	174.7	174.2	174.5	174.3	175.1
N2- Ru-N4	96.0	97.5	96.8	98.3	98.4	99.8	98.9	98.3	98.6
N2- Ru-N3	89.2	88.0	88.1	85.5	85.1	86.4	85.5	86.2	85.8
N1- Ru-N6	90.4	89.5	89.7	85.6	85.5	86.6	86.3	85.8	85.5
N1- Ru-N5	97.1	97.0	96.8	98.1	98.5	97.6	97.8	97.6	98.0
N1- Ru-N4	170.6	172.9	172.4	174.8	174.9	175.8	175.2	174.7	175.1
N1- Ru-N3	93.4	96.8	96.5	98.4	98.4	98.98	98.8	98.2	98.4
N1- Ru-N2	78.4	77.9	77.8	77.6	77.7	77.48	77.6	77.7	77.7
Ru-N1-C5	116.0	115.8	115.6	115.7	115.7	116.2	116.0	115.7	115.7
Ru-N1-C1	126.2	125.1	125.1	124.5	124.3	123.9	123.9	124.5	124.2
Ru-N2-C10	126.2	125.3	124.8	124.6	124.0	124.8	124.4	124.7	124.1
Ru-N2-C6	116.0	115.6	115.8	115.6	115.9	115.5	115.6	115.5	115.8
Ru-N3-C15	115.2	115.8	115.8	115.5	115.8	115.1	115.4	115.4	115.6
Ru-N3-C11	126.9	125.0	124.8	124.7	124.7	125.2	124.7	124.9	124.4
Ru-N4-C20	126.2	125.3	125.2	124.8	124.5	124.4	124.0	124.5	124.5
Ru-N4-C16	115.7	115.6	115.6	115.4	115.6	115.8	116.0	115.6	124.5

Ru-N5-C25	116.6	115.9	116.0	116.1	115.9	114.3	115.2	115.0	115.1
Ru-N5-C21	125.0	124.4	124.3	123.7	123.6	125.6	124.4	125.6	125.2
Ru-N6-C26	118.1	116.0	116.2	115.5	115.9	113.8	114.8	114.2	113.8
Ru-N6-C29	125.1	124.6	124.4	124.0	123.6	127.8	126.4	127.3	127.7
N7-C27-C30	114.7	114.7	114.3	115.5	114.9	116.1	114.8	115.9	117.3
N8-C30-C27	116.3	116.3	116.6	124.0	116.3	116.6	117.2	119.5	118.0
N7-C27-C30-N8	-107(145)a	144.9	135.3	149.5	139.1	147.3	137.44	166.54	164.4
N6-C26-C25-N5	7 (10)a	-11.0	-10.3	-11.7	-11.7	-10.4	-9.94	-11.6	-11.3

a-Inorganica chimica acta 360, 2007, 1154-1162 [111]

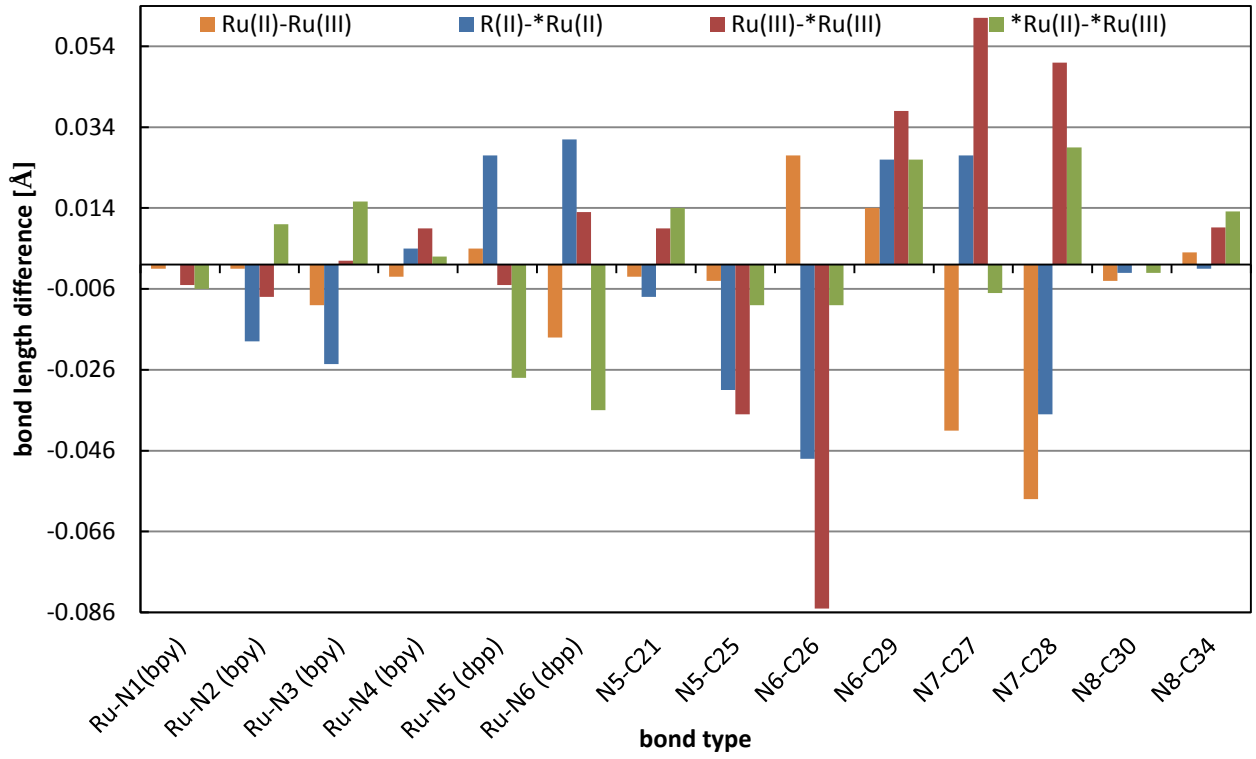

Figure 53. Selected bond length in $[Ru(bpy)_2dpp]^{2+}$.

Previously reported crystallographic data [112] showed the bond length of Ru-N as 2.096Å in pyrazine ring, and 2.060Å for the average in Ru-N (pyridine ring) bond length. Bonds are longer in Ru(III) than in Ru(II), (with the exception for pyrazine ring), and this is consistent with the data for $[Ru(bpy)_3]^{2+/3+}$. Excited molecule *Ru(II/III) has longer bonds than its ground state equivalent with the exception for pyrazine ring. Ring with two nitrogens (N6, N7) tend to be the most affected by any change in oxidation state or excitation. Dihedral angles in dpp ligand are consistent with the data presented in [110, 111]. Torsional angle N7-C27-C30-N8 is more planar when excitation or oxidation state change occurs, and varies from 145 degree in $[Ru(bpy)_2dpp]^{2+}$ to 166 degree in $*[Ru(bpy)_2dpp]^{3+}$ complex. The inner angle of dpp ligand bonded to the ruthenium metal forms the dihedral angle of (N6-C26-C25-N5), which varies in the range of two degrees between in the ground and excited states of $[Ru(bpy)_2dpp]^{2+/3+}$.

8.3 Geometry of $[Ru^n(bpy)_2dppH_y]^{n+1}$ and $[Ru^n(bpy)_2dppH_z]^{n+1}$

Due to the lack of crystallographic data for protonated species, only selected bond length and angles are presented in Table XXIV. Dihedral angles are compared with suggested experimental NMR findings [Zambrana]. Species of $[Ru^n(bpy)_2dppH_y]^{n+1}$ are simplified to the form of $[Ru^nH_y]^{n+1}$, and $[Ru^n(bpy)_2dppH_z]^{n+1}$ are simplified to the form of $[Ru^nH_z]^{n+1}$, with oxidation states n =2+, 3+. The computational data for $[^{S0}Ru^{2+}]^{2+}$ reproduce experimental findings very well as shown in Table XXIV. Here, the notation of N8-Hy, represents the protonated site of $[Ru^n(bpy)_2dppH_y]^{n+1}$ on dpp ligand, on the pyridine ring, and the notation of N7-Hz stands for $[Ru^n(bpy)_2dppH_z]^{n+1}$ the protonation on dpp ligand, pyrazine nitrogen.

Table XXIV. Comparison of calculated geometry of $[Ru^{n}(bpy)_2dppH]^{n+1}$ in aqueous solution.

$[Ru(bpy)_2dpp]^{2+}$ Aqueous	$[^{S0}Ru^{n+}]^{n+}$		$[^{S0}Ru^{n}H_y]^{n+1}$		$[^{S0}Ru^{n}H_z]^{n+1}$		$[^{*}Ru^{n}H_y]^{n+1}$		$[^{*}Ru^{n}H_z]^{n+1}$	
geometry, n=	2+	*3+*	2+	*3+*	2+	*3+*	2+	*3+*	2+	*3+*
Ru-N1(bpy)	2.110	2.108	2.107	2.112	2.111	2.117	2.108	2.109	2.111	2.091
Ru-N2 (bpy)	2.106	2.102	2.109	2.106	2.113	2.109	2.120	2.100	2.109	2.110
Ru-N3 (bpy)	2.106	2.107	2.105	2.094	2.117	2.094	2.105	2.093	2.107	2.175
Ru-N4 (bpy)	2.109	2.113	2.107	2.105	2.118	2.109	2.111	2.113	2.114	2.195
Ru-N5 (dpp)	2.099	2.101	2.100	2.111	2.096	2.103	2.091	2.119	2.103	2.175
Ru-N6 (dpp)	2.086	2.112	2.086	2.128	2.057	2.126	2.103	2.126	2.085	2.125
$N8\text{-}H_y$	-	-	1.022	1.021	-	-	1.019	1.020	-	-
$N7\text{-}H_z$	-	-	-	-	1.017	1.020	-	-	1.012	1.020
N5-Ru-N6	77.6	77.2	77.8	76.990	78.15	76.72	78.24	77.34	77.39	69.21
N4- Ru-N6	97.3	98.5	99.09	100.33	97.21	100.04	98.83	99.40	97.96	91.10
N4- Ru-N5	89.0	85.6	88.08	85.43	88.60	86.12	85.95	84.76	85.66	87.44
N3- Ru-N6	172.4	174.1	174.66	175.65	173.05	175.14	175.52	175.60	174.38	164.06
N3- Ru-N5	96.4	99.1	97.55	98.78	97.01	98.66	98.47	98.82	98.52	105.98
N3- Ru-N4	77.8	77.9	77.92	78.15	77.55	77.93	77.80	77.98	77.76	73.30
N2- Ru-N6	97.5	98.7	96.53	98.57	97.60	100.23	97.55	97.47	98.91	90.13
N2- Ru-N5	172.8	174.7	173.30	174.83	173.90	175.09	174.00	174.30	174.87	158.81
N2- Ru-N4	96.8	98.4	96.46	98.08	96.34	98.26	99.01	98.52	98.44	97.94
N2- Ru-N3	88.1	85.1	88.24	85.70	87.59	84.48	85.95	86.46	85.41	95.19
N1- Ru-N6	89.7	85.5	87.50	84.25	90.71	84.63	85.052	85.16	85.63	89.37
N1- Ru-N5	96.8	98.5	97.96	98.91	97.70	98.15	97.67	99.08	98.42	96.08
N1- Ru-N4	172.4	174.9	171.91	174.34	170.77	174.33	175.19	174.63	175.10	176.38
N1- Ru-N3	96.5	98.4	95.87	97.52	94.92	97.65	98.47	97.64	98.86	106.41
N1- Ru-N2	77.8	77.7	78.01	77.84	77.85	77.63	77.58	77.97	77.64	78.47
N7-C27-C30-N8	135.3	139.1	24.14	25.62	123.47	127.61	17.21	12.61	124.57	118.05
N6-C26-C25-N5	-10.3	-11.7	16.51	15.33	-7.62	-9.94	14.86	12.57	-12.08	26.36
$C27\text{-}C30\text{-}N8_{Hy}$	114.3	114.9	115.49	114.81	114.91	114.37	115.88	116.00	115.91	117.69
$C30\text{-}C27\text{-}N7_{Hz}$	116.6	116.3	112.21	112.53	115.27	116.18	113.93	115.83	114.72	114.32

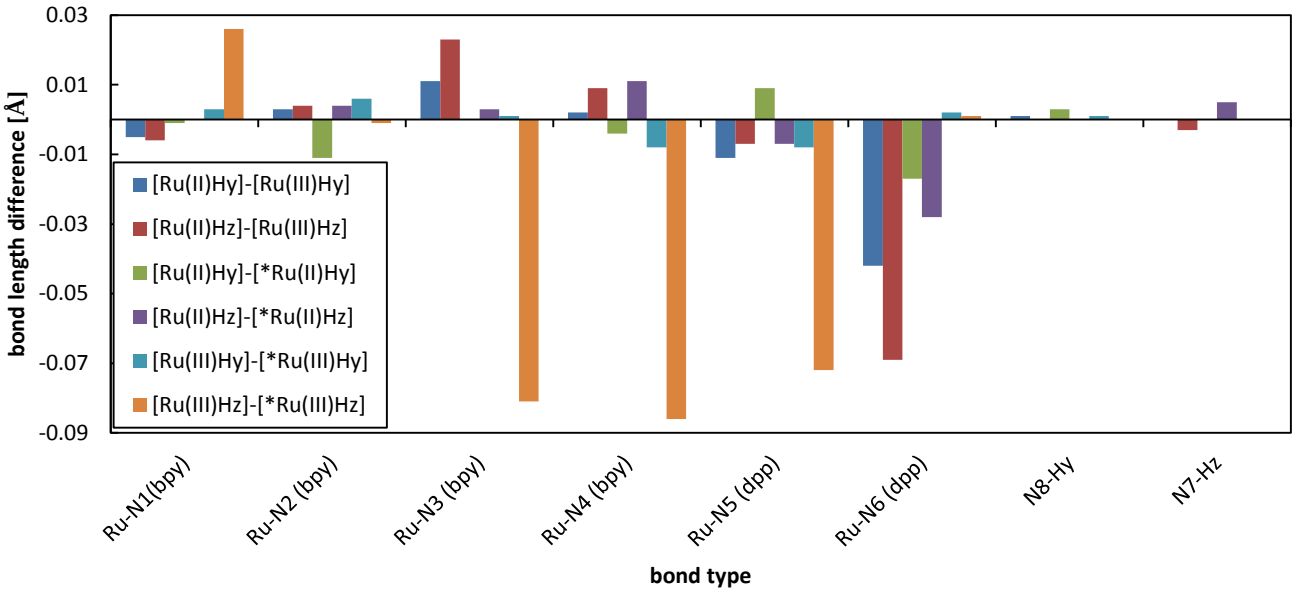

Figure 54. Comparison of selected bond length in $[Ru^{n}(bpy)_2dppH]^{n+1}$.

There is no significant change in the increasing bond length of Ru-N when ruthenium complex gets protonated to pyridine site, $[Ru^{n}\,H_y]^{n+1}$, for both oxidation states in the ground state. Those bonds get longer when molecule is protonated on pyrazine site, $[Ru^{n}\,H_z]^{n+1}$. At the same time, protonated species in the ground state exhibit longer hydrogen bond (N8-H_y) and shorter distances for protonated pyrazine site, N7-H_z.

Excited states of $[*Ru^{n}\,H_y]^{n+1}$ have longer Ru-N bonds for all three ligands (with the exception for shorter length for Ru-bpy bonds in $[*Ru^{3+}\,H_y]^{4+}$ molecule) when compared with their ground state equivalents. Excited states of $[*Ru^{n}\,H_z]^{n+1}$ exhibit shorter Ru-bpy bonds and longer Ru-dpp bonds in contrast to their ground state geometry. Hydrogen bonds of N8-H_y and N7-H_z do not change significantly during the excitation. There are no changes in the bond length when ruthenium is in 3+ oxidation state. N7-H_z has significantly shorter bonds in Ru^{2+} when compared with N8-H_y. As in the case of unprotonated molecules, Ru-N bonds are longer in Ru(III) than in Ru(II).

Table XXV. Average Ru-N bonds per ligand. Distance of Ru-N1, Ru-N2 presented as average Ru-bpy1; Ru-N3, Ru-N4 presented as average Ru-bpy2, whereas Ru-N5 and Ru-N6 presented as average Ru-dpp.

$[Ru(bpy)_2dpp]^{2+}$	$[^{So}Ru^{n}]^{n}$		$[^{So}Ru^{n}H_y]^{n+1}$		$[^{So}Ru^{n}H_z]^{n+1}$		$[^{*}Ru^{n}H_y]^{n+1}$		$[^{*}Ru^{n}H_z]^{n+1}$	
Data in soln, n=	2+	*3+*	2+	*3+*	2+	*3+*	2+	*3+*	*2+*	*3+*
Ru - bpy1	2.103	2.105	2.108	2.109	2.112	2.113	2.114	2.105	2.110	2.101
Ru - bpy2	2.108	2.100	2.106	2.100	2.118	2.102	2.108	2.103	2.105	2.185
Ru - dpp	2.093	2.107	2.093	2.120	2.077	2.114	2.097	2.123	2.094	2.150
N8-H_y	-	-	1.022	1.021	-	-	1.019	1.020	-	-
N7-H_z	-	-	-	-	1.017	1.020	-	-	1.012	1.020

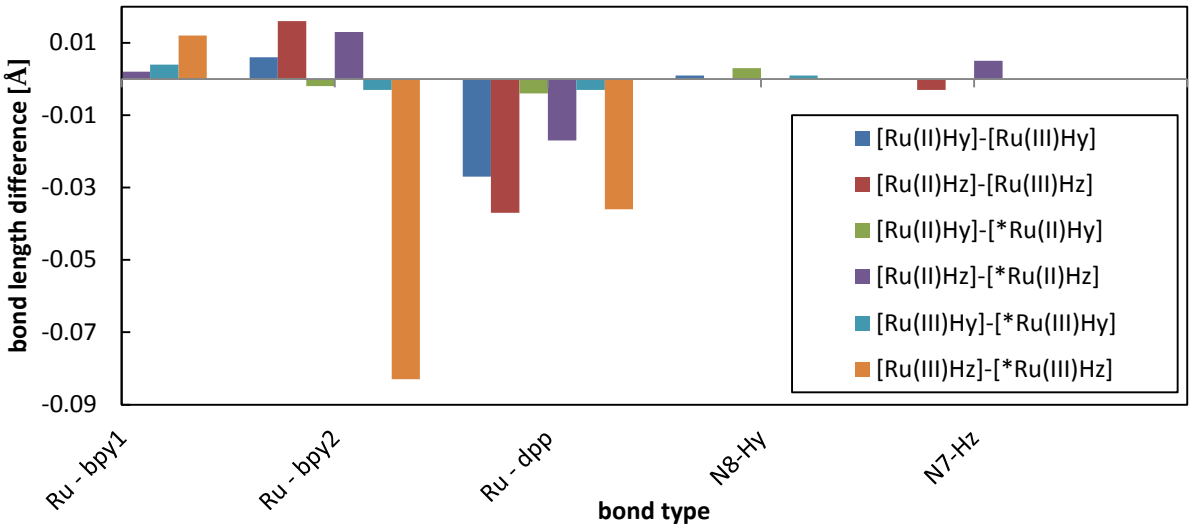

Figure 55. Comparison of an average Ru-N bond lengths per ligand in $[Ru^{n}(bpy)_2dppH]^{n+1}$.

8.5 Mulliken Charges Of $[Ru(bpy)_2dpp]^{n+}$ and $[Ru(bpy)_3]^{n+}$

Mulliken population analysis allows analyzing the charge on each atom in the molecule. It is a useful tool to investigate nucleophilic and electrophilic sites in the molecule that contains atoms with similar electronegativity. However, it is somewhat arbitrary in that it produces the charge of each atom by dividing orbital overlap equally between the atoms involved.

Table XXVI. Mulliken charges on ruthenium center in unprotonated species. Ground state values are in the first line, data with the star are for species in their excited state; (aqueous species in parenthesis).

Mulliken density on Ru center	$[Ru^{2+}(bpy)_2L]^{2+}$	$[Ru^{3+}(bpy)_2L]^{3+}$
L=bpy	1.151 (1.174) 1.343* (1.375)*	1.354 (1.372) - 1.362*
L=dpp	1.154 (1.179) 1.320* (1.376)*	1.351 (1.415) 1.353* (1.359)*

Table XXVII. Mulliken charges on ruthenium center in protonated species. Ground state values are in the first line, data with the star are for species in their excited state; (aqueous species in parenthesis).

Mulliken density on Ru center	$[Ru^{2+}(bpy)_2dppH]^{3+}$	$[Ru^{3+}(bpy)_2dppH]^{4+}$
H_y	1.173 (1.206) 1.342* (1.401)*	1.351 (1.430) 1.352* (1.432)*
H_z	1.209 (1.231) 1.351* (1.404)*	1.352 (1.364) - (1.431)*

Table XXVIII. Mulliken charges on peripheral nitrogen (in pyridine, Ny, or pyrazine ring, Nz) in unprotonated species. Ground state values are in the first line, data with the star are for species in their excited state; (aqueous species in parenthesis).

Mulliken density on peripheral nitrogen	$[Ru^{2+}(bpy)_2dpp]^{2+}$	$[Ru^{3+}(bpy)_2dpp]^{3+}$
Ny	-0.419 (-0.430) -0.432* (-0.426)*	-0.440 (-0.422) -0.428* (-0.432)*
Nz	-0.360 (-0.378) -0.378* (-0.433)*	-0.339 (-0.380) -0.370* (-0.394)*

Atomic charges determined by Mulliken population analysis remain virtually constant from one state to another. This is understandable because the electronic structures are similar. Different oxidation state indicates different values of electron density localized on ruthenium metal. All the data shown in Table XXVI-XXVIII indicate that higher oxidation state shows

more positive Mulliken charge on the metal. Experimental findings [24, 25] suggest that $[Ru^{2+}(bpy)_2dpp]^{2+}$ is protonated on pyridine site in the ground state, whereas the protonation of pyrazine site occurs in the excited state. Mulliken charge in the ground state of $[Ru^{2+}(bpy)_2dpp]^{2+}$ on peripheral nitrogen in pyridine ring, is more negative than Mulliken charge on peripheral nitrogen in pyrazine ring (-0.430 vs -0.378, respectively, in aqueous solution), which indicates more attraction of the proton to the pyridine site. On the other hand, the electron density changes in the excited state. It increases on the pyrazine site, and decreases on pyridine nitrogen (-0.433 vs -0.426, respectively, in aqueous solution). This indicates the protonation of pyrazine in the excite state. Also, similarities of electron density on the peripheral nitrogens Ny and Nz in their excited state (-0.426 vs -0.433, respectively, in the aqueous solution) are consistent with suggested experimental finding [25] of sharing the proton between two sites in the excite state of $[Ru^{2+}(bpy)_2dpp]^{2+}$. These conclusions were derived from the data in the aqueous solution and compared with experimental data, also in aqueous solution. Some discrepancies of the charges of the peripheral nitrogens exist in the gas phase and their solvated species as shown in Table 10. The data for gas phase are not as conclusive as those for their aqueous equivalents. Thus, the nature of the preferred site of protonation and the implication of Mulliken population analysis in different solvents need to be investigated further for better understanding of this process. In addition, natural population analysis would provide complimentary information.

9. Molecular Assignment of the Absorption Spectra

Ruthenium(II) complex has octahedral structure, O_h, with low spin $(t_{2g})^6$, and fully occupied, closed shell configuration. It has characteristic metal-to-ligand charge transfer, MLCT, described as $(t_{2g})^6 \rightarrow \pi_L$. On the other hand, ruthenium(III), $(t_{2g})^5$ also of O_h symmetry with low spin, exhibits ligand-to-metal charge transfer, LMCT; $\pi_L \rightarrow (t_{2g})^5$.

Properties of ruthenium(III) diimines are less known, due to their very low intensities ($\varepsilon \leq$ 500 M^{-1} cm^{-1}) and their nonemissive character: ($\varepsilon[Ru(bpy)_3]^{2+}$ = 1.46 x 10^4 at 452nm, $\varepsilon[Ru(bpy)_3]^{3+}$ = 72 at 662nm [113, 114]).

M. K. Nazeerudin et al. [19] discussed LMCT in a series of 20 complexes of Ru^{3+} and Os^{3+} ions. The nature of LMCT in $[Ru(bpy)_n(L)_{3-n}]^{3+}$ complexes (L=bibenzimidazole and triazole) as a function of ligand strength has been discussed and rationalized.

LMCT is observable typically in the visible region. However, the corresponding transitions have very weak absorption intensities ($\varepsilon \leq$ 7000 M^{-1} cm^{-1}) in 350 -500 nm region, and an additional band at longer wavelength above 500 nm. Complexes with mixed ligand are expected to have LMCT transition at longer wavelength than their equivalent complexes with the same ligand [19].

The general MO diagram of octahedral structure of ruthenium complexes with indication of possible transitions is shown in Fig. 10. The energy of charge transfer transition depends on the identity of metal, its oxidation state and the nature of ligand, which are discussed to a moderate extent in Ref. [19].

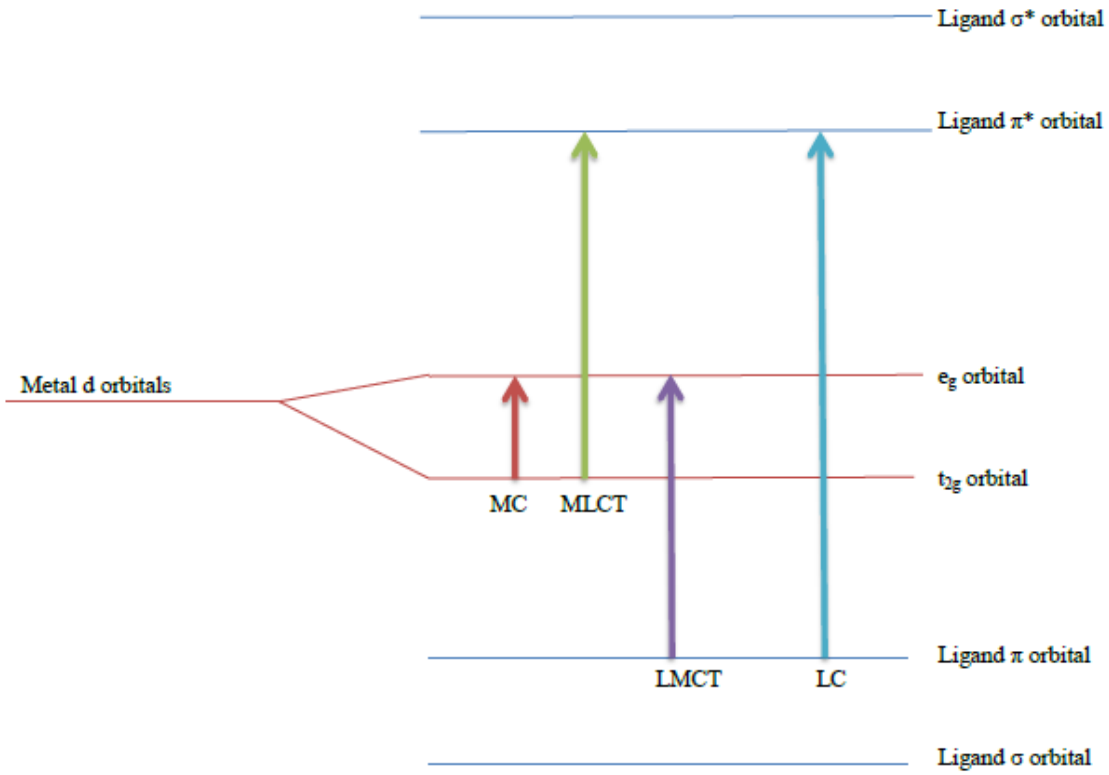

Figure 56. Energy level diagram for octahedral complex.

All of transitions involved are briefly described below.

- Metal centered transition, MC, occurs from nonbonding, metal π_M orbitals (t_{2g}) to antibonding metal σ^*_M orbitals (e_g symmetry).
- Ligand centered transition, LC, occurs from bonding ligand π_L orbitals to antibonding, ligand π^*_L orbitals.
- Ligand-to-metal charge transfer, LMCT, occurs from bonding ligand π_L orbitals to antibonding metal σ^*_M orbitals.
- Metal-to-ligand charge transfer, MLCT, occurs from nonbonding metal π_M orbitals (t_{2g}) to antibonding, ligand π^*_L orbitals. MLCT often participates in electron transfer reactions.

Molecular orbitals are linear combination of atomic orbitals. Even though the first three highest MOs belong to ruthenium in octahedral structure, small percentage of atomic orbitals from ligands are also involved in those MO. Ru^{3+} is a doublet. Thus, unrestricted formalism separates α and β orbitals. To simplify the assignment of absorption band, α β notification were omitted but considered in the orbital description, as presented in Table XXIX. Peaks presented in this section are selected due to their strong intensity (large oscillator strength, f) and their good possibility of match with experimental data.

Table XXIX. The simplified assignment of unrestricted MO.

# MO	α	β	Description
151	–	–	LUMO α listed as a LUMO LUMO+1 β listed as a LUMO+1
150	↥	–	HOMO α listed as a HOMO LUMO β listed as a LUMO
149	↥	↧	HOMO-1 α listed as a HOMO-1 HOMO β listed as a HOMO
148	↥	↧	HOMO-2 α listed as a HOMO-2 HOMO-1 β listed as a HOMO-1

The transitions in $[Ru(bpy)_2L]^{3+}$ of protonated and unprotonated species above 400 nm are in general due to beta orbitals.

9.1 $[Ru(bpy)_3]^{n+}$

$[Ru^{II}(bpy)_3]^{2+}$

The HOMO-1 and HOMO-2 consist of 77% of ruthenium (II) d-orbitals, and HOMO has 84% of ruthenium d-orbitals. The other occupied molecular orbitals, HOMO-3, HOMO-4 and those with the lower energy are localized on the ligands. Unoccupied orbitals are all due to atomic orbitals of ligands; however, they have small amount (less than 10%) of Ru, especially LUMO+6, LUMO+7. Thus, transitions at 315 nm and 326 nm have mainly the MLCT character, but the MC transition can be also considered. These features are consistent with the spectra presented by Balzani [64], which however are not well characterized and discussed in the literature. Peaks below 300 nm are clearly due to LC transition; peaks around 450 nm mostly correspond to the MLCT bands.

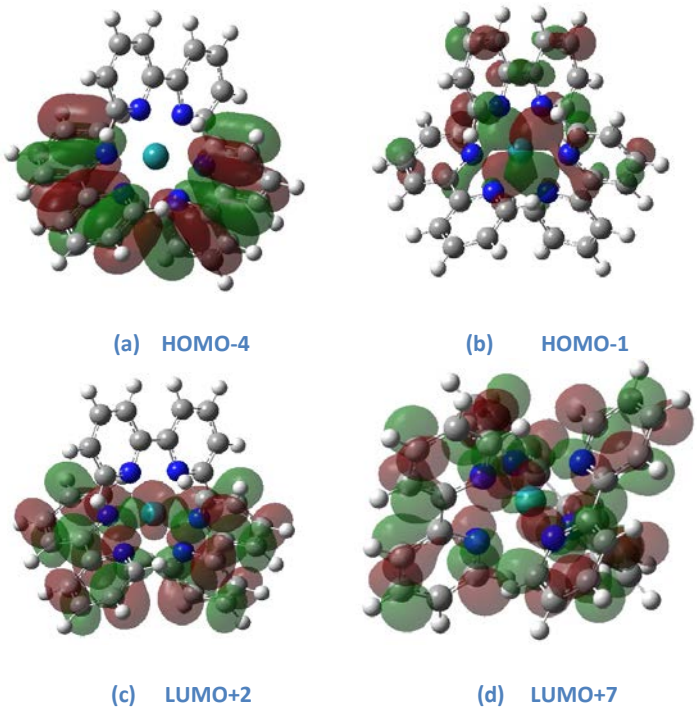

Figure 57. Selected orbitals in $[Ru^{2+}(bpy)_3]^{2+}$.

$[Ru^{III}(bpy)_2(bpy)^{-1}]^{2+}$

The molecular orbitals of HOMO-3 and below are localized only on the ligands. HOMO-3 is localized on bpy with a negative localized charge on that ligand. HOMO, HOMO-1, HOMO-2 are 82%, 75% and 79% contributed by ruthenium, respectively. The LUMO orbital, which contains 91% of bpy with a negative charge, is included in the 281 nm transition and is responsible for a distinctive 467 nm (MLCT) band. LUMO+1, LUMO+2 are located on the other 2,2'-bipyridine ligands. LUMO+3 and higher MOs include all three ligands, in which percentage of two neutral ligands decreases (from 73% to 54%) whereas the percentage of bpy^{-1} increases, from 25% (LUMO+3) to 43% (for LUMO+8). The same is true for $[Ru^{2+}(bpy)_3]^{2+}$, where LUMO+5 and LUMO+8 consist of small (less than 10%) contribution from ruthenium. Therefore, 311 nm and 329 nm bands are mostly due to the MLCT with very small contribution by the MC transitions.

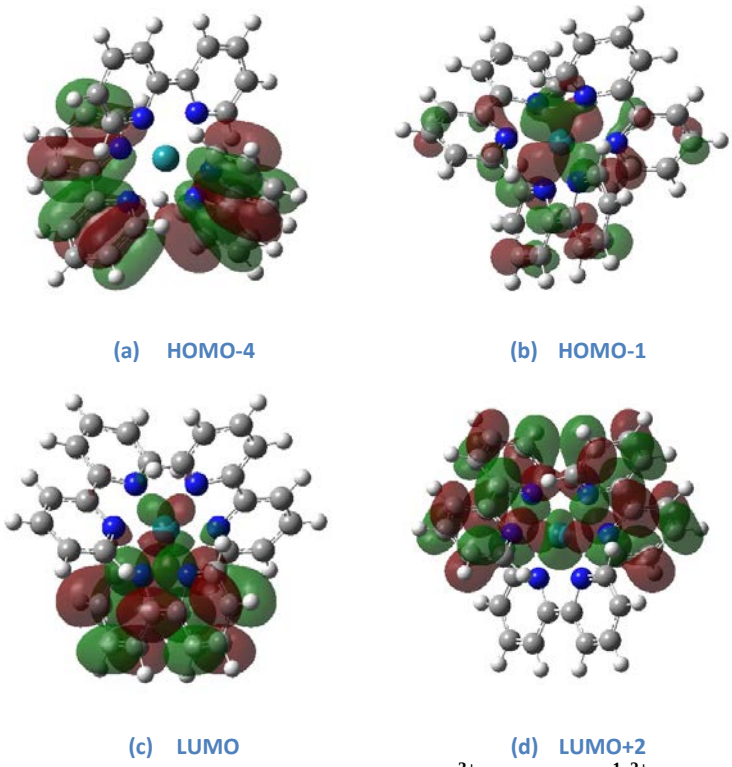

(a) HOMO-4 (b) HOMO-1

(c) LUMO (d) LUMO+2

Figure 58. Selected orbitals in $[Ru^{3+}(bpy)_2(bpy)^{-1}]^{2+}$.

$[Ru^{III}(bpy)_3]^{3+}$

The HOMO consists of the largest amount of ruthenium (89%) but is barely involved in the transitions. HOMO-1, HOMO-2 contain only 62% of ruthenium, and their main contributions are below 300 nm and 663 nm peaks. These MOs are difficult to assign either to the metal or ligand orbitals. HOMO-3 incorporates only 10% of ruthenium. HOMO-4 and HOMO-5 include 67% of Ru and participate in 295 m, 335 nm, and 663 nm bands. Orbitals below, i.e. HOMO-6, HOMO-7 and so on are purely those of ligands, and are present in 350 – 410 nm range in the spectrum of Ru^{3+}. LUMO is made up of 84% of ruthenium. Thus, new band at 663 nm is due to the MLCT, and some combination of the LC transitions. Also bands at 348 nm, 406 nm, and 409 nm are due to LMCT, as opposed to Ru^{II} that has MLCT within that range. The rest of the unoccupied orbitals are localized at ligands, with small 10% (Ru-p orbital) in LUMO+1.

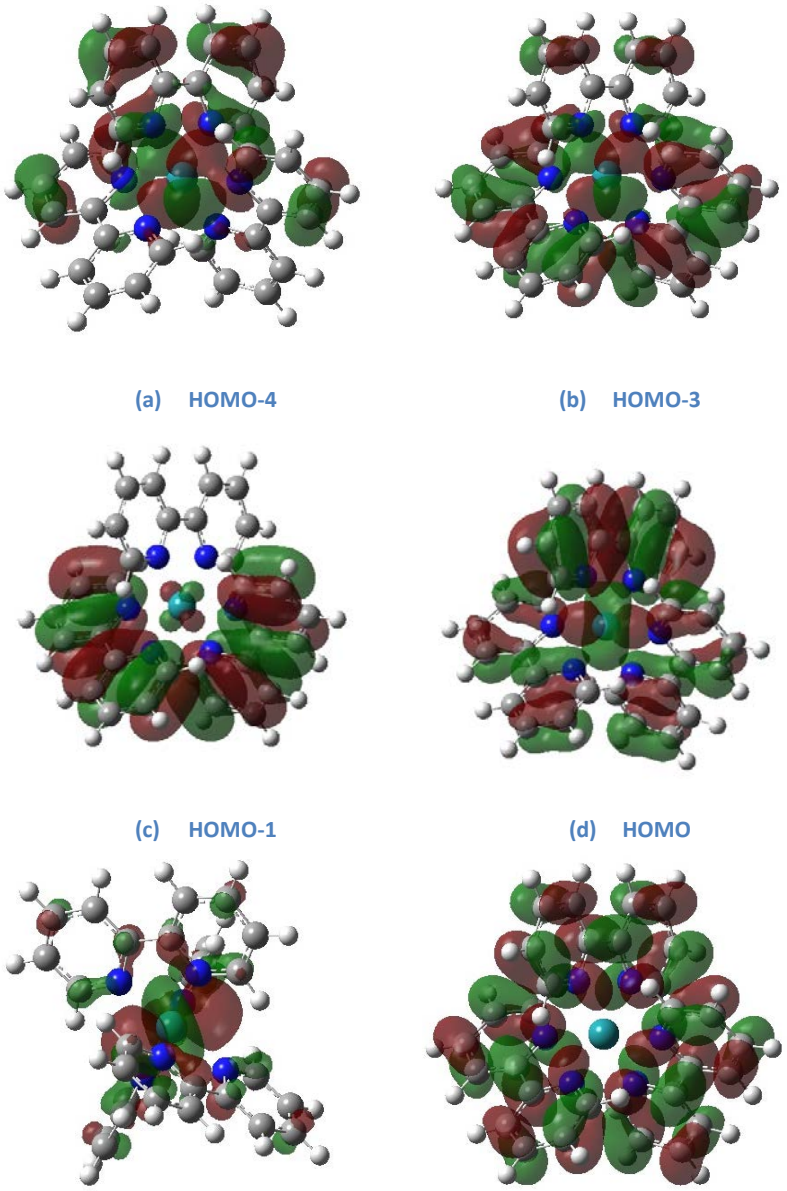

(a) HOMO-4 (b) HOMO-3

(c) HOMO-1 (d) HOMO

(e) LUMO (f) LUMO+2

Figure 59. Selected orbitals in $[Ru^{3+}(bpy)_3]^{3+}$.

Table XXX. Molecular assignment for [$Ru(II)(bpy)_3]^{n+}$, and comparison with experimental data.

$[Ru(II)(bpy)_3]^{2+}$ _exp	$[Ru(II)(bpy)_3]^{2+}$ *1.151mulliken charge*		$[Ru(III)(bpy)_2bpy^{-1}]^{2+}$ *1.174 mulliken charge*		$Ru(III)(bpy)_3]^{3+}$ *1.354 mulliken charge*	
λ(nm)_ water	λ(nm) (f) _water	λ(nm) (f) Assignment	λ(nm) (f)	Assignment	λ(nm) (f)	Assignment
276, 285 π→π*	271 (0.991)	267 (0.756) LC_M H-4→L+2 31% H-3 → L+1 31%	268 (0.618) LC	H-5→L+1 39% H-4→L+2 46%	295 (0.022) MLCT, LC	H-4→L+2 27% H-2→L+2 18%
	275 (0.270)	271 (0.226) LC H-5 →L+1 50%	281 (0.234) LC	H-5→L+1 36% H-3→L 27%	299 (0.025) LC_M	H-2→L+1 13% H-1→L 13%
323, 345 MC	321 (0.044)	315 (0.046) MLCT H-2→L+4 38% H-1→L+5 38%	311 (0.022) MLCT	H-2→L+5 64%	335 (0.004) MC, LC	H-2→L+2 30% H-3→L+2 30%
	329 (0.023)	326 (0.016) MC or MLCT H-1→L+6 13% H→L+7 87%	329 (0.024) MLCT	H→L+8 78%	348 (0.006) LMCT	H-10→L 11% H-12→L 72%
450 MLCT	436 (0.140)	429 (0.114) MLCT H-2→L+2 38% H-1→L 24% H-1→L+1 18%	421 (0.112) MLCT	H-2→L+1 63% H-1→L+2 37%	406 (0.015) LMCT	H-6→L 100%
	458 (0.013)	452 (0.007) MLCT H-1→L 74%	467 (0.103) MLCT	H-2→L+2 2% H-1→L 95% H-1→L+1 3%	409 (0.005) LMCT	H-8→L 91%
		- -	-	-		
675* MLCT					663 (0.003) LMCT MC	H-3→L 44% H-1→L 56% H-4→L 44% H→L 56%

* only for Ru^{3+}. In $[Ru(bpy)_3)]^{3+}$ LMCT is presented in 690 ± 40 nm [ref. Phys. Chem. 1993, 97, 9607-9612].

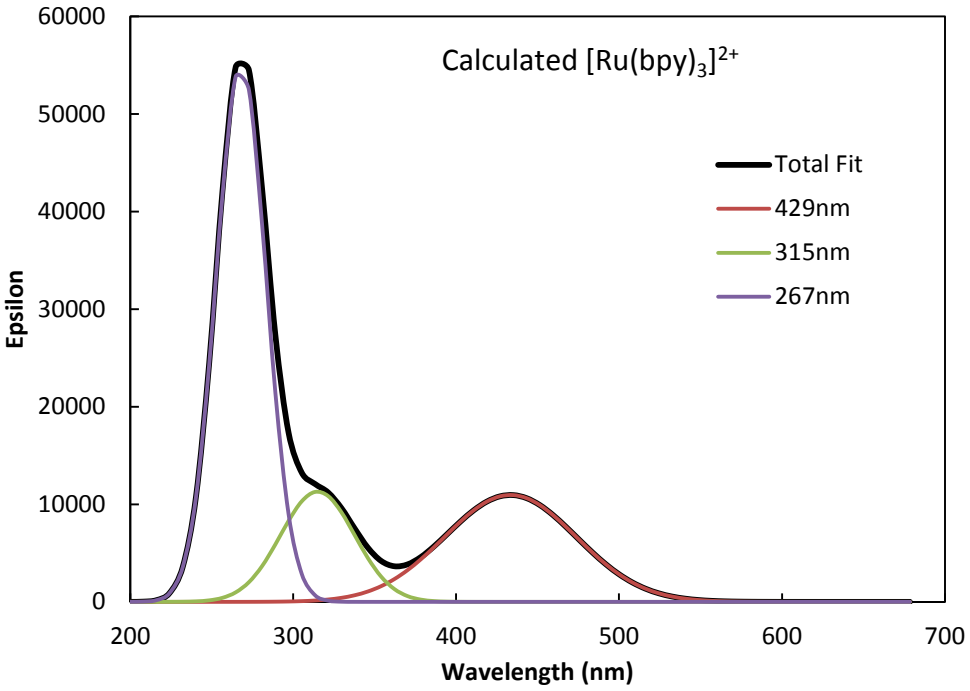

Figure 60. Peak assignment based on calculated spectra of $[Ru(bpy)_3]^{2+}$ with half-width of 0.3eV.

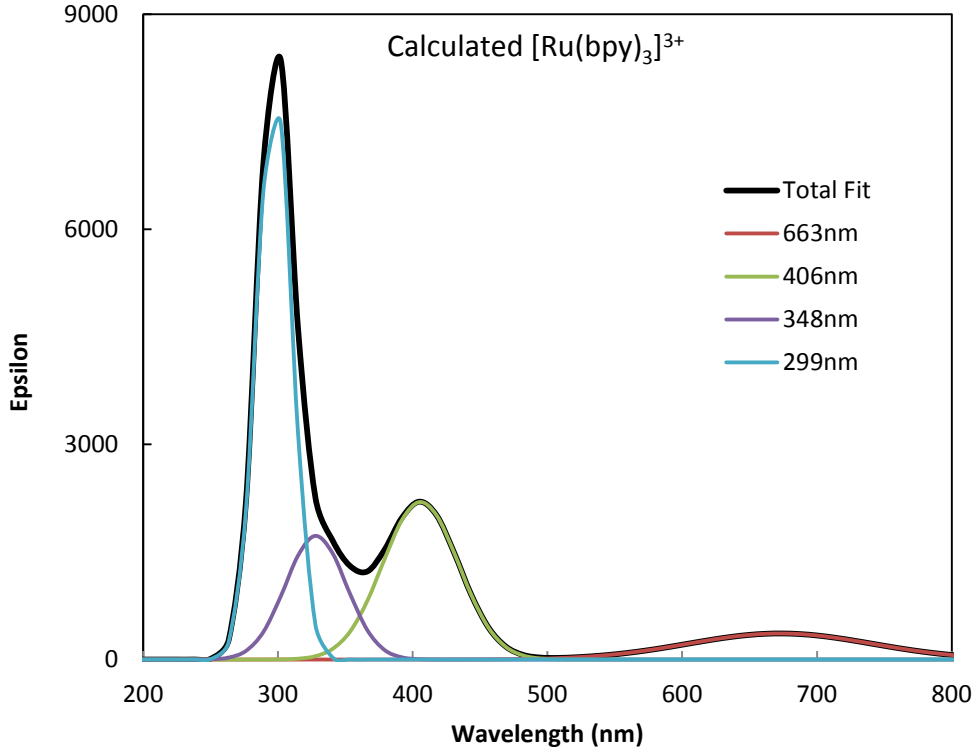

Figure 61. Peak assignment based on calculated spectra of $[Ru(bpy)_3]^{3+}$ with half-width of 0.3eV.

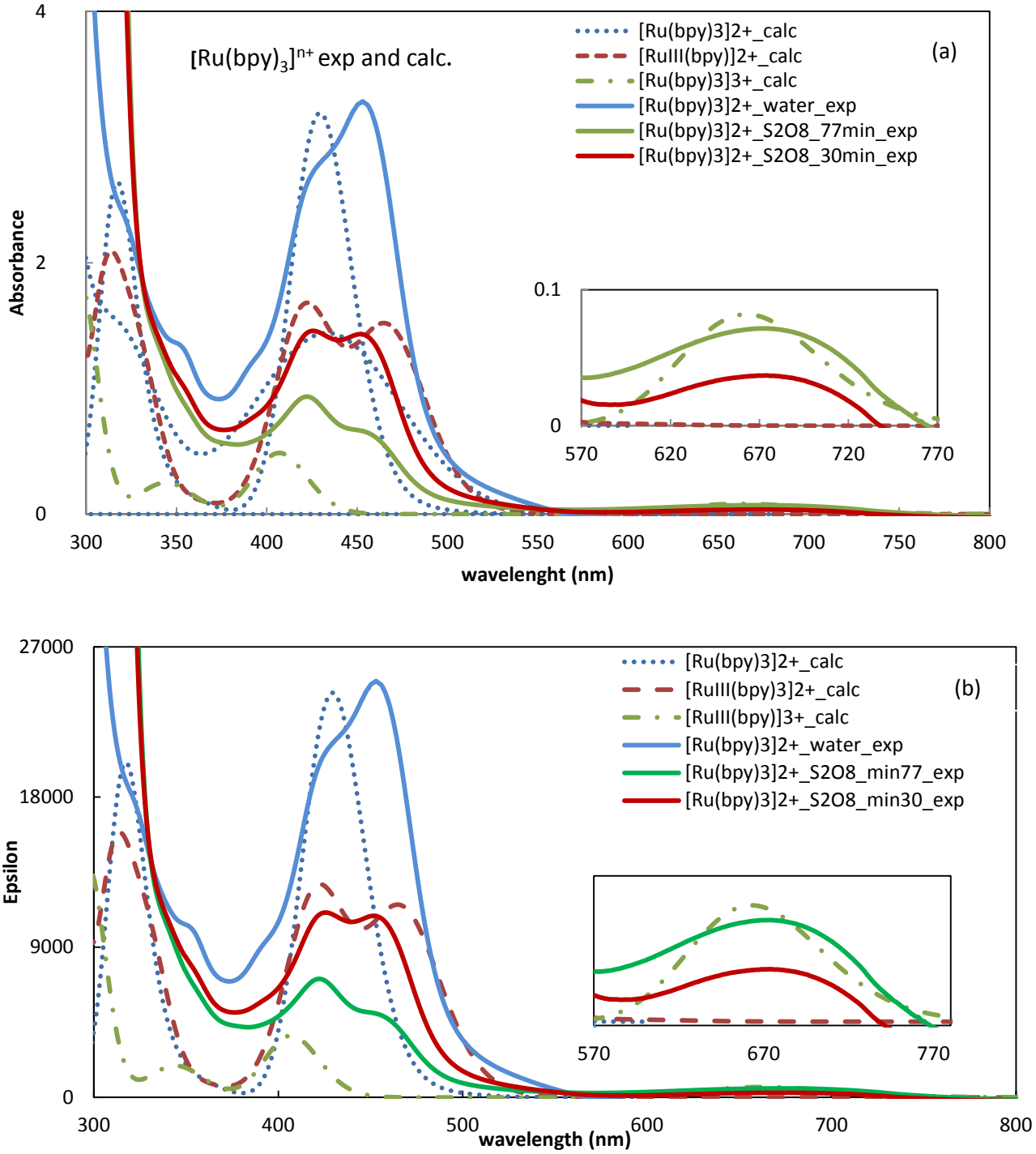

Figure 62. Comparison of calculated and experimental spectra of $[Ru(bpy)_3]^{n+}$. Broken lines represent calculated data in the gas phase and solid lines – experimet of $[Ru(II)(bpy)^3]^{2+}$ itself and with $K_2S_2O_8$ at 30 and 77minute of the reaction. (a) absorbance vs. wavelength , (b) molar extinction coefficient, epsilon, vs wavelength.

Figures 60-61 show peak assignments for the calculated spectra of $[Ru(bpy)_3]^{2+/3+}$, with more detailed information in the Table XXX. Metal-centered transition, MC, is merely distinguishable in the experimental and theoretical spectra, and it will not be discussed further. Figure 62 shows the experimental and the calculated absorption spectra. There are three calculated species, $[Ru^{(II)}(bpy)_3]^{2+}$, $[Ru^{(III)}(bpy)_2(bpy)^{-1}]^{2+}$, and $[Ru^{(III)}(bpy)_3]^{3+}$. Experimental data taken from the reaction of $[Ru^{(II)}(bpy)_3]^{2+}$ with $K_2S_2O_8$ (see section 3.3.2) are also shown. The intensity of all the calculated spectra was adjusted to that of the experimental spectra by multiplying appropriate empirical factor. Figure 62b shows the calculated data with the experimental spectra adjusted to the calculated spectra using the same empirical factor. Spectrum of $[Ru^{(II)}(bpy)_3]^{2+}$ with $K_2S_2O_8$ at 77 minute of the reaction was chosen due to its best peak at 675 nm where Ru^{3+} is expected.

Table XXXI. Comparison of molar extinction coefficient of of $[Ru^{(II)}(bpy)_3]^{2+}$ with $K_2S_2O_8$ at 77min of reaction.

Epsilon	425nm	455nm	675nm
Calculated	3.7×10^3	2.6×10^3	2.8×10^2
Experiment (section 3.3.2)	4.0×10^3	2.9×10^3	3.2×10^2

Results from Figure 62b are presented in Table XXXI. The molar extinction coefficients were successfully reproduced as well as the absorption lineshape.

9.2 $[Ru(bpy)_2dpp]^{n+}$

$[Ru^{II}(bpy)_2dpp]^{2+}$

The HOMO consists of only 59% of ruthenium and does not have major contribution to spectrum. It is present only in 355nm band and makes contribution of only about 3% and 6% (HOMO to LUMO+3, LUMO+4) to that transition. HOMO-1, HOMO-2, HOMO-3 contain 79%, 74%, 23% of Ru-d orbital, respectively. The HOMO-4 is mainly (46%) localized at the dpp_y ligand. The lowest virtual orbital belongs to dpp ligand. LUMO+1, +2 are localized on bpy, whereas the LUMO+3 contributes to the dpp_z. Thus, these assignments agree with the experiment, which shows that peak at 430 nm is due to the ML(bpy)CT, and 470 nm is due to the ML(dpp)CT.

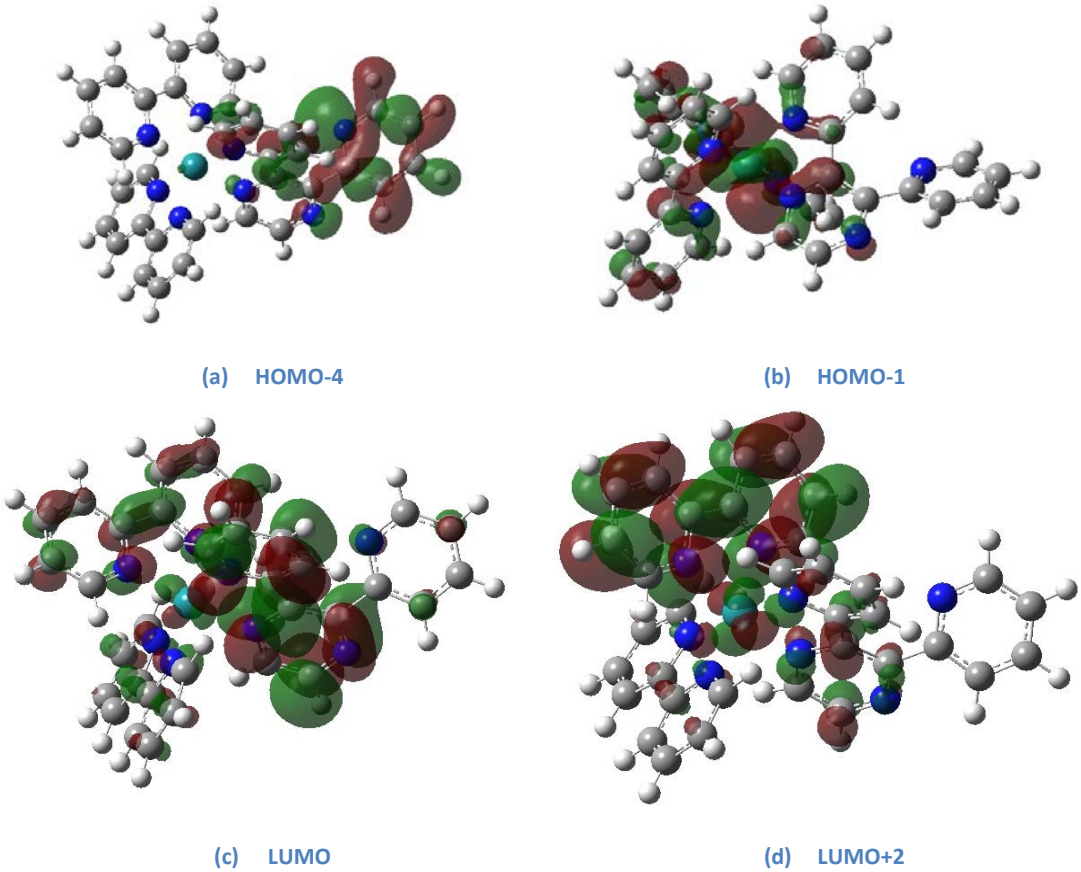

Figure 63. Selected orbitals in $[Ru^{II}(bpy)_2dpp]^{2+}$.

$[Ru^{III}(bpy)_2dpp^{-1}]^{2+}$

The three highest occupied orbitals, HOMO, HOMO-1 and HOMO-2, contain 84%, 74% and 78% of ruthenium respectively. HOMO-3, HOMO-4, and HOMO-5 are due to dpp^{-1} ligand with localized minus one charge on it (in 97-99%). The unoccupied orbitals are localized mainly on ligands, i.e. , LUMO = dpp (67%) + bpy (30%). The dpp ligand forms the LUMO (in 67%) and the LUMO+3 (in 92%). On the other hand, 81% of LUMO+1 and LUMO+2 are localized at the bpy ligand. Thus, as in the case for $[Ru^{II}(bpy)_2dpp]^{2+}$, band around 355 nm, assigned from experiment as ππ* transition, also includes the MLCT (HOMO-2 = Ru (78%) + bpy (14%) to LUMO+3 that is in 92% localized on dpp). Bands at 425 nm and 431 nm are clearly due to the ML(bpy)CT, whereas 448 nm is due to the ML(dpp)CT.

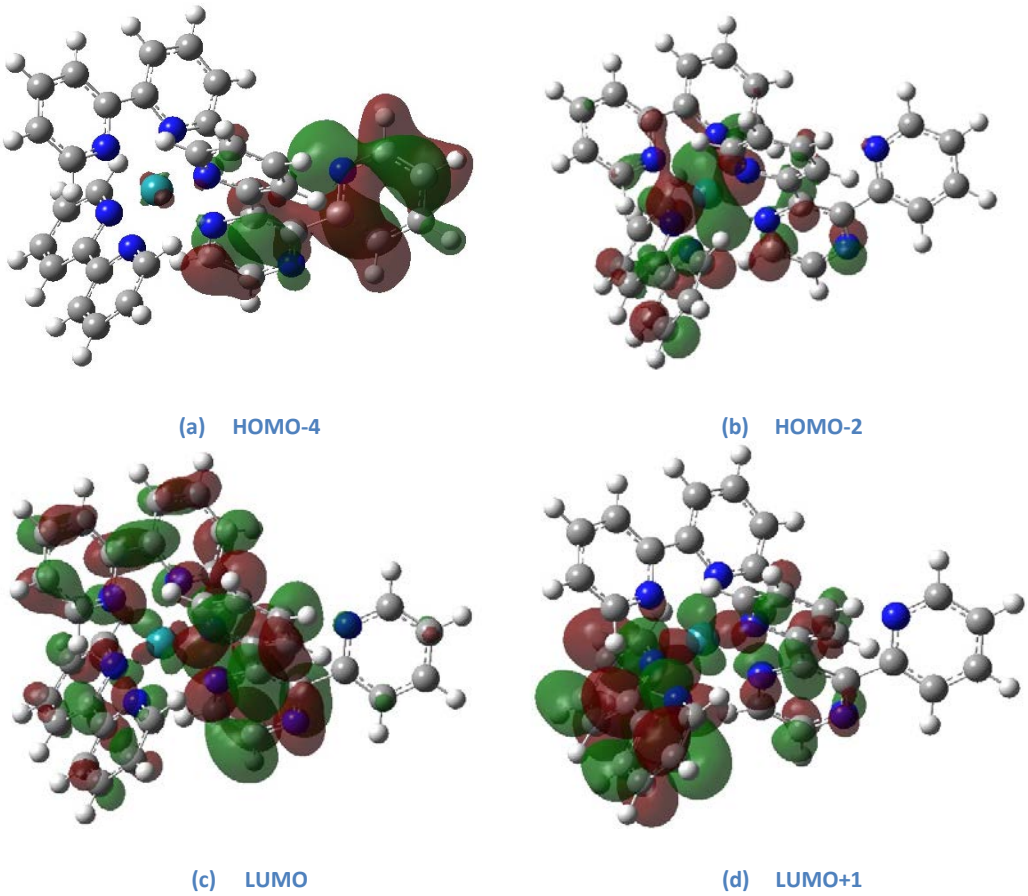

Figure 64. Selected orbitals in $[Ru^{III}(bpy)_2dpp^{-1}]^{2+}$.

$[Ru^{III}(bpy)_2dpp]^{3+}$

The LC transition at 340 nm band is mostly within the dpp ligand, with minor MLCT. The low intensity 663 nm band is a signature of $[Ru^{III}(bpy)_2dpp]^{3+}$ species, and represents the LMCT. Electron goes from lower occupied orbitals to the lowest unoccupied orbital, 150β. Unlike the other species of Ru^{2+}, LUMO of $[Ru^{III}(bpy)_2dpp]^{3+}$ is 84% of ruthenium metal. HOMO and HOMO-1 are mainly localized at the dpp, and LUMO+1 is a combination of dpp and bpy with less than 10% contribution from the ruthenium. Thus, the transitions at 424 and 445 nm, are due to L→L(M)CT, and 663 nm transition is assigned as the LMCT. The latter band is composed of 64% of L(dpp_z)MCT and 24% of L(bpy)MCT.

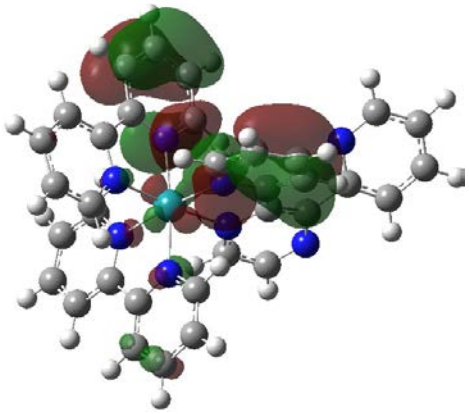

(a) 140b, HOMO-9

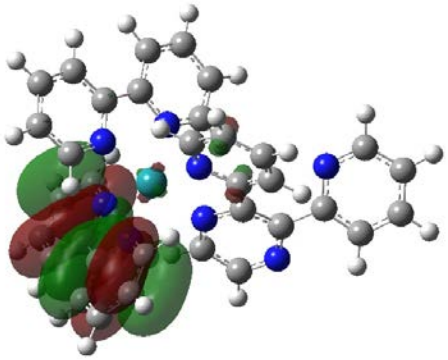

(b) 145b, HOMO-4

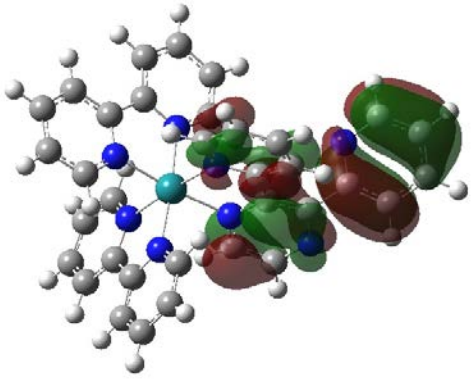

(c) 150a, HOMO

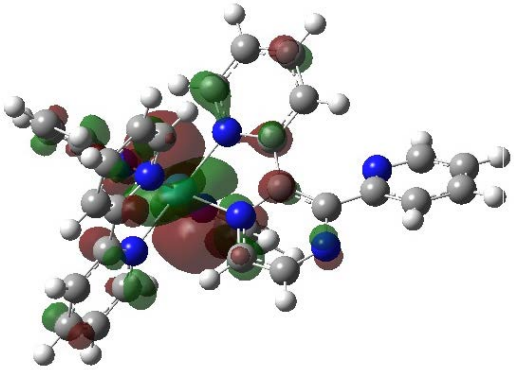

(d) 150b, LUMO

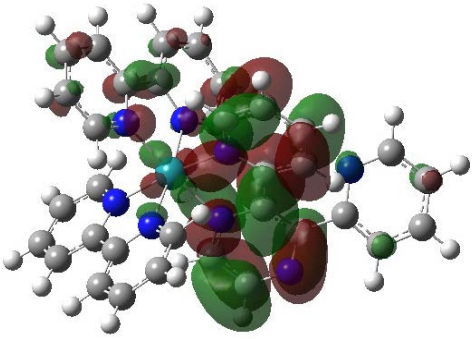

(e) 151a, LUMO

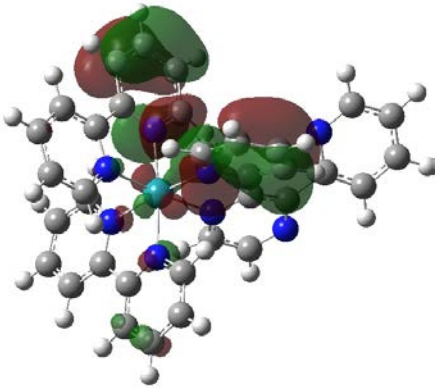

(f) 151b, LUMO+1

Figure 65. Selected orbitals in $[Ru^{3+}(bpy)_2dpp]^{3+}$

Table XXXII. Molecular assignment for $[(bpy)_2Ru(II)dpp]^{n+}$, and comparison with experimental data.

$[(bpy)_2Ru^{(II)}dpp]^{2+}$ _exp		$[(bpy)_2Ru(II)dpp]^{2+}$ *1.153 mulliken charge*		$[(bpy)_2Ru(III)dpp^{-1}]^{2+}$ *1.146 mulliken charge*		$[(bpy)_2Ru(III)dpp]^{3+}$ *1.351 mulliken charge*		
λ(nm)_water	λ(nm)(f)_ water	λ(nm) (f)	Assignment	λ(nm) (f)	Assignment	λ(nm) (f)_ water	λ(nm) (f)	Assignment
280 π→π*	340 (0.077)	*355(0.089)* LC (*)	H-2→L+3 54% H-4→L 17% H-3→L 21%	355(0.082) LC	H-2→L+3 55% H-3→L 20% H-4→L 16%	343 (0.148)	341(0.198) LC	H→L+3 17% H-1→L+3 38% H-2→L+3 20%
							356 (0.038) LC	*H-3→L 32% H-3→L+1 29%*
430 d→π*(bpy) MLCT	420 (0.053)	424(0.109) ML(bpy)CT	H-2→L+1 46% H-1→L+2 34%	425(0.108)	H-2→L+1 46% H-1→L+2 33%			
	422 (0.118)	*431(0.066)* ML(bpy)CT	H-2→L+2 76% H-1→L+1 8%	431(0.073)	H-2→L+2 73% H-1→L+1 9%	423 (0.012)	424(0.012) L(bpy)MCT	H-9→L 93%
470 d→π* MLCT(dpp)	464 (0.139)	448(0.072) ML(dpp_z)CT ML(bpy)CT	H-2→L 64% H-2→L+2 14% H-1→L 10% H-1→L+1 9%	448(0.071)	H-2→L 65% H-2→ L+2 15%	454 (0.050)	445(0.067) M(dpp)LCT	H-1→L+1 27% H→L+1 28% H-1→L+1 19% H-1→L+1 20%
N/A	-	-	-	-	-	660(0.003)	663(0.003) L(dpp_z)MCT L(bpy)MCT	H-5→L 60% H-4→L 24%

(*) 390nm band is due to MC transition, is included in Fig. 32.

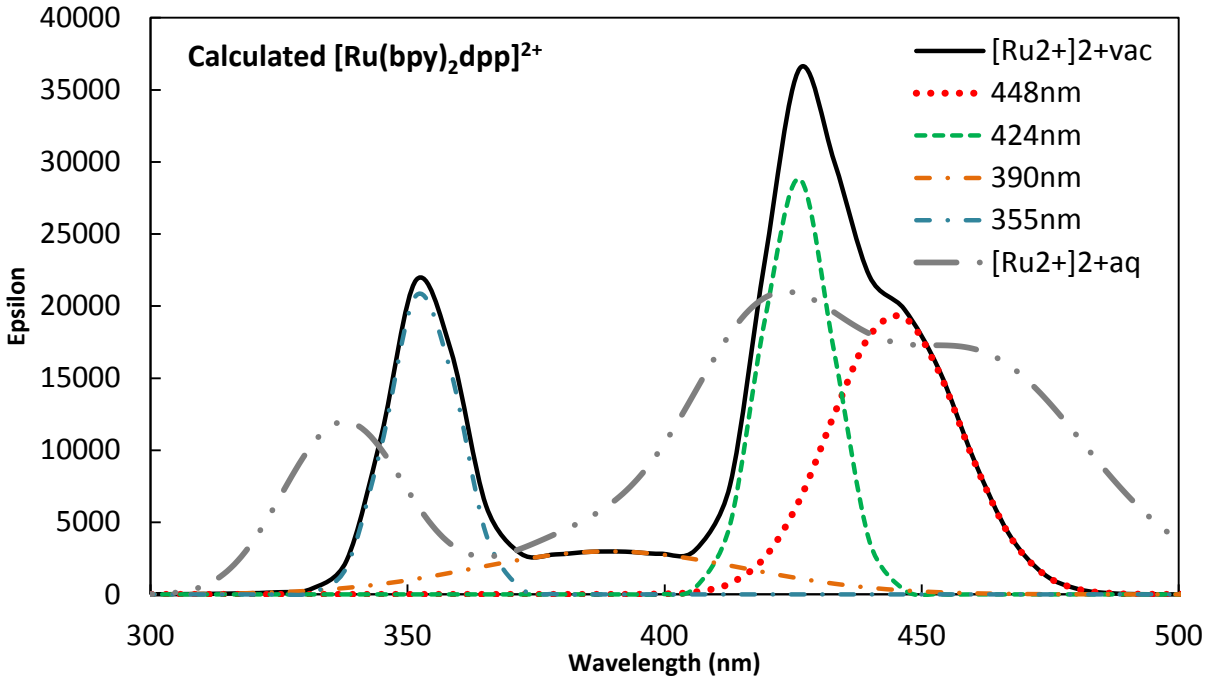

Figure 66. Peak assignment based on calculated spectra of $[Ru(bpy)_2dpp]^{2+}$, with half-width of 0.10eV.

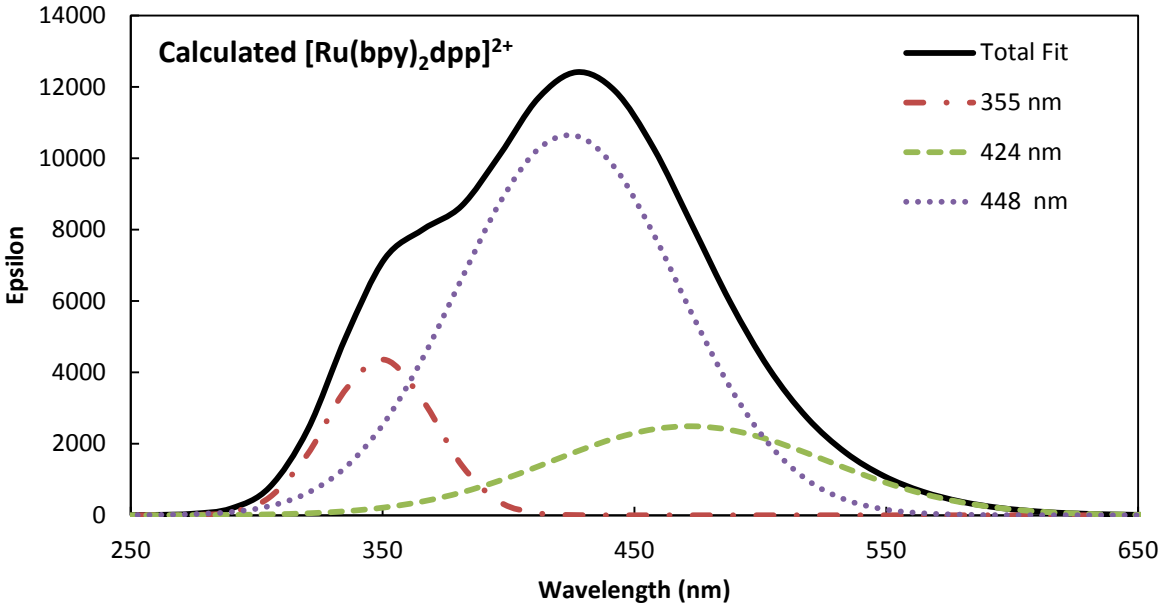

Figure 67. Peak assignment based on calculated spectra of $[Ru(bpy)_2dpp]^{2+}$, with half-width of 0.3eV.

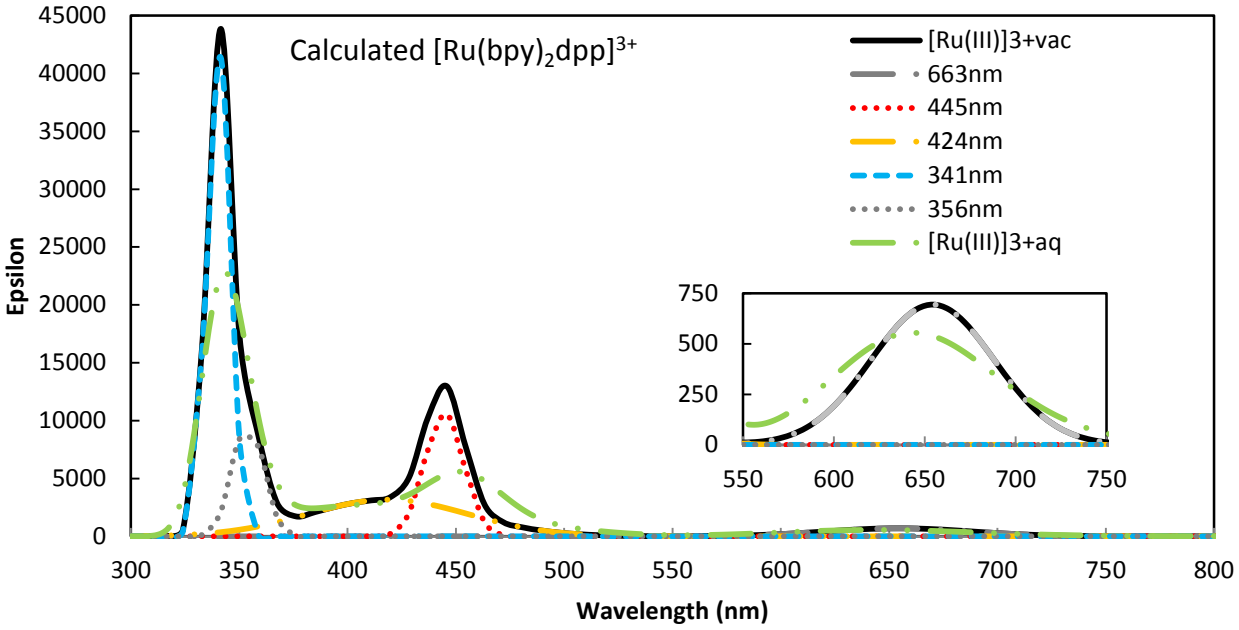

Figure 68. Peak assignment based on calculated spectra of $[Ru(bpy)_2dpp]^{3+}$, with half-width of 0.10eV.

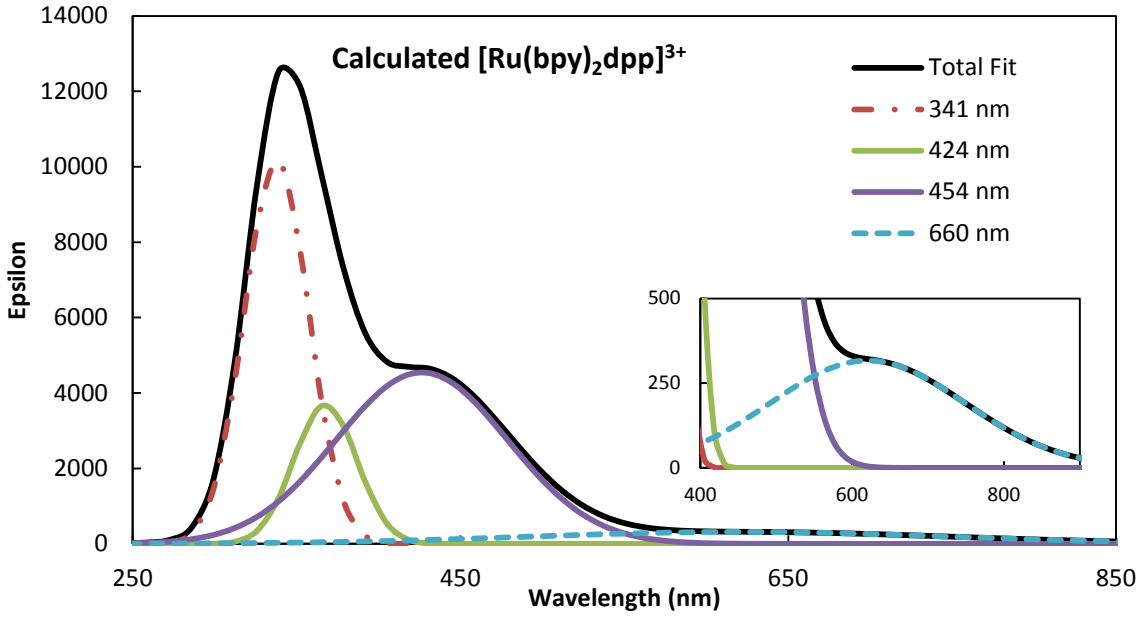

Figure 69 Peak assignment based on calculated spectra of $[Ru(bpy)_2dpp]^{3+}$, with 0.13eV half-width.

Computed peaks can be matched to experimental data as presented in Table XXXII. However, band shapes deviate significantly from experimental data. Figures 66-69 exhibit different shape of the spectra with different half-widths. Spectrum with 0.10 eV band width, shown in Fig. 66, is more detailed and express MC transition that is not included in the Table XXXII, which will not be discussed further. Figure 70 shows calculated spectra of gaseous species with 0.13 eV band width, and one with 0.30 eV that shows how peak shape and height changes. If the half width increases, the height of peak decreases leading to different value of molar absorptivity (epsilon). Thus, in order to avoid confusion, molar extinction coefficient was calculated directly from experiment, and the calculated one was derived after matching the experimental spectra. Even though band in 400-500 nm look like a single band, it contains in fact two transitions in it (425 and 448 nm). Experimental spectrum, which was used to relate to the results of DFT calculation, was taken from a sample that contains 1.25 x 10^{-4}M $[Ru(bpy)_2dpp]^{2+}$ and 2.50 x 10^{-4}M Fe(III).

Table XXXIII. Comparison of molar extinction coefficient of of $[Ru(bpy)_2dpp]^{2+}$ with Fe^{3+}.

Epsilon	425nm	455nm	660nm
Calculated	3.7 x 10^3	6.9 x 10^3	4.9 x 10^2
Experiment (Section 3.1.2)	7.5 x 10^3	6.9 x 10^3	2.6 x 10^2

Figure 70 was prepared in the same manner as Figure 62. The experimental band shape of Ru^{3+} is not easy to identify, but it can be estimated to be in the same range as the theoretical spectrum.

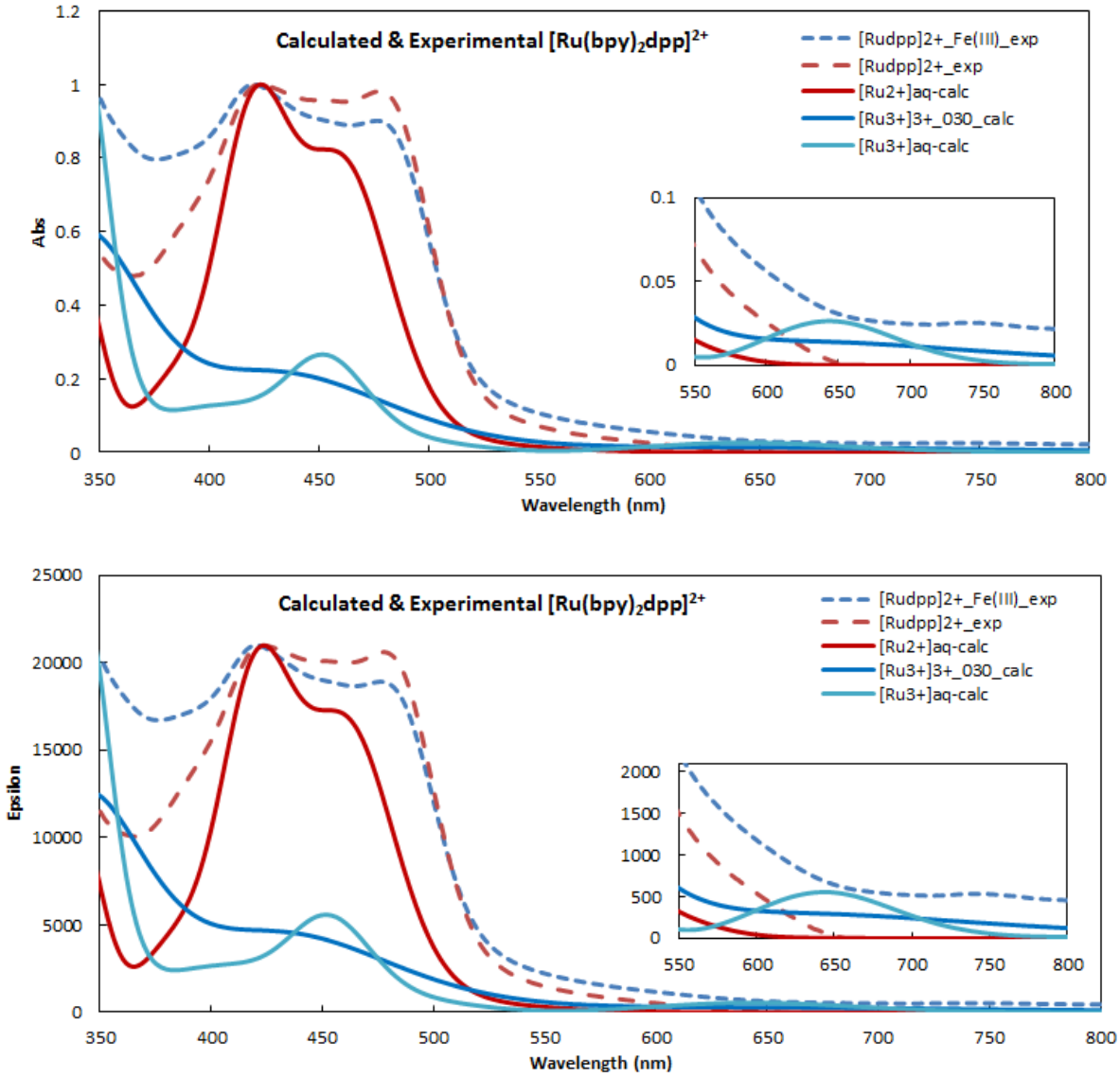

99

Figure 70. Comparison of calculated (broken lines) and experimental (solid lines) spectra of $[Ru(bpy)_2dpp]^{n+}$ presented as $[Ru^{n+}dpp]^{n+}$, $(bpy)_2$ was omitted for simplicity. (a)absorbance vs. wavelength , (b) epsilon vs wavelength. Additional line of calculated $[Ru(III)(bpy)_2dpp]^{3+}$ is added, with 0.30eV band-width.

9.3 Molecular Assignment of Electronic Spectra of Protonated Species

$[Ru^{2+}(bpy)_2dppHy]^{3+}$

HOMO, HOMO-1 and HOMO-2 consist of 82%, 77%, and 72% of the ruthenium d-orbitals, respectively. The lower occupied orbitals belong to the ligands. That is HOMO-3 is due to bpy, and HOMO-5 represents dpp. LUMO, LUMO+1 and LUMO+2 are composed of dpp ligand, second unoccupied MO is localized mainly at the pyrazine site, whereas LUMO+2, the third unoccupied MO mainly involves pyridine site of dpp. LUMO+3 and LUMO+4 are made up of bpy ligands. Thus, most of the transitions can be assigned to MLCT, with small contribution of LC at 374 nm band.

$[Ru^{3+}(bpy)_2dppHy]^{4+}$

HOMO, HOMO-1 are composed of the bpy ligand, and in general, do not contribute to absorption transitions. The band localized at 322 nm consists of combination of MLCT in 57% (there is 55% of ruthenium in HOMO-4), and of LC (dpp) transition in 7%. Peaks located at 324 and 335 nm contain 40% and 16% of LC transitions; however HOMO-2 is due to 25% of the ruthenium, and provides small MLCT. Bands at 435 and 463 nm incorporate mainly L(bpy) to M(83%) CT, with 6% of L(dpp) to MCT.

$[Ru^{2+}(bpy)_2dppHz]^{3+}$

All transitions are combinations of MLCT and LC transitions, with major contribution of ruthenium. HOMO, HOMO-1 and HOMO-2 consist of 78%, 74%, 64% of ruthenium d-orbitals, respectively. LUMO contain dpp ligand and small fraction of ruthenium orbital (17%). It is unusual that Ru^{2+} has contribution to the lowest unoccupied orbitals. LUMO+1 is composed of

dpp, and higher unoccupied orbitals belong to bpy ligands. Because HOMO-2 has 64% and LUMO has 17% of ruthenium, the peaks at 446 and 518 nm do not have conclusive character.

$[Ru^{3+}(bpy)_2dppHz]^{4+}$

Assignment of $[Ru^{3+}(bpy)_2dppHz]^{4+}$ bands are less ambiguous than $[Ru^{3+}(bpy)_2dppHy]^{4+}$. Both transitions at 367 nm are from bpy to dpp ligand, and 517 nm band is due to the electron density reorganization within dpp ligand (LUMO α). LUMO β listed as LUMO in 371, 730, 898 nm bands consists of 81% of ruthenium d-orbitals. HOMO-12, -13 contain 20% and 19% of d-orbitals of ruthenium, and the rest is mainly localized at the bpy ligand. Because of this small percentage of metal at 371 nm, the transitions at this band are assigned as a combination of MC and LMCT. Very weak bands at 730 and 898 nm are due to L(dpp)MCT and L(dpp)MCT, respectively.

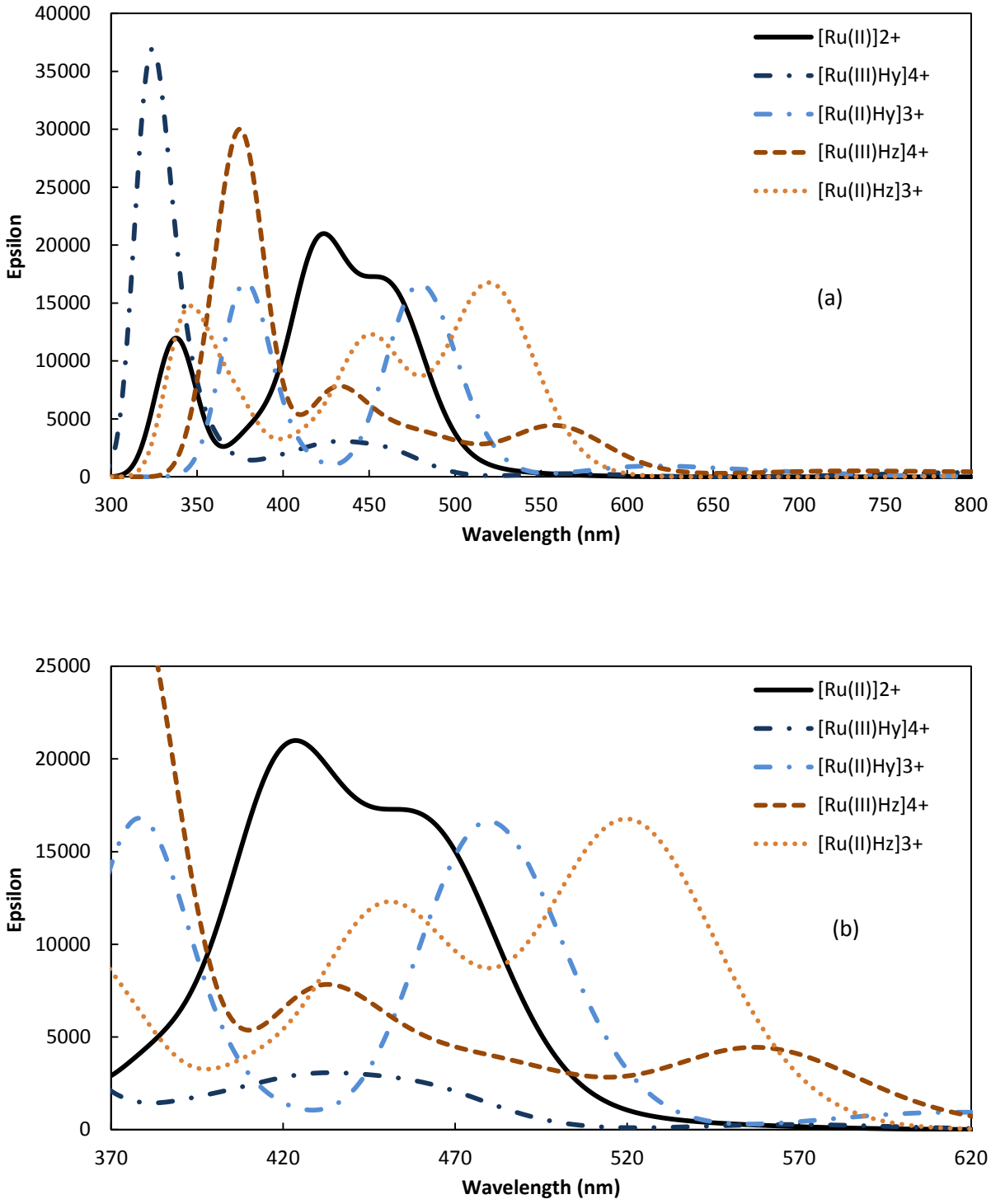

Figure 71 Peak assignment based on calculated spectra of $[Ru(bpy)_2dppH]^{3+/4+}$, with 0.13eV band width, including $[Ru(bpy)_2dpp]^{2+}$. (a) in the range 300-800 nm; (b) in the range of 370-620 nm.

Table XXXIV. Molecular assignment for $[(bpy)_2RudppHy]^{n+}$, and comparison with $[(bpy)_2Ru^{(II)}dpp]^{2+}$.

$[(bpy)_2Ru^{(II)}dpp]^{2+}$ _exp		$[(bpy)_2Ru(II)dppHy]^{3+}$ *1.172 mulliken charge*		$[(bpy)_2Ru(III)dppHy]^{4+}$ *1.350 mulliken charge*		
λ(nm)_water	λ(nm)(f)_water	λ(nm) (f)	Assignment	λ(nm) (f)_water	λ(nm) (f)	Assignment
280 π→π*	369 (0.051)	374 (0.027) MLCT(dpp) LC 25%	H-3 → L+1 25% H-2 → L+2 62%	321 (0.198) 322 (0.073)	322 (0.170) LC MLCT 324 (0.129) LC MLCT	H-4→ L+1 57%* H-4 → L+1 7% H-2→ L+1 22% H-4 → L+2 40%
430 d→π*(bpy) MLCT	379 (0.061)	381 (0.059) MLCT (bpy)	H-2 → L+3 58% H-1 → L+4 16%	336 (0.039)	335 (0.046) LC MLCT	H-2→ L+1 28% H-4→ L+1 16%
	384 (0.050)	385 (0.026) MLCT (bpy)	H-2 → L+3 43% H-2 → L+4 36%	434 (0.017)	435 (0.015) L(dpp)MCT L(bpy)MCT	H-7→ L 91% H-9→ L 6%
470 d→π* MLCT(dpp)	480 (0.160)	478 (0.175) MLCT(dpp)	H-2 → L+1 95%	463 (0.018)	463 (0.019) L(bpy)MCT	H-5 → L 100%
N/A	605 (0.004)	596 (0.006) MLCT(dpp)	H → L 58% H→ L+1 42%	834 (0.003)	829 (0.003) L(bpy)MCT	H → L 93%
	699 (0.002)	643 (0.003) MLCT(dpp)	H-2 → L+1 92%			

* LUMO+1 α is due to dpp ligand. LUMO that listed are LUMO β (83% d-Ru).

Table XXXV. **Molecular assignment for $[(bpy)_2RudppHz]^{n+}$, and comparison with $[(bpy)_2Ru^{(II)}dpp]^{2+}$.**

$[(bpy)_2Ru^{(II)}dpp]^{2+}$ _exp		$[(bpy)_2Ru(II)dppHz]^{3+}$ *1.209 mulliken charge*		$[(bpy)_2Ru(III)dppHz]^{4+}$ *1.352 mulliken charge*		
λ(nm)_water	λ(nm)(f)_water	λ(nm) (f)	Assignment	λ(nm) (f)_water	λ(nm) (f)	Assignment
280 π→π*	355 (0.063)	354 (0.059) MLCT	H-2 → L+2 35% H-1 → L+3 61%	378 (0.126)	367 (0.253) LC	H-3→ L+1 41% H-3→ L+2 47%
430 d→π*(bpy) MLCT	448 (0.094)	446 (0.100) MC? LC? MLCT	H-2 → L 8% H-1 → L+1 77%	431 (0.040)	371 (0.060) LMCT MC	H-13→ L 59% H-12→ L 12%
470 d→π* MLCT(dpp)	521 (0.158)	518 (0.165) MC? LC? MLCT (dpp)	H-2 → L 75% H → L+1 12%	561 (0.036)	517 (0.024) LC	H-3→ L* 26% H-3→ L+1 31%
N/A	899 (0.001)	880 (0.001) MC? LC? MLCT	H-1 → L 95%	747 (0.003) 904 (0.002)	730 (0.003) L(dpp)MCT 898 (0.003) L(bpy)MCT	H-3→ L 84% H-1→ L 95%

* LUMO α is due to dpp ligand. Other LUMO that listed are LUMO β (81%) d-Ru

Experimental absorption spectra of $[Ru(bpy)_2dpp]^{2+}$ in the pH range of 0-8 as presented in Fig. 10 shows no new visible peak formation, which indicates no spectral difference of any protonated species being formed in that pH range. However, small shift was observed from 428 to 422 nm and from 476 to 490 nm (section 1.2.3). The calculated protonated species $[Ru(bpy)_2dppH]^{3+/4+}$ tend to shift to longer wavelength. The spectra of the species protonated on the peripheral pyrazine site, $[Ru(bpy)_2dppHz]^{3+/4+}$ have clearly distinguished two bands, whereas $[Ru(bpy)_2dppHy]^{3+/4+}$ has only one visible peak present (Fig. 71). It is important to point out that protonated species of Ru^{3+} $[Ru(III)(bpy)_2dppH]^{4+}$ have weak absorption bands in 400-500 nm range, which are consistent with low absorptivity of non-protonated species of $[Ru(bpy)_2dpp]^{3+}$. Because $[Ru(bpy)_2dpp]^{3+}$ complex is not stable, their protonated equivalents were not analyzed in the previous study [23].

9.4 Summary

Theoretical absorption spectra for $[Ru(bpy)_3]^{2+/3+}$ have been calculated by the DFT method. Good agreement with experiment was found in both band shape and molar extinction coefficient. The spectra of $[Ru(bpy)_2dpp]^{2+/3+}$ were analyzed in the same manner. While theoretical excitation energies, shown in Table XXXII, are in reasonable agreement with xperimental data, band shape was not easy to reproduce. Despite this difficulty, the peak for $[Ru(bpy)_2dpp]^{3+}$ was confirmed and observed at very low absorbance in the ranges of 400-500 nm and 650-750 nm. $[Ru(bpy)_2dpp]^{2+/3+}$ were protonated on two sites of the dpp ligand; (a) on pyridine $[Ru(bpy)_2dppHy]^{2+/3+}$, and (b) pyrazine location $[Ru(bpy)_2dppHz]^{2+/3+}$. Their absorption spectra were related to $[Ru(bpy)_2dpp]^{2+}$. While the obtained results are in reasonable agreement with the previous studies [24, 25], they were not analyzed extensively due to their absence in the experimental results in this study.

10. PCET

The main focus of the present study is on two oxidation states of ruthenium, $[Ru(bpy)_2dpp]^{2+/3+}$, and their protonated species. Theoretical analysis of free energies provides understanding of the basic thermodynamics of the system. Calculations were carried out as described in the Chapter 7. All free energy data were extracted and used in graphs presented below. Computational modeling of solvation is highly advanced field of research with various methods available [90, 91] among which conductor like polarizable continuum model (CPCM) [115, 116] is used in the present work. The same method was used successfully in other studies [68, 69]. Solvation energy can be calculated by considering a non-equilibrium process, depicted in Fig. 26 below, where relaxation to the lowest vibrionic state is excluded.

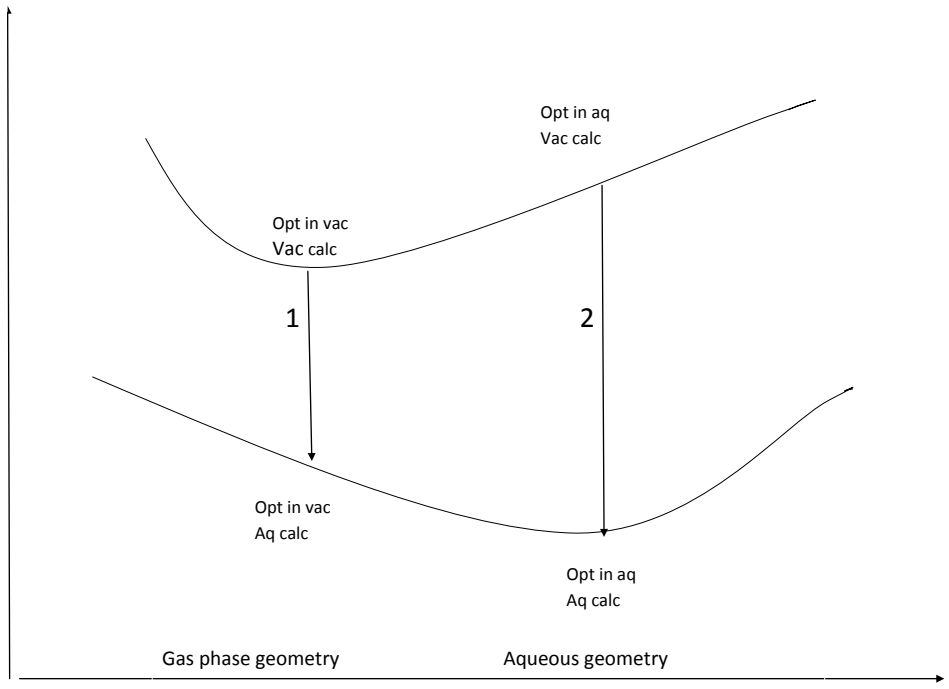

Figure 72. Energy differences in gas phase and an aqueous geometry optimization.

The free energy changes for the two processes 1 and 2 in Fig. 72 can be similar if there are no significant changes in the geometry observed in the full optimization and in energies at different phases, i.e., vacuum and aqueous solutions.

As shown in Jablonski Diagram in Fig. 2, emission occurs from the lowest vibrational state of the first triplet electronic state. Electron transfer is one of the option in the possible quenching processes, which also occurs from T_1 electronic state and goes to lowest vibrionic state in the ground state [15].

10.1 Computational Details used in PCET.

In this research, full optimizations and frequency analysis were performed in both vacuum and aqueous phase. CPCM method as implemented in Gaussian09 was used, where optimized aqueous free energy already includes gas phase and solvation free energies. Kelly et al.[88] analyzed the performance (single point calculations) of PCM models and suggested that 6-31G (d) is the best basis set, along with the HF method for predicting ΔG_s. All the calculations of optimization including solvation effect, with LanL2DZ basis for ruthenium and with 6-31G for other atoms were performed at CUNY high performance computing center [117].

In the theoretical analysis of the present investigation, free energy for redox and protonation reaction in water was calculated by

$$\Delta G_{O/R(aq)} = G_{aq}(O) + G_{aq}(e^-) - G_{aq}(R) \quad (93)$$

$$\Delta G_{(aq)} = G_{aq}(A^-) + G_{aq}(H^+) - G_{aq}(HA) \quad (94)$$

assuming equilibrium process. Thus, relaxation from higher vibrionic states of the ground state is neglected. Table XXXVI provides values that were used to calculate free energies of the reaction and their redox potentials.

Table XXXVI. Constant values used in ΔG, pKa and E^0 calculations.

Constant	Value [kcal/mol]	Explanation
$\Delta G_{aq}(e^-)$	-0.006	$\Delta G_g(e^-)+ \Delta G_s(e^-)=$ -0.006+0[69,87-88]
$\Delta G_{aq}(H^+)$	-272.18	$\Delta G_g(H^+)+ \Delta G_s(H^+)=$ -6.28-265.9
ΔG_{SHE}	98.70	4.28V[88]
1 Faraday	23.061*	96 485 C

* The units are kcal $mol^{-1}V^{-1}$

The scheme shown in Fig. 73 provides the PCET model used for the analysis of the investigated reaction (Eq. 45).

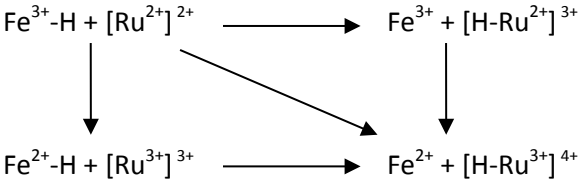

Figure 73. My Basic PCET model w/total charge.

Fe^{n+}-H represents $[Fe(H_2O)_6]^{n+}$, Ru^{m+} stands for $[(bpy)_2Rudpp]^{m+}$, and H-Ru^{m+} is a simplified expression for $[(bpy)_2RudppH]^{m+}$. Detailed discussion of protonation will be discussed later in this chapter, based on the discussion from Chapter 4. Because the major focus of present research is $[Ru(bpy)_2dpp]^{2+/3+}$, diagrams that follow will be for this complex only.

10.2 Hydrogen Atom Transfer (HAT) vs. Proton Transfer (PT)

Hydrogen atom transfer (HAT) describes electronically adiabatic process (only in the ground state). However, it can be vibrationally adiabatic or nonadiabatic [83]. In this case, electron responds instantly to proton motion: $\tau_e << \tau_p$ where τ_e is the electronic transition time and τ_p is the proton tunneling time. Proton transfer can be described as an electronically nonadiabatic process, where electron does not respond instantly to proton motion and $\tau_e > \tau_p$.

HAT reaction, $H^{\cdot} \leftrightarrow H^{+} + e^{-}$, does not involve significant charge redistribution, which means that the solvent reorganization energy is very small, and solvent coordinates may not provide a physically meaningful description [85]. The major focus of the present research is excited electron transfer reaction that occurs during the quenching process of $*[Ru(bpy)_2dpp]^{2+}$. HAT is not a possible option for the excited state of $[Ru(bpy)^2dpp]^{2+}$ and will not be considered here.

10.2 Computational Investigation of PCET Mechanism

The investigated reaction occurs during quenching process resulting in the excited electron transfer between $*[Ru(bpy)_2dpp]^{2+}$ and Fe^{3+}_{aq}, see Chapter 5. In the table below, the $*[Ru(bpy)_2dpp]^{2+}$ is considered in the lowest triplet excited state (for species with 2+ and 4+ of total charg), and quartet (for with 3+ of total charge). Calculated standard potentials were obtained with respect to the SHE.

Table XXXVII Calculated standard potentials for given reaction with respect to NHE. The $[Ru(bpy)_2dpp]^{n+}$ is written as $[Ru]^{n+}$ for simplicity. The oxidation state of the metal is included in parenthesis, whereas the total charge of the molecule is given outside of the parethesis. (*Experimental findings are in parenthesis).*

Reaction	ΔG(kcal/mol)	E^0(V) *(Exp. value)*	pK_a *(Exp. value)*
$*[Ru^{II}]^{2+} \rightarrow e^- + *[Ru^{III}]^{3+}$	141	-1.9	-
$*[Ru^{II}]^{2+} \rightarrow e^- + [Ru^{III}]^{3+}$	90	0.4 *(0.53)*	-
$*[Ru^{3+}]^{3+} + e^- \rightarrow [Ru^{II}]^{2+}$	-181	12.1	-
$[Ru^{3+}]^{3+} + e^- \rightarrow [Ru^{II}]^{2+}$	-129	-1.3 *(-1.23)*	-
$*[H_{py}\text{-}Ru^{II}]^{3+} \rightarrow e^- + [H_{py}\text{-}Ru^{III}]^{4+}$	101	-0.1	-
$[H_{py}\text{-}Ru^{II}]^{3+} \rightarrow e^- + [H_{py}\text{-}Ru^{III}]^{4+}$	134	-1.5	-
$*[H_{py}\text{-}Ru^{II}]^{3+} \rightarrow e^- + *[H_{py}\text{-}Ru^{III}]^{4+}$	154	-2.4	-
$*[H_{pz}\text{-}Ru^{II}]^{3+} \rightarrow e^- + [H_{pz}\text{-}Ru^{III}]^{4+}$	117	-0.8	-
$[H_{pz}\text{-}Ru^{II}]^{3+} \rightarrow e^- + [H_{pz}\text{-}Ru^{III}]^{4+}$	139	-1.8	-
$*[H_{pz}\text{-}Ru^{II}]^{3+} \rightarrow e^- + *[H_{pz}\text{-}Ru^{III}]^{4+}$	161	-2.7	-

$*[Ru^{II}]^{2+} + H^{+} \rightarrow *[H_{py}Ru^{II}]^{3+}$	-6	4.5	4.3
$*[Ru^{II}]^{2+} + H^{+} \rightarrow [H_{py}Ru^{II}]^{3+}$	-39	6.0	28.8
$*[H_{py}Ru^{II}]^{3+} \rightarrow H^{+} + [Ru^{II}]^{2+}$	-33	5.7	-24.4
$[H_{py}Ru^{II}]^{3+} \rightarrow H^{+} + [Ru^{II}]^{2+}$	0	4.3	0.2 *(1.12)*
$*[Ru^{3+}]^{3+} + H^{+} \rightarrow [H_{py}Ru^{III}]^{4+}$	-47	6.3	34.1
$[Ru^{3+}]^{3+} + H^{+} \rightarrow [H_{py}Ru^{III}]^{4+}$	5	4.1	-3.8
$*[Ru^{3+}]^{3+} + H^{+} \rightarrow *[H_{py}Ru^{III}]^{4+}$	6	4.0	-4.7
$*[Ru^{II}]^{2+} + H^{+} \rightarrow *[H_{pz}Ru^{II}]^{3+}$	-7	4.6	5.3 (5.8)
$*[Ru^{II}]^{2+} + H^{+} \rightarrow [H_{pz}Ru^{II}]^{3+}$	-29	5.6	21.5
$*[H_{pz}Ru^{II}]^{3+} \rightarrow H^{+} + [Ru^{II}]^{2+}$	-32	5.7	-23.3 (-4.9)
$[H_{pz}Ru^{II}]^{3+} \rightarrow H^{+} + [Ru^{II}]^{2+}$	-10	4.7	-7.1 (-4.9)
$*[Ru^{3+}]^{3+} + H^{+} \rightarrow [H_{pz}Ru^{III}]^{4+}$	-32	5.7	23.1
$[Ru^{3+}]^{3+} + H^{+} \rightarrow [H_{pz}Ru^{III}]^{4+}$	20	3.4	-14.7
$*[Ru^{3+}]^{3+} + H^{+} \rightarrow *[H_{pz}Ru^{III}]^{4+}$	13	3.7	-9.2
PCET and after			
$*[Ru^{II}]^{2+} + H^{+} \rightarrow [H_{py}Ru^{III}]^{4+} + e^{-}$	95	0.2	-69.4
$*[Ru^{II}]^{2+} + H^{+} \rightarrow *[H_{py}Ru^{III}]^{4+} + e^{-}$	148	-2.1	-108.2
$[H_{py}Ru^{3+}]^{4+} + e^{-} \rightarrow [Ru^{II}]^{2+} + H^{+}$	-134	10.1	-98.0
$*[H_{py}Ru^{3+}]^{4+} + e^{-} \rightarrow [Ru^{II}]^{2+} + H^{+}$	-187	12.4	-136.9
$*[Ru^{II}]^{2+} + H^{+} \rightarrow [H_{pz}Ru^{III}]^{4+} + e^{-}$	110	-0.5	-80.4
$*[Ru^{II}]^{2+} + H^{+} \rightarrow *[H_{pz}Ru^{III}]^{4+} + e^{-}$	154	-2.4	-112.7
$[H_{pz}Ru^{3+}]^{4+} + e^{-} \rightarrow [Ru^{II}]^{2+} + H^{+}$	-149	10.7	-109.0
$*[H_{pz}Ru^{3+}]^{4+} + e^{-} \rightarrow [Ru^{II}]^{2+} + H^{+}$	-193	12.7	-141.3
$*[Ru^{II}]^{2+} \rightarrow [Ru^{II}]^{2+}$	-39	1.7 (1.76)	
$[H_{py}Ru^{II}]^{3+} \rightarrow H^{+} + [Ru^{III}]^{3+} + e^{-}$	129	-1.3	94.4
$*[H_{py}Ru^{II}]^{3+} \rightarrow H^{+} + [Ru^{III}]^{3+} + e^{-}$	96	0.1	69.9

$*[H_{py}Ru^{II}]^{3+} \rightarrow H^{+} + *[Ru^{III}]^{3+} + e^{-}$	147	-2.1	107.8
$[H_{pz}Ru^{II}]^{3+} \rightarrow H^{+} + [Ru^{III}]^{3+} + e^{-}$	119	-0.9	87.1
$*[H_{pz}Ru^{II}]^{3+} \rightarrow H^{+} + [Ru^{III}]^{3+} + e^{-}$	97	0.1	71.0
$*[H_{pz}Ru^{II}]^{3+} \rightarrow H^{+} + *[Ru^{III}]^{3+} + e^{-}$	149	-2.2	108.8

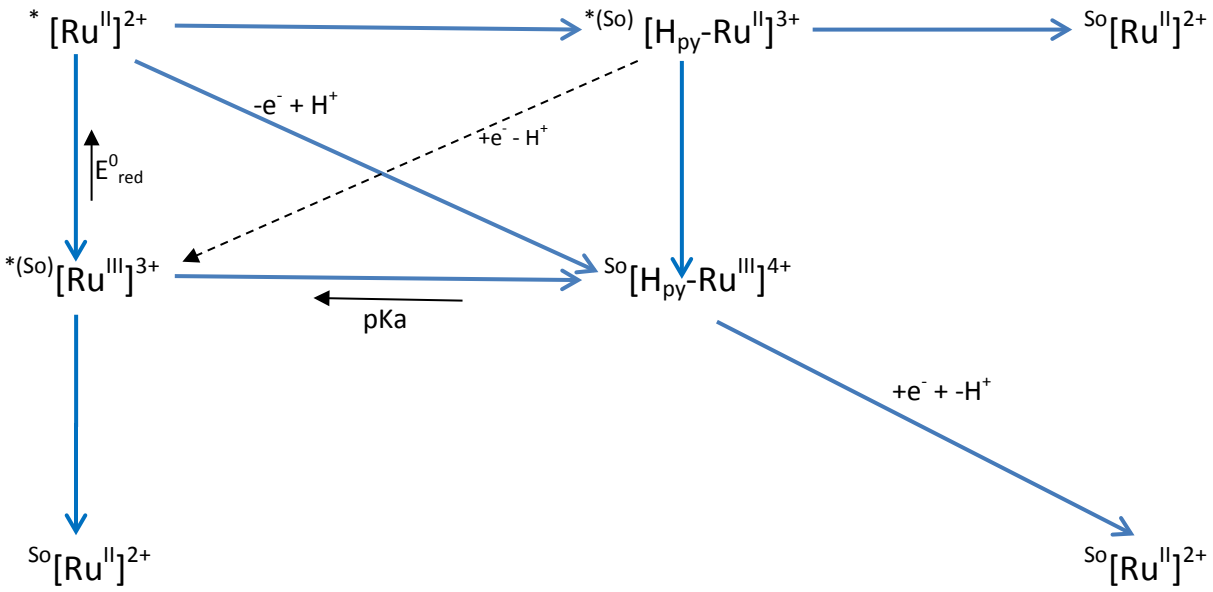

Figure 74. Scheme for electron, proton transfer processes for $[Ru(bpy)_2dpp]^{2+}$ complex and its derivatives.

Data shown in Figs. 74-80 represent reaction free energies, in kcal/mol of the reactions indicated by the arrow. Numbers in parentheses indicate transitions in the ground state. All values can be found in Table XXXVII.

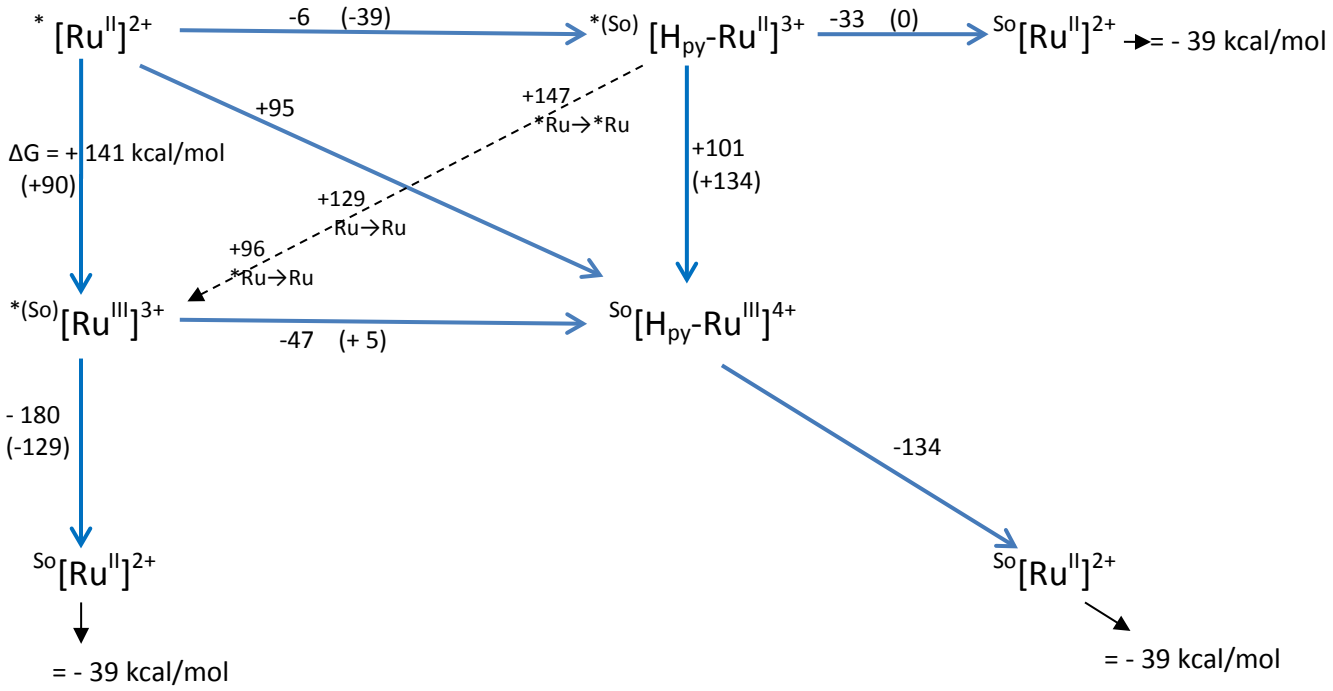

Figure 75. Scheme for all processes in aqueous environment with ruthenium protonated on pyridine site (H_{py}). S_0 notifies the ground state, * excited state. $[H_{py}\text{-}Ru^{3+}]^{4+}$ is in the ground state.

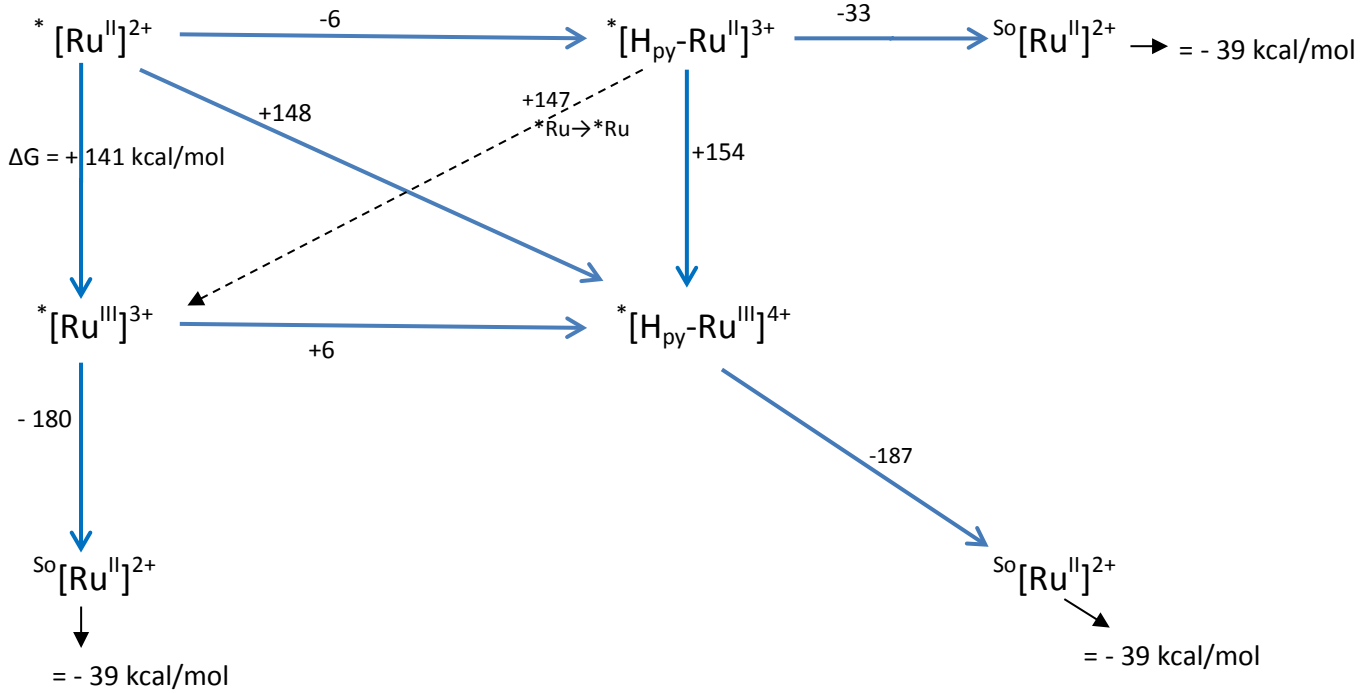

Figure 76. Scheme for all processes in aqueous environment with ruthenium protonated on pyridine site (H_{py}). S_0 notifies the ground state, * excited state. $[H_{py}\text{-}Ru^{3+}]^{4+}$ is in the excited state.

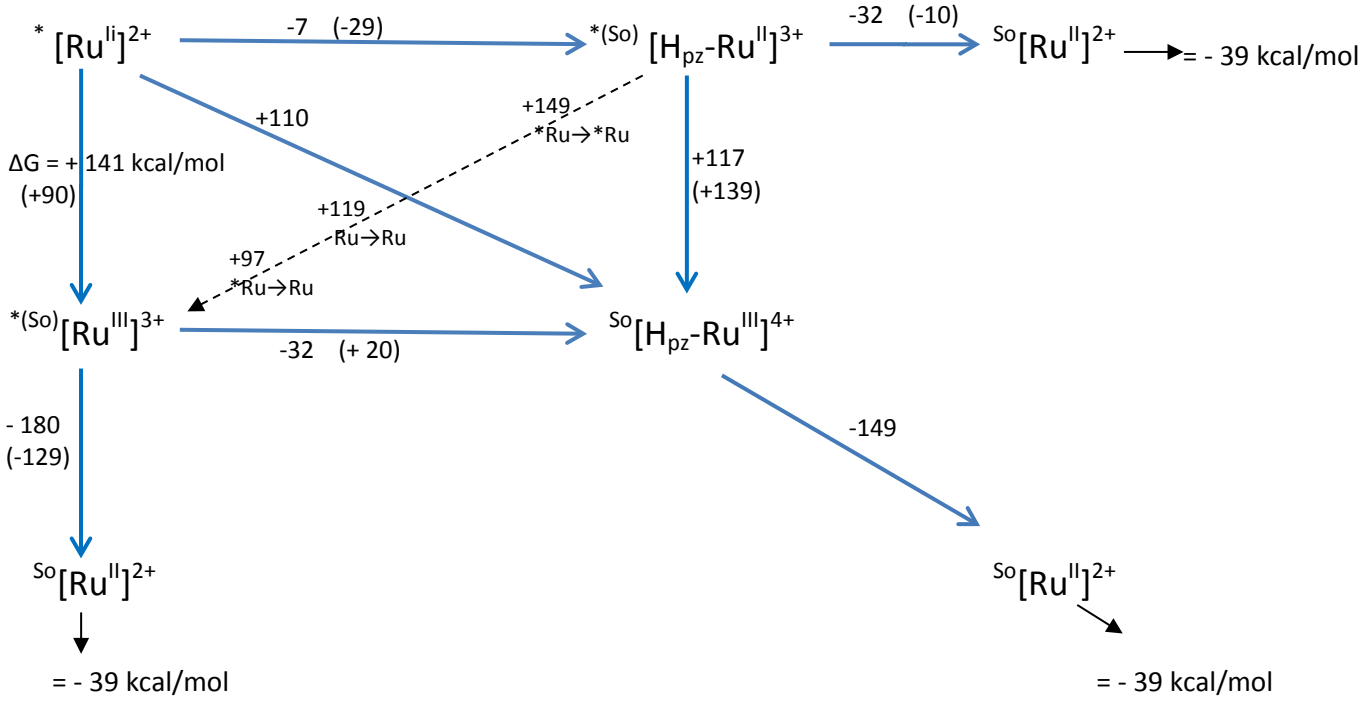

Figure 77. Scheme for all processes in aqueous environment with ruthenium protonated on pyrazine site (H_{pz}). S_0 notifies the ground state, * excited state. $[H_{pz}\text{-}Ru^{3+}]^{4+}$ is in the ground state.

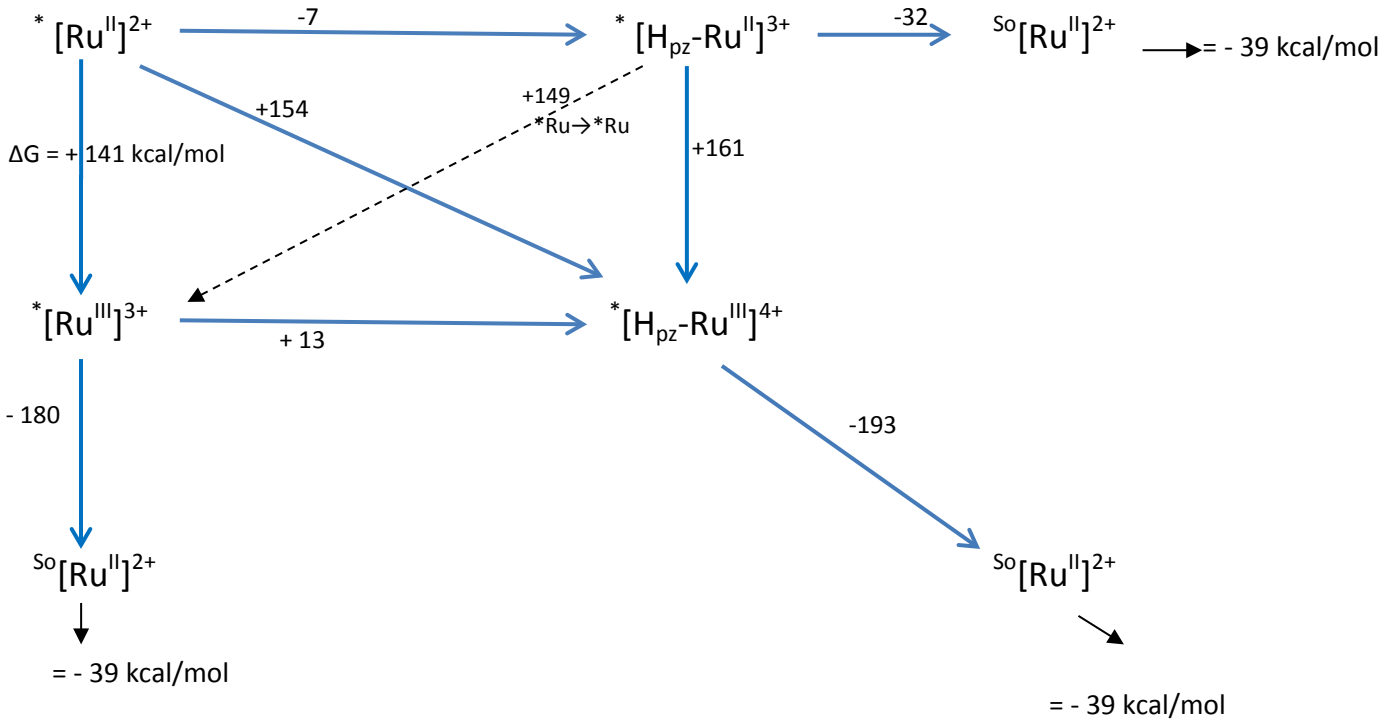

Figure 78. Scheme for all processes in aqueous environment with ruthenium protonated on pyrazine site (H_{pz}). S_0 notifies the ground state, * excited state. $[H_{pz}\text{-}Ru^{3+}]^{4+}$ is in the exited state.

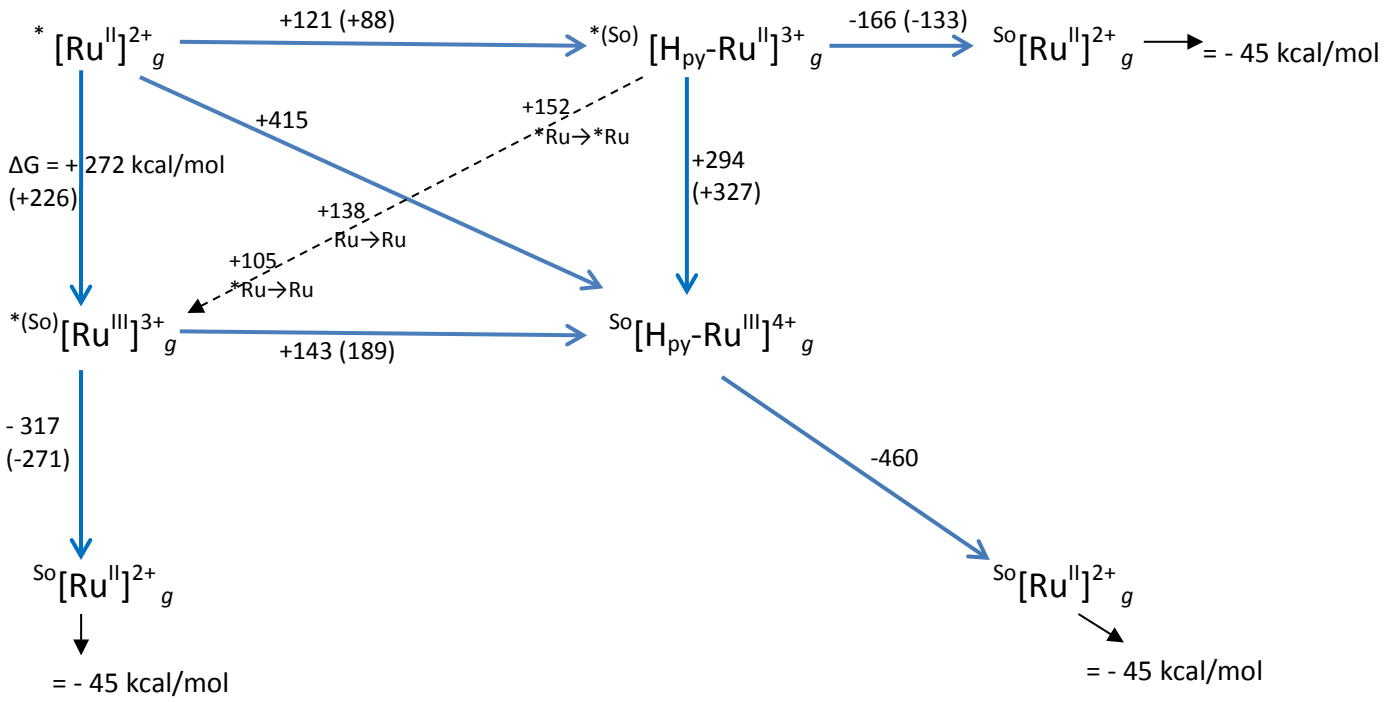

Figure 79. Scheme for all processes in the gas phase with ruthenium protonated on pyridine site (H_{py}).

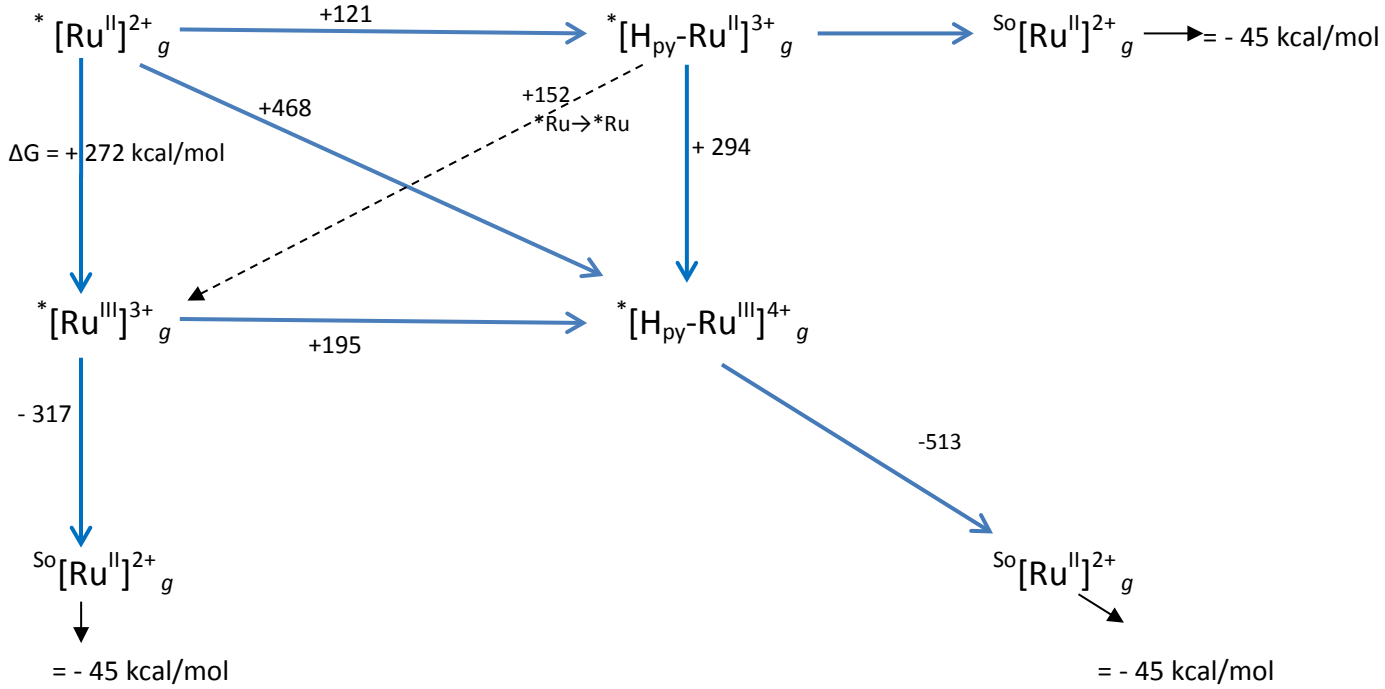

Figure 80. Scheme for all processes in the gas phase with ruthenium protonated on pyridine site (H_{py}).

Free energies of all possible reactions between $[(bpy)_2Rudpp]^{2+}$ are shown, Figs. 75-80. To compare aqueous environment with non-aqueous, Figs. 79-80 provide free energy for reaction in the gas phase. Under those conditions, protonation is no longer favored. We can see that the protonation occurs spontaneously in the aqueous solution. However, these reactions take place at low acidic solution, for $[Hpy\text{-}Ru^{2+}]^{3+} \rightarrow [Ru^{2+}]^{2+} + H^+$ and $[Hpz\text{-}Ru^{2+}]^{3+} \rightarrow [Ru^{2+}]^{2+} + H^+$, $pK_a = 1.12$ (calculated value, 0.2); and $pK_a = -7.2$ (calculated value, - 4.9), respectively, as shown in Table XXXVII. Calculated data are in good agreement with experimental [24, 25] findings. Despite the fact that protonations can easily occur in aqueous solution, such processes are not observed under the condition of this experimental study, where reactions were carried out at higher pH, and no physical evidence of any proton transfer was observed. Also, protonation at the pyrazine sites occurs at very high acidic solution (Hammett's acidity function) [24, 25], which were well reproduced by the DFT study. Thus, the next lowest free energy for the analyzed reaction is the electron transfer, $[*Ru^{II}]^{2+} + e^- \rightarrow [Ru^{II}]^{3+}$, where $\Delta G^0 = 90$ kcal/mol = 0.43 eV and its experimental equivalent is 0.53 eV.

11. Electron Transfer Rates

11.1 Electron Transfer Rate for $[Fe(H_2O)_6]^{2+/3+}$

At the simples level, the electron transfer rate can be related to the activation energy defined by Eyring's equation (Eq. A.1), $k_{eT} = \nu_n e^{(-\Delta G^{\ddagger}/RT)}$. The activation energy is expressed as a sum of three components (Eq. A.2): free energy change due to electrostatic interaction between the reactants $\Delta G_c^{\ddagger}$; free energy change due to distortion of inner sphere of the transition state, $\Delta G_i^{\ddagger}$; free energy change due to solvent rearrangement during the reaction, $\Delta G_o^{\ddagger}$.

The values of electrostatic interactions were calculated according to Eq. A.4 and are presented in the Table XXXVIII below, with the collisional distance expressed as a sum of spherical radii, $r_{12} = r_1 + r_2$ (Fig. 17, Chapter 1).

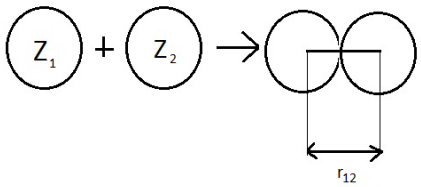

Figure 17, See Chapter 1. The oxidant charge for Z_1, (Fe^{3+}); the reductant charge is Z_2, (Ru^{2+}).

The ionic strength for samples presented in Table XXXVIII was calculated with Eq. 41, including the charge and concentration of both counter ions, PF_6^- and SO_4^{2-}. Thus, the ionic strength in the water solvent varies from 0.004 to 0.1 M^{-1} s^{-1}, whereas in the buffered solution it varies from 0.02 to 0.2 M^{-1} s^{-1}.

Table XXXVIII. Values of $\Delta G_c^{\ddagger}$ (kcal/mol) in water (D=78.5) at 298K, when Z_1Z_2=6, r_{12} varies from 3 to 12 Å, at different ionic strength.

r_{12} =	3	4	5	6	7	8	9	10	11	12	μ [M^{-1} s^{-1}]
	8.44	6.33	5.06	4.22	3.62	3.16	2.81	2.53	2.30	2.11	0
	6.17	4.17	3.01	2.26	1.74	1.37	1.10	0.89	0.73	0.60	0.1
	5.42	3.51	2.42	1.74	1.29	0.97	0.75	0.58	0.45	0.36	0.2
	7.34	5.25	4.01	3.19	2.61	2.18	1.85	1.59	1.38	1.21	0.02
	7.93	5.82	4.56	3.72	3.13	2.68	2.33	2.06	1.83	1.64	0.004

11.1.1 Free Energy of Inner Sphere Reorganization Energy, $\Delta G_i^{\ddagger}$.

The inner sphere reorganizational free energy can be calculated and expressed in two ways [60, 103], as mentioned in Chapter 6. Those values are used as contributions to the activation energy (Table XLI) for self-exchange electron process between aqueous iron species.

11.1.2 Free Energy of Outer Sphere Reorganization Energy, $\Delta G_o^{\ddagger}$.

The outer sphere free energy is due to the solvent reorganization energy λ_o. It is calculated based on Eqs. A.11 and A.12 with coefficient m= -1/2. With the estimated radii of spheres, the outer sphere reorganization energy λ_o and the free energy of outer sphere $\Delta G_o^{\ddagger}$ have been calculated and are presented in Tables XXXIX-XL.

Table XXXIX. Outer sphere reorganization energy λo (kcal/mol) based on Eq A.12, with different values of r (Å).

$r_1\downarrow$ \ $r_2\rightarrow$	2	3	4	5	6	7
2	45.79	39.68	38.16	37.94	38.16	38.52
3		30.53	27.26	25.95	25.44	25.29
4			22.89	20.86	19.84	19.33
5				18.32	16.93	16.13
6					15.26	14.26
7						13.08

Table XL. Free energy of outer sphere, $\Delta G_o^{\ddagger}$ (kcal/mol), based on Table XXXIX.

$r_1\downarrow$ \ $r_2\rightarrow$	2	3	4	5	6	7
2	11.45	9.92	9.54	9.48	9.54	9.63
3		7.63	6.81	6.49	6.36	6.32
4			5.72	5.21	4.96	4.83
5				4.58	4.23	4.03
6					3.82	3.56
7						3.27

With all the values of free energies taken into consideration, the activation energy can be calculated.

Eberson [60] presented the data for self–exchange reaction of $[Fe(H_2O)_6]^{2+/3+}$ as shown below, Eq. 95 and Table XLI.

$$[Fe'(H_2O)_6]^{2+} + [Fe(H_2O)_6]^{3+} \rightarrow [Fe'(H_2O)_6]^{3+} + [Fe(H_2O)_6]^{2+} \quad (95)$$

Table XLI. Calculated values that contributes to total $\Delta G^{\ddagger}$. All values are in kcal/mol for $[Fe(H_2O)_6]^{2+/3+}$.

r_1 [Å]	r_2 [Å]	$\Delta G_c^{\ddagger}$	λ_i	$\Delta G_i^{\ddagger}$	λ_o	$\Delta G_o^{\ddagger}$	$\Delta G^{\ddagger}$	$\Delta G_{obs}^{\ddagger}$	Ref.
3.59	3.43	3.6*	48.4	12.1	26.1	6.5	22.2	14.2	Eberson [60]
							20.8[a] 25[b]	15-20	Kuharski [74]
		$4.1^{\mu=0}$ $3.6^{\mu=0.004}$		**			27.1(23.6 [c]) 26.6(23.1 [c])		
3.15**	3.05**	$3.1^{\mu=0.02}$ $2.2^{\mu=0.1}$ $1.7^{\mu=0.2}$	62.4	15.6***	29.6	7.4	26.1(22.6 [c]) 25.5(22.0 [c]) 24.7(21.2 [c])		This work

*(at μ=0), ** [75, 76] *** [103], c with inner free energy 12.1 not 15.6 kcal/mol; (a) at r_{12} = 5.5Å, (b) at r_{12} = 6.5Å,

Using Eyring's equation (Eq. A.1), the electron transfer rate constant of $[Fe(H_2O)_6]^{2+/3+}$ for self-exchange reaction was calculated, Table XLII.

Table XLII. Summary of electron rate constant, k_{11} for $[Fe(H_2O)_6]^{2+/3+}$

$\Delta G^{\ddagger}$ (kcal/mol)	14.2	22.2	27.1	26.6	26.1	25.5	24.7	21.2
k_{11}	247.2	3.42E-04	8.81E-08	2.05E-07	4.76E-07	1.31E-06	5.05E-06	1.85E-03

11.2 Electron Transfer Rate for $[Ru(bpy)_2dpp]^{2+*/3+}$

As in the case of iron complexes, employing the relations detailed in the Appendix A, electron transfer rate can be calculated for self-exchange electron transfer $[Ru(bpy)_2dpp]^{2+*/3+}$ reaction, where $[Ru(bpy)_2dpp]^{2+}$ is in the excited state, as shown in Eq. 96.

$$*[Ru(bpy)_2dpp]^{2+} + [Ru'(bpy)_2dpp]^{3+} \rightarrow [Ru(bpy)_2dpp]^{3+} + [Ru'(bpy)_2dpp]^{2+} \quad (96)$$

The spherical distances r_1 and r_2 were obtained from optimized aqueous geometry of $[Ru(bpy)_2dpp]^{2+*/3+}$. Distances considered are included in Table XLIII.

Table XLIII. Selected radii in the $[Ru(bpy)_2dpp]^{n+}$ that describe distance from the ruthenium to the peripheral pyridine nitrogen N8, or to the peripheral pyrazine nitrogen N7, (see Fig. 6). The second pair provide radii when the hydrogen in attached to the peripheral pyridine nitrogen N8, or to the peripheral pyrazine nitrogen N7.

Type of bond	r_2 $*[Ru(bpy)_2dpp]^{2+}$	r_1 $[Ru(bpy)_2dpp]^{3+}$	r_2 $[Ru(bpy)_2dpp]^{2+(a)}$
$Ru\text{-}N(8)_{py}$	5.55	5.58	5.60
$Ru\text{-}N(7)_{pz}$	4.85	4.86	4.85
$Ru\text{-}H_{py}$(at pyridine nidrogen)	6.74	6.73	6.69
$Ru\text{-}H_{pz}$(at pyrazine nidrogen)	5.83	5.84	5.77

(a) data for r_2 $[Ru(bpy)_2dpp]^{2+}$ in the ground state, are used in section 11.4 for the back reaction

11.2.1 Electrostatic Free Energy Change

The electrostatic free energy change is obtained with Eq. A.4 and presented in Table XLIV below.

Table XLIV. Values of $\Delta G_c^{\ddagger}$ (kcal/mol) in water (D=78.5) at 298K, when $Z_1Z_2=6$, $r_{12} = r_1 + r_2$; at different ionic strength.

r_{12}	11.13	9.71	13.47	11.67	μ $[M^{-1}\ s^{-1}]$
	2.27	2.61	1.88	2.17	0
	0.71	0.95	0.46	0.64	0.1
	0.44	0.62	0.26	0.39	0.2
	1.35	1.66	1.00	1.26	0.002
	1.80	2.13	1.42	1.70	0.004

11.2 2 Free Energy of Inner Sphere Reorganization Energy, $\Delta G_i^{\ddagger}$.

As described in Ref. [103], the inner sphere reorganization energy for $[Ru(bpy)_2dpp]^{2+*/3+}$ was estimated. See section 6.4.2.1.

$$\Delta G_i = \Delta G[Ru^{3+}]_i = G[Ru^{3+}]_{opt} - G[*Ru^{3+}]_{\text{at the geom. for } *Ru^{2+}} \quad (97)$$

$$\Delta G_i = \Delta G[*Ru^{2+}]_i = G[*Ru^{2+}]_{opt} - G[*Ru^{2+}]_{\text{at the geom. for } Ru^{3+}} \quad (98)$$

$$\Delta G[total]_i = \Delta G[Ru^{3+}]_i + \Delta G[*Ru^{2+}]_i = 5.76 + 1.94 = 7.70 \text{ kcal/mol} \quad (99)$$

Table XLV. Inner sphere reorganization energy for $[Ru(bpy)_2dpp]^{2+/3+ \text{ (low spin states)}}$.

$[Ru((bpy)_2dpp]^{n+}$	ΔG_i (kcal/mol)	Ru-N bond (Å)
*n=2+	1.94	2.105
n=3+	5.76	2.111

* Ru^{2+} is in triplet state

11.2.3 Free Energy of Outer Sphere Reorganization Energy, $\Delta G_o^{\ddagger}$.

The calculation of solvent reorganizational energy can be made in two different ways. First, a simple approach is calculating the free energy at equilibrium in the gas phase and water, with a single point calculation in water. Data and procedures are presented in Fig. 81 and Table XLVI. The resulting value is comparable to $\Delta G_o^{\ddagger} = \lambda / 4 \approx 2.3$ kcal/mol [36].

Table XLVI. Reorganization energy due to the solvent.

ΔG (kcal/mol)	ΔG (equilibrium) (b)-(a)=(d)	ΔG (non-equilibrium) (c)-(a)=(e)	ΔG_0 (d)-(e)
$*Ru^{2+}$	-120.66	-119.714	0.946
Ru^{3+}	-256.677	-255.383	1.294

$$\Delta G[total]_o = \Delta G[Ru^{3+}]_o + \Delta G[*Ru^{2+}]_o = 1.294 + 0.946 = 2.24 \text{ kcal/mol} \quad (100)$$

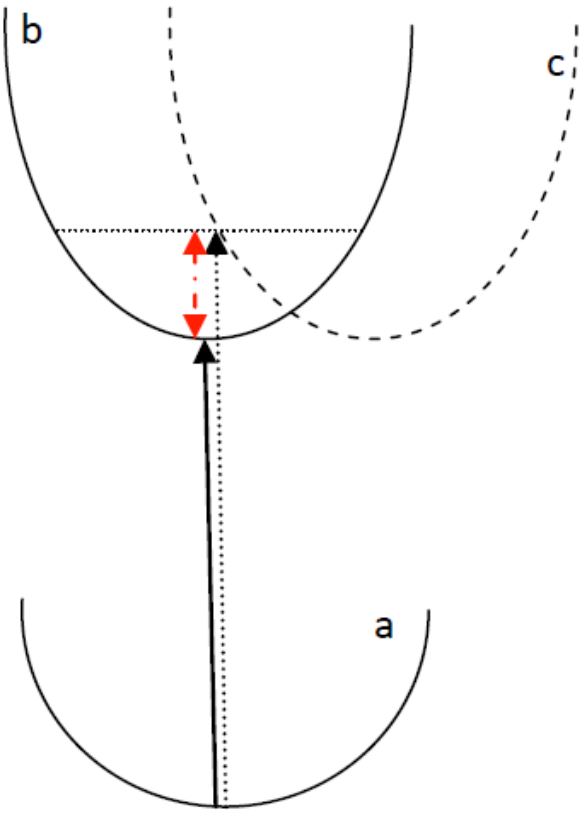

Figure 81. Graphic representation of outer reorganization energy. (a) Represents free energy of optimized structure in the gas phase; (b) Represents the free energy of optimized structure in the solvent; (c) is single point calculation in the solvent on the optimized structure in the gas phase. Thus, solid arrow can represents the difference of free energy, in the equilibrium, of the gas phase and solvent, dotted arrow is assigned to non-equilibrium solvation process. Solvent reorganization energy, presented as small red arrow, is the difference between two black arrows.

The second and more advanced approach involves consideration of outer sphere reorganization energy as a function of radii (r_1, r_2). The results are presented in Table XLVII-XLVIII.

Table XLVII. Outer sphere reorganization energy λo (kcal/mol) based on (A.12), with different values of r (Å).

r_1↓ \ r_2→	5.58	4.86	6.73	5.84
5.55	16.46	17.75	15.19	16.10
4.85		18.86	16.67	17.43
6.74			13.60	14.71
5.83				15.68

Table XLVIII. Free energy of outer sphere, $\Delta G_o^{\ddagger}$ (kcal/mol), based on Table XXXIX.

r_1↓ \ r_2→	5.58	4.86	6.73	5.84
5.55	4.12	4.44	3.80	4.03
4.85		4.71	4.17	4.36
6.74			3.40	3.68
5.83				3.92

Table XLIX. Calculated values that contribute to total $\Delta G^{\ddagger}$ for $[Ru(bpy)_2dpp]^{2+*/3+}$. All values ΔG and λ are in kcal/mol.

r_1 [Å]	r_2 [Å]	$\Delta G_c^{\ddagger}$	λ_i	$\Delta G_i^{\ddagger}$	λ_o	$\Delta G_o^{\ddagger}$	$\Delta G^{\ddagger}$
5.55	5.58	$2.27^{\mu=0}$	30.8	7.70	16.46 (8.98*)	4.12 (2.24*)	14.09 (12.21*)
		$0.44^{\mu=0.2}$					12.26 (10.38*)
4.85	4.86	$2.61^{\mu=0}$			18.88	4.71	15.05 (12.55*)
		$0.62^{\mu=0.2}$					13.03 (10.56*)
6.74	6.73	$1.88^{\mu=0}$			13.60	3.40	12.98 (11.82*)
		$0.26^{\mu=0.2}$					11.36 (10.20*)
5.83	5.84	$2.17^{\mu=0}$			15.68	3.92	13.79 (12.11*)
		$0.20^{\mu=0.2}$					11.82 (10.14*)

* from my equilibrium calculation (**Table XLVI**).

Table XLIX presents the total activation energy calculated with Eq. A.2. The resulting electron self-exchange rate constant for ruthenium calculated by Erying equation (Eq. A.1) are presented in Table L.

Table L. Summary of self-exchange electron rate constant k'_{22} for $[Ru(bpy)_2dpp]^{2+*/3+}$ in the excited state for selected $\Delta G^{\ddagger}$(kcal/mol).

$\Delta G^{\ddagger}$	14.09	10.38	15.05	10.56	12.98	10.20	13.79	10.14
k'_{22}	2.97E+01	2.53E+05	5.89E+01	1.14E+05	1.93E+03	2.1E+05	4.93E+02	2.32E+05

11.3 Marcus Cross –Relation

Marcus theory is based on the assumption of weak electronic coupling between reactants. The self-exchange electron transfer rate of two reactants can be combined together within Marcus cross-relation, and the electron transfer (ET) rate between two different reactants can be estimate (Appendix B).

The free energy for excited state electron transfer between $*[Ru(bpy)_2dpp]^{2+}$ and Fe^{3+}_{aq} (see Eq. 45) producing $[Ru(bpy)_2dpp]^{3+}$ and Fe^{2+}_{aq} is ΔG^o = -33.8 kcal/mol according to the electrochemical measurements, $\Delta G^o = -nFE^o_{rxn}$. (see Table II).

With the values of self-exchange reactions presented in two previous sections, k_{11}=3.3 $M^{-1}s^{-1}$ and k'_{22} = 2.32 x 10^5 $M^{-1}s^{-1}$, for iron and ruthenium, and the selected total reorganization energy of ruthenium and iron (Tables XLI and XLIX) λ_{12} is equal to 121.8 kcal/mol as a sum of 47.3 and 74.5 kcal/mol; the value of f = 1.36 x 10^{-7} can be obtained from Eq. B.7. The resulting equilibrium constant K_{12} is equal to 2.52 x 10^{39} (from Eq. B.8) and the electron transfer rate k'_{12} is 6.20 x 10^{12} $M^{-1}s^{-1}$ (Eq. B.4) for excited state electron transfer between iron and ruthenium.

On the other hand, by using different approach with the same values of k_{11} and k_{22}, but with $K_{12}=\exp(-\Delta G^0_{12}/RT)$ = 7.74 x 10^{24}, the estimate of k'_{12}= 8.98 x 10^{11} $M^{-1}s^{-1}$ (when f is calculated with Eq. B.6), or k'_{12} = 2.43 x 10^{15} $M^{-1}s^{-1}$ (with the assumption of f = 1) can be obtained. Results for other possible values are presented in Table XXXIV below.

Table LI. Elestimates of excited state electron trasfer k'_{12} using different assumptions.

k_{11}	k'_{22}	$\log(K_{12})$	K_{12}[a]	$\log(f)$	f [b]	k'_{12}	k'_{12} when f=1
3.3[e]	2.32E+05	3.94E+01	2.52E+39	-1.97E+01	1.99E-20	6.20E+12	4.39E+22
			7.74E+24[c]		1.36E-07[d]	8.98E+11	2.43E+15
247.2	2.32E+05	3.57E+01	4.49E+35	-1.78E+01	1.49E-18	6.20E+12	5.08E+21
			7.74E+24 [c]		1.36E-07 [d]	8.67E+12	2.11E+16
1.05E-07	2.32E+05	5.38E+01	6.53E+53	-2.69E+01	1.24E-27	6.20E+12	1.60E+00
			7.74E+24 [c]		1.36E-07 [d]	2.50E+08	6.07E+11
3.3	5.89E+01	4.66E+01	3.91E+46	-2.33E+01	5.06E-24	6.20E+12	2.76E+24
			7.74E+24 [c]		1.36E-07 [d]	1.43E+10	3.88E+13

[a] calculated from Eq. B.8, depends on values of k_{11} and k_{22}. [b] calculated from Eq. B.6, depends on values of k_{11} and k_{22}. [c] calculated from Eq. B.5, fixed value, depends on reaction free energy. [d] calculated from Eq. B.7, fixed value, depends on reaction free energy. [e] experimental electron transfer rate.

Theoretical overestimation of k'_{12} is plausible (when f = 1 is assumed) due to change in multiplicity, substantial changes in λ_i, and the formation of bimolecular intermediates.

For photoexcited electron transfer reaction, inverted region is often observed due to highly exogernic reaction (see Figs. B.1 and C.2). Inverted region in the quenching of ruthenium(II) polypyridine complexes have been found by Creutz and Sutin [118] and Berkoff et al. [94]. According to Marcus theory, $\log(k_{et})$ is parabolic with respect to ΔG^0 and is maximum at $\Delta G^0 = -\lambda$. Thus, in order to calculate the activation free energy, the reorganizational energy λ must be obtained, from which the normal and inverted regions can be defined (see Fig. B.1). Since $-\Delta G^o_{12}$ for the reaction btween $[*Ru(bpy)_2dpp]^{2+}$ and $[Fe(H_2O)_6]^{3+}$ is ~ 34 kcal/mol, the condition for inverted region is not fulfilled (Fig. B.1) due to high reorganizational energy requirement. Thus, the reaction does not appear to be in the inverted region. This situation is supported by the following hypothetical situation. Using the experimental value, $k_{11} = 3.3\ M^{-1}s^{-1}$

(self-exchange reaction for iron) and calculated value k'_{22} = 2.32 x 10^5 $M^{-1}s^{-1}$ (self-exchange reaction for $[Ru(bpy)_2dpp]^{2+*/3+}$), the equilibrium constant K_{12} (Eq. B.14) for inverted region can be calculated to be 1.52 x 10^{39} and f = 1.19 x 10^{-5} (Eq. B.7). These results in the electron transfer rate k'_{12} equals to 1.39 x 10^{20} $M^{-1}s^{-1}$, which is unphysically large (see Table LII).

Table LII. The hypothetical electron transfer rate for $[*Ru(bpy)_2dpp]^{2+}$ and $[Fe(H_2O)_6]^{3+}$ assuming inverted region.

k_{11}	k_{22}	k'_{12}
3.3	2.32 x 10^5	1.51 x 10^{20}
277.2	2.32 x 10^5	2.88 x 10^{19}
2.05 x 10^{-7}	4.93x 10^2	7.67 x 10^{23}

On the other hand, the self-exchange reaction $[Ru(bpy)2dpp]^{2+*/3+}$ appears to be in the inverted region (ΔG_{11}^o = -39 kcal/mol and $\lambda_{tot} = \lambda_i + \lambda_o$ = 34.92 kcal/mol). The data for reaction between $[Ru(bpy)2dpp]^{2+*}$ and Fe^{3+}_{aq} (see Eq. 45) suggests that $-\Delta G^o_{12} < \lambda_{12,}$ (ΔG_{12}^o = -34 kcal/mol and $\lambda_{tot} = \lambda_{Ru} + \lambda_{Fe}$ varies between 110-127 kcal/mol), which implies that the reaction is in the normal region despite the fact that the reactant is in the excited state. Marcus theory can overestimate the electron transfer rate in the inverted region due to a couple of reasons. The exothermic process usually occurs at a large distances $r = r_D + r_A + r_{extra\ distance}$ beyond the collision model. Collision distance implies smaller values of r, which in turn means larger λ and activation energy and smaller k_{et}. On the contrary, for large value of r, the probability of electron transfer is $\kappa << 1$ making the reaction more nonadiabatic.

11.4 Electron Transfer Rate for $[Ru(bpy)dpp]^{2+/3+}$ and the Back Reaction

Experimental efficiency of excited state electron transfer is low. The quantum yield of the formation of Fe^{2+} was determined as 1.25 $x10^{-5}$ number of molecules per quanta, which is about 3.03% of produced concentration of $[Fe^{2+}]$ with respect to the used concentration of $[Fe^{3+}]$. Self-exchange reaction of $[Ru(bpy)_2dpp]^{2+/3+}$ in the ground state allows to compare the rate of this reaction and the rate of self-exchange reaction of $[Ru(bpy)_2dpp]^{2+*/3+}$ in the excited state. The polypyridine complexes can accept or donate electron. Their ground state and excited state electron transfer with Ru(II)/Ru(III) involve $(t_{2g})^6(e_g)^0$ / $(t_{2g})^5(e_g)^0$ orbitals, respectively. For those metal complexes with low spin t_{2g}^6/t_{2g}^5 electronic structure, the metal-ligand bond length does not differ much, so the inner sphere reorganization energy is not expected to be different significantly, and the self-exchange reaction rate is expected to be similar [36, 64, 118].

$$[Ru(bpy)_2dpp]^{2+} + [Ru'(bpy)_2dpp]^{3+} \rightarrow [Ru(bpy)_2dpp]^{3+} + [Ru'(bpy)_2dpp]^{2+} \qquad (101)$$

The spherical radii considered for an aqueous $[Ru(bpy)_2dpp]^{2+}$ in the ground state is 5.60 Å or 6.69 Å, instead of 5.50 and 6.74 Å, respectively (Table XLIII). By using the radii of $[Ru(bpy)_2dpp]^{2+}$ and $[Ru(bpy)_2dpp]^{3+}$, the Coulombic and outer sphere reorganization free energies were recalculated by Eqs. A.4 and A.12. The inner sphere reorganization energy was recalculated for $[Ru(bpy)_2dpp]^{2+/3+}$ using Eqs. 97 - 99 and is equal to 7.44 kcal/mol.

Table LIII. Calculated values that contribute to total $\Delta G^{\ddagger}$ for $[Ru(bpy)_2dpp]^{2+/3+}$. All values ΔG and λ are in kcal/mol.

r_1 [Å]	r_2 [Å]	$\Delta G_c^{\ddagger}$	λ_i	$\Delta G_i^{\ddagger}$	λ_o	$\Delta G_o^{\ddagger}$	$\Delta G^{\ddagger}$
5.60	5.58	$2.26^{\mu=0}$	29.8	7.44	16.38	4.10 (20.2)	13.09
		$0.44^{\mu=0.2}$					11.98
4.85	4.86	$2.61^{\mu=0}$			18.86	4.72	14.77
		$0.62^{\mu=0.2}$					12.78
6.69	6.73	$1.89^{\mu=0}$			13.65	3.41	12.74
		$0.26^{\mu=0.2}$					11.11
5.77	5.84	$2.18^{\mu=0}$			15.77	3.94	13.56
		$0.39^{\mu=0.2}$					11.77

The activation energy for the ground state electron transfer for $[Ru(bpy)_2dpp]^{2+/3+}$ is in the range og $\Delta G^{\ddagger}_{tot}$ ~ 11.11-14.77 kcal/mol, including all three of Columbic, inner sphere reorganization and outer sphere reorganization energies. Thus, the self-exchange electron transfer rate for the ground state of $[Ru(bpy)_2dpp]^{2+/3+}$ is in the range of $k_{22} = 4.53 \times 10^4 – 9.45 \times 10^1$ M^{-1} s^{-1}. The self-exchange electron transfer rate in the excited state, under the same conditions ($\Delta G^{\ddagger}_{tot}$ ~ 11.36 -15.05 kcal/mol), is in range of $k'_{22} = 2.97 \times 10^4 – 5.89 \times 10^1$ M^{-1} s^{-1}, Table XLIX.

Thus, according to the Marcus cross-relation, the relative rates for reaction of Eq. 45 and its back electron transfer (Eq. 102)

$$[Ru(bpy)_2dpp]^{3+} + Fe^{2+} \rightarrow [Ru(bpy)_2dpp]^{2+} + Fe^{3+} \qquad (102)$$

are $k'_{12} = 3.21 \times 10^{11} – 1.43 \times 10^{10}$ $M^{-1}s^{-1}$ (Eq. 45) and $k_{21} = 3.97 \times 10^{11}$ - 1.81×10^{10} $M^{-1}s^{-1}$ (Eq. 102), respectively. The value of $k_{11} = 3.3$ M^{-1} s^{-1} for experimental electron transfer rate of $[Fe(H_2O)_6]^{2+/3+}$ was used. The ratio of rates (45) to (102) shows that the back reaction to the ground state (Eq. 102) is about 20% faster than the forward reaction.

11.5 Summary

The data reported in this chapter were used to calculate cross-reaction rates according to Marcus theory, involving *$[Ru(bpy)_2dpp]^{2+}$ + $[Fe(H_2O)_6]^{3+}$ complexes.

The focus has been on the analysis of the activation energy and its effect on self-exchange electron transfer rate constant. Calculated self-exchange rate constant for $Fe^{2+/3+}$ are slightly different from experimental value of $k_{11} = 3.3 – 4\ M^{-1}s^{-1}$. Calculated self-exchange rate constant for $[Ru(bpy)_2dpp]^{*2+/3+}$ are close to experimental value, but smaller in its magnitude. This is probably due to possible errors in the terms included in the activation free energy. Thomas Meyer group [36] assumed $\Delta G_c^{\ddagger}$ to be zero and no geometry change in large inorganic molecules which corresponds to $\Delta G_i^{\ddagger} = 0$. Thus, only the outer sphere reorganization energy was defined as an activation barrier for electron transfer. All the contributions were included in this research, (Eq. A.2) which results in increase in the height of the activation barrier and slower rate constant for $Ru^{*2+/3+}$.

Overall, Marcus theory reasonably reproduces the experimental electron rate constant k'_{12} for the following key reaction:

$$[Ru(bpy)2dpp]^{2+*} + Fe^{3+}_{aq} \rightarrow [Ru(bpy)_2dpp]^{3+} + Fe^{2+}_{aq}.$$

The condition of $-\Delta G^{o}_{12} > \lambda_{12}$ for the inverted region is not observed in this particular reaction. In addition, the assumption of $f = 1$ may not be reliable here due to different multiplicity of the reactants.

12. Final Conclusions

The purpose of this research was to establish the products of the reaction between Fe^{3+}_{aq} and an excited state $[Ru(bpy)_2dpp]^{2+}$. By trapping experiments, the product of the electron transfer has been identified and quantified by calculating the quantum yield of the Fe(II) formation. Based on a previous study on protonated $[Ru(bpy)_2dppH]^{3+}$ and detailed consideration of experimental condition in this research, it is concluded that protonated species of $[Ru(bpy)_2dppH]^{3+}$ are not observed during the excited electron transfer process between $[Ru(bpy)_2dpp]^{2+}$ and Fe^{3+}_{aq}. The electron transfer rate has been obtained based on reasonable assumptions and models (Stern-Volmer equation, diffusion equation).

In the second part the thesis, the spectroscopic properties of $[Ru(bpy)_2dpp]^{2+/3+}$ and $[Ru(bpy)_3]^{2+/3+}$ complexes have been analyzed. With the help of DFT calculation, $[Ru(bpy)_2dpp]^{3+}$ with the LMCT transition can be identified in the 600-800 nm range, although the experimental absorption peak is very weak. The possibility of PCET reaction has been tested by determining the energetics of all possible reactions including the $[Ru^{(II/III)}(bpy)_2dppH]^{3+/4+}$ species in the gas phase and aqueous solution. Calculated redox potentials and pKa's are in very good agreement with the available experimental data and allowed to rule out the proton transfer and concerted PCET mechanism. Finally, Marcus theory has been used to calculate the excited electron transfer rate and has been shown to successfully reproduce experimental values.

.

Appendix A: Aspects of Electron Transfer and Activation Energy

Given that electronic coupling between the donor and the acceptor is weak, the electron transfer can be viewed as a simple barrier crossing over the non- adiabatic free energy surface, Figure 16. Within the transition state theory, the rate can be expressed as

$$k_{eT} = \nu_n e^{(-\Delta G^{\ddagger}/RT)} \tag{A.1.a}$$

where ν_n is the nuclear frequency of the charge-transfer complex. At the simplest level, it can be expressed as $\nu_n = k_BT/h = 6.2 \times 10^{12}\ s^{-1}$, with values of $k_BT = 0.592$ kcal/mol and Planck's constant, $h = 9.54 \times 10^{-14}$(kcal/mol)·s.

The non-adiabatic Marcus theory (Eq. A.1.b) assumes a weak coupling between two reactants, with the probability $0 < \kappa < 1$ of reactants being converted to products. The collision frequency Z, describes an effective frequency of the encounter complex between the reactants. Its value can vary on the environment (~ $10^{13}\ M^{-1}s^{-1}$ in the gas phase) and the charge of reacting species (~ 10^{11}-$10^{12}\ M^{-1}s^{-1}$ for two uncharged reactants in the solution).

$$k = \kappa Z e^{(-\Delta G^{\ddagger}/RT)} \tag{A.1.b}$$

A.1 Activation Energy, ΔG‡.

The transition state energy used in Eq. A.1 can be defined as

$$\Delta \boldsymbol{G}^{\ddagger} = \Delta \boldsymbol{G}_{\boldsymbol{c}}^{\ddagger} + \Delta \boldsymbol{G}_{\boldsymbol{i}}^{\ddagger} + \Delta \boldsymbol{G}_{\boldsymbol{o}}^{\ddagger} \tag{A.2}$$

where each component can be described as follows:

- Free energy change due to electrostatic interaction between the reactants, $\Delta G_c^{\ddagger}$
- Free energy change due to distortion of inner sphere of the transition state, $\Delta G_i^{\ddagger}$
- Free energy change due to solvent rearrangement during the reaction, $\Delta G_o^{\ddagger}$.

A.1.1 Electrostatic Free Energy Change, $\Delta G_c^{\ddagger}$.

The electrostatic free energy change is defined as the work required to bring reactant at the close distance and can be expressed as [60]

$$\Delta G_c^{\ddagger} = \frac{Z_1 Z_2 e^2}{\varepsilon r_{12}} \exp\left(-r_{12}\left[\frac{8\pi e^2 N_A \mu}{1000 k_B \varepsilon T}\right]^{1/2}\right) \quad \text{(A.3)}$$

where Z_1 and Z_2 are the charges of the reactants, e is the electronic charge, r_{12} is the distance between the reactants (Fig. 17), ε dielectric constant, N_A Avogadro number, μ ionic strength, k_B Boltzmann constant, and T the absolute temperature.

This equation (A.3) can be reduced to [60]:

$$\Delta G_c^{\ddagger} = \frac{331.3\, Z_1 Z_2}{\varepsilon r_{12}}\, 10^{-(21.9 r_{12}\sqrt{\mu/DT})} \quad \text{(A.4)}$$

For μ = 0, with collision distance r_{12} in angstroms, the electrostatic free energy change can be presented as (in kcal/mol)

$$\Delta G_c^{\ddagger} = \frac{331.3\, Z_1 Z_2}{\varepsilon r_{12}} \quad \text{(A.5)}$$

Typical values for the free energy of electrostatic change in water (dielectric constant, ε =78.5) are presented in section 11.1.

A.1.2 Free Energy Inner Sphere Reorganization Energy, $\Delta G_i^{\ddagger}$.

The inner sphere reorganizational energy can be assumed mostly from structural change of complexes. The free energy of inner sphere, $\Delta G_i^{\ddagger}$, a function of inner sphere reorganization energy λ_i, is expressed as

$$\Delta G_i^{\ddagger} = m^2 \lambda_i \,, \quad \text{(A.6)}$$

$$m = -\frac{1}{2} - \frac{\Delta G^{o\prime}}{2\lambda} \,, \quad \text{(A.7)}$$

$$\Delta G^{o\prime} = \Delta G^{o} + (Z_1 - Z_2 - 1)\frac{e^2}{\varepsilon r_{12}}, \quad \text{(A.8)}$$

$$\Delta G^{o\prime} = \Delta G^{o} + w. \quad \text{(A.9)}$$

Often, $\Delta G^{o\prime}$ is described as the sum of standard free energy and work (an electrostatic term that brings two charge species together down to the distance r_{12} in the specific solvent with dielectric constant ε, Eq. A.9. Corrected $\Delta G^{o\prime}$ is a free energy difference between precursor and successor. Z_1 is the charge of the electron acceptor, and Z_2 is the charge of electron donor. In research presented in this thesis Z_1-Z_2 = 1, and all work term is cancelled. This means that free energy of precursor and successor does not differ from separated products and reactants.

$$A^n + B^{n+1} \overset{fast}{\Longleftrightarrow} [A^n, B^{n+1}] \overset{k_{et}}{\Leftrightarrow} [A^{n+1}, B^n] \overset{fast}{\Longleftrightarrow} A^{n+1} + B^n$$

reactants ↔ precursor ↔ successor ↔ products

Scheme A.1. Debye-Smoluchowski model

For self-exchange reaction, net free energy of reaction is equal to zero, $\Delta G^{o} = 0$, ($Z_1 - Z_2 - 1 = 0$), and coefficient m is equal to - ½. Thus, the free energy of inner sphere reorganization energy is express as

$$\Delta G_i^{\ddagger} = \frac{\lambda_i}{4} \quad \text{(A.10)}$$

The corrected $\Delta G^{o\prime}$ for reaction analyzed in this thesis, between $*[Ru(bpy)_2dpp]^{2+}$ and Fe^{3+}_{aq} (see Eq. 45) is equal to ΔG^{o} = -33.8 kcal/mol and is obtained from the electrochemical measurement of $\Delta G^{o} = -nFE^{o}_{rxn}$.

A.1.3 Free Energy of Outer Sphere Reorganization Energy, $\Delta G_o^{\ddagger}$.

The outer sphere free energy is due to the solvent reorganization energy λ_o and can be expressed as:

$$\Delta G_o^{\ddagger} = m^2 \lambda_o \tag{A.11}$$

$$\lambda_o = e^2 \left(\frac{1}{2r_1} + \frac{1}{2r_2} - \frac{1}{r_{12}}\right)\left(\frac{1}{\varepsilon_n} - \frac{1}{\varepsilon}\right) \tag{A.12}$$

where e is charge of the electron, r_1, r_2 are the spherical radii of the donor and acceptor, with $r_{12} = r_1 + r_2$ (Fig. 17) $\varepsilon_n = n^2$ corresponds to the optical dielectric constant of the solvent, n is the refractive index of the solvent, for water n = 1.33; ε is the static dielectric constant of the solvent. For water, ε = 78.5. For self-exchange electron transfer reaction, Eq. A.12 reduces to:

$$\boldsymbol{\lambda_o = e^2 \left(\frac{1}{2r}\right)\left(\frac{1}{\varepsilon_n} - \frac{1}{\varepsilon}\right)} \tag{A.13}$$

where $2r = r_1 = r_2$.

Thus, collecting all contributions to the transition state, we can derive the expression for the total activation free energy (Eq. A.2), $\Delta G^{\ddagger} = \Delta G_c^{\ddagger} + \Delta G_i^{\ddagger} + \Delta G_o^{\ddagger}$, as follows (assuming ionic strength is zero):

$$\Delta G^{\ddagger} = \frac{Z_1 Z_2 e^2}{\varepsilon r_{12}} + m^2\lambda_i + m^2\lambda_o \tag{A.14}$$

$$\Delta G^{\ddagger} = \frac{Z_1 Z_2 e^2}{\varepsilon r_{12}} + m^2\lambda \tag{A.15}$$

where total reorganization energy $\lambda = \lambda_i + \lambda_o$ is the sum of inner and outer sphere reorganization energies, and the coefficient m is defined by Eq. A.7. This leads to Eqs. A.16 and A.17.

$$\Delta G^{\ddagger} = \frac{Z_1 Z_2 e^2}{\varepsilon r_{12}} + \lambda \left[\frac{1}{4}\left(1 + \frac{2\Delta G^{o\prime}}{\lambda} + \frac{\Delta G^{o\prime}}{\lambda}\right)\right] \quad \text{(A.16)}$$

$$\Delta G^{\ddagger} = \frac{Z_1 Z_2 e^2}{\varepsilon r_{12}} + \frac{\lambda}{4}\left(1 + \frac{\Delta G^{o\prime}}{\lambda}\right)^2 \quad \text{(A.17)}$$

The last form of Eq. A.17 can be found in any physical chemistry textbooks, and can be simplified further for uncharged species to

$$\Delta G^{\ddagger} = \frac{\lambda}{4}\left(1 + \frac{\Delta G^{o\prime}}{\lambda}\right)^2 \quad \text{(A.18)}$$

For the self-exchange electron transfer reaction in the ground electronic state reaction investigated in this study can be estimated as $\Delta G^{o\prime} = \Delta G^{o} = 0$. Thus, above equation can be simplified to $4\Delta G^{\ddagger} = \lambda$. On the other hand, the activation energy for two different, positively charged reactatnts are calculated by Eq. A.17.

Appendix B: Marcus Cross Relations

In many cases, Marcus theory is used for cross-redox reactions (reactions that resulting in a net chemical change). Two self-exchange reactions can be combined together and result in non-bonded electron transfer between two different reactants A and B, as described below.

$$A^{n+1} + A'^{n} \overset{k_{11}}{\leftrightarrow} A^{n} + A'^{n+1} \tag{B.1}$$

$$B^{n+1} + B'^{n} \overset{k_{22}}{\leftrightarrow} B^{n} + B'^{n+1} \tag{B.2}$$

$$A^{n+1} + B'^{n} \overset{k_{12}}{\leftrightarrow} A^{n} + B'^{n+1} \tag{B.3}$$

$$k_{12} = (k_{11}k_{22}K_{12}f)^{1/2} \tag{B.4}$$

$$K_{12} = \exp(-\frac{\Delta G_{12}^{0}}{RT}) \tag{B.5}$$

where k_{11} and k_{22} are rate constants for self-exchange redox reactions (Eq. B.1-2), k_{12} is the rate constant of the cross electron transfer reaction (Eq B.2), and $k_{12} \sim [A^{n+1}][B'^{n}]$. An equilibrium constant of the cross electron transfer reaction, $K_{12,}$ is defined by Eq. B.5.

The f constant can expressed as Eq B.6 as previously reported [36, 94, 95][6]

$$\log f = \frac{(\log K_{12})^2}{4\log\left(\frac{k_{11}k_{22}}{\xi^2}\right)} \tag{B.6}$$

with $\xi \sim 6.2\text{x}10^{12}$ $M^{-1}s^{-1}$ of collision frequency. It can be rewritten in terms of free energy as follows

$$\log f = -\frac{1}{2.303RT}\frac{\left(\Delta G_{12}^{o\prime}\right)^2}{(\lambda_{11}+\lambda_{22})} \tag{B.7}$$

[6] Some papers use log(f) [36, 94], while the other one uses ln(f) [95].

Also, K_{12} is sometimes presented as:

$$\log K_{12} = 2log\left(\frac{\xi^2}{k_{11}k_{22}}\right) \tag{B.8}$$

Following Marcus' assumption of a single universal value for the collision frequencies ξ, the f value becomes

$$f = \frac{\xi_{12}^2}{\xi_{11}\xi_{22}}. \tag{B.9}$$

Some papers use the assumption of f = 1, and k_{12} is calculated based on $(k_{11}k_{22}K_{12})^{1/2}$. Ratner and Levine [95] discussed the conditions, when this assumption can be made. First, activation energy for all species does not depend on its reaction partner. Second, species in the transition state are the same for the cross reaction and for the self-exchange reactions. The assumption of f = 1 is valid for larger ligands, rather than smaller one, and for outer-sphere electron transfer, rather than for inner-sphere electron transfers. The assumption of $f \neq 1$, has to be used when reactants are of '*very different charges and sizes*' [95].

The inverted region is defined when the reaction is strongly exergonic and the equilibrium constant K_{12} and product of the rates $k_{11}k_{22}$ are large. The corresponding condition is $-\Delta G^{o}_{12} > 2(\Delta G_{11}^{\ddagger} + \Delta G_{22}^{\ddagger})$, or simply:

$$-\Delta G^{o}_{12} > \lambda_{12} \tag{B.10}$$

With the assumption of similar spherical shapes of molecules (Eqs. B.11-12)

$$\lambda_{12} = (\lambda_{11} + \lambda_{22}) / 2 \tag{B.11}$$

$$\Delta G^{\ddagger}_{12} = (\Delta G^{\ddagger}_{11} + \Delta G^{\ddagger}_{22}) / 2 \tag{B.12}$$

and utilizing the fact that $\Delta G^{\ddagger}_{12} = \lambda_{12}/4$,

the following relations can be obtained:

$$2(\Delta G^{\ddagger}_{11} + \Delta G^{\ddagger}_{22}) = \lambda_{12} \tag{B.13}$$

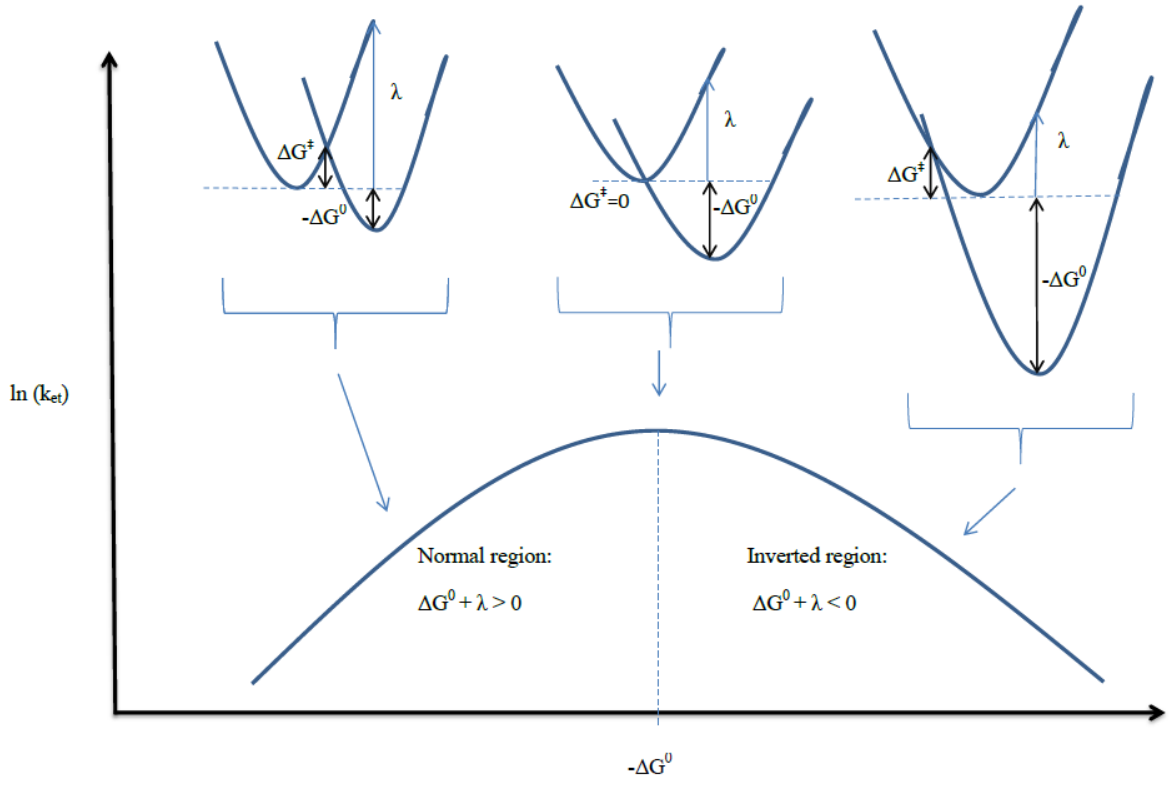

Figure B.1. Plot of the logarithm of the electron transfer rate vs the free energy change for the reaction.

For inverted region, K_{12} [94, 119] is given by

$$logK_{12} = 2log\left(\frac{\xi^2}{k_{11}k_{22}}\right) \tag{B.14}$$

Appendix C: The Photoinduced Electron Transfer. The Rehm-Weller Approach

The Rehm-Weller equation (Eq. C.5) verifies experimental data for photoinduced electron transfer. This equation calculates the free energy of photoinduced reaction from the redox potentials and excitation energies and shows that the value of excited state electron transfer rate, k'_{12} (Fig. C.1), reaches a limiting value of diffusion controlled process (Fig. C.2).

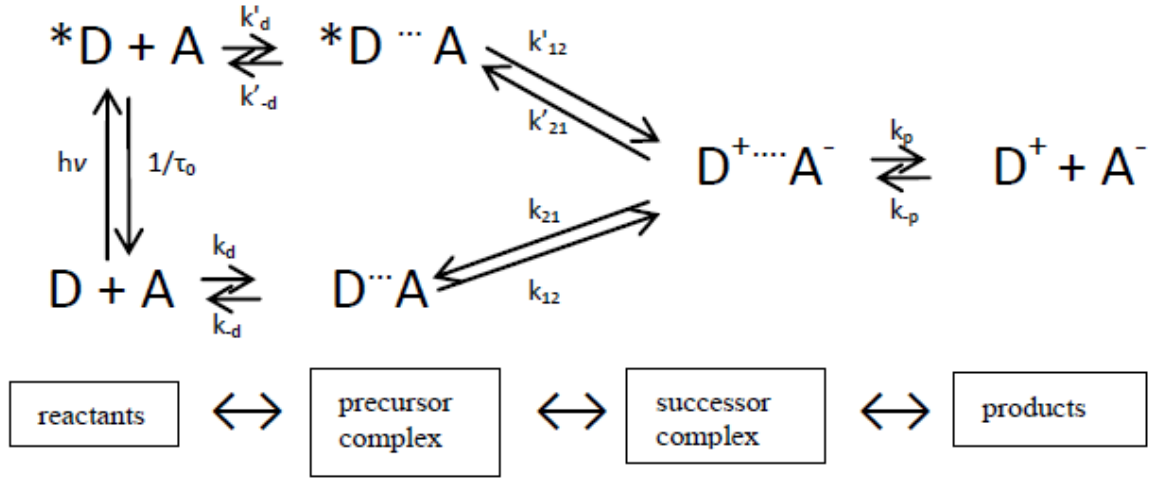

Figure C.1. Scheme for excited state electron transfer between donor and acceptor. k_d, k_{-p}, k'_d are diffusion rate constants, k_{-d}, k_p, k'_{-d} are dissociation rate constant of the precursor and successor rate constant, k_{12}, k_{21}, k'_{12}, k'_{21} are rate constant for forward and back electron transfer in the ground state and excited state; $1/\tau_0$ deactivation of excited state of the donor complex

Under this scheme, excited state *D is quenched by the acceptor in its ground state. Quenching may lead to electron transfer products between D^+ and A^-.

With this diagram in mind (Fig. C.1), the steady state approximation for quenching constant can be expressed as:

$$k_q = \frac{k'_d}{1+\frac{k'_{-d}}{k'_{12}}+\frac{k'_{-d}k'_{21}}{k'_{12}(k_{21}+k_p)}} \quad \text{(C.1)}$$

which examines the following possibilities:

a. If $k_q = k'_{d,}$ reaction is a diffusion controlled process

b. If $k'_{-d} > k'_{12}$ and $k'_{21} << (k_{21} + k_p)$, then

$$k_q = k'_d k'_{12} / k'_{-d} \quad \text{(C.2)}$$

with k'_{12} as a rate demining step of electron transfer at the precursor complex

c. If $k'_{-d} > k'_{12}$ and $k'_{21} >> (k_{21} + k_p)$, then

$$k_q = k'_d (k'_{12}(k_{21} + k_p)) / k'_{-d}k'_{21} \quad \text{(C.3)}$$

with rate(s) determining step of electron transfer to the ground state (k_{21}) and dissociation to the final product (k_p)

d. If $k'_{-d} \sim k'_{12}$ and $(k_{21} + k_p) >> k'_{21}$, the last term in Eq. C.1 is neglected: $[(k'_{-d}k'_{21}) / (k'_{12}(k_{21}+k_p))] \sim 0$ and

$$k_q = (k'_d k'_{12}) / (k'_{-d} + k'_{12}) \quad \text{(C.4.a)}$$

and with a further assumption that $k'_d = k'_{-d}$ is usually written as [97]:

$$1/k_q = 1/k_{et} + 1/k_{diff} \quad \text{(C.4.b)}$$

where $k'_{12} = k_{et}$ is an excited state electron transfer rate, and k'_d is assigned as k_{diff} in the text.

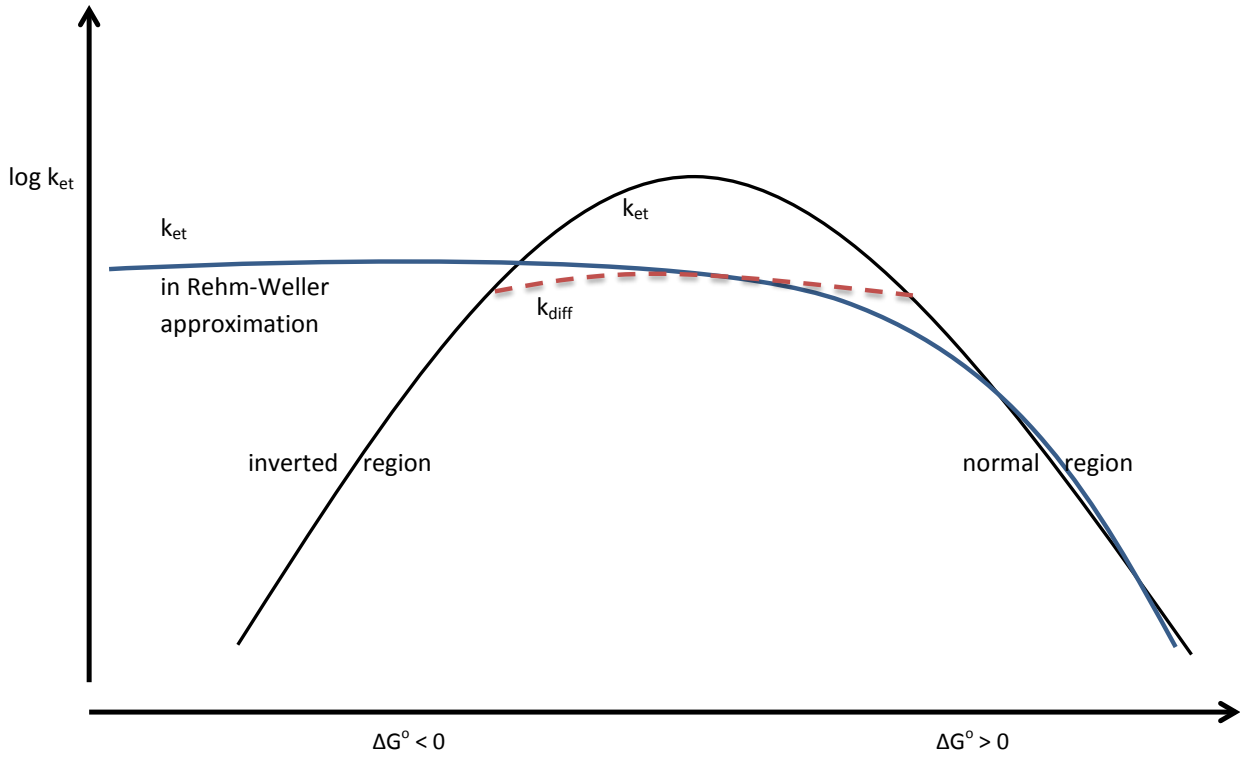

Figure C.2. Parabolic shape of the Marcus theory, where electrons transfer rate k_{et}, depends on thermodynamics of the reaction. Often, k_{et} is greater than diffusion rate, k_{diff}.

For an endothermic reaction, $\Delta G^{0}_{12} > 0$, Rehm-Weller plot agrees with Marcus theory and shows decreased value of k_{et} as the free energy of reaction increases, Fig. C.2. On the other hand, as the reaction becomes more exergonic, $\Delta G^{0}_{12} < 0$, k_{et} is limited to the diffusion rate $k_{diff} \approx 10^{11}\ M^{-1} \cdot s^{-1}$ (for uncharged species). Despite very rapid reaction, all electron transfer reaction cannot go faster than diffusion rate; $1/k_q = 1/k_{diff} + 1/k_{et.}$ The Rehm-Weller equation includes the Columbic forces which does not allowed for the inverted region go beyond the diffusion process and $k_{diff} \approx k_{et,}$ Fig. C.2. The Rehm-Weller equation for photoinduced electron transfer is defined in Eq. C.5.

The free energy of the reaction and the transition state are

$$\Delta G_{12}^{0} = E_{(D/D+)} - E_{(A-/A)} - E_{0-0} - \frac{e^2}{D(r_D + r_A)} \quad \text{(C.5)}$$

where $E_{(D/D+)}$ is the oxidation potential of the donor

$$D \rightarrow D^{+} + e^{-} \quad \text{(C.6)}$$

$E_{(A/A-)}$ is the reduction potential of the acceptor

$$A + e^{-} \rightarrow A^{-} \quad \text{(C.7)}$$

$E_{0\text{-}0}$ is the excitation energy for either donor or acceptor, and the last term describes coulombic attraction between two ions (Eq. A.5).

The transition state is defined as

$$\Delta G_{12}^{\ddagger} = \frac{\Delta G_{12}^{0}}{2} + \left[\left(\frac{\Delta G_{12}^{0}}{2}\right)^2 + \left(\frac{\lambda}{4}\right)^2\right]^{1/2} \quad \text{(C.8)}$$

where λ is the reorganization energy. The reorganization energy is discussed in detail in the Appendix A.

References

1. Basic Research Needs for Solar Energy Utilization: Report of the Basic Energy Sciences Workshop on Solar Energy Utilization, A., 2005, US Department of Energy Office of Basic Energy Sciences

2. Cyrille Costentin, C., et al., *Concerted proton-coupled electron transfers in aquo/hydroxo/oxo metal complexes: Electrochemistry of* $[Os^{II}(bpy)_2py(OH_2)]^{2+}$ *in water.* PNAS, 2009. **106**(29): p. 11829-11836.

3. Conception, J.J., et al., *mechanism of Water Oxidation by Single-Site Ruthenium Complex Catalysts.* JACS, 2010. **132**: p. 1545-1557.

4. Franca`s, L., et al., *Ru Complexes That Can Catalytically Oxidize Water to Molecular Dioxygen.* Inorg. Chem., 2008. **47**: p. 1824-1834.

5. Goez, M., et al., *Photoionization of* $[Ru(bpy)_3]^{2+}$ *: A Catalytic Cycle with Water as Sacrificial Donor.* J. Phys. Chem. A, 2004. **108**: p. 1090-1100.

6. Tarnowsky, A.N., et al., *Photoexcitation of Aqueous Ruthenium(II)-tris-(2,2-bipyridine) with High-Intensity Femtosecond Laser Pulses.* J. Phys. Chem. B, 2006. **110**: p. 26497-26505.

7. Bock, C.R., Meyer, T. J., Whitten, D. G., *Electron Transfer Quenching of the Luminescent Excited State of Tris(2,2'-bipyridine)ruthenium(II). A Flash Photolysis Relaxation Technique for Measuring the Rates of Very Rapid Electron Transfer Reactions.* J. Amer. Chem. Soc. , 1974. **96**: p. 4710-4712.

8. Navon, G. and N. Sutin, *Mechanism of the Quenching of the Phosphorescence of Tris(2,2'-bipyridine)ruthenium(II) by Some Cobalt(III) and Ruthenium(III) Complexes.* Inorg. Chem., 1974. **13**: p. 2159-2164.

9. Lin, C.T. and N. Sutin, *Quenching of the Luminescence of the Tris(2,2'-bipyrydine) Complexes of Ruthenium (II) and Osnium (II). Considerations and Photogalvanic Effects.* J. Phys. Chem., 1976. **80**: p. 97-105.

10. Thompson, D.W., et al., *Efficient Generation of the Ligand Field Excited State of Tris-(2,2'-bipyridine)-ruthenium(II) through Sequential Two-Photon Capture by* $[Ru(bpy)_3]^{2+}$ *or Electron Capture by* $[Ru(bpy)_3]^{3+}$*.* J. Phys. Chem. A, 2001. **105**(35): p. 8117-8122.

11. Sun, H. and M.Z. Hoffman, *Reductive Quenching of the Excited States of Ruthenium(II) Complexes Containing 2,2'-Bipyridine, 2,2'-Bipyrazine, and 2,2'-Bipyrimidine Ligands.* J. Phys. Chem., 1994. **98**: p. 11719-11726.

12. Sun, H., A. Yoshimura, and M.Z. Hoffman, *Oxidative Quenching of the Excited State of Tris(2,2'-bipyridine)ruthenium(2+) Ion by Methylviologen. Variation of Solution Medium and Temperature.* J. Phys. Chem., 1994. **98**: p. 5058-5064.

13. Braunstein, C.H., et al., *Spectroscopic and Electrochemical Properties of the Dimer Tetrakis (2,2'-bip yridine) (p- 2,3- bis (2-pyridyl) pyrazine diruthenium (II) and Its Monomeric Analogue.* Inorganic chemistry, 1984, **23**: p. 857-864.

14. Rangan, K., et al., *Solar energy conversion using photochemical molecular devices: photocatalytic hydrogen production from water using mixed-metal supramolecular complexes.* Energy & Environmental Science, 2009. **2**(4): p. 410-419.

15. Jaffe, H.H. and A.L. Miller, *The fates of electronic excitation energy.* Journal of Chemical Education, 1966. **43**(9): p. 469.

16. Dougherty, T., et al., *Excited-State Coordination Chemistry: A New Quenching Mechanism.* JACS, 1998. **120**: p. 4226-4227.

17. Hosek, W., et al., *Enhanced Excited-State Basicities of Coordinated Bridging Bis(diimines) (BL) in* $Ru(bpy)_2(BL)^{2+}$ *(bpy = 2,2 '-Bipyridine).* Inorganic chemistry, 1989. **28**: p. 1228-1231.

18. Quayle, W.H. and J.H. Lunsford, *Tris(2,2'-bipyridine)ruthenium(III) in zeolite Y: characterization and reduction on exposure to water.* Inorganic Chemistry, 1982. **21**(1): p. 97-103.

19. Nazeeruddin, M.K., S.M. Zakeeruddin, and K. Kalyanasundaram, *Enhanced intensities of the ligand-to-metal charge-transfer transitions in ruthenium(III) and osmium(III) complexes of substituted bipyridines.* The Journal of Physical Chemistry, 1993. **97**(38): p. 9607-9612.

20. Demas, J.N. and A.W. Adamson, *Tris (2,2'-bipyridine)ruthenium(II) sensitized reactions of some oxalato complexes.* Journal of the American Chemical Society, 1973. **95**(16): p. 5159-5168.

21. Rubinstein, A. and A.J. Bard, *Electrogenerated Chemiluminescence. 37. Aqueous Ecl Systems Based on Ru(2,2'-bipyridine)*$_3^{2+}$ *and Oxalate or Organic Acids.* JACS, 1981. **103**: p. 512-516.

22. Campagna, S., et al., *Photochemistry and Photophysics of Coordination Compounds: Ruthenium*, in *Photochemistry and Photophysics of Coordination Compounds I*, V. Balzani and S. Campagna, Editors. 2007, Springer Berlin Heidelberg. p. 117-214.

23. Zambrana J. L. Jr., *EXCITED-STATE ACID-BASE & COORDINATION CHEMISTRY OF RUTHENIUM(II) DIIMINES: ASSOCIATION WITH VARIOUS METAL CATIONS*, Ph. D. Thesis, *Graduate Center*2007, CUNY: New York.

24. Zambrana, J.L. Jr., et al., *Multiple Charge-transfer Emissions from Different Metal-Ligand Pairs in Ruthenium Diimines.* Inorg. Chem., 2008. **47**: p. 2-4.

25. Zambrana, J.L. Jr, E.X. Ferloni, and H.D. Gafney, *Excited-State Coordination Chemistry: Excited-State basicity of Bis(2,2'-bypyridyl)(2,3-dipyridylpyrazine)Ruthenium (II).* J. Phys. Chem. A, 2009. **113**: p. 13457-13468.

26. Ferloni, E., *Ground - and excited state chemistry of [bis(2,2'-bypyridine)(2-(2-pyrydyl)pyrazine) ruthenium(II)]: protonation and coordination, Ph.D. Thesis, Graduate Center CUNY*2012: New York.

27. Laurence, G.S. and V. Balzani, *Reduction by the Triplet C harge-Transfer State of Tris(bipyridyl)ruthenium(II) Photochemical Reaction between Tris(bipyridyl)ruthenium(II) and Thallium(III).* Inorg. Chem., 1974. **13**: p. 2976-2982.

28. Lin, C.T. and N. Sutin, *Steady-State Considerations in the Electron-Transfer Quenching of the Tris(2,2‘ bipyridine)ruthenium(II) Luminescence.* J. Amer. Chem. Soc., 1975. **97**: p. 3543-3545.

29. Lin, C.T., et al., *Mechanism of the quenching of the emission of substituted polypyridineruthenium(II) complexes by iron(III), chromium(III), and europium(III) ions.* JACS, 1976. **98**(21): p. 6536-6544.

30. Creutz, C., et al., *Lifetimes, Spectra, and Quenching of the Excited States of Polypyridine Complexes of Iron(II), Ruthenium(II), and Osmium(III).* JACS, 1980. **10**(4): p. 1309-1319.

31. Geletii, Y.V., et al., *Homogeneous Light-Driven Water Oxidation Catalyzed by a Tetraruthenium Complex with All Inorganic Ligands.* Journal of the American Chemical Society, 2009. **131**(22): p. 7522-7523.

32. Kaledin, A.L., et al., *Insights into Photoinduced Electron Transfer between $[Ru(bpy)_3]^{2+}$ and $[S_2O_8]^{2-}$ in Water: Computational and Experimental Studies.* J. Phys. Chem. A, 2010. **114**: p. 73-80.

33. Libby, W.F., *Theory of Electron Exchange Reactions in Aqueous Solution.* The Journal of Physical Chemistry, 1952. **56**(7): p. 863-868.

34. Taube, H., H. Myers, and R.L. Rich, *OBSERVATIONS ON THE MECHANISM OF ELECTRON TRANSFER IN SOLUTION1.* Journal of the American Chemical Society, 1953. **75**(16): p. 4118-4119.

35. Hammershoi, A., D. Geselowitz, and H. Taube, *Redetermination of the hexaaminecobalt(III/II) electron-self-exchange rate.* Inorganic Chemistry, 1984. **23**(7): p. 979-982.

36. Young, R.C., F.R. Keene, and T.J. Meyer, *Measurement of rates of electron transfer between tris(2,2'-bipyridine)ruthenium(3+) and tris(1,10-phenanthroline)iron(2+) ions and between tris(1,10-phenanthroline)ruthenium(3+) and tris(2,2'-bipyridine)ruthenium(2+) ions by differential excitation flash photolysis.* Journal of the American Chemical Society, 1977. **99**(8): p. 2468-2473.

37. Man-Sheung, C. and A.C. Wahl, *Rate of electron exchange between iron, ruthenium, and osmium complexes containing 1,10-phenanthroline, 2,2'-bipyridyl, or their derivatives from nuclear magnetic resonance studies.* The Journal of Physical Chemistry, 1978. **82**(24): p. 2542-2549.

38. Farid, S., et al., *Reexamination of the Rehm–Weller Data Set Reveals Electron Transfer Quenching That Follows a Sandros–Boltzmann Dependence on Free Energy.* Journal of the American Chemical Society, 2011. **133**(30): p. 11580-11587.

39. Prasad, E. and K.R. Gopidas, *Photoinduced Electron Transfer in Hydrogen Bonded Donor−Acceptor Systems. Study of the Dependence of Rate on Free Energy and Simultaneous Observation of the Marcus and Rehm−Weller Behaviors†.* Journal of the American Chemical Society, 2000. **122**(13): p. 3191-3196.

40. Yamaguchi, T., et al., *Determination of the Hydration Structure of Silver Ions in Aqueous Silver Perchlorate and Nitrate Solutions from EXAFS using Synchroton Radiation.* Acta ChemicaScandinavica A, 1984. **38**: p. 423-428.

41. Stefánsson, A., K.H. Lemke, and T.M. Seward, *Iron(III) complexation in hydrothermal solutions – An experimental and theoretical study.* Inorg. Chem., 1981. **20**: p. 3565-3566.

42. Hair, N.J. and J.K. Beattie, *Structure of hexaaquairon(III) nitrate trihydrate. Comparison of iron(II) and iron(III) bond lengths in high-spin octahedral environments.* Inorganic Chemistry, 1977. **16**(2): p. 245-250.

43. Bu, Y., S. Liu, and X. Song, *Ab initio calculation of inner-sphere reorganization energy for the Fe2+ (H2O)6/Fe3+ (H2O)6 electron transfer system.* Chemical Physics Letters, 1994. **227**(1–2): p. 121-125.

44. Flynn, C.M., *Hydrolysis of inorganic iron(III) salts.* Chemical Reviews, 1984. **84**(1): p. 31-41.

45. Harris, D., G.H. Loew, and A. Komornicki, *Structure and Relative Spin-State Energetics of [Fe(H2O)6]3+: A Comparison of UHF, Møller−Plesset, Nonlocal DFT, and Semiempircal INDO/S Calculations.* The Journal of Physical Chemistry A, 1997. **101**(21): p. 3959-3965.

46. Zeng, X., et al., *Calculating solution redox free energies with ab initio quantum mechanical/molecular mechanical minimum free energy path method.* The Journal of Chemical Physics, 2009. **130**(16): p. 164111-8.

47. Jolivet, J.-P., C. Chaneac, and E. Tronc, *Iron oxide chemistry. From molecular clusters to extended solid networks.* Chemical Communications, 2004. **0**(5): p. 481-483.

48. Whittemore, D.O. and D. Langmuir, *Standard electrode potential of Fe3+ + e- = Fe2+ from 5-35.deg.* Journal of Chemical & Engineering Data, 1972. **17**(3): p. 288-290.

49. Gafney, H.D. and A.W. Adamson, *Chemiluminescence. An illuminating experiment.* Journal of Chemical Education, 1975. **52**(7): p. 480.

50. Sun, H. and M.Z. Hoffman, *Photo-induced charge separation by ruthenium (II) photosensitizers.* Proc. Indian Acad. Sci. (Chem. Sci.), 1993. **105**(6): p. 487-494.

51. Hoffman, M.Z., *Study of intermediates from transition metal excited state electron transfer reactions* 1992, Department of Energy: Boston.

52. Calvert, J.G. and J.N. Pitts, *Photochemistry*, New York: Wiley, 1968.

53. Zambrana, J.L. Jr., et al., *Multiple Charge-Transfer Emissions from Different Metal–Ligand Pairs in Ruthenium Diimines.* Inorganic Chemistry, 2008. **47**(1): p. 2-4.

54. Zambrana, J.L. Jr., E.X. Ferloni, and H.D. Gafney, *Excited-State Coordination Chemistry: Excited-State Basicity of Bis(2,2′-bipyridyl)(2,3-dipyridylpyrazine)ruthenium(II).* The Journal of Physical Chemistry A, 2009. **113**(48): p. 13457-13468.

55. Damrauer, N.H., et al., *Femtosecond Dynamics of Excited-State Evolution in $[Ru(bpy)_3]^{2+}$.* Science, 1997. **275**: p. 54-57.

56. Georgopoulos, M. and M.Z. Hoffman, *Cage escape yields in the quenching of tris (2,2'-bipyridine)ruthenium(II) by methylviologen: presence of triethanolamine as a sacrificial electron donor.* The Journal of Physical Chemistry, 1991. **95**(20): p. 7717-7721.

57. Hoffman, M., *Study of intermediates from transition metal excited-state electron-transfer reactions*, in *DOE*1997, Department of Energy.

58. Hoffman, M.Z., *Study of Intermediates from Transition Metal Excited-State Electron-Transfer Reactions*, 1993, Deparment of Energy: Boston.

59. Reader, J. and J. Sugar, *Energy levels of iron, Fe I through Fe XXVI.* Journal of Physical and Chemical Reference Data, 1975. **4**(2): p. 353-440.

60. Eberson, L., *Electron-Transfer Reactions in Organic Chemistry*, in *Advances in Physical Organic Chemistry*, V. Gold and D. Bethell, Editors. 1982, Academic Press. p. 79-185.

61. Haga, M.-a., et al., *Proton-Induced Tuning of Electrochemical and Photophysical Properties in Mononuclear and Dinuclear Ruthenium Complexes Containing 2,2'-Bis(benzimidazol-2-yl)-4,4'-bipyridine: Synthesis, Molecular Structure, and Mixed-Valence State and Excited-State Properties.* Inorganic chemistry, 1996. **35**: p. 3335-3347.

62. Balzani, V., et al., *Designing Dendrimers Based on Transition-Metal Complexes. Light-Harvesting Properties and Predetermined Redox Patterns.* Acc. Chem. Res., 1998. **31**: p. 26-34.

63. Campagna, S., et al., *Syntheses, Absorption Spectra, Luminescence Properties, and Electrochemical Behavior of Mono- and Binuclear Ruthenium(II) Complexes of Isomeric Bis(2-pyridyl)pyrazines.* Inorganic chemistry, 1989. **28**: p. 2565-2570.

64. Juris, A., et al., *Ru(II) POLYPYRIDINE COMPLEXES: PHOTOPHYSICS, PHOTOCHEMISTRY, ELECTROCHEMISTRY, AND CHEMILUMINESCENCE.* Coordination Chemistry Reviews, 1988. **84**: p. 85-277.

65. Wu, A., et al., *Synthesis and Characterization of Ruthenium Bis(β–diketonato) Pyridine-Imidazole Complexes for Hydrogen Atom Transfer.* Inorganic chemistry, 2007. **46**: p. 11190-11201.

66. Manner, V.W., A.G. DiPasquale, and J.M. Mayer, *Facile Concerted Proton–Electron Transfers in a Ruthenium Terpyridine-4′-Carboxylate Complex with a Long Distance Between the Redox and Basic Sites.* Journal of the American Chemical Society, 2008. **130**(23): p. 7210-7211.

67. Henrich, J.D., et al., *Ultrafast Electron Transfer Dynamics in Ruthenium Polypyridyl Complexes with a π-Conjugated Ligand.* J. Phys. Chem. B, 2010.

68. Small, Y.A., et al., *Proton management as a design principle for hydrogenase-inspired catalysts.* Energy & Environmental Science, 2011. **4**(8): p. 3008-3020.

69. Tsai, M.-K., et al., *Characterization of Redox States of Ru(OH2)(Q)(tpy)2+ (Q = 3,5-di-tert-butyl-1,2-benzoquinone, tpy = 2,2′:6′,2″-terpyridine) and Related Species through Experimental and Theoretical Studies.* Inorganic Chemistry, 2009. **48**(10): p. 4372-4383.

70. Badaeva, E., et al., *Effect of deprotonation on absorption and emission spectra of Ru(ii)-bpy complexes functionalized with carboxyl groups.* Physical Chemistry Chemical Physics, 2010. **12**(31): p. 8902-8913.

71. Wang, T., G. Brudvig, and V.S. Batista, *Characterization of Proton Coupled Electron Transfer in a Biomimetic Oxomanganese Complex: Evaluation of the DFT B3LYP Level of Theory.* J. Chem. Theory Comput., 2010. **6**: p. 755-760.

72. Zheng, K.C., et al., *Theoretical Studeis on the electronic structures and related properties of [Ru(L)3]2+ (L=bpy, bpm, bpz) with DFT method.* Journal of Molecular Structure: THEOCHEM, 2002. **582**: p. 1-9.

73. Xu, L.-C., et al., *DFT-TDDFT studies on electronic absorption and emission spectra of* $[Ru(bpy)_2(L)]^{2+}$ *(L=pip, o-mopip and p-mopip) in aqueous solution.* Journal of Molecular Structure: THEOCHEM, 2008. **855**: p. 77-81.

74. Kuharski, R.A., et al., *Molecular model for aqueous ferrous-ferric electron transfer.* J. Chem. Phys., 1988. **89**: p. 3248-3257.

75. Jarzęcki, A.A., A.D. Anbar, and T.G. Spiro, *DFT Analysis of Fe(H2O)63+ and Fe(H2O)62+ Structure and Vibrations; Implications for Isotope Fractionation.* The Journal of Physical Chemistry A, 2004. **108**(14): p. 2726-2732.

76. Yapo-Kicho, D., P. Lagant, and G. Vergoten, *The SPASIBA Force Field for Studying Iron-Tannins Interactions : Application to Fe3+ /Fe2+ Catechol Complexe.* International Journal of Molecular Sciences, 2007. **8**(3): p. 259-272.

77. Costentin, C., M. Robert, and J.M. Saveant, *Concerted proton-electron transfers in the oxidation of phenols.* Phys. Chem. Chem. Phys., 2010. **12**: p. 11179-11190.

78. Cukier, R.I. and D.G. Nocera, *PROTON-COUPLED ELECTRON TRANSFER.* Annu. Rev. Phys. Chem., 1998. **49**: p. 337-369.

79. Gagliardi, C.J., et al., *Integrating proton coupled electron transfer (PCET) and excited states.* Coordination Chemistry Reviews, 2010. **254**: p. 2459-2471.

80. Hammes-Schiffer, S. and A.V. Soudackov, *Proton-Coupled Electron Transfer in Solution, Proteins, and Electrochemistry†.* The Journal of Physical Chemistry B, 2008. **112**(45): p. 14108-14123.

81. Mayer, J.M., *PROTON-COUPLED ELECTRON TRANSFER: A Reaction Chemist's View.* Annu. Rev. Phys. Chem., 2004. **55**: p. 363-390.

82. Huynh, M.H.V. and T.J. Meyer, *Proton-Coupled Electron Transfer.* Chem. Rev., 2007. **107**: p. 5004-5064.

83. Skone, J.H., A.V. Soudackov, and S. Hammes-Schiffer, *Calculation of Vibronic Couplings for Phenoxyl/Phenol and Benzyl/Toluene Self-Exchange Reactions: Implications for Proton-Coupled Electron Transfer Mechanisms.* JACS, 2006. **128**: p. 16655-16663.

84. Edwards, S., A.V. Soudackov, and S. Hammes-Schiffer, *Driving force dependence of rates for nonadiabatic proton and proton-coupled electron transfer: Conditions for inverted region behavior.* J. Phys. Chem. B, 2009. **113**(44): p. 14545-14548.

85. Hammes-Schiffer, S. and A.V. Soudackov, *Proton-Coupled Electron transfer in Solution, proteins, and Electrochemistry.* J. Phys. Chem. B, 2008. **112**: p. 14108-14123.

86. Hammes-Schiffer, S. and A.A. Stuchebrukhov, *Theory of Coupled Electron and Proton Transfer Reactions.* Chem. Rev., 2010. **110**: p. 6939-6960.

87. Kelly, C.P., C.J. Cramer, and D.G. Truhlar, *Single-Ion Solvation Free Energies and the Normal Hydrogen Electrode Potential in Methanol, Acetonitrile, and Dimethyl Sulfoxide.* J. Phys. Chem. B, 2007. **111**: p. 408-422.

88. Kelly, C.P., C.J. Cramer, and D.G. Truhlar, *Aqueous Solvation Free Energies of Ions and Ion-Water Clusters based on an Accurate Value for the Absolute Aqueous Solvation Free Energy of the Proton.* J. Phys. Chem. B, 2006. **110**: p. 16066-16081.

89. Ruthkosky, M., et al., *Electron and energy transfer from Cu(I) MLCT excited states.* Coordination Chemistry Reviews, 1998. **171**: p. 309-322.

90. Bashford, D. and D.A. Case, *GENERALIZED BORN MODELS OF MACROMOLECULAR SOLVATION EFFECTS.* Annual Review of Physical Chemistry, 2000. **51**(1): p. 129-152.

91. Cramer, C.J. and D.G. Truhlar, *Implicit Solvation Models: Equilibria, Structure, Spectra, and Dynamics.* Chemical Reviews, 1999. **99**(8): p. 2161-2200.

92. Meyer, T.J. and H. Taube, *Electron-transfer reactions of ruthenium ammines.* Inorganic Chemistry, 1968. **7**(11): p. 2369-2379.

93. Przystas, T.J. and N. Sutin, *Kinetic Studies of Anion-Assisted Outer-Sphere Electron Transfer Reaction.* JACS, 1973. **95**(17): p. 5545-5555.

94. Berkoff, R., K. Krist, and H.D. Gafney, *Measurement of the rates of the electron-transfer reactions between tris(2,2'-bipyridine)ruthenium(3+) and tris(1,10-phenanthroline)cobalt(2+) or tris(2,2'-bipyridine)cobalt(2+) by flash photolysis techniques.* Inorganic Chemistry, 1980. **19**(1): p. 1-7.

95. Ratner, M.A. and R.D. Levine, *A thermodynamic derivation of the cross-relations for rates of electron-transfer reactions.* Journal of the American Chemical Society, 1980. **102**(15): p. 4898-4900.

96. Sutin, N., *Nuclear, electronic, and frequency factors in electron transfer reactions.* Accounts of Chemical Research, 1982. **15**(9): p. 275-282.

97. Sutin, N. and C. Creutz, *Electron-transfer reactions of excited states.* Journal of Chemical Education, 1983. **60**(10): p. 809.

98. KAVARNOS, G.J. and N.J. TURRO, *Photosensitization by Reversible Electron Transfer: Theories, Experimental Evidence, and Examples.* Chem. Rev., 1986. **86**: p. 401-449.

99. Durham, B., et al., *Photoinduced Electron-Transfer Kinetics of Singly Labeled Ruthenium Bis(bipyridine)Dicarboxybipyridine Cytochrome c Derivatives.* Biochemistry, 1989. **28**: p. 8659-8665.

100. Kaledin, A.L., et al., *Insights into Photoinduced Electron Transfer Between* $[Ru(mptpy)_2]^{4+}$ *(mptpy= 4′ (4-methylpyridinio)-2,2′ :6′ ,2′′ -terpyridine) and* $[S_2O_8]^{2-}$*: Computational and Experimental Studies.* J. Phys. Chem. A, 2010. **114**: p. 6284-6297.

101. Stranks, D.R., *Mechanisms of some electron exchange reactions.* Discussions of the Faraday Society, 1960. **29**(0): p. 73-79.

102. Sutin, N., *Electron Exchange Reactions.* Annual Review of Nuclear Science, 1962. **12**(1): p. 285-328.

103. Sigfridsson, E., M.H.M. Olsson, and U. Ryde, *A Comparison of the Inner-Sphere Reorganization Energies of Cytochromes, Iron−Sulfur Clusters, and Blue Copper Proteins.* The Journal of Physical Chemistry B, 2001. **105**(23): p. 5546-5552.

104. Guarr, T., E. Buhks, and G. McLendon, *Quantum effects of high-frequency modes in inorganic electron transfer: kinetic isotope effects in redox reactions of hexaaquairon(2+) ion ([Fe(H2O)6]2+, hexa(aqua-d2)iron(2+) ion ([Fe(D2O)6]2+), and hexa(aqua-18O)iron(2+) ion ([Fe(18OH2)6]2+).* Journal of the American Chemical Society, 1983. **105**(12): p. 3763-3767.

105. Gaussian 09, R.B., Frisch, M. J.; Trucks, G. W.; Schlegel, H. B.; Scuseria, G. E.; Robb, M. A.; Cheeseman, J. R.; Scalmani, G.; Barone, V.; Mennucci, B.; Petersson, G. A.; Nakatsuji, H.; Caricato, M.; Li, X.; Hratchian, H. P.; Izmaylov, A. F.; Bloino, J.; Zheng, G.; Sonnenberg, J. L.; Hada, M.;

Ehara, M.; Toyota, K.; Fukuda, R.; Hasegawa, J.; Ishida, M.; Nakajima, T.; Honda, Y.; Kitao, O.; Nakai, H.; Vreven, T.; Montgomery, Jr., J. A.; Peralta, J. E.; Ogliaro, F.; Bearpark, M.; Heyd, J. J.; Brothers, E.; Kudin, K. N.; Staroverov, V. N.; Kobayashi, R.; Normand, J.; Raghavachari, K.; Rendell, A.; Burant, J. C.; Iyengar, S. S.; Tomasi, J.; Cossi, M.; Rega, N.; Millam, J. M.; Klene, M.; Knox, J. E.; Cross, J. B.; Bakken, V.; Adamo, C.; Jaramillo, J.; Gomperts, R.; Stratmann, R. E.; Yazyev, O.; Austin, A. J.; Cammi, R.; Pomelli, C.; Ochterski, J. W.; Martin, R. L.; Morokuma, K.; Zakrzewski, V. G.; Voth, G. A.; Salvador, P.; Dannenberg, J. J.; Dapprich, S.; Daniels, A. D.; Farkas, Ö.; Foresman, J. B.; Ortiz, J. V.; Cioslowski, J.; Fox, D. J. Gaussian, Inc., Wallingford CT, 2009.

106. Charlot, M.-F., et al., *A Theoretical Investigation into the Photophysical Properties of Ruthenium Polypyridine-Type Complexes.* Chemistry – A European Journal, 2006. **12**(3): p. 796-812.

107. Becke, A.D., *Density-functional thermochemistry. III. The role of exact exchange.* The Journal of Chemical Physics, 1993. **98**(7): p. 5648-5652.

108. Hay, P.J. and W.R. Wadt, *Ab initio effective core potentials for molecular calculations. Potentials for K to Au including the outermost core orbitals.* The Journal of Chemical Physics, 1985. **82**(1): p. 299-310.

109. Biner, M., et al., *Crystal and molecular structures of [Ru(bpy)3](PF6)3 and [Ru(bpy)3](PF6)2 at 105 K.* Journal of the American Chemical Society, 1992. **114**(13): p. 5197-5203.

110. Ferrari, M.B., et al., *Crystal and molecular structure of [Ru(bpy)2(2,3-dpp)]Cl2 • 3H2O • CH3CN and 1H and 99Ru NMR spectra of [Ru(bpy)2(2,n-dpp)][PF6]2 (bpy=2,2′-bipyridine, dpp=bis (2-pyridyl)pyrazine, n=3 or 5).* Inorganica Chimica Acta, 1998. **275–276**(0): p. 320-326.

111. Marcaccio, M., et al., *Electrochemistry and spectroelectrochemistry of polypyridine ligands: A theoretical approach.* Inorganica Chimica Acta, 2007. **360**(3): p. 1154-1162.

112. Rillema, D.P., et al., *Structure and redox and photophysical properties of a series of ruthenium heterocycles based on the ligand 2,3-bis(2-pyridyl)quinoxaline.* Inorganic Chemistry, 1987. **26**(4): p. 578-585.

113. Kalyanasundaram, K., *Photophysics, photochemistry and solar energy conversion with tris(bipyridyl)ruthenium(II) and its analogues.* Coordination Chemistry Reviews, 1982. **46**(0): p. 159-244.

114. Du, H., et al., *Technical and Software Note PhotochemCADtt: A Computer-Aided Design and Research Tool in Photochemistry* Photochemistry and Photobiology, 1998. **68**(2): p. 141-142.

115. Barone, V. and M. Cossi, *Quantum Calculation of Molecular Energies and Energy Gradients in Solution by a Conductor Solvent Model.* The Journal of Physical Chemistry A, 1998. **102**(11): p. 1995-2001.

116. Cossi, M., et al., *Energies, structures, and electronic properties of molecules in solution with the C-PCM solvation model.* Journal of Computational Chemistry, 2003. **24**(6): p. 669-681.

117. This research was supported, i.p., under National Science Foundation Grants CNS-0958379 and CNS-0855217 and the City University of New York High Performance Computing Center at the College of Staten Island.

118. Creutz, C. and N. Sutin, *Vestiges of the "inverted region" for highly exergonic electron-transfer reactions.* Journal of the American Chemical Society, 1977. **99**(1): p. 241-243.

119. Bruck, D. and M. Rabinovitz, *Vestiges of the inverted region for highly exergonic electron-transfer reactions.* JACS, 1977. **99**: p. 241-243.